UNIVERSIDAD AUTÓNOMA DE MADRID

FACULTAD DE CIENCIAS

STUDY OF THE EVOLUTION OF IRRADIATION INDUCED DEFECTS IN $FeCr_x$ MODEL ALLOYS FOR FUSION APPLICATIONS BY MEANS OF *IN-SITU* RESISTIVITY TECHNIQUES

BEGOÑA GÓMEZ-FERRER HERRÁN

A dissertation submitted in partial fulfillment of the requirements for
the degree of Doctor of Philosophy
(Physics)

September 2014

Laboratorio Nacional de Fusión
Centro de Investigaciones Energéticas, Medioambientales y Tecnológicas

Centro de Micro-Análisis de Materiales
Universidad Autónoma de Madrid

STUDY OF THE EVOLUTION OF IRRADIATION INDUCED DEFECTS IN Fe-Cr MODEL ALLOYS FOR FUSION APPLICATIONS BY MEANS OF *IN-SITU* RESISTIVITY TECHNIQUES

Author: Begoña Gómez-Ferrer Herrán

Directors: Rafael Alberto Vila Vázquez, Ph. D. in Physics, CIEMAT
David Jiménez Rey, Ph. D. in Physics, CMAM

Tutor: Aurelio Climent Font, Ph. D. in Physics, Professor of the "Departamento de Física Aplicada" of UAM

September 2014

A Francis y Ramón, mis padres.

Resumen

Los aceros ferrítico/martensíticos de baja activación son materiales candidatos para los futuros reactores de fusión. Su comportamiento bajo radiación puede ser simulado en primera aproximación mediante aleaciones modelo Fe-Cr. Se ha demostrado que concentraciones significativas de Cr, entre 6-14 at.%, son necesarias para proveer a los aceros buenas propiedades mecánicas de resistencia a la radiación y a la corrosión. Se sabe también que la evolución de la microestructura de los materiales inducida por la radiación neutrónica depende del contenido en Cr. El conocimiento del papel del Cr en la evolución de defectos es por tanto vital, pero en el presente aún incompleto. Dentro de este marco, el objetivo de este trabajo es ampliar el estudio experimental de la interacción y la cinética de defectos puntuales en estas aleaciones concentradas. Esto permite ampliar la cantidad de datos experimentales fiables para validación de simulaciones computacionales y poder así consolidar su desarrollo. Por tanto, con este fin, se ha diseñado y construido un sistema experimental adecuado y posteriormente llevado a cabo experimentos de Recuperación de Resistividad en Fe_{1-x}-Cr_x (x = 0, 0.05, 0.10, 0.14).

En los primeros capítulos el lector encontrará la motivación de este trabajo (Capítulo 1) y un capítulo introductorio donde se explican los principios básicos de la naturaleza de la resistividad en aleaciones binarias no-simples, los efectos de la radiación y la naturaleza y metodología de los experimentos de Recuperación de Resistividad (Capítulo 2).

El Capítulo 3 está dedicado a explicar en profundidad el diseño, desarrollo y puesta a punto del sistema experimental que ha sido la principal actividad desarrollada en esta tesis doctoral. Descrito brevemente, el método consiste en irradiar las muestras a temperaturas criogénicas con iones altamente energéticos para inducir daño por desplazamiento e inmovilizar los defectos formados. Posteriormente, las muestras se someten a un proceso de recocido por pasos donde la temperatura es incrementada una cierta cantidad a cada paso. La evolución del daño en la microestructura se monitoriza con medidas de la resistividad de la muestra irradiada a cada paso del recocido. La variación registrada de la resistividad provee información sobre la movilidad, recombinación y agregación de defectos. Cabe destacar, que en el transcurso de este trabajo, además de montar la técnica experimental se ha propuesto un método mejorado para medir la recuperación de la resistividad en aleaciones concentradas, que se detalla en el Capítulo 2.

En el Capítulo 4 se presenta un resumen de lo que se sabe específicamente de las aleaciones Fe-Cr, incluyendo la discusión y el repaso del estado del arte en el Fe puro y las aleaciones diluidas dado que resulta fundamental para dar el salto a la comprensión del

sistema Fe-Cr concentrado que todavía presenta muchas incógnitas tanto desde el punto de vista experimental como de simulaciones.

Finalmente los resultados experimentales, la discusión y las conclusiones se presentan en los capítulos 5 y 6. El nuevo método propuesto abre una posibilidad de obtener resultados de recuperación de la resistividad más adecuados para las simulaciones computacionales. También pone de manifiesto fenómenos, no observados anteriormente, relativos al comportamiento del Cr en presencia de migración de defectos que aún no se entienden bien y deben ser estudiados. Finalmente la comparativa de las medidas obtenidas en este trabajo con los escasos datos experimentales de la literatura, permite hacer una discusión crítica sobre la utilidad de esta técnica, poniendo de manifiesto su complejidad tanto experimental como de interpretación.

Abstract

Reduced activation ferritic/martensitic steels are candidate structural materials for future fusion reactors. These steels can, to a first approximation, be modelled by considering the behavior of binary Fe-Cr alloys. It has been shown that a significant amount of Cr, in the range of 6-14at%, is necessary to provide good mechanical properties of radiation and corrosion resistance. The microstructure evolution induced by neutron irradiation is known to depend on the Cr content. Current knowledge of the role of Cr in the effects of neutron radiation is therefore essential, but still incomplete. The current objective is to extend the experimental study of the point-defect interaction and kinetics in concentrated alloys. This would allow increasing a reliable database of experimental results for validation of computational simulations in order to consolidate the development of models. Thus, to this end, a suitable experimental set-up has been designed and built and subsequently Resistivity Recovery experiments have been run in Fe_{1-x}-Cr_x (x = 0, 0.05, 0.10, 0.14).

In the first chapters the reader will be able to find the motivation of the work (Chapter 1), and an introductory chapter where basic principles on the nature of the resistivity of non-simple binary alloys, the radiation effects in resistivity and the nature and methodology of the Resistivity Recovery experiments will be explained (Chapter 2).

Chapter 3 is devoted to deep explanation of the experimental technique and the development of the experimental set-up which has been the central activity of this doctoral thesis. Briefly described, the method consists of the irradiation of prepared samples at cryogenic temperatures with high energetic ions in order to produce displacement damage and immobilize the created defects. Subsequently, the studied materials undergo iterative annealing process where temperature is increased certain amount at every step. The evolution of the microstructural damage is monitored by means of resistivity measurements of the irradiated sample after each step of the annealing. The registered variation of the resistivity provides rich information on the mobility, recombination, clustering and dissociation of defects in the material. It is noteworthy that in the course of this work, besides of setting-up the experimental technique, it has been proposed an improvement of the method for measuring resistivity recovery in concentrated alloys which has been described in Chapter2.

Chapter 4 presents an overview of what is known up to date of Fe-Cr alloys, including the revision and discussion of the state of the art on pure Fe as well as dilute Fe-Cr alloys given that its understanding is fundamental to understand concentrated Fe-Cr systems

which still presents many unknowns, not only from the experimental point of view but also in the simulations.

Finally the results, discussion and conclusions are presented in Chapters 5 and 6. The new proposed method opens a possibility to obtain resistivity recovery results better suitable for validation of computational simulations. Moreover it shows previously unobserved phenomena related to Cr behaviour in the presence of migrating defects, which are not well understood and have to be studied. Finally the comparison of the experimental data obtained in this work with the few data from the literature, allows a critical discussion on the usefulness of the technique, in sight of its complexity not only experimental but also interpretative.

"Through the fire and through the flames

You won't even say your name, only I am that I am"

Ya-Hey, Ezra Koeing

Acknowledgments

Al Laboratorio Nacional de Fusión y al CMAM-UAM, por haber puesto a mi disposición sus recursos e instalaciones. Al CIEMAT, al ministerio de Economía y Competitividad, a la Comunidad de Madrid y a Eurofusión, por haber co-financiado este proyecto. A todas aquellas personas que han trabajado para garantizar la financiación.

A mi director de tesis Rafael Vila y a mi co-director David Jiménez, a mis compañeros de trabajo que me aprecian y me han ayudado y apoyado (mucho). A mi familia, en especial mis padres, mi centro de gravedad permanente, sin ellos no hubiera sido capaz. A mis amigos, los de siempre, los recientes y los que son consecuencia de esta tesis doctoral, por lo profundo, por lo importante, por lo frívolo y lo absurdo, por lo amargo y por lo alegre, gracias.

Mención especial para: Diana, Elisabetta, Juanma, Teresa, Laura, Dídac, Juanan, Gádor, Elisa y Vicky.

Un último agradecimiento etéreo a todas las artes: la música, el cine, la pintura, la literatura, la danza, el teatro, la ópera, la música, la música, la música…

Table of contents

List of figures

List of Tables

Abbreviations, acronyms and signs

α	ratio between spin-down (↓) and spin-up (↑) resistivity contributions
α_i	Warren-Cowley parameter
AKMC	Atomistic kinetic Monte-Carlo
CIEMAT	Centro de Investigaciones Energéticas Medioambientales y Tecnológicas
C_{Cr}	Cr concentration
Cr_s	Cr atom in substitutional position
CMAM	Centro de Micro-Análisis de Materiales
D	deuterium
D	diffusion coefficient
DBTT	ductile-brittle transition temperature
DEMO	Demonstration Power Plant
DFT	density functional theory
dpa	displacement per year
DRR	difference resistivity recovery analysis
DUT	device under test
$\mathcal{E}$	electric field
E_m	energy migration of defects
EFDA	European Fusion Development Agreement
E_F	Fermi energy
FIA	foreign interstitial atom
FP	Frenkel pair
h	constant rate of heating
HFRW	high frequency resistance welding
IFMIF	International Fusion Materials Radiation Facility
I	interstitial
I_n	interstitial cluster made of n interstitials
IA	interstitial atom
ITER	International Thermonuclear Experimental Reactor
K	defect jump rate
LHe	liquid helium
low-T-Irr	low-temperature irradiation at 50 K
LRM	long-range migration
LRO	long-range order
n	neutron
$N_{s,d}(E_F)$	density of states in the s- or d- bands at the Fermi level
MC	Monte-Carlo
MD	molecular dynamics
MIA	mixed interstitial atom
ODS	oxide dispersion strengthened
OKMC	object kinetic Monte-Carlo

p	proton
PA	positron anihilation
PID	proportional integral derivative
PKA	primary knock-on atom
pre-Irr	pre-irradiation of RR sample at 400 K
RAFM	reduced activation ferritic/martensitic
ρ_0	residual resistivity
ρ_{Cr}*	specific resistivity of Cr in Fe
ρ_D	Frenkel defect residual resistivity contribution
ρ_F	specific resistivity of FP
ρ_S	short-range order residual resistivity contribution
R_C	contact resistance
R_V	impedance of the voltmeter
R_W	wire resistance
RCR	resistivity change rate
RIC	radiation induced conductivity
RIR	radiation induced resistivity
RIED	radiation induced electrical degradation
RIEMF	radiation induced electro motive forces
RT	rate theory
RR	resistivity recovery
SFM	stage of free migration
SIA	self-interstitial atom
SD670	external silicon diode
SRO	short-range order
T	tritium
T_a	annealing temperature
T_q	quenching temperature
v_d	electron drift velocity
V	vacancy
V_n	vacancy cluster formed of n vacancies
VdP	van der Pauw

Chapter 1. Thermonuclear Fusion

1.1.The *green* solution

World's increasing energy demand (see Fig. 1-1), the reduction of the fossil fuels reserves and the planet's global warming pushes men to research and develop new sources of energy [1,2]. It is preferable and in fact convenient that energy sources under study will be renewable. Renewable energy is defined as "the one that comes from resources which are naturally replenished on a human timescale, whether that is by the immense amount of energy that holds or because is able to regenerate naturally". In view of such definition, the controversy lies on the classification of fusion energy as renewable or non-renewable. In simplified terms the main fuel of fusion energy is hydrogen, which forms water and thus is a nearly endless energy source. Going further into the detail, indeed the fusion fuel is hydrogen, but in their isotopic forms, i.e. hydrogen (H = ^{1}H), deuterium (D = ^{2}H) and tritium (T = ^{3}H). The first is an element made of one proton only (p) in his nucleus, D has two nucleons, proton and neutron (n) and T contains a proton and two neutrons in his atomic nucleus. The natural abundances of every isotope vary dramatically given that 99,98% is the natural abundance of H, 0,0026% is the one of D which is found in the sea water in higher concentration and as for T only traces can be found and it has to be produced from Li in fission reactors. This last one is also a radioactive element which, by beta decay, produces a non-radioactive Helium isotope, ^{3}He. Combining the different hydrogen isotopes, they can be found several nuclear reactions of interest for fusion energy production [3]:

$D + T \rightarrow {}^{4}He\ (3{,}54) + n\ (14{,}05)$	E_{yield} = 17,59 MeV	1-1
$D + D \rightarrow {}^{3}He\ (0{,}82) + n(2{,}45)$	3,27 MeV	1-2
$D + D \rightarrow T\ (1{,}01) + p(2{,}45)$	4,03 MeV	1-3
$T + T \rightarrow n + n + {}^{4}He$	11,3 MeV	1-4
$D + {}^{3}He \rightarrow {}^{4}He(3{,}66) + p(14{,}6)$	18,3 MeV	1-5
$p + {}^{6}Li \rightarrow {}^{4}He + {}^{3}He$	4,02 MeV	1-6
$p + {}^{11}B \rightarrow 3({}^{4}He)$	8,68 MeV	1-7

The main objective of ITER[1] project is to operate with D-T (eqn. 1-1), given that it is the most favorable reaction in the current conditions of Tokamaks. Thus it can be state that the efforts on fusion research are mainly focused on achieve operation with this

[1]International Thermonuclear Experimental Reactor (http://www.iter.org/proj)

reaction[2]. The fusion of deuterium + tritium leads to the production of He impurities (at 3.5 MeV) and highly energetic neutrons (typically of 14 MeV). Such high-energy neutrons are used for two purposes. On one hand for energy production and on the other hand for the tritium production inside the reactor, in which is called the breeding blanket. The development and verification of tritium production technologies through nuclear reactions is another fundamental objective of ITER project [3]:

$$^{6}Li + n \rightarrow T(2{,}73) + {}^{4}He(2{,}05) \quad \text{1-8}$$

$$^{7}Li + n \rightarrow T + {}^{4}He + n \quad \text{1-9}$$

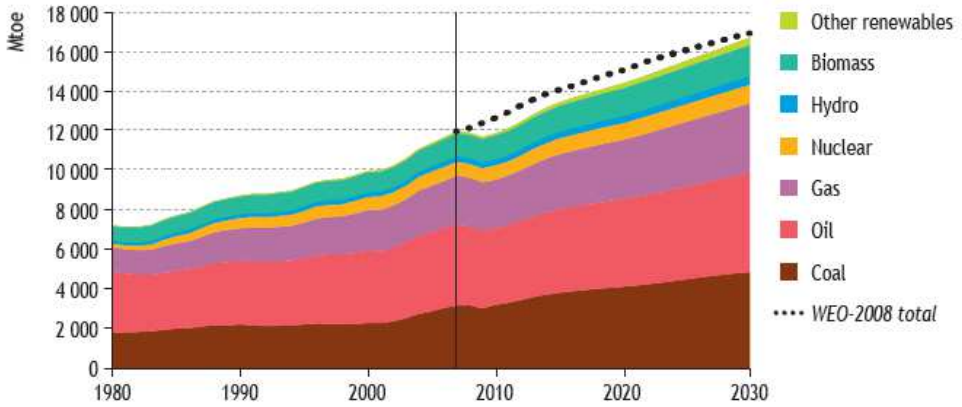

Fig. 1-1: World primary energy demand by fuel.

Whether the tritium breeding concepts will be verified then it will be possible to state that fusion energy requires a nearly inexhaustible source and thus is a renewable energy. Besides, its efficiency is high compared to fission energy, given that it releases approximately 4 times more energy per nucleon. And, of course is enormously efficient when it is compared with energies based on chemical reactions which only liberate energies of the order of 10-100 eV per molecule.

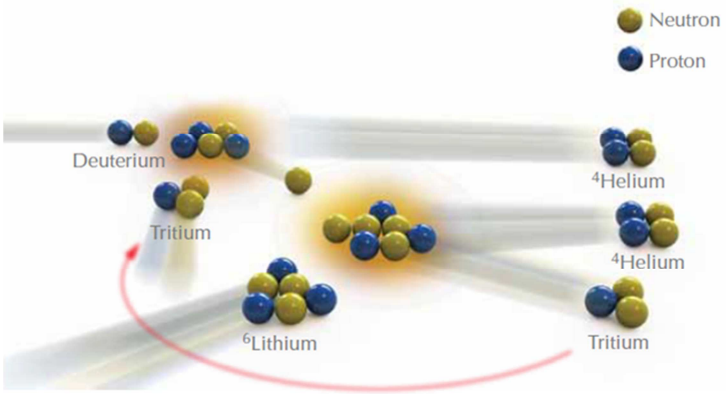

Fig. 1-2: The deuterium-tritium reaction, giving as products, an alpha particle (^{4}He) and a high-energy neutron. The neutron-lithium reaction for T re-generation is depicted as well.

[2] In the future, it has to be noted that there are other reactions, indicated in the text, which use ^{3}He, Li or B and are completely free of radioactivity. Note that lithium and boron are safe and abundant elements.

Another necessary consideration required to classify energy as sustainable is to understand if its production does not make by-products which might have a negative impact on the environment. In the case of nuclear fusion there is again controversy. Despite of the emission of 14 MeV neutrons and gamma radiation[3], which come from the inner vessel and are going to activate the materials in the plasma diagnostics and at least the first wall, it is a mandatory requirement in the development of fusion technologies that the materials used will be low activation materials. This means that the activation levels will be as low as possible and the created isotopes will have decays with mean lifetimes within a maximum of few hundreds of years. Hence in a period of one hundred years they can be classified as low hazard wastes. This is an amount of time astonishingly small if it is compared with the lifetime of fission radioactive wastes, which have half-lives of 10^4- 10^6 years. On the other hand there is the tritium, which is part of the fuel and as it has been previously indicated, is radioactive. The idea of the future fusion reactors is that T will be contained in closed circuits and thus on one hand it will feed the fusion reaction and on the other it will recapture the T generated in the breeding blanket. This arrangement will ensure that the T amount in the reactor is always small, preventing the problem of possible leaks of great importance. Even so, the tritium is going to contaminate the reactor component materials, nevertheless the energy of the β particles that it emits is small and they cannot pass through the skin. Also, the half-life of T is only 12.32 years. To sum up it is expected that the nuclear fusion would produce some radioactive waste but with half-lives and activation levels much lower than current fission nuclear wastes and then its impact on the environment will be less and better controlled.

Finally, concerning the security, it is interesting again to make comparisons between the two types of nuclear energy: fusion and fission. Besides it is going to be highlighted one of the greatest advantages of fusion energy which at the same time is one of the key issues that make so difficult the progress of fusion reactors. In a fission reactor there is a chain reaction where produced neutrons are used to produce new fission reactions in their neighboring atoms. The nuclear moderators can move to control the neutrons velocity and sustain the chain reaction. If the control is lost, the reaction bolts and there is an accident. In fusion, the hydrogen is heated up to his plasma state, where the temperature is high enough to detach the electrons from the atomic nucleus, creating a kind of “soup” of charged particles which reacts in the presence of electromagnetic fields. As the temperature required to get fusion plasmas is higher that the temperature inside the sun, the reaction cannot take place in a conventional container, a magnetic vessel will

[3] Gamma radiation is originated in fusion reactos from different processes like:
$D + p \rightarrow {}^3He + \gamma$ (5.5MeV)
$T + p \rightarrow {}^4He + \gamma$ (20 MeV)
$D + D \rightarrow {}^4He + \gamma$ (24 MeV)
$D + T \rightarrow {}^5He + \gamma$ (17 MeV)
${}^9Be + {}^4He \rightarrow n + {}^{12}C + \gamma$ (4.44MeV)
${}^{10}B + {}^4He \rightarrow p + {}^{13}C + y$ (3.1, 3.7, 3.85 MeV)
+… every nuclear reaction between the generated neutrons with the constituent reactor materials.

be used in this case[4]. If the magnetic confinement fails, there are problems to maintain the combustion of the plasma and the reaction decays in milliseconds. Thus the possibility of a nuclear accident by loss of control in nuclear fusion reactors is eliminated. Nevertheless, the maintenance of the ignition is one of the biggest difficulties that are currently facing the plasma physics researchers.

Despite of the benefits of fusion in terms of security, the presence of high radiation doses, as well as the activation, implies other kind of problems which certainly affect the reactor's engineering. The radiation seriously damages the microstructure of materials leading to dramatic changes in their macroscopic properties and thus degenerating the reliability and durability factors. The creation of advanced radiation resistant materials is fundamental for the development of fusion reactors. The work of this doctoral thesis is framed on this particular issue, specifically oriented to fusion structural materials.

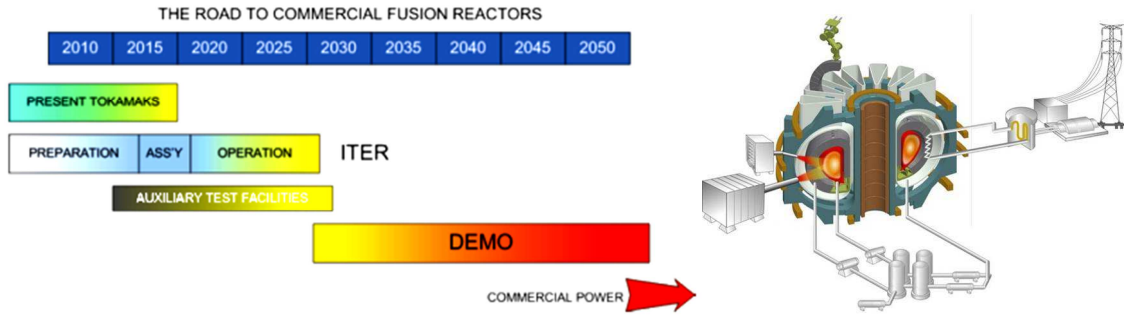

Fig. 1-3: A possible schedule for developing fusion power [4].

As it has been reflected in previous paragraphs, research and development of fusion energy is a very complex topic. As we develop our understanding of the wide issues that need to be addressed to make a "little sun" on earth, it is evident that still many international efforts are required to achieve success. Nowadays is fascinating the big progress that has been achieved and the smart solutions that have been figured out to solve some of the problems. In order to move forward it is required to keep identifying the technological problems and try to solve them. In conclusion, it is enormously difficult to develop fusion energy to make it efficient and stable but, if it would be eventually achieved, we will have an inexhaustible energy source which might be able to replace fossil fuels and slow the global warming.

Achieving full development of nuclear fusion energy is a worldwide goal. For instance the ITER project has involved a great number of countries which represent more than 50% of world's population (E.U., China, Japan, India, South Korea, Russia and U.S.A.). The European Union contributes the 45% of the project's budget while the other countries contribute only with 9% of participation. Inside Europe it was created an agreement between the European fusion research centers and the European Commission (European Fusion Development Agreement, EFDA), which recently in 2014 has changed its name to

[4] In the case of magnetic confinement fusion. Inertial confinement fusion (ICF) is also a developing energy. In ICF reactors D + T ignition will be produced by means of concentration of powerful laser beams in the central point of a vacuum chamber where the fuel pellet will be placed.

Eurofusion. This agreement coordinates and integrates the fusion research tasks which are still necessary to make possible the development of ITER and DEMO[5], the next step to ITER. The task of this doctoral thesis is part of one of the strategic objectives of the Materials topical group of EFDA. Besides, at the national level, fusion research is a topic of great interest and this work has also been co-suported by the "Plan Nacional" (projects RADIAFUS II and III) to state level and by Madrid community through the TECHNOFUSIÓN project.

The work carried out in this doctoral thesis represents a small contribution to this immense collective effort of identification and answer to the technological issues; in particular, in the field of radiation resistant materials for future fusion reactors (also applicable to next generation of fission reactors) and more specifically in the field of structural materials. The target of this work is to make a contribution to the understanding of the fundamental physical processes that affect the Fe-Cr alloys[6] when these are under radiation damage regardless of the incident particle. The defect kinetics and their interaction with solutes affect the migration, annihilation and aggregation of lattice defects created by radiation. In this study a deep revision of the state of the art has been carried out and new experimental data of resistivity recovery (RR) is supplied. The tasks of designing, assembling and developing of the experimental technique used are fully included within the objectives of this thesis; as well as the analysis of first results and first contributions to the topic, leaving the way paved to keep investigating in this new research line that has been developed in the Materials Group for Fusion Materials of the National Fusion Laboratory at CIEMAT.

1.2.Materials problem in fusion reactors

The materials which will form the fusion nuclear reactors are going to withstand extreme operation conditions, not only due to the high temperatures (800 and 1100K expected in ITER and DEMO fist wall respectively), the intense magnetic fields and the mechanical stresses due to plasma instabilities, but also because of the high radiation levels which will be product of the nuclear reaction in the reactor vessel. The hot plasma will generate a high flux of high-energy neutrons as well as electrons, ions and gamma radiation.

The neutrons produce damage by two different processes: transmutation and displacement damage. Nuclear transmutations are responsible for activation and impurity formation in the materials, being H and He the most important ones. On the other hand, the elastic collisions of the neutrons with the lattice are going to displace the atoms from their lattice sites. The atoms displaced by the incident neutron are called primary knock-on atoms (PKA). Depending on its energy, the PKA will be able to produce collision cascades which will lead to many kinds of defects. Displacement damage produces point defects in metals and insulators: vacancies (V), interstitials (i) and clusters of them (i_n or

[5] Demonstration Power Plant (http://fusionforenergy.europa.eu/understandingfusion/demo.aspx)
[6] The model alloys Fe_{1-x}-Cr_x are the base of the reduced-activation ferritic/martensitic steels which have been chosen as main candidates to build the structure of the first wall in future fusion reactors.

V_n). A conceptual representation of neutron damage effects is shown in Fig. 1-4. The displacement damage is measured in dpa (displacement per atom) [5,6]. One dpa means that on average every atom of the material has been displaced once. The total radiation doses expected for ITER and DEMO are in the range of 3 and 25 dpa respectively.

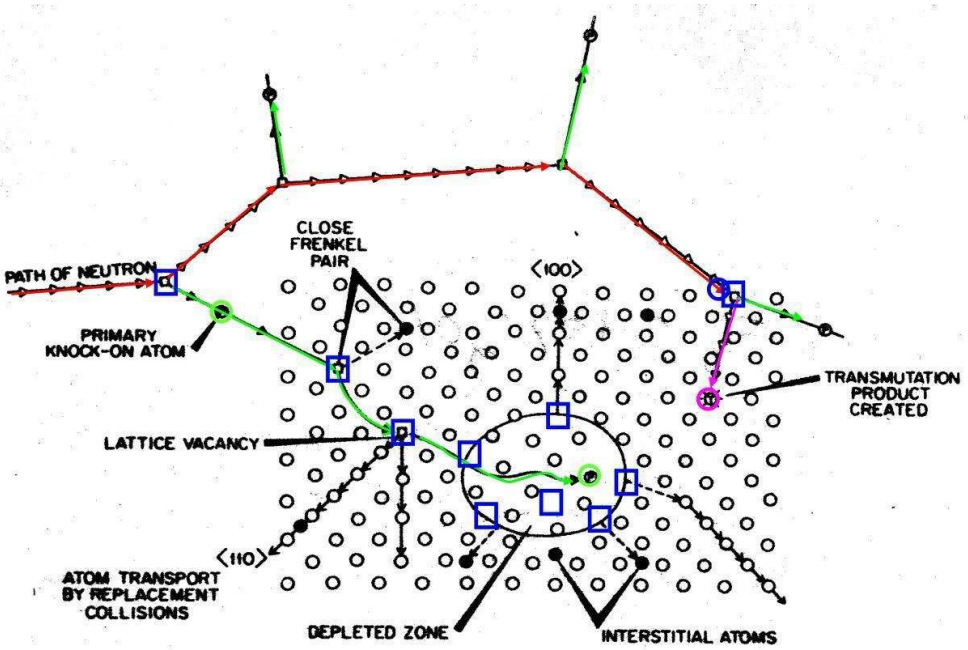

Fig. 1-4: Conceptual representation of collision cascade. Different effects produced are represented: collision cascade and transmutation products of neutron irradiation.

The gamma radiation will be present in the plasma coming from the reactions indicated in note 3 but some radiation will also remain once operation is off. Important radiation levels will be present during remote handling operation but will decay with time (see Fig. 1-5). The ionizing (gamma) dose is measured in Gray (Gy = J/Kg). The expected gamma dose rate in ITER first wall is estimated about 2 kGy/s and not very different value has been calculated for in DEMO.

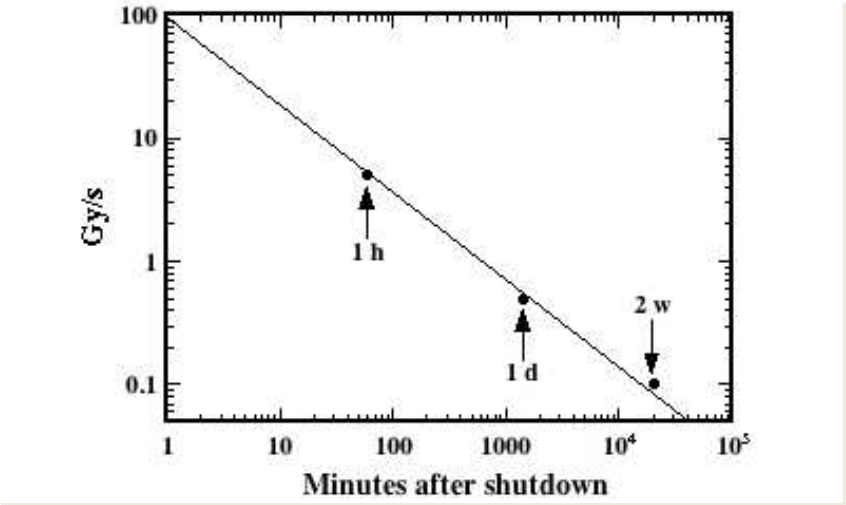

Fig. 1-5: Radiation level of remote handling rapidly reduces.

Identification and development of nuclear materials capable to withstand hostile environments is one of the principal challenges facing the achievement of future nuclear reactors (e.g. ITER, DEMO). The large amount of radiation in the vessel will not only activate the materials but also will degrade its macroscopic properties. These phenomena will have dramatic impact on both functional and structural materials, affecting their functionality and reliability. Functional materials will be used in the diagnostics as insulators, optical fibres, windows or mirrors and in the breeding blanket[7]. These materials will feel the effect of both displacement damage and ionizing radiation. The gamma radiation produces excitation of the electronic systems of insulators which changes charge state of impurities and induces energy transfer from lattice which can lead to defect formation. The accumulated damage will induce light emission (radioluminescence) and loss of optical transmission in windows, fibre materials or mirrors. Also other effects as radiation induced conductivity (RIC), radiation induced electrical degradation (RIED), surface degradation or radiation induced voltages (RIEMF) will affect the quality of dielectrics and mineral insulated coaxial cables. Concerning structural materials the most damaging elements will be neutrons; these materials will be placed just behind the plasma facing components and thus will barely feel interactions with charged particles which would collide directly to the walls of the reactor's chamber. The impurities and defects, created by neutrons through inelastic and elastic collisions, evolve with dose and temperature and are able to cluster and form dislocations or voids and allow the solutes of the alloys to re-arrange in the matrix. These processes lead to materials swelling, embrittlement, modification of its phase stability, reduction of its resistance and enhancement of corrosion.

The ideal situation for developing new radiation resistant materials would be testing them when submitted to the same environments as in the plasma vessel. Unfortunately, reproducing such conditions is not possible nowadays. Despite of the existence of high energetic neutron sources, as fission reactors or spallation sources, currently there is no neutron source in the world able to reproduce the expected neutron spectra for ITER and DEMO. Available sources do not provide neutrons with comparable energy or flux intensity (in the order of 10^{18} $m^{-2}s^{-1}$). Furthermore their accessibility is very limited. From this lack of a fusion relevant neutron source arises the International Fusion Materials Irradiation Facility, IFMIF[8]. It is an accelerator-based neutron source that will use Deuterium-Lithium stripping reactions to simulate 14 MeV neutrons from D-T fusion reactions. The magnitude of IFMIF project is comparable to ITER in terms of technological challenge, schedule and budget. While IFMIF is being built, the study of radiation effects in materials is carried out using particle accelerators and gamma and X-ray sources. Indeed early understanding of radiation effects is necessary to drive and select the most interesting materials and specific experiments that will be studied at IFMIF facility.

[7] Also liquid breeder blanket technology is being considered as an alternative to solid breeders in future fusion devices.
[8] (http://www.ifmif.org)

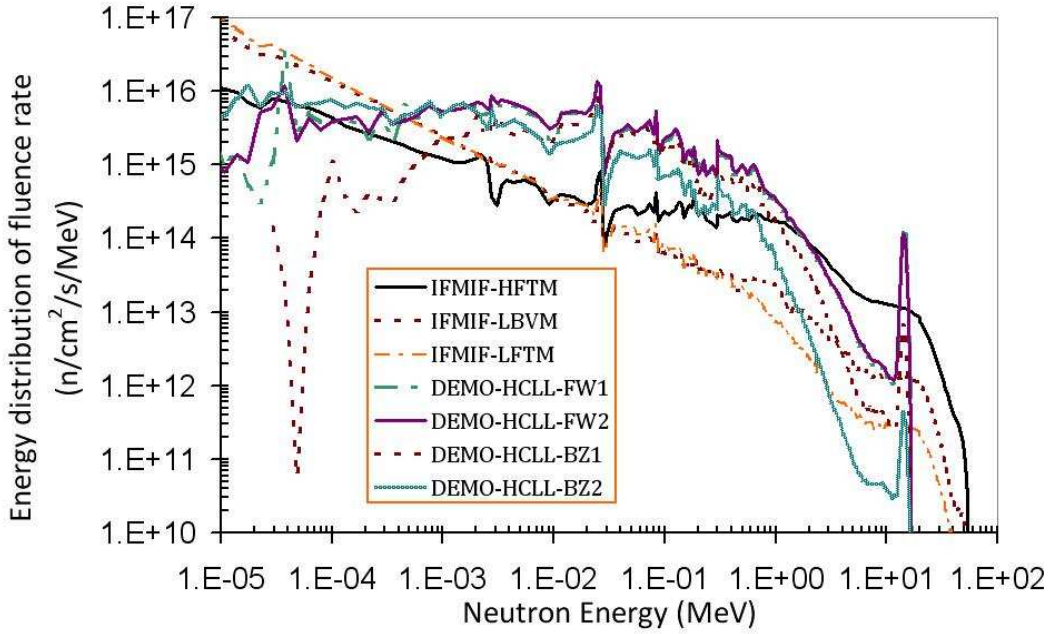

Fig. 1-6: Neutron spectra for different facilities and irradiation spot [7].

The irradiation with ion beams can be used to simulate the effect of neutrons. While irradiations with H and He simulate the transmutation effects, the heavy ion irradiation can produce point defects [8,9]. Such irradiations can be performed separately or simultaneously (on double or triple beam facilities) to reveal possible synergistic effects [10]. The use of particle accelerators allows to achieve low (or insignificant) activation in the samples and to greatly reduce the irradiation times. Despite this kind of experiments do not necessarily produce a damage effect equivalent to neutrons in every case, they have the power to put in evidence physical processes allowing the progress of the existing models and materials engineering. Every experiment must be carefully designed to isolate the physical phenomenon that wants to be disclosed whilst the rest of variables remain constant or well controlled. However, purely experimental approach to understanding the effects of irradiation is not practicable. It is a matter of costs on design and execution of irradiations, costs of post-irradiation examination of radioactive materials and a combinatorial problem given by the broad range of materials, phenomena, and irradiation conditions, such as dose, dose rate, temperature, loading conditions or coolants. Hence, computational codes are concurrently being used to implement models which might help to understand and identify the physical mechanisms of relevance in the field of radiation damage of materials. Radiation damage is a phenomenon of multi-scale nature and thus the modelling has to treat the problem at different scales.

1.3.Modelling and experimental validation

A physical model is a conceptual representation of a physical system, where a set of variables are connected by a set of logical or mathematical relationships, used to explain its experimentally observed behaviour. These relationships are based on accepted

theories, physical laws and assumptions on the fundamental mechanisms governing the physical system at study. The use of this physical approach is the proposed study strategy to achieve this long-term goal of developing advanced radiation resistant materials. It is believed that a comprehension of radiation effects based on fundamental physical laws is the only way to have reliable bases for the development of correlations that, in the long term, will be able not only to provide trends that nuclear materials in operation are expected to follow, but also to guide the design of reactor components and properly guarantee their safety, maintenance and operational life. Exponential growth of computers' hardware and performance has made computational simulations to become fundamental tools for reaching this approach.

Computational modelling methods have become a powerful tool because they can supply an alternative system for testing neutron damage on materials. Modelling of materials would help to understand damage mechanisms in materials under fusion conditions, being able to predict what would happen with the materials in different conditions and thus significantly reducing the number of time-consuming laboratory experiments required to test a new component design, resulting in faster development of new materials. In the short-term it is unrealistic to expect that the physical approach can produce fully predictive models, quantitatively valid for direct technological applications, *i.e.* for real materials such as steels. Nonetheless, it will become clear in next section that advances in **multiscale modelling can help in the medium-term.**

The origin of "multiscale" modelling designation arises on the multiscale nature of the radiation damage that creates defects which alter the microstructure and the mechanical properties of the material. The evolution of defects upon irradiation and annealing has to be studied at different scales: from interaction of first ps where the displacement cascades take place in spaces of the order of nm^3 [11] up to defect diffusion which can take hours or even years over longer distances. Therefore, the study of defect evolution requires a multilevel analysis which spans from atomistic to continuum approaches which are achieved by different codes such as *ab-initio* calculations, Monte-Carlo (MC) methods, molecular dynamics (MD), rate theory (RT), finite element methods and others. All this methods implement different theoretical models that try to reproduce reality. Therefore multiscale approach is a result of an iterative process where the outputs from some codes are the inputs of others and at the same time codes and models have to be validated by well-designed experiments which are driven by results of simulations as well. Fig. 1-7 depicts the essence of this methodology. Brief description of the methods and their main features will come out along this text, especially in sections 4.4 and 5.1.

It should be pointed out that, in the rapidly developing field of fusion materials modelling it is easy to stretch a model beyond its range of validity. This leads to disagreement between predictions made using alternative approaches, with confusing outcomes where significant features are not correctly described. Thus every task on materials modelling must involve quantitative comparison with appropriate validation experiments. RR, gas desorption, diffuse neutron scattering or Mössbauer spectroscopy experiments are just few examples of experimental techniques that might be used as model experiments or can provide data to validate models and codes.

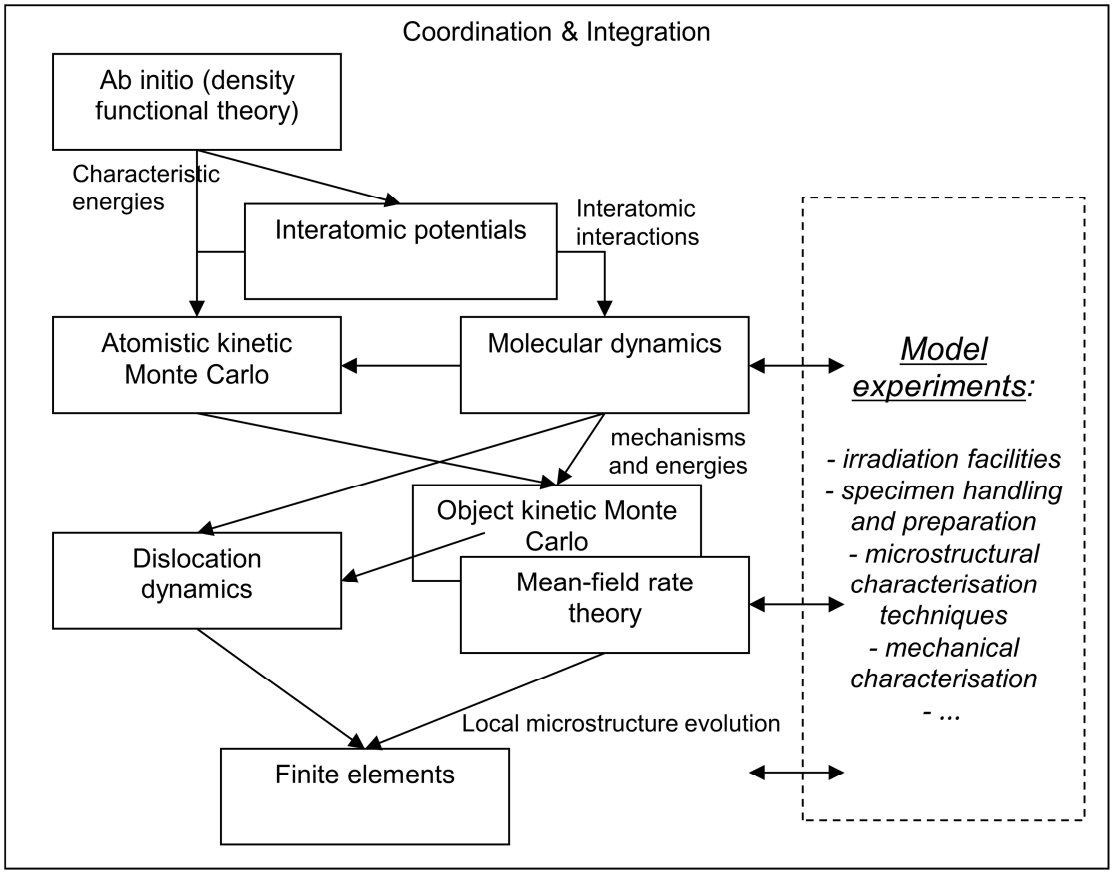

Fig. 1-7: Schematic illustration of the different fields of expertise required in a multiscale modelling approach and their interconnection.

1.4.Interest of Fe-Cr alloys

Candidate structural materials for fusion applications are based on reduced-activation ferritic/martensitic steels (RAFM), alloys made of W and V and SiC ceramic composites. It is well known that RAFM are the most promising candidates for fusion and fission applications. Among RAFM there are different families: EUROFER, EUROFER ODS[9] (9% Cr) and ODS Ferritic Steels (12-14% Cr). Several of these advanced alloys developed by fusion researchers are being spun off for near-term commercial applications in other fields, such as, pressurized water reactors, microturbine recuperators, or fossil energy pressure vessel applications [12]. In general micro-structural modification of conventional materials to develop the radiation resistant ones, also improve their unirradiated overall properties.

EUROFER is going to be tested in some parts of ITER (in the tritium breeding blanket). Its optimized Cr concentration is typically ~9% with smaller quantities of W, V and Ta. This choice of 9% of Cr is based on the experimentally observed minimum radiation-

[9] Nanocomposited oxide-dispersion-strengthened (ODS) ferritic steels

induced ductile-brittle transition temperature (DBTT) shift [13,14]. The hardening (and therefore embrittlement) is a result of aggregation of point defects. It is equally well known that higher Cr concentrations will increase protection against corrosion [15] while the minimum in radiation induced DBTT shift is lost. Thereby the choice of the steel composition becomes a compromise between the two desired effects: better mechanical behavior under irradiation and better protection against corrosion.

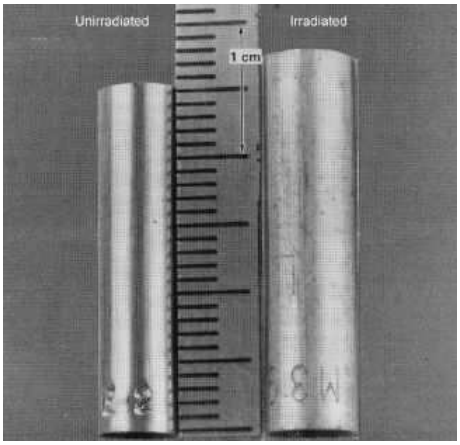

Fig. 1-8: Example of materials swelling. Comparison of an unirradiated sample vs. a neutron irradiated specimen which has received a fluence of 1,5 x 10^{23} neutrons/m^2

Although the physical reason that explains this 9% minimum has not been given yet, it may be related to the behavior of atomic species and created defects in the Fe-Cr system. The distribution of the Cr solutes is by nature never fully random (see section 2.1.4) [16] leading to specific local atomic distributions. Namely, Cr tends to precipitate above 9%Cr [17,18] but models, confirmed by experiments, have shown that below this concentration Cr atoms are soluble in Fe even at very low temperature and tend to repel each other, thereby taking a partially ordered distribution. On the other hand, models and experiments have clearly revealed that point defects (specifically self-interstitials) have strong attractive interactions with Cr. It is believed that when Cr concentration is of 9%, the defect-trapping effect is maximum since Cr is in a state of maximum random distribution which hinders the formation of hardening aggregates and thus minimizes the radiation embrittlement. It is postulated that trapping of interstitials and interstitial clusters due to Cr atoms in Fe alloys might explain the reduced swelling and enhanced nucleation of interstitial loops compared to pure Fe [19].

If this contention is proven by specific atomic-level simulation studies, as well as by targeted experiments, it may become possible to modify the composition of steels by adding elements that change the phase stability in Fe-Cr alloys and move the "9% minimum" to higher Cr concentrations. This would provide, simultaneously, the best mechanical response under irradiation and the desired protection against corrosion. This result could be obtained without being able to quantitatively predict with models the actual DBTT shift in Fe-Cr alloys as a function of composition, dose and temperature, which is a far-fetched objective.

Now it has become clear that composition of steels will influence the materials performance under irradiation, and that proper understanding of the underlying physics that runs the motion of solutes and defects would effectively help to develop radiation resistant materials for fusion. It is also interesting to take a look to the operation temperature windows which need to be defined and optimized. At relatively low temperatures (below 700 K), radiation induced hardening and embrittlement are of concern, whereas at high temperatures, creep, He-driven cavity formation and void swelling become the problem. Simulations and experiments, once again, can also contribute to clarify these processes and provide a well-defined lower limit of the temperature window of operation: The degradation of the material at low temperatures is due to the fact that aggregated point-defects impede the dislocation motion. A precise prediction of how these defects form, evolve and annihilate, as well as of the effect of their presence on the population of dislocations, is in principle required to be able to establish the lower limit of the window of acceptability.

It has then become clear that in order to identify suitable structural materials for fusion reactors and establish boundary conditions for such materials in operation, it is crucial to fully understand the radiation effects, which can be done using a physically-based modelling approach. This can be achieved undertaking computational simulations to reproduce well-designed experiments carried out under well controlled irradiation conditions and on model alloys. This method allows validating parts of our models and can provide additional information on the atomistic mechanisms responsible for defect evolution. This approach is non-straightforward and strong efforts are still needed to develop the models and to obtain new experimental data. RR experiments take part of this group of validation experiments which can provide useful information on the formation and kinetics of metallic materials.

RR experiments have been extensively used to study the radiation damage in metals [20–32]. In the field of nuclear energy advanced materials development the results in RR are being used to address the design of structural steels and divertor armour materials. Concurrently to materials engineering, big efforts are being made to get a physical approach, based on multiscale modeling together with validation experiments, which will establish reliable bases to understand the physics responsible of the radiation degradation processes [33–36]. The RR experiments are used as validation experiments given that they are able to monitor the changes in defect populations which can be also reproduced by modeling simulations [24,30,37–40]. The particular interest of RR is that it is able to “see” the interstitial type of defects as well as vacancy-type, in contrast to other techniques such as positron annihilation (PA). The well-known work of Fu et al. [39] demonstrated that overall agreement can be achieved between modeling (ab-initio and kinetic Monte-Carlo (kMC)) and experiments (RR and PA [24,41]) of electron irradiated utra-pure Fe. However same agreement has not been reached up to date concerning concentrated alloys.

In order to fully understand the defect kinetics in Fe-Cr systems, some attempts to match theoretical predictions and experiments are being performed [42]. A recent work [40] which combines MD, atomistic kMC (AKMC) coupled to an artificial neural

network and RT has modeled several experimental results of RR in dilute [30,37] and concentrated electron-irradiated Fe-Cr alloys [38]. This work succeeds on reproduction of correlated recombination stages but it shows limitations given that it only simulates a single recombination process in Stage II and the most important thing; the amplitude of Stage III cannot be accurately estimated. This last limitation is, as the authors' state, probably due SRO effects which are not included in the model. This is actually one of the main limitations of computational simulations that are devoted to reproduce RR results.

Detailed explanation of the above mentioned important works is provided in chapter 4. Before, an introduction to theoretical concepts and details on the experimental method and set-up developed are given in chapters 2 and 3. Finally the results provided in the present work on concentrated Fe-Cr alloys under 5 MeV proton irradiation are presented and discussed in chapter 5. The major output of this work is the contribution to enlarge the database of RR results on concentrated Fe-Cr which are very limited but necessary to validate the developing modelling approaches.

Chapter 2. Resistivity and experimental techniques

As stated by Dulca in his doctoral thesis [43], understanding the electrical resistivity of a concentrated metallic alloys is a discouraging task, because of the large number of contributions that may be involved. The electrical resistivity is a physical property that depends on the density of states at the Fermi level. Its value is composed by many contributions such as phonon interaction, concentrations of defects, atomic arrangements or magnetic interactions. Understanding how such contributions influence the resistivity is the key to be able to design and perform experiments based on resistivity techniques.

The presence of solutes is going to change the resistivity values of pure metals by means of the so-called short-range order (SRO) effects and also by its magnetic contribution to the magnetic spin populations of conducting electrons (explained by the two-current model). In this doctoral thesis the research is focused on the Fe-Cr concentrated model alloys thus it is important to be able to evaluate how addition of Cr to Fe and presence of defects is going to influence the residual resistivity values of the materials under study, in order to interpret the RR results and also to make appropriate comparisons with the more extensively studied pure and impure Fe. Sections 2.1 and 2.2 are devoted to this purpose. Some of the concepts described in section 2.1 will be especially helpful for understanding the literature on modelling, RR and quenching experiments.

Additionally, in section 2.3, it is clearly explained the origin of evolution of defects as the sample temperature is increased and the processes that such simple defects can undergo as the annealing goes. The fundamentals of the RR experiments are described in section 2.4. And finally, based on the predicted SRO residual resistivity changes in the presence of migrating defects, there is a detailed explanation on the new RR method that has been developed and tested along the development of this thesis in section 2.5. The new method proposed allows making RR experiments erasing the SRO contribution.

2.1.Resistivity Basics

2.1.1. Electronic Band structures

The first thing that is necessary to understand about Fe-Cr alloys when we are facing their study is that such alloys belong to the category of non-simple magnetic metals, or non-simple magnetic alloys. Thus the mathematical treatment and the quantitative

understanding of their behavior become considerably complex. To understand the differences between simple and non-simple metals, it is necessary to consider formally the ideas of electronic band structures.

The band structure is obtained by solving the Schrödinger equation to find the distribution of energy states of the electrons. As a reminder, the simple form of the Schrödinger equation for electrons under the influence of a periodic potential, usually referred as Bloch's equation is:

$$-\frac{\hbar^2}{2m}\left(\frac{\partial^2\psi}{\partial r^2}\right)+V(r)\psi=E\psi \qquad 2\text{-}1$$

The solution of the equation E(k), being k the wavevector, is multivalued, this is that for certain value of the wavevector there exist several permitted values of E. Also there are certain energy bands which are forbidden. The band structure (i.e. the solutions) is usually represented as a function of k, along various directions of symmetry in k-space defined in the Brillouin zone (see Fig. 2-1 [16]).

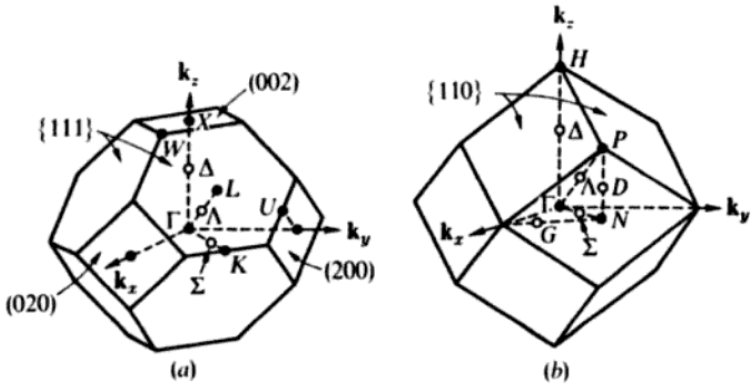

Fig. 2-1: Symmetry lines and points in the Brillouin zone for the fcc (a) and bcc (b) structures

As an example, the band structure of Al, a non-ferromagnetic metal, is shown in Fig. 2-2. The Fermi level, also indicated in Fig. 2-2, is the highest filled energy level and it does not necessarily correspond to a permitted energy level (e.g. in an insulator the Fermi level lies in the band gap). As it can be observed in the Fig. 2-2 some energy bands are totally filled by electrons, and some others are partially filled. For each partially filled band there will be a surface in k-space separating the occupied form the unoccupied levels. The set of all those surfaces defines the Fermi surface, the shape of which is directly related to the band structure. If we consider a metal with a Fermi level low enough so that the electrons lie in the lower levels of the band structure, so that their Fermi surface can be considered spherical and the conduction electrons are nearly free, then we are talking of a simple metal. In this case the electrons on the Fermi surface have an s-like character and their wavefunctions can be treated as a linear combination of plane waves.

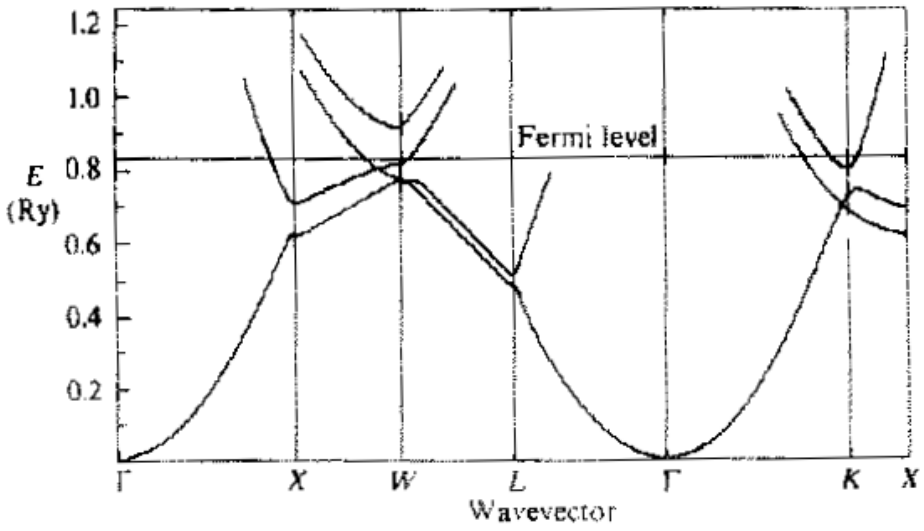

Fig. 2-2: The energy bands of Al along various symmetry directions as calculated by Segall (1961) [44]

The treatment of simple metals simplifies the solutions of Bloch's equation, which provides the band structure and leads the understanding of the behavior of metals and semiconductors. The non-simple metals are those in which there is a significant density of states at the Fermi level that do not have an s-like character. For example, let's consider a material with a Fermi energy (E_F) such that the density of states contains both s and d electrons. In such case the motion of both s and d electrons in the applied electric field should be considered, as should both the density of states $N_s(E_F)$ and $N_d(E_F)$ in the s- and d- bands respectively. These factors add considerable complexity to the determination of electrical resistivity of an ideal solid. In the case of Fe, it has an incomplete 3d shell.

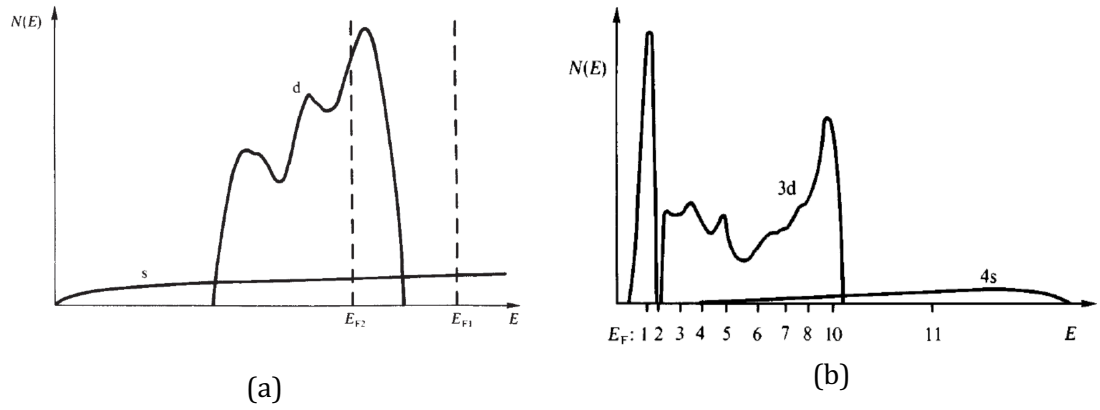

Fig. 2-3: (a) Density of states of a hypothetical solid containing both s and d electrons. The Fermi level occurs at E_{F1} in a simple metal and at E_{F2} in a non-simple metal. (b) Density of states of a typical transition metal alloys determined by Slater in 1936 [16].

2.1.2. Quantum Drude model

When an electric field $\mathcal{E}$ is applied to a conductor, each electron will experience a force $-e\mathcal{E}$ and it will undergo an acceleration in the direction of that force. The electrons, in a very short period of time, produce a net electron current in spite of continue increasing its velocity as the electric field is maintained. This is due to the interaction of the electrons with the lattice by several scattering mechanisms. Thus the electrons can discontinuously change its momentum from an initial state φ_k into a final state $\psi_{k'}$ within the Fermi surface. The electrical resistivity is the property which puts into manifest these phenomena and it relates the current density *j* and the field *E* by:

$$j = \sigma\mathcal{E} = \frac{\mathcal{E}}{\rho} \qquad 2\text{-}2$$

where $\rho=1/\sigma$ is the electrical resistivity and σ the electrical conductivity. The current density *j* is obtained by summing the contribution of the extra drift velocity ev_d of all electrons:

$$j = nev_d \qquad 2\text{-}3$$

A metal is approximated as a gas of electrons enclosed in the macroscopic volume of the metal. The electrons do interact with the metallic lattice, but they do not actually collide with the ions as it is described by the classical picture. We are dealing with a strongly interacting quantum-mechanical system. If we now consider an electron in a metal described as a gaussian wavepacket centered in state k_0, the group velocity of this wavepacket is by definition:

$$v(k) = \frac{1}{\hbar}\frac{dE(k)}{dk} \qquad 2\text{-}4$$

The work produced by the electric force on the electron over a time interval will be:

$$\delta E = F\delta r = Fv(k)\delta t = \frac{F}{\hbar}\frac{dE(k)}{dk}\delta t \qquad 2\text{-}5$$

At the same time:

$$\delta E = \frac{\partial E(k)}{\partial k}\delta k \qquad 2\text{-}6$$

By combining equations 2-5 and 2-6 the semiclassical motion equation of the electron is thus:

$$F = \hbar\frac{dk}{dt} \qquad 2\text{-}7$$

If we derivate the group velocity with respect to time and combine it with the semiclassical motion equation we obtain:

$$\frac{dv(k)}{dt} = \frac{1}{\hbar}\frac{d}{dt}\left(\frac{dE(k)}{dk}\right) = \frac{1}{\hbar}\left(\frac{d^2E(k)}{dk^2}\right)\frac{dk}{dt} = \frac{1}{\hbar^2}\left(\frac{d^2E(k)}{dk^2}\right)F \qquad 2\text{-}8$$

which has the shape F=m·a if we identify:

$$\frac{1}{m^*} = \frac{1}{\hbar^2}\left(\frac{d^2E(k)}{dk^2}\right) \quad 2\text{-}9$$

where m* is the effective mass of the electrons. In the case of free electrons ($E(k)=\hbar^2k^2/2m_e$) m* equals the mass of the electron m_e. Considering these definitions of effective mass of the electrons and current density, a classical kinetic treatment [45] of the forces involved when the electric field is applied to a conductor results as follows:

$$F = |e\mathcal{E}| = m^*\frac{dv}{dt} \quad 2\text{-}10$$

Integrate over the period of time τ between two collisions:

$$e\mathcal{E}\tau = m^*(v_2 - v_1) = m^*v_d \quad 2\text{-}11$$

By combining equations 2-2, 2-3 and 2-11 we obtain the resistivity expression in the quantum model based on the Drude formula:

$$\rho = \frac{m^*}{ne^2\tau} \quad 2\text{-}12$$

The relaxation time between two collisions τ, is inversely related to the transition probability $P_{kk'}$ which is given by the Fermi's golden rule:

$$\frac{1}{\tau} = P_{kk'} = \frac{2\pi}{\hbar}|\langle\psi_k|V(r)|\varphi_k\rangle|^2N(E_F) \quad 2\text{-}13$$

which specify the dependence on the matrix element of the scattering potential V(r) between the states φ_k and $\psi_{k'}$, and the density of states at the Fermi level $N(E_F)$. The actual transition probabilities have to be multiplied by the number of k states in a volume Ω in k space:

$$P_{kk'}\frac{\Omega}{(2\pi)^3} \quad 2\text{-}14$$

The resistivity is thus obtained by means of the quantum Drude formula. All the information related to physical processes which contribute to electron scattering (defects, solute arrangement, phonons, magnetic effects) is intrinsic to the transition probability which should be integrated over the Fermi surface. As we will see along this chapter some approximations can be made and analytical expression of the resistivity where some of the scattering processes are shown explicitly can be obtained for simple alloys. This will give us a qualitative approach to the physics involved; unfortunately it won't be the case for non-simple metal alloys. Next sections provide an overview on how intrinsic mechanisms are related to the real resistivity in Fe-Cr alloys in order to ease qualitative understanding of the state of the art, the results obtained in this doctoral thesis and the limitations of the technique used (RR).

2.1.3. Matthiessen's rule

The electrical resistivity is determined by the rate at which this scattering between initial and final k states is produced. In a perfectly periodic lattice at zero temperature the electron waves are not scattered by the lattice except for very special values of the wavevector which satisfies the Bragg condition (which is $k=g_n$, being g_n a reciprocal lattice vector). This can be explained in a simple manner by assuming that if the lattice is regular an electron is attracted to the ions as much in one direction as it will be in the opposite direction. The result is that general destructive interference occurs and so the electron travels undeviated. It is only if the lattice arrangement is not perfect than the destructive interference is not complete and the electron is scattered. In order to discuss the electrical resistance, the ways in which the periodicity might be disturbed might be studied. These are the main types of lattice imperfections in metal alloys which can contribute to the electrical resistivity:

(i) The presence of impurity atoms and other point defects: they will upset the lattice periodicity. At zero temperature only these effects might manifest in the so-called residual resistivity, ρ_0.

(ii) In some specific cases if the size of the studied specimen is small enough (~150 μm [46]) the residual resistivity will be increased by the effect of external surfaces. Similar behavior will be expected in the presence of the so-called internal surfaces such as dislocations or grain boundaries. The overall effect will be an increase in ρ_0. No further theoretical investigation is provided in this chapter given that their contribution will be constant along the RR experiments.

(iii) The thermal vibration of the lattice: implies the presence of phonons which carry momentum $\pm q_{ph}$. Phonons can interact with s and p electrons producing electron scattering. Phonon scattering implies emission or absorption by the conduction electrons and thus is always considered inelastic process; that conserves the crystal momentum. Such processes are called Umklapp processes, $k'-k = g \pm q_{ph}$ (cf. [16] Rossiter pp. 14 y 16).

(iv) Also in magnetic materials the presence of localized magnetic moments allows the interaction with the conduction electrons. Such interaction would depend on both the electron spin and the magnitude of the localized spin. The magnetic scattering can be elastic if there is no energy change and inelastic if there is change in energy, i.e. change in the spin state. This phenomenon is called spin-flip.

The total resistivity is therefore given by the Matthiessen's rule:

$$\rho(T) = \rho_0 + \rho_h(T) + \rho_m(T) \qquad 2\text{-}15$$

where ρ_0 is the residual resistivity, $\rho_h(T)$ is the phonon resistivity of the host material (in the case of an alloy) and $\rho_m(T)$ is the magnetic contribution to the resistivity.

If we regard now carefully the residual resistivity term, it is the result of specific physical phenomena such as short-range order distributions (ρ_S), size effects of solutes (ρ_{SE}) (impurities/ alloys) and atomic displacements, i.e. defects (ρ_D), every one of them with a characteristic relaxation time:

$$\rho_0 = \rho_0 + \rho_S + \rho_{SE} + \rho_D \qquad 2\text{-}16$$

The scattering process with the smallest relaxation time dominates the resistivity value. Consequently the specific system under study should be adequately interpreted in order to apply the proper use the equation 2-16 (considering only the significant terms).

The main assumption made in the application of the Mattiessen's rule is that the relaxation time is isotropic in k-space, this implies that:

$$\left\langle \frac{1}{\tau(k)} \right\rangle = \left\langle \frac{1}{\tau_0(k)} \right\rangle + \left\langle \frac{1}{\tau_h(k)} \right\rangle \qquad 2\text{-}17$$

In non-simple metals and alloys where electrons cannot be considered free (non-spherical Fermi surface) the relaxation time becomes anisotropic, i.e. its value, τ(k), varies over the Fermi surface. Thus in general the following equation is not true:

$$\left\langle \frac{1}{\tau(k)} \right\rangle = \frac{1}{\langle \tau(k) \rangle} \qquad 2\text{-}18$$

A consequence of such anisotropy is that the Matthiessen's rule exhibits strong deviations. This has been confirmed in iron alloys containing transition metals [47]. Such deviations have been explained by the two-current model which is based on the magnetic properties of the valence electrons. This model will be explained in further section along this chapter.

2.1.4. SRO effects

When analyzing the electrical resistivity of an alloy with respect to a pure single metal, some significant contributions start to play a role, for example the creation of new conduction bands or the distribution of the alloying elements within the lattice. Let's evaluate the effect of the atomic arrangements in resistivity. In order to describe this influence, it is necessary to study Fe-Cr systems as solid solutions.

The concentrated alloy systems are those which have enough solute concentration to perturb the electronic structure and the phonon spectrum. Typically this composition range starts at 1-2 % of solute concentration. These perturbations on the electronic structure lead to an atomic configuration which is never fully random; there are certain correlations which may be described as SRO. The SRO parameters, also called the Cowley-Warren parameters, are defined as the correlation between first- and next-nearest neighbors of an atom in a solid solution [16]. If we describe the site occupation parameters as follows:

$$\begin{aligned} \sigma_i^A &= 1 \quad if\ an\ A\ atom\ is\ at\ site\ r_i \\ &= 0 \quad if\ not \end{aligned} \qquad 2\text{-}19$$

In the case of a substitutional binary alloy (as it is the case in Fe-Cr) the single-site average is $<\sigma_i^A>$ and is just the probability of finding an A atom at any site, this is given by the atomic fraction of A atoms $c_A = <\sigma_i^A>$. At the same time $c_B = <\sigma_j^B>$ is the concentration of B atoms in the alloy. It can also be defined the deviation of having a fully random alloy:

$$< \sigma_i \sigma_j >= c_A c_B - < \sigma_i^A \sigma_j^B > \quad 2\text{-}20$$

It is possible to simplify the description of such deviation by defining a pairwise correlation parameter α_{ij} used by Warren and Cowley:

$$< \sigma_i \sigma_j >= c_A c_B \alpha_{ij} \quad 2\text{-}21$$

In cubic materials the atomic distribution can be represented by shells of atoms about a central atom. Table 2-1 illustrates the characteristics of the shells in BCC lattice [43]. This leads to the description of c_i atoms in the *i*th shell at a distance r_i from the central atom. In this case, the appropriate Warren-Cowley parameter is described as:

$$< \sigma_0 \sigma_i >= c_A c_B \alpha_{0i} = c_A c_B \alpha_i \quad 2\text{-}22$$

where $<\sigma_0\sigma_i>$ expresses the deviation from the mean pair occupation, $c_A = <\sigma_i^A>$ and $c_B = <\sigma_j^B>$ are the concentrations of A and B atoms respectively and α_i is the Warren-Cowley parameter indicating the correlation between the central atom and the *i*th shell. If $<\sigma_0\sigma_i>$ (or α_i) is positive and i represents the first shell of neighbors, then there is a number of like near neighbors in excess of the random probability. This is described as atomic clustering (see Fig. 2-4(right)). If $<\sigma_0\sigma_i>$ (or α_i) is negative, then there is an excess of unlike near neighbors. This is short-range (SRO) atomic ordering (see Fig. 2-4(left)). The variation of $<\sigma_0\sigma_i>$ (or α_i) with separation of the sites r_i gives information about the spatial variation of the pairwise atomic correlations and can be used to obtain a model of the structure.

Atomic clustering is a precursor of alloy decomposition into two separate phases, i.e. precipitation, in the case of Fe-Cr alloys at low concentrations and temperatures iron-rich phases (α) and chromium-rich phases (α') will co-exist above the two-phase solvus or miscibility gap. Precipitation will occur after age hardening but clustering specifically implies local deviations from the average concentration and it cannot exist as a homogeneous state. Concerning ordering, it is assumed to proceed uniformly through the specimen, however there is no correlation between distant sites, i.e. widely separated regions may or may not contain the same ordering sequence. Both ordering and clustering structures may develop into a long range ordered (LRO) structure by ageing beneath the order-disorder solvus. If the solid has LRO there will be no decay in the range of atomic correlations with distance and the parameters $<\sigma_0\sigma_i>$ will be independent of the separation r_i although they will depend on the location sites i. Further information can be found in ref. [16], chapter 2.

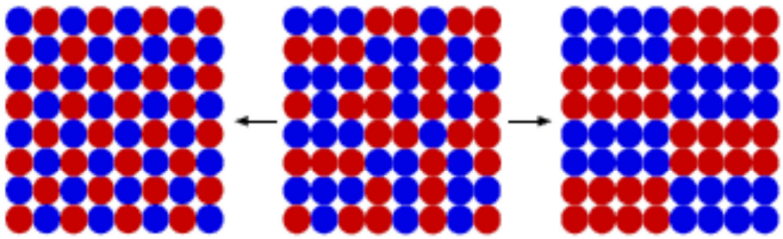

Fig. 2-4: Schematic representation of solid solutions: Left-hand side: ordered substitutional. Center: random. Right-hand side: clustering.

Shell	No. of sites in shell	Generating vector	Shell radious	No. of sites in cluster
0	1	(0.0, 0.0, 0.0)	0.00	1
1	8	(0.5, 0.5, 0.5)	0.75	9
2	6	(1.0, 0.0, 0.0)	1.00	15
3	12	(1.0, 1.0, 0.0)	2.00	27
4	24	(1.5, 0.5, 0.5)	2.75	51
5	8	(1.0, 1.0, 1.0)	3.00	59
…	…	…	…	…

Table 2-1: Shells and clusters in BCC lattice

In materials which only present SRO (i.e. no LRO) the pair correlation of the atoms become uncorrelated at distances that are many atoms away. In terms of resistivity the pair-correlation (two-particle cluster) is enough to entirely describe the effects of SRO.

It is not the objective of this thesis to derive the analytical expression of the resistivity in non-simple alloys. Nevertheless, it is in the scope of this thesis to understand the contributions to the resistivity and main terms in the analytical expression, in order to evaluate the utility and scope of the technique used in this work, which is the Resistivity Recovery. Below the analytical expression of the residual resistivity is being shown for simple non random alloys in absence of atomic displacement effects (note that the development of the expression of resistivity that we are about to show is referred in Appendix A and also in the book of Rossiter [16] and many other texts on electrical resistivity on metals):

$$\rho = \frac{C'}{N} c_A c_B \sum_i c_i \alpha_i Y_i \qquad 2\text{-}23$$

being, N the total number of atoms, α_i the Warren-Cowley parameter, c_i the number of atoms in the *ith* shell and C' and Y_i are given by:

$$C' = \frac{3\pi m^2 \Omega}{4\hbar^3 e^2 k_F^6} \qquad 2\text{-}24$$

$$Y_i = \int_0^{2k_F} \frac{\sin(qr_i)}{qr_i} \left|\langle k+q \left| w^d(r) \right| k \rangle\right|^2 q^3 dq \qquad 2\text{-}25$$

The function Y_i is integrated over the spherical Fermi surface (as we are considering a simple alloy) with diameter $2k_F$, and it contains the structure factor and the form factor in which the transition probability matrix can be decomposed when pseudopotential (*w(r)*) approximation is applied (see further section 2.1.5). Y_i is an oscillating function which depends on q and decays as *i* grows, thus is clear that only first few coordination shells will play a role. Depending on the material even the resistivity could be proportional to the linear combination of first and second SRO parameters, α_{12}.

It has been shown that the presence of migrating defects enhances changes in SRO parameters leading to changes of residual resistivity. Typically such investigations have been done by means of quenching experiments. Such experiments consist on the creation of thermal vacancies by heating up the samples (up to the so-called quenching temperature T_q) followed by an extra-fast cooling up to the annealing temperature at which isothermal annealing is going to be performed. The excess of thermal vacancies created by quenching are able to migrate within the material and the residual resistivity values which are monitored are shown to change. Changes in ρ_0 are due to re-arrangement of solutes enhanced by the presence of migrating vacancies. This phenomenon is also going to occur in our measured Fe-Cr samples as the RR experiments will be run. Thus this effect will have to be taken into account when analysing the data. Much research has been done on SRO kinetics using quenching and irradiation experiments [48–54] in concentrated alloys but no works have been found in the study of Fe-Cr alloys.

2.1.5. Non-simple metals: the s-p interaction

In simple metals, as it has been already said, the Fermi surface is assumed to be a sphere of diameter $2k_F$., and thus electrons behave as nearly-free. In general is assumed that core electrons do not move and the valence electrons can be approximated to plane wave functions where the nearly-free electrons “see” an effective potential which is a result of smoothing the real Coulomb potential (see Fig. 2-5). This is the pseudopotential approximation. In alloys containing transition metals, however, the distinction between the valence and core states is no longer so clear-cut. The amplitude of the wavefunctions of d-states in transition alloys play a role outside the core region either forming a narrow d-band by overlapping with adjacent atoms or hybridizing with sp conduction bands. Also the Fermi surface becomes quite irregular by mixing s-like parts with d-like parts. This fact significantly increases the complexity of the calculations so this will be out of scope of this work. Still by means of smart approximations again, it is possible to understand the physics involved.

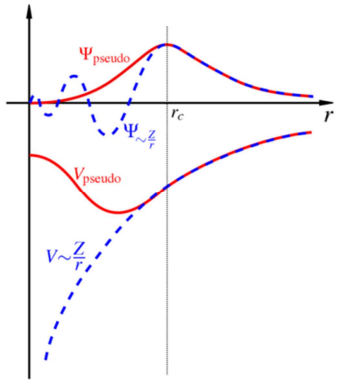

Fig. 2-5: Scheme of pseudopotential approximation (red, continuous line) vs. real part of true wavefunction in the presence of Coulomb potential (blue, dotted line).

In non-simple alloys it is assumed that most of the current is carried by the electrons in the "s-band", because of the value of its effective mass (close to that of electrons in copper, Mott and Jones 1936), while the "d-electrons" have much higher effective mass and therefore much lower mobility (see equation 2-12). Impurities, phonons and electron-electron interactions will cause scattering of the s electrons into vacant s- and d- states, but since the scattering probability depends upon the density of states into which the electrons are scattered (equation 2-13), s-d scattering mechanisms occurs much more frequently than s-s scattering. Electrons scattered into de "d-band" increase the resistivity because of their increased effective mass. The importance of the density of states in the d-band can also lead to a modification of the temperature dependence of the resistivity, given by a rapid increase of $N_d(E_F)$ with temperature. Such effect would lead to an additional temperature dependent term [46] with respect to equation 2-15:

$$\rho(T) = \rho_0 + \rho_h(T) + BT^2 + \rho_m(T) \qquad 2\text{-}26$$

If we now look at the residual resistivity value of non-simple alloys, it has come clear that the s-d scattering probability has to be taken into account. At this point some qualitative understanding of this phenomenon is possible under the rigid band model. The following explanation is based on empirical observations on the system Ag-Pd. Let's assume in general a transition metal A which has an s-band similar to that of B transition metal and also a narrow d-band which overlaps the s-band and E_F near the top of d-band. Then as B metal is added to A, the s-electrons of B atoms are supposed to fill the d-band leading to a decrease in $N_d(E_F)$ until the d band is filled at c_i concentration of B. The density of states of the unfilled d-band can be described approximately as:

$$N_d(E_F) \sim (c_i - c_A)^2, \quad c_A \leq c_i \qquad 2\text{-}27$$

If the atoms are randomly distributed (no SRO effects) an average lattice potential can be described from the constituent ion potentials of the alloy. This is called the virtual crystal approximation:

$$\langle V \rangle = c_A V_A + c_B V_B \qquad 2\text{-}28$$

Such potential can be described by analogy to equation A-18 (see Appendix A) as $V = \bar{V} + V^d$, where V^d is the difference potential. The probability of scattering from an s-state to a d-state is given by:

$$\int \left|\psi_d V^d \psi_d \mathrm{dS}\right|^2 \mathrm{N_d(E_F)} \qquad 2\text{-}29$$

The magnitude of scattering potential at a A atom site is $c_A V^d$ (cf. Rossiter 4.67 [16]) and the fraction of such sites is $(1 - c_A) = c_B$. The scattering probability is thus proportional to:

$$(c_i - c_A)^2 c_A^2 c_B \qquad 2\text{-}30$$

If we assume independent contributions from s-s and s-d scattering, as s-s interaction has been determined in the previous section (equation 2-23), then the total residual resistivity might be written as:

$$\rho = \rho_{ss} + \rho_{sd} \propto c_A c_B \left(\left[\frac{C'}{N} \sum_j c_j \alpha_j Y_j \right] + [(c_i - c_A)^2 c_A] \right) \qquad 2\text{-}31$$

2.1.6. Magnetic effects and deviations from Matthiessen's rule: the two current model

Some complications can arise when the non-simple alloy under study is magnetic or nearly magnetic material as it is the case of the Fe-Cr system, and therefore need to be considered. Iron, which is the host material, is ferromagnetic (alignment of spins in a parallel array) whilst the solute, chromium, is antiferromagnetic (alignment of spins in an antiparallel array). In transition metals the orbital angular momentum of the electrons is almost zero[10], so only the spin magnetic moment of the electrons which are in incomplete shells contribute to the magnetic moment. It is believed that the inversion of SRO parameters at Cr concentrations of about 10% is due to some magnetic frustration effect of the Cr spins, but we will discuss further this question in chapter 4.

When thinking about energy distribution of conduction electrons, their alignment is governed by a special type of interaction known as the exchange interaction which the determines that the energy of electron states is a minimum when the electrons line up with their spins parallel provided that the Pauli exclusion principle is not violated. As a result, there will be different populations of spin-up (↑) and spin-down (↓) conduction electrons which create a dipole moment. Qualitative picture for Fe conduction electrons is represented in Fig. 2-6, from Campbell and Gomès (1967) [55]. It has been confirmed that scattering of spin ↑ is different than the scattering of spin ↓ electrons. Thus a new model has been adopted to understand the electrical resistivity in ferromagnetic materials which also justifies the large deviations on the Matthiessen's rule which were mentioned in section 2.1.3. The resistivity can no longer been understood as an effect produced by an electron current but by two currents, one referred to spin ↑ and the other to spin ↓. The two-current (or two-band) model is based on the suitable definition of the function ϕ_k in

[10] This effect is usually termed "quenching" of the orbital angular momentum and it means that when the ion is in the crystal there is no orbital magnetic momentum.

the variational method of Köler (cf. Appendix A, Ziman 1960 [56] or Fert and Campbell 1967 [47]) as a linear combination of two functions each of them associated to a certain carrier type, σ = ↑, ↓:

$$\phi_k = \sum_{\sigma'} \eta_{\sigma'} \phi_{\sigma'} \delta_{\sigma\sigma'} \qquad 2\text{-}32$$

Such differentiation of the distribution function for every spin type in the Boltzmann equation leads to an expression of the resistivity based on the independent (and conveniently defined [47]) resistivity terms for elastic scattering of spin ↑ electrons, $\rho_\uparrow$, and spin ↓, $\rho_\downarrow$, respectively, and an spin mixing term, $\rho_{\uparrow\downarrow}$:

$$\rho = \frac{\rho_\uparrow \rho_\downarrow + \rho_{\uparrow\downarrow}(\rho_\uparrow + \rho_\downarrow)}{\rho_\uparrow + \rho_\downarrow + 4\rho_{\uparrow\downarrow}} \qquad 2\text{-}33$$

The Matthiessen's rule is applicable to $\rho_\uparrow$, $\rho_\downarrow$ and $\rho_{\uparrow\downarrow}$ given that every term depends linearly on their scattering operator:

$$\rho_\sigma = \rho_{0\sigma} + \rho_{i\sigma}(T) \qquad 2\text{-}34$$
$$\rho_{\uparrow\downarrow} = \rho_{0\uparrow\downarrow} + \rho_{i\uparrow\downarrow}(T) \qquad 2\text{-}35$$

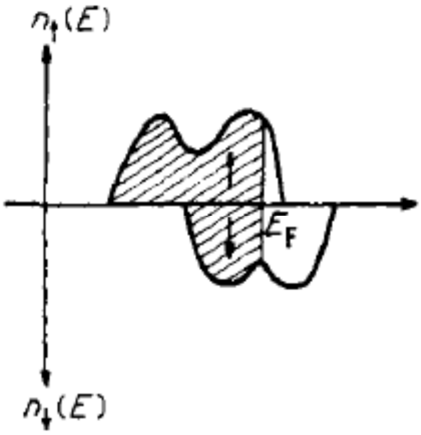

Fig. 2-6: The usually adopted band model for iron consists of an almost filled ↑ spin sub-d-band and half filled ↓ spin sub-d-band.

In the absence of spin-flip collisions $\rho_{\uparrow\downarrow}$ cancels out and the resistivity is expressed in a model where the current is carried by two independent currents:

$$\rho = \frac{\rho_\uparrow \rho_\downarrow}{\rho_\uparrow + \rho_\downarrow} \qquad 2\text{-}36$$

The inelastic scattering (spin mixing) occurs by collisions with spin waves and collision between spin ↑ and spin ↓ electrons. Both processes contribute to the temperature dependent term of the resistivity $\rho_{\uparrow\downarrow}(T)$ but the second one can be neglected. The residual term also contains a spin-flip mechanism that contributes to resistivity, $\rho_{0\uparrow\downarrow}$, which is induced by impurities in dilute alloys and can also be neglected in such cases. As it has been deduced in some experimental works [57], the spin-mixing term can no longer be neglected when impurity contents rise and alloys start no to be dilute any longer. In

chapter 6 we will provide a discussion on the influence of this term in the studied Fe-Cr alloys which we have been able to deduce form residual resistivity measurements.

The two-current model has provided justification for experimental observations in residual resistivities in dilute alloys [58–60]. The parameter α has been conveniently re-defined based on the concepts included in equations 2-33 to 2-36, are used for characterization and quantitative analysis of alloys residual resistivity. Parameter α describes the relation between the resistivity contributions of spin-down and spin-up resistivities:

$$\alpha = \frac{\rho_{0\downarrow}}{\rho_{0\uparrow}} \qquad 2\text{-}37$$

Fert and Campbell [58], applied the two current model to calculate the residual resistivity of ternary alloys. The application of such developments allowed unambiguous calculation of α_i parameters, from experimental data. The sub-index i refers to a specific solute in the pure host metal. Such development was also applied by Maury et al. to explain the apparent solute specific resistivity in metals (this will be shown in chapter 4 and 5) [37,57]. The development of the model goes as follows. Assuming that spin-mixing term can be neglected (eqn. 2-36) the resistivity of a binary alloy, MA, is:

$$\rho_A = c_M c_A \frac{\rho_{A\uparrow}\rho_{A\downarrow}}{\rho_{A\uparrow} + \rho_{A\downarrow}} \qquad 2\text{-}38$$

where c_M and c_A are the concentrations of M host metal and A solute respectively. If the alloy is dilute, i.e. $c_A << c_M$ the residual resistivity can be approximated to:

$$\rho_A = c_A \frac{\rho_{A\uparrow}\rho_{A\downarrow}}{\rho_{A\uparrow} + \rho_{A\downarrow}} \qquad 2\text{-}39$$

In the case of a ternary dilute alloy, MAB, the Matthiessen's rule is obeyed for each current, and the impurities A and B add their resistivity in each current ($\rho_\sigma = c_A \cdot \rho_{A\sigma} + c_B \cdot \rho_{B\sigma}$). Combining such form with equations 2-36, 2-39 and $\alpha_i = \rho_{i\downarrow}/\rho_{i\uparrow}$ it gives:

$$\Delta\rho = \rho_{AB} - (\rho_A + \rho_B) = \frac{(\alpha_A - \alpha_B)^2 \rho_A \rho_B}{(1+\alpha_A)^2 \alpha_B \rho_A + (1+\alpha_B)^2 \alpha_A \rho_B} \qquad 2\text{-}40$$

The study of ternary alloys has been of interest because it allowed unambiguous experimental calculation of α_i values [58]. Sometimes the systems under study are treated as ternary alloys when besides of the specific solute A, there is another element that can be treated as an impurity, such as created irradiation defects [37,57], o phonons created by the effects of non-zero temperature [59].

Further re-definition of α parameter as it follows [57]:

$$z = \frac{\rho_{0\downarrow} - \rho_{0\uparrow}}{\rho_{0\downarrow} + \rho_{0\uparrow}} = \frac{\alpha - 1}{\alpha + 1} \qquad 2\text{-}41$$

is going provide double advantage. On one hand it will be possible re-express the residual resistivity of binary alloys including the spin-mixing term, $\rho_{\uparrow\downarrow} = \rho_m$ (eqn. 2-33) as:

$$\rho(\mathrm{MA}) = \frac{\rho_0 + \rho_m}{1 + (1 - z^2)\,{}^{\rho_m}/_{\rho_0}} \qquad 2\text{-}42$$

and this will allow the analysis of the apparent Cr specific resistivity in our Cr alloys (in chapter 5). On the other hand, the development of the two-current model formalism for the study of the radiation induced resistivity reveals that the specific resistivity of the Frenkel pairs (FPs) can be expressed as a function of z and no longer on the defect concentration:

$$\rho_F^* = \rho_F \left[1 + \frac{(z - z_F)^2}{(1 - z_F^2)}\right] \qquad 2\text{-}43$$

The last concepts just mentioned such as radiation induced resistivity, specific resistivity of FPs are explained in the next section, concerning the radiation effects on the resistivity. The discussions concerning the influence of FP specific resistivity in RR experiments of Fe-Cr alloys and description of the z_F (in eqn. 2-43) are provided in chapters 4 and 5.

2.2.Radiation effects on resistivity

Once it has been understood how the characteristics of concentrated Fe-Cr alloys are going to influence their electrical conductivity at low temperatures, let's have a look on how radiation is going to affect the microstructure of the alloys and eventually its resistivity, which is one of the main objectives of this work.

In general the electron and proton irradiations are going to produce simple defects, i.e. FPs made of a vacancy and an interstitial atom[11]. At low concentrations (~ppm range) it is assumed that every FP increases the resistivity of the alloy by a certain amount (typically measured in μΩ cm at.%). This change in resistance is mainly due to an increase of the residual resistivity of the metal. Some changes in the thermal component, ρ(T), occur as well, but since the thermal component is poorly known and small and is difficult to estimate theoretically, irradiations and measurements are usually made at sufficiently low temperature to avoid the problem. As the residual resistivity is very sensitive to the presence of imperfections (as explained in previous sections) its change is then the appropriate measurement of the generated defect concentration. The residual resistivity can be monitored during irradiation in order to measure the radiation induced resistivity (RIR), Δρ, which has a linear relation with the particle fluence in the low dose regime [31]. The RIR is given by:

[11] Indeed a study on the type of damage and FP distribution of the irradiations with 5 MeV protons performed in this work will be given in the chapter devoted to experimental results.

$$\Delta\rho = \rho_F \sigma_D \Phi \qquad 2\text{-}44$$

where ρ_F is the specific resistivity contribution of a simple Frenkel defect, σ_D is the defect production cross-section and Φ is the particle fluence. The defect population created, n, is determined by the product of the creation cross-section and the fluence of irradiating particles. The resistivity of the FP can be described as a sum of discrete contributions from the vacancy, ρ_v, and the interstitial, ρ_i, respectively:

$$\Delta\rho = \rho_F n = \rho_i c_i + \rho_v c_v \qquad 2\text{-}45$$

Thus this physical property is sensitive to both types of defects and separable monitoring of their populations should be possible although very difficult. This feature represents an advantage with respect to other techniques such as positron annihilation (PA) spectroscopy given that they are only sensitive to vacancies.

The study of RIR has been extensively performed; at very low energies and doses it allowed the measurement of threshold energies for FP creation for different materials in the principal crystal directions [22,61] also RIR studies have been used to measure defect production cross-sections and damage efficiency [31]. This last experiments revealed than at high doses intra-cascade recombination decreased the damage efficiency whereas at high mean PKA energies sub-threshold elastic effects and electronic excitations start to play a role. The RIR measurements made in this work (in Fe-5%Cr, Fe-10%Cr and Fe-14%Cr) confirm that the increase in resistivity with fluence is very close to linear so the physics underlying match very well with the previous explanation.

2.3.Annealing theory

The annealing is the process of disappearance of the defects which are in the material in excess of the thermodynamic equilibrium. When performing a particle irradiation or a quenching experiment (high temperature heat-up followed by abrupt freezing), we are producing a so-called super-saturated crystal. In such crystals there is a thermodynamic driving force that tends to reduce the defect concentration. At suitable temperature intervals the defect mobility becomes significant. The disappearance of the defects is then experimentally observable and it is associated to migration to sinks (such as dislocations and other internal or external surfaces) or to recombination with complementary defects (e.g. interstitial-vacancy annihilation). In the case of defect clusters, its disappearance is mostly due to dissociation into smaller more mobile defects which eventually recombine.

2.3.1. Defect diffusion

The point defects created in a solid become mobile at sufficient high temperature. The events that they can perform as a consequence of the temperature of the system are diffusion jumps, dissociation from clusters or interact with other defects or impurities. The thermal motion of the defects is going to provide them some probability to jump over a potential barrier/saddle point from one equilibrium position to another. A statistical mechanics treatment of the problem [62] let show that the probabilities of these events

are given by the migration and binding energies. It is well known that the individual defect jump rate, *i.e.* the probability for a defect to undergo one migration jump (K), is proportional to the effective vibration frequency (K_0) and its migration energy (E_M):

$$\Gamma = \Gamma_0 e^{\left(-E_M/kT\right)} \qquad 2\text{-}46$$

being k the Boltzmann's constant and T the absolute temperature. If the considered jump involves not only migration but also dissociation from a trap (cluster or impurity) then the jump rate also includes the binding energy (E_B):

$$\Gamma = \Gamma_0 e^{\left(-[E_M+E_B]/kT\right)} \qquad 2\text{-}47$$

These type of expressions which relate a rate exponentially to the reciprocal of the absolute temperature, are often referred to as Arrhenius equation.

The diffusion coefficient is related to the jump rate as:

$$D = \delta a_0^2 \Gamma \qquad 2\text{-}48$$

where δ is a geometrical constant and a_0 the lattice parameter.

When studying close to real materials, all the different defects together with their different interactions and diffusion rates need to be calculated simultaneously. This involves non-simple analytical solutions but more complex models and computational approaches that are indicated in next section.

2.3.2. Rate theory

Pure atomistic treatment of the defect kinetics in solids, as kinetic Monte-Carlo, where the diffusion of every atom is considered individually, is very limited approach from the point of view of simulations given that it does not allow to simulate macroscopic systems but only cells on the order of nm (10^3-10^6 atoms) and thus no extrapolation can be applied to real physical systems. A formalism based on rate equations, where the study is made over mean concentrations of defects which obey the suitable jump rate for every specific reaction, is allowing simulations of macroscopic systems with current computational tools and also sets a mathematical base to interpret indirectly observed defect kinetics in resistivity experiments. In the rate theory formalism [62,63], the reactions between defects are supposed to occur via binary reactions of the type:

$$A + B \underset{K_C}{\overset{K_{A+B}}{\rightleftharpoons}} C \qquad 2\text{-}49$$

where K_{A+B} is the forward constant rate of diffusion of the reactants A and B and K_C is the backward constant rate. Constant rates are directly proportional to the diffusion coefficients of the species involved. The law of mass action is fulfilled for this reaction and thus the time evolution of the mean concentration of each species (c_i with i=A, B, C) can be describe by the partial differential equation:

$$\frac{dC_A}{dt} = -K_{A+B}c_A c_B + K_c c_C \qquad 2\text{-}50$$

Thus the time evolution of the system is governed by a set of nonlinear coupled partial differential equations which when solved will describe the complete annealing behavior of the system. In some special very simple system descriptions, solutions can be found easily and simulations of time evolution of defect concentrations can be depicted. As an example Fig. 2-7 shows the variation of vacancy (V_1), interstitial (i) and trapped-interstitial (C) with impurities (I) concentrations with time in a system which considers vacancy-interstitial annihilation plus interstitial trapping at impurities also described as:

$$V_1 + i \xrightarrow{K_{V_1+i}} anihilation \qquad 2\text{-}51$$

$$i + I \underset{K_C}{\overset{K_{i+I}}{\rightleftharpoons}} C \qquad 2\text{-}52$$

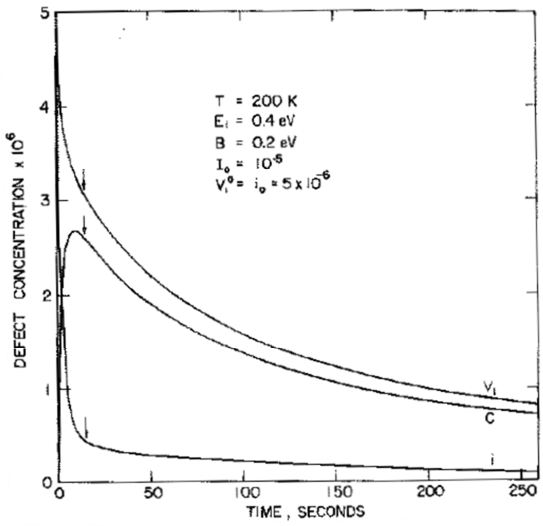

Fig. 2-7: Plot of the defect populations calculated in the simple system i-V annihilation with trapping of interstitials by impurities. They are also indicated parameters used for the calculations: annealing temperature (T), migration energy (E_i), binding ener gy (B), initial impurity concentration (I_0) and initial concentrations of i and v (V_1^0 and i_0). Plot taken from reference [62].

It is important to set the basis for a good qualitative understanding of the subsequent analysis of resistivity recovery results and to describe the fundamental annealing processes in which the rate equations are based. The migrating defect can either diffuse randomly until it disappears on a sink or it reacts with another impurity or defect leading to annihilation or clustering. The following is a short review of these 3 processes.

Random diffusion to sinks

This is the simplest process in which the mobile species diffuse to a fixed number of unfillable sinks (dislocations, grain boundaries or external surfaces). The long-time solution is always a simple exponential decay and it can be shown by rate theory. Let's consider thus the situation described by:

$$n \xrightarrow{K} \text{sink} \qquad 2\text{-}53$$

The rate equation which describes the number of remaining defects in the metal is:

$$\frac{dn}{dt} = -Kn \qquad 2\text{-}54$$

The solution to this equation is:

$$n = n_0 e^{-Kt} \qquad 2\text{-}55$$

being the rate constant proportional to diffusion coefficient D and to a parameter α which contains the information related to the geometry of external surfaces or the concentration of dislocation (i.e. the fixed sink concentration):

$$K = \alpha D = K_0 e^{(-E_M/kT)} \qquad 2\text{-}56$$

where K_0 is a constant including the geometrical factor, the lattice parameter and the sink distribution. Thus the solution of the random migration of single defects is:

$$n = n_0 e^{-K_0 \exp(-E_M/kT)t} \qquad 2\text{-}57$$

Anihilation and clustering

When interstitial and vacancy type of defects are present simultaneously in the crystal, their diffusion can lead them to annihilate each other:

$$i + \mathrm{V} \xrightarrow{K} anihilation \qquad 2\text{-}58$$

The rate equation for n-type of defects is:

$$\frac{dc_i}{dt} = -Kc_i c_V \qquad 2\text{-}59$$

In an irradiation experiments when initial concentrations of vacancies and interstitials are equal, the number of interstitials that have disappear must equal the number of the vacancies destroyed, $c_i = c_{i0} - c_{V0} + c_V$ and the rate of decay of the defects can be described by a simple second order equation:

$$\frac{dc_i}{dt} = -Kc_i^2 \qquad 2\text{-}60$$

Note that in a more generic situation the decay of vacancy concentration is not necessarily equal to the interstitials decay and thus the order of the reaction wouldn't be 2.

In the case of clustering a similar process would occur but including not only the possibility of binding but also a backward process of dissociation. A generic example of the process and the partial differential equation is indicated in eqns. 2-49 and 2-50.

Generic Rate equation

The order of the reaction is important to interpret the annealing process, since every single activated process is described by the generic chemical rate equation:

$$\frac{dn}{dt} = -K_0 F(n) e^{(-E_M/kT)} \qquad 2\text{-}61$$

Where F(n) = n^{γ} is any continuous function of n and γ is the order of the equation. Diffusion to sinks was a first order reaction, and i-V annihilation was a reaction of order two.

2.4.Resistivity recovery method

When a sample containing irradiation defects is gradually warmed at a constant rate of heating (h), the defects undergo diffusion and at suitable temperature intervals recombination stages, in which also trapping, diffusion to sinks and clustering can happen. The residual resistivity is a property related to the number of defects, as indicated in equation 2-45. When the increasing heating is made in steps, the residual resistivity can be monitored (at low temperatures), and thus the defect concentrations. This process is called isochronal annealing. In such experimental conditions the constant rate of heating allows to relate time and temperature by the relation: T=ht. In the simplest picture it can be considered that every stage corresponds to a single activation process with constant activation energy. The defect concentration will decay with increasing temperature as described in equation 2-57, a graphical representation is provided in Fig. 2-8. The diffusion rate which follows the Arrhenius law increases rapidly with temperature, as qualitatively depicted in Fig. 2-9. By a simple change in variable, the time evolution of defect population can be expressed as a temperature evolution. From equation 2-61 now it follows that:

$$-\frac{dn}{dT} \propto n(T) e^{(-E_M/kT)} \qquad 2\text{-}62$$

A graphical solution provides easier visualization of what happens with defects given that equation 2-62 will be the result of multiplying the defect population (as a function of

temperature) times the diffusion rate, giving for the reaction rate a peak at a characteristic annealing temperature, T_a. The annealing peak is depicted in Fig. 2-10.

In a real RR experiment, the residual resistivity is increased by particle irradiation. The irradiation is followed by an isochronal annealing process while the residual resistivity is monitored at every step. For the sake of clarity a graphical description of the experimental method is provided in Fig. 2-11. Along this thermal process the created defects will gain enough thermal energy to diffuse and annihilate or clusterize or even dissociate at high temperatures. Thus, though the different processes and equations previously showed, the residual resistivity of the irradiated sample might eventually recover its original value (non-irradiated residual resistivity) as the temperature is increased and most of the defects are recombined. This provides the overall RR curve containing all this information. If the steps of the annealing are close enough the derivative of the resistivity with temperature can be depicted and the appearance of peaks might reveal recovery stages in the so-called RR rate curve (or RR derivative). A schematic representation of RR kinetic processes in pure Fe and its recovery peaks as a function of defect population evolution taken from Fu et al. is indicated in Fig. 2-12 and Fig. 2-13. The recovery stages associated to different species diffusion and recombination are called stages I_{D2}, I_E, II and III.

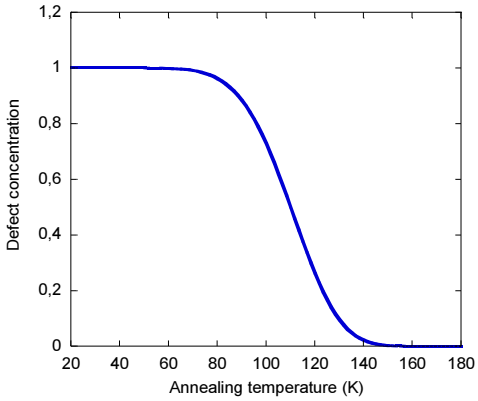

Fig. 2-8: Defect population evolution, of a single diffusion process in isochronal annealing experiment.

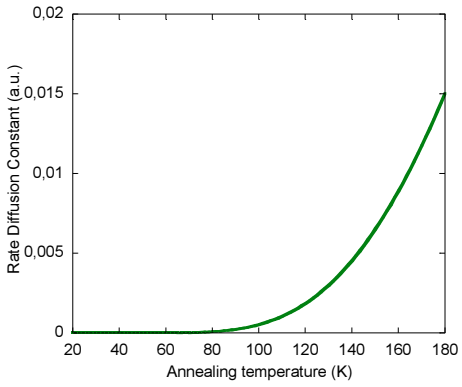

Fig. 2-9: Rate diffusion evolution as isochronal annealing goes.

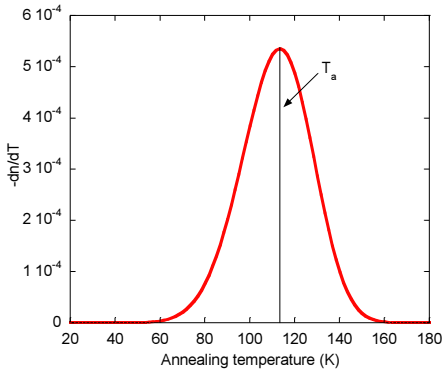

Fig. 2-10: Annealing peak characteristic of a recombination process.

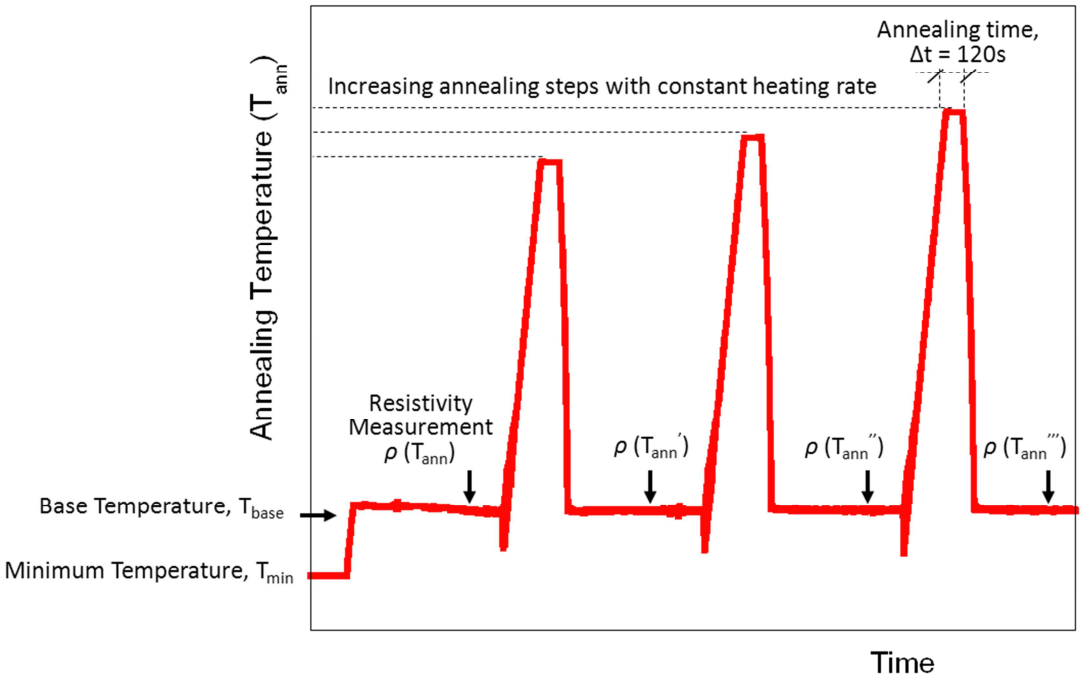

Fig. 2-11: RR experimental method: illustration of temperature ramps and resistivity measurements along isochronal annealing. Heating rate (10 K/min).

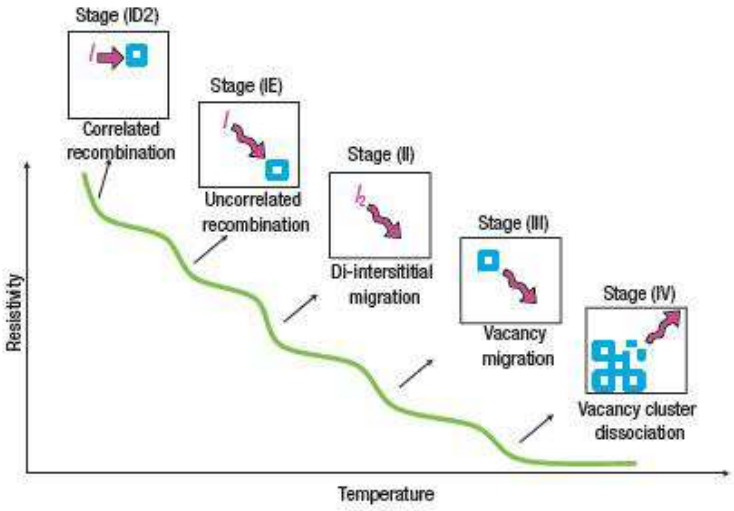

Fig. 2-12: RR stages after electron irradiation. Schematic representation of the different recovery stages as a function of increasing annealing temperature and associated mechanisms as proposed in electron irradiated iron by Takaki *et al.* [24,39]. The labels I, I_2 and squares represent mono- and di-interstitials and vacancies respectively.

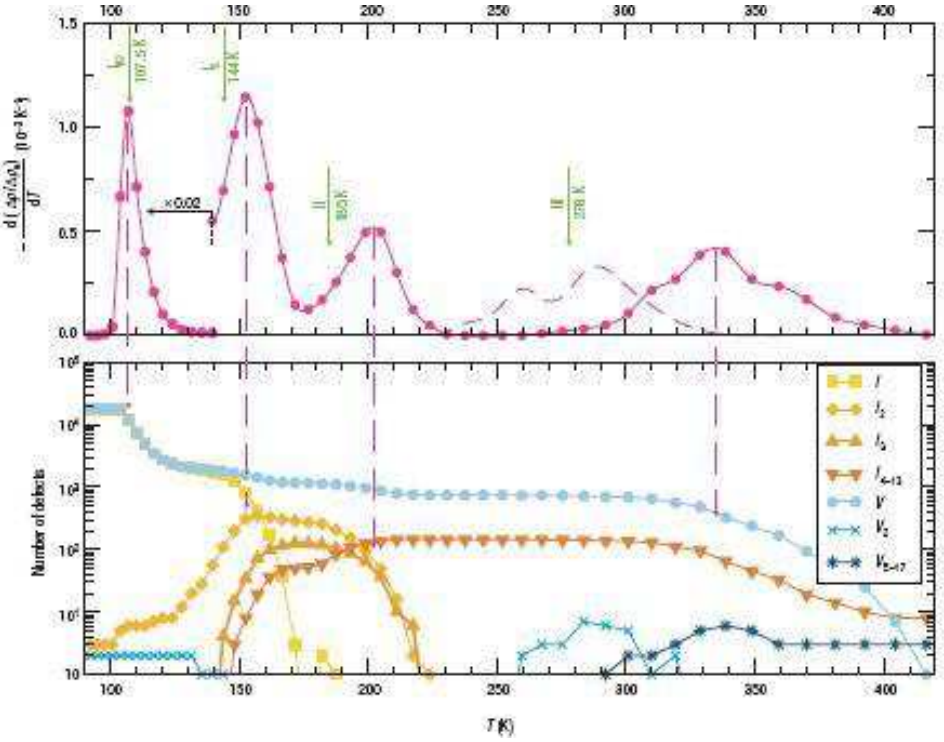

Fig. 2-13: Simulated RR peaks and defect population evolution along isochronal annealing after electron irradiation. Upper graph shows the derivative with respect to temperature of the simulated RR showing the recovery stages identified by peaks. Green arrows indicate the positions of the experimental peaks. Below 140 K, the curve was scaled down by a factor of 50 to reduce the intensity of stages. The lower graph depicts the associated defect population evolution (for 16 x 10^9 atoms). The magenta dashed arrows indicate the stage positions in the simulation. The concentrations of clusters V_3 and V_4 are negligible: these defects disappear almost immediately after they are formed because of their low migration energies.

2.5.Improved RR Method

The above explained RR experimental method, which is basically based on low-temperature irradiation followed by subsequent annealing, works very well when studying defect kinetics of pure metals or the effect of impurities on such kinetics. Nevertheless in the case of concentrated alloys the long range migration of defects is going to enhance re-arrangement of solutes within the alloy, as it has been introduced in section 2.1.4. As it is shown in equation 2-23 there is a linear relation between ρ and the SRO parameters. Thus the residual resistivity of a given concentrated alloy can be expressed as a function of different contributions:

$$\rho = \rho_o + \rho_D + \rho_S \qquad 2\text{-}63$$

being ρ_0 the residual resistivity of the metal free of irradiation defects, ρ_D the resistivity contribution of point defects and ρ_S a contribution imposed by the SRO state. The term ρ_D is proportional to the defect concentrations and its specific resistivity (as indicated in equation 2-45) whereas ρ_S was defined by Schülze and Lücke as [54]:

$$\rho_S = Bs \qquad 2\text{-}64$$

where B is a suitable constant with resistivity dimensions and s is a suitable dimensionless parameter which characterizes the degree of SRO.

Based on such description, the time evolution of the defects will induce two types of changes in the resistivity, one due to the migration of defects and other due to Cr rearrangement. The mechanism that might promote the short-range rearrangement of Cr atoms in the vicinity of trapped defects has been recently described and depicted by Nikolaev (Figs. 6 and 7 of [64]) for vacancy-carbon defects. The results obtained in the present thesis suggest that a similar mechanism with trapped I´s and V's should operate in the case of non C-doped Fe-Cr samples. The mechanism suggested is depicted in Fig. 2-14 in the case of clustering. It can be seen that the long-range migration of vacancies is very effective changing SRO by Cr-Fe permutation reactions.

The effect of resistivity change enhance by SRO effects during isochronal annealing has been qualitatively depicted for systems supersaturated with only vacancies [48,50]. The case where the change of SRO produces an increase in resistivity is shown in Fig. 2-15.

Therefore, in a classical RR experiment preformed in a concentrated alloy it is expected to find the RR peaks distorted by variations of SRO, which might even change the sign of the slope of the RR curves (causing an *increase* of resistivity instead of a decrease, as it will be show in our results). Obviously this can mask or change the different recovery peaks due to pure defect recombinations (and therefore the interpretation of RR curve). Indeed this side effect has almost not been considered and no solution has been provided up to now. In order to study such phenomena, and given that the kMC or Rate theory computational methods still cannot introduce the values of ρ_S contributions we have conceive a modification upon the traditional RR method which might be able to eliminate the effects of SRO contributions to the RR curves.

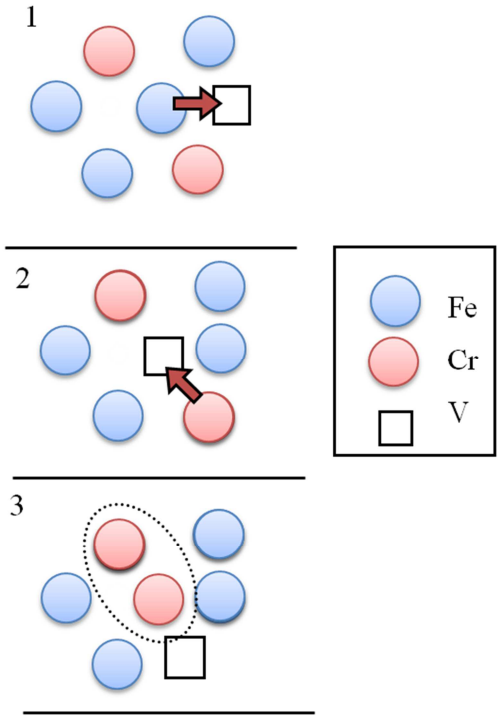

Fig. 2-14: Defect migration mechanisms can enhance re-arrangement of Cr

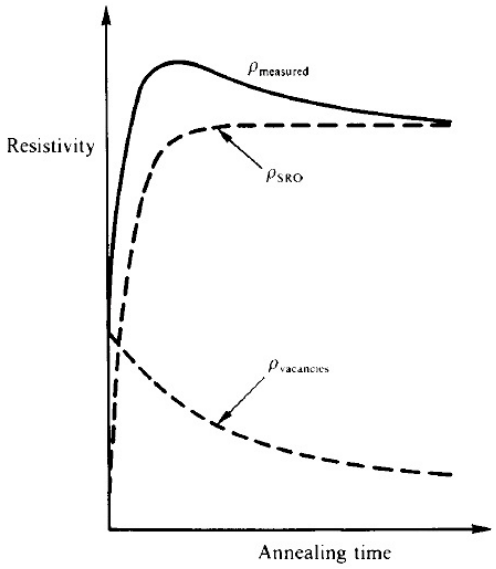

Fig. 2-15: Schematic variation of the residual resistivity due to SRO and vacancy anihilation as a function of annealing time.

The new method is based on the idea that SRO, in the presence of migrating defects, saturates at certain characteristic time. Saturation means that ρ does not change its value any longer in the presence of migrating defects. The phenomenon can be understood as follows: the solute re-accommodates enhanced by defect migration until the internal energy of the solid solution is minimized. Then a stationary state is reached where further movement of solutes does not change the state of SRO any longer. This phenomenon has

been experimentally observed in many alloys but also in Ni-11,4%Cr [65] which is non-simple binary alloy made of transition metals and with Cr concentrations very similar to the ones that have been studied in this research. It is well known that at 400 K simple defects have enough energy to freely migrate. Thus a 400 K irradiation (in the future called "pre-Irr") prior to a classical RR experiment (i.e. low temperature irradiation ("low-T-Irr") + isochronal annealing) should lead our samples to their SRO equilibrium state. For the sake of clarity a graphical representation of the expected effects of pre-Irr in our studied Fe-5%Cr, Fe-10%Cr and Fe-14%Cr specimens is provided in Fig. 2-16.

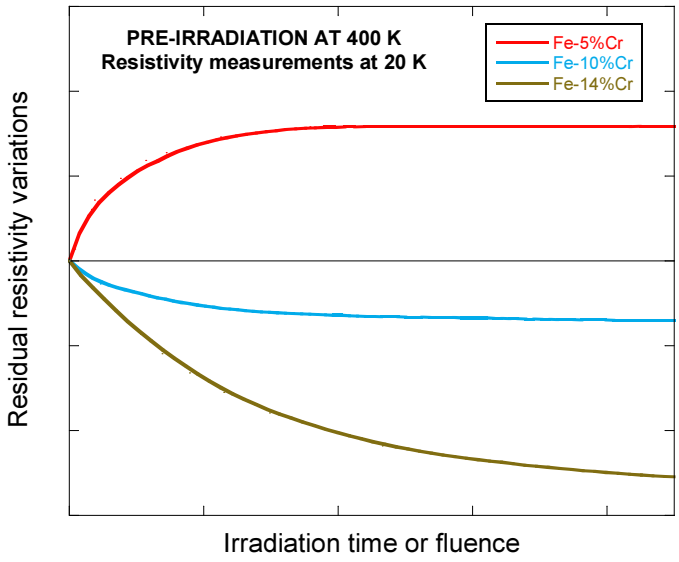

Fig. 2-16: Qualitative picture of the expected resistivity increment produced by 5 MeV proton irradiation at 400 K. The sign of the increment is associated with the sign in SRO. Positive increment implies ordering and negative increment implies Cr clustering.

The new method proposed in the present work consists on performing a pre-Irr to the Fe-Cr sample under study at 400 K, i.e. temperature high enough to ensure full recombination of created vacancies and interstitials. After this pre-Irr step, the sample is cooled down to liquid He temperature. Then, regular low-temperature irradiation at 50 K and subsequent isochronal annealing with follow-up of the resistivity is performed. The advantage of using the pre-Irr step, is that the sample now is close to its SRO equilibrium value. Therefore, it is expected that at temperatures where defects would migrate and SRO would normally change (in a classic RR experiment), no appreciable variation of the SRO will occur, and hence no change due to ρ_S will be observed. Thus, at the end of the RR experiment, the recovery of the resistivity should be almost complete. Whether this would be observed this would demonstrate that the material has come back to its original micro-structural state after pre-Irr step and thus the RR curve only shows effects due to defect migration.

In summary, we have proposed a novel RR measurement method to suppress the SRO contribution in the resistivity. The proposed method for performing RR measurements on

binary alloys has been tested in the case of Fe-5%Cr, Fe-10%Cr and Fe-14%Cr alloys, which have been investigated by both, the classical RR method and the improved RR method.

Chapter 3. Experimental on Resistivity

The present chapter encloses the primary objective of this thesis, at which most of the invested time and efforts have been devoted, this is the design and development of an experimental system to perform "in-situ" RR experiments at the end of one of the beam lines of a Tandetron ion irradiation facility. Such task has required the acquisition, design and assembling of every component of the set-up and the acquisition system, testing of sensors and probes (sensibility and performance), developing of data adquisition program and optimizing the measurement methodology as well as the data warehousing and treatment. Additionally a specific method for the specimens preparation and assembly in the developed set-up had to be invented. The experimental technique has turned out to be very exigent from a technical point of view as it will be explained along the chapter.

As explained in Chapter 2 a classical RR experiment consist of monitoring the residual resistivity of a metallic sample after irradiation at low temperature. It is measured at cryogenic temperature, typically 4.2 – 30 K, in order to eliminate the electron-phonon contribution to the resistivity and get a resistivity value dependent on point defects and "ordering" of the sample lattice. The low-temperature irradiation is going to create defects in the sample lattice which would increase its residual resistivity. This phenomenon is called RIR and has been described above. A step-like thermal annealing subsequent to irradiation will typically lead to a recovery of non-irradiated residual resistivity values providing the RR curves. The derivative of such curve provides indirect information on the migration processes that created defects perform. Hence information related to damage creation, recombination and clustering of defects, both vacancies and interstitials can be obtained performing this type of experiments.

This section provides a detailed explanation of the experimental techniques and methods used for the resistivity measurements, as the choice of the appropriate probe configuration and measurement methodology is non-straightforward in the case of metallic samples with very low values of electrical resistance. The four-point probe technique in the particular configuration of van der Pauw (VdP) [66] has been chosen to prepare the sample and the delta method has been used for clean measurement of low voltages by removing the thermoelectric voltage contributions. Beyond these basic concepts the requirements and difficulties for undertaking the RR measurements on samples irradiated at cryogenic temperatures are outlined. An explanation of experimental details and highlight of the technological difficulties needed to be overcome in such experiments is also presented as this discussion is interesting in order to understand the reliability and comparability among results from different authors. In particular, the design of the sample holder which assembles all the systems for resistivity

measurements, heating and temperature monitoring is carefully described as it is a fundamental piece to guarantee the success of the RR measurements. Finally an effort it has been made to treat the whole uncertainties of a resistivity measurement in a clear and sincere way because in literature this issue is normally omitted.

3.1. Four-point probe method: VdP technique

When measuring the resistivity of a sample, using a two-point probe method could seem, at first, a simplest method and easiest to implement, however this simpler arrangement introduces in the measurement the values of the wire or probe resistances (R_W) and the contact resistances (R_C) between the wire and the device under test (DUT). The four-point probe method avoids such resistance contributions and is the most commonly used to measure the resistivity of metal plates. It provides an absolute measurement without recourse to calibrated standards and is sometimes used to provide standards for other resistivity measurements [67].

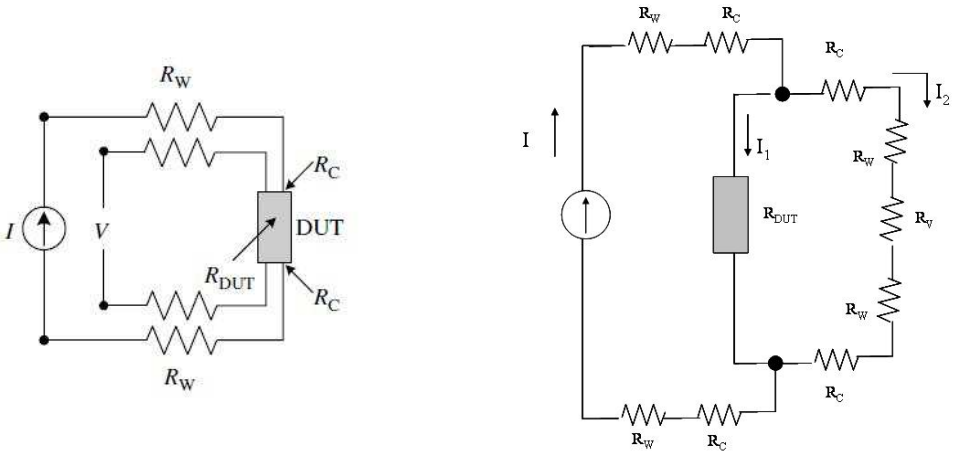

Fig. 3-1: (a) Four-terminal resistance measurement arrangement. (b) Four-point probe equivalent circuit.

Following reasoning leads to understanding of the method. Let's consider that the resistance of DUT test of Fig. 5.3(a) wants to be determined, its equivalent circuit is shown in Fig. 5.3(b). From Kirchoff laws, it can be stated:

$$I = I_1 + I_2 \quad 3\text{-}1$$

$$I_1 \times R_{DUT} = I_2 \times (2R_W + 2R_C + 2R_V) \quad 3\text{-}2$$

where R_W is the wire or probe resistance, R_C is the contact resistance, R_V is the input impedance of the voltmeter and R_{DUT} is the resistance of the device under test. The measured voltage drop is thus equal to:

$$V = I_1 \times R_{DUT} - I_2 \times (2R_W + 2R_C) \quad 3\text{-}3$$

by combining equations 3-1 and 3-3 resistance of DUT is obtained:

$$R_{DUT} = \frac{V}{(I - I_2)} + \frac{I_2}{(I - I_2)} \times (2R_W + 2R_C) \quad 3\text{-}4$$

It can be shown that for four-point configuration the current passing through the voltage path, I_2, is very low due to high input impedance of voltmeter (around 10GΩ). Hence voltage drops across R_W and R_C are negligibly small and can be neglected and the measured voltage is essentially the voltage drop across the DUT:

$$R_{DUT} = \frac{V}{I} \quad 3\text{-}5$$

Once it has been proven that the four-point probe method is the most suitable to measure the resistivity of our sample the next important concern is the arrangement of such probes. There are many possible probe configurations [66,68,69] which are closely related to the shape and dimensions of the specimen under study. In the case of the present experiment, the chosen probe configuration was the one proposed by VdP [66] on a clover-leaf shaped sample (see Fig. 3-2). The VdP method assumes that samples are homogeneous, isotropic, and two-dimensional (thickness small compared to breadth and width) and that the sample boundaries are sharply defined. The "clover-leaf" geometry of the sample allows maximum profit of the slices cut from the departing $Fe_{1-x}Cr_x$ bars, avoiding other highly damaging mechanising processes (i.e. cold rolling techniques) - as the microstructure of the "as-received" material has to be preserved (see section 3.4) -. In the ASTM standards it is recommended for samples of arbitrary shape [70], resulting in a less strict configuration concerning the sample dimensions and probe position (as it is in the bridge configuration). It is also recommended in order to reduce any errors due to non-ideal contacts [66,71,72] and to improve the geometric factor (this is the factor which relates the electrical resistance with the resistivity and usually depends on the shape of the sample and the position of the electrodes). Some finite element simulations were made with ANSYS code to observe the current density and the potential distribution in the clover-leaf samples (see Fig. 3-3). It has been demonstrated that measurement results are independent of the wanderings of probes in a region near the border and therefore it is unnecessary to determine the precise positions of probes in order to make corrections for the boundary effects [73]. A schematic representation of that calculation applied to our clover-leaf shaped specimen is depicted inFig. 3-4. Another advantage that was taken into account when choosing the specimen geometry and the position of the current and voltage probes was that the cross-cuts made on the samples will allow not full homogenous irradiation of the area of the samples. In other words, our samples where thin discs of 11 mm diameter, whereas it was be significantly easier and faster to get a proton beam area of ~7x7 mm, then by means of performing the cross-cuts that result in clover shape the area measured is reduced and the small beam is enough to irradiate the area of interest. Based on the work of Matsumura, who made finite-element calculations, and on our ANSYS simulations it was possible to confirm that the impact of the squared beam area on the voltage reading will be reduced by the clover-leaf cuts.

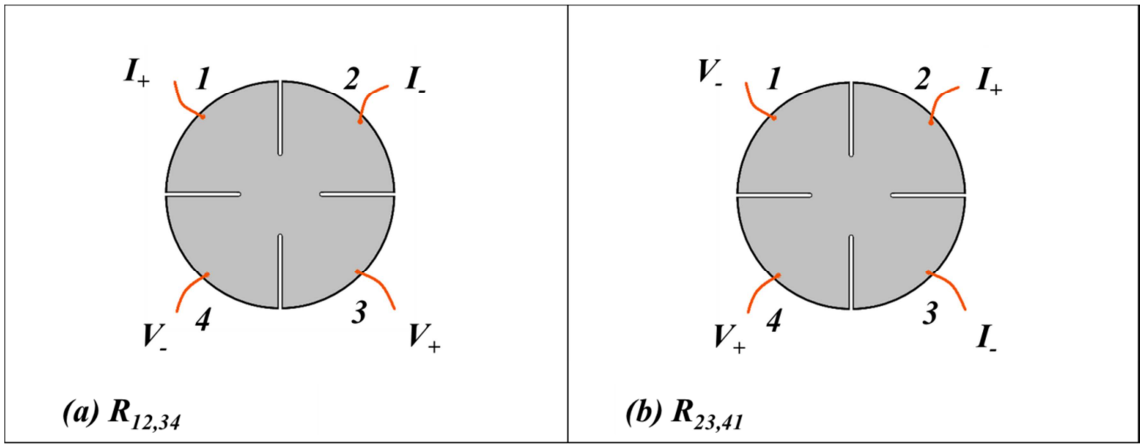

Fig. 3-2: (a) R12 probe configuration for VdP: current passes through probes 1 and 2 and voltage drop is measured between 3 and 4. (b) R23 configuration: current is applied to probes 2 and 3, and voltage is measured between 4 and 1.

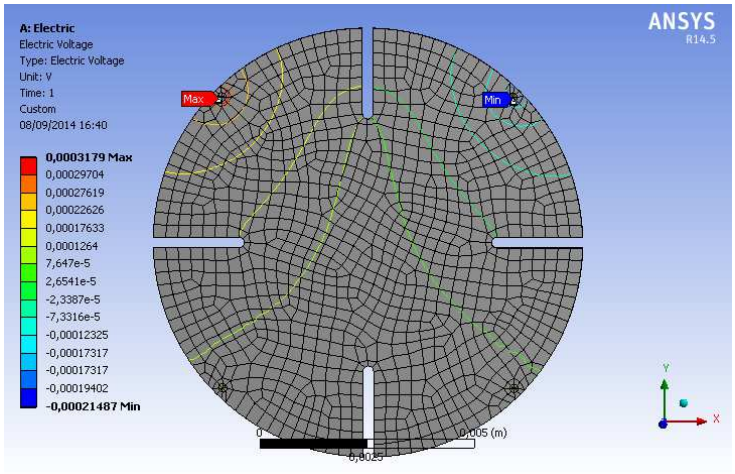

Fig. 3-3: Example of calculated electrical potential distribution in the sample with the geometry used in this work.

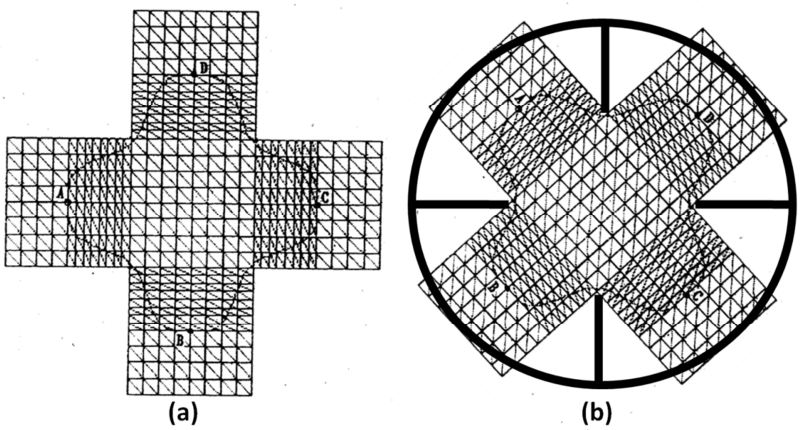

Fig. 3-4: (a) Finite elements division of a cross sample and the demarcation curve outside which the modified VdP method is suitable [73]. (b) Adaptation to our clover leaf geometry.

The resistivity value can be obtained by measuring R_{12} and R_{23} (see Fig. 3-2):

$$\rho = \frac{\pi t}{\ln 2} \times \frac{(R_{12} + R_{23})}{2} \times f\left(\frac{R_{12}}{R_{23}}\right) \quad 3\text{-}6$$

where t is the thickness of the sample and $f(R_{12}/R_{23})$ is a function which, when R_{12} and R_{23} are almost equal can be approximated by the formula:

$$f \approx 1 - \left(\frac{R_{12} - R_{23}}{R_{12} + R_{23}}\right)^2 \times \frac{\ln 2}{2} - \left(\frac{R_{12} - R_{23}}{R_{12} + R_{23}}\right)^4 \times \left\{\frac{(\ln 2)^2}{4} - \frac{(\ln 2)^3}{12}\right\} \quad 3\text{-}7$$

In order to proceed with consecutive measurements of R_{12} and R_{23}, it was required to install a system based on relays which were able to interchange the electrical connections. The implemented system allows to switch the voltage and current connections to the 4 wires and measuring each time in the two configurations. Also all the resistivity measurement process was implemented in a computer by using LABVIEW code, and thus the VdP resistivity measurement could be realized and recorded. The measurement of every R_{ij} requires specific methodology in order to avoid undesired thermoelectric noises, this is the Delta method which is explained in the next section.

3.2.Low-voltage measurement technique: Delta Method

Thermoelectric voltages are very common source of errors in low voltage measurements, as it is the case of resistivity measurements in metals [74]. These voltages are generated when different parts of a circuit are at different temperatures and when conductors made of different materials are joined together. One way to eliminate a constant thermoelectric voltage is to use a delta method where voltage measurements are made first at a positive and then at a negative test current. A modified technique can be used to compensate for changing thermoelectric voltages by considering the thermoelectric drift as a linear function of time during short periods. The difference between consecutive voltage readings is the slope or rate of change in thermoelectric voltage. This slope is constant, so it can be canceled by alternating the current source three times to make two delta measurements: one at a negative-going step and one at a positive-going step. For the linear approximation to be valid, the current source must alternate quickly, and the voltmeter must make accurate measurements within a short period of time. If these conditions are met, the three-step delta technique provides an accurate voltage reading of the intended signal unaffected by thermoelectric offsets and drifts.

Following analysis of the mathematics for one three-step delta cycle will demonstrate how the technique compensates for temperature differences in the circuit, reducing measurement error. Let's consider the case of a circuit where the temperature is linearly increasing and that in a very short period of time three reversed voltage measurements occur (as indicated in the Fig. 3-5), then if the three measurements are so close in time it can be considered that the variation of thermoelectric voltage, dV_t, is increasing constantly between, V_1, V_2, and V_3. Thus voltages measured will be equal to:

$$V_1 = V + V_{th} \quad 3\text{-}8$$

$$V_2 = -V + V_{th} + dV_{th} \quad 3\text{-}9$$
$$V_3 = V + V_{th} + 2dV_{th} \quad 3\text{-}10$$

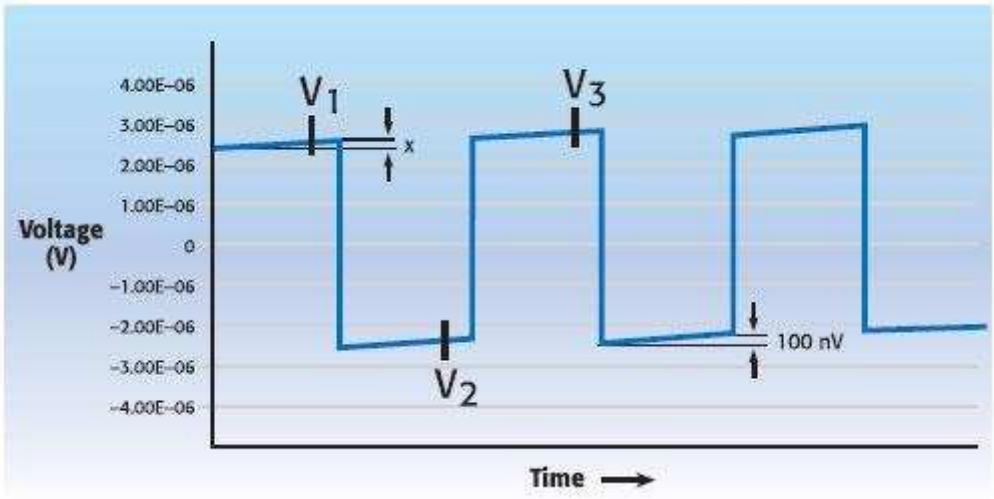

Fig. 3-5: Three-point delta method showing a changing thermoelectric voltage error.

These voltages include an error due to thermoelectric voltage in the circuit and are no longer of equal magnitude. However using the absolute difference between the measurements it is possible to cancel this term. This first step is to calculate the delta voltages. The first delta voltage V_a is equal to:

$$V_a = \frac{V_1 - V_2}{2} = V - \frac{dV_{th}}{2} \quad 3\text{-}11$$

V_a is referred to negative-going step. The second delta voltage V_b is made at the positive-going current step and is equal to:

$$V_b = \frac{V_3 - V_2}{2} = V + \frac{dV_{th}}{2} \quad 3\text{-}12$$

The thermoelectric voltage adds a negative error term in V_a and a negative error term in the calculation of V_b. When thermal drift is linear these error terms are equal in magnitude. Thus, the error can be canceled by taking the average of V_a and V_b:

$$V = \frac{V_a - V_b}{2} \quad 3\text{-}13$$

The three-step delta technique eliminates error due to changing thermoelectric voltages and is the best choice for high-accuracy resistance measurements.

3.3. System requirements

The experimental system described in this thesis was totally developed in order to be able to irradiate thin metal alloy foils using protons of some MeV's at cryogenic temperatures

in order to achieve an almost homogeneous damage in the bulk of the order of 10^{-4} dpa. Then, once irradiated, the residual resistivity of the sample would be monitored near liquid He (LHe) temperatures along a step-like annealing process. The maximum annealing temperature is 500 K. The system was installed, tested and finally operated at the 5 MV Tandetron accelerator of CMAM (Centro de Micro-Análisis de Materiales) [75] of Universidad Autónoma de Madrid (UAM). This facility can provide a 5 MeV proton beam at currents from 10-40 nA (to assure a negligible sample heating) so a total sample irradiation time of few hours is needed to achieve the desired dose.

After studying all the constraints and requirements, the basic conditions for achieving reliable RR measurements are the following:

(i) A thin sample with well controlled microstructure and impurity content.

(ii) An experimental chamber for irradiation at cryogenic temperatures with an *ad-hoc* sample holder.

(iii) A reliable system for monitoring and control the sample temperature (crucial issue).

(iv) An *in-situ* analysis technique for the resistivity measurements and the temperature cycles.

(v) A suitable proton beam and its associated beam control systems.

3.4. Sample preparation

Fulfillment of required experimental conditions (bulk irradiation, high temperature range from cryogenics to 500 K, low-voltage measurements, temperature cycling) together with sensitive subsequent treatment of the experimental data (derivative of the experimental curve) makes RR experiments difficult to perform. Several authors have developed experimental RR systems for wire-like and bridge-type [70] samples of tens to hundreds of μm thick foil samples [24,27,29,30,38,76,77]. In such cases, the sample preparation methods used involved mechanizing processes that may alter the microstructure and composition of the departing material and thus give rise to unclear results. In the present work we wanted to avoid cold-rolling to prepare the specimens in order to guarantee that the purity, grain size, Cr distribution and low dislocation density of the departing material is maintained. The problems associated to cold-rolling and other common preparation procedures are discussed later in this section.

The chromium ferritic/martensitic base alloys used were designed in the framework of EFDA contract [78,79] and provided by "L´Ecole Nationale Supérieure des Mines" (CNRS) in the form of small bars of 10.9 mm of diameter with well controlled composition and guarantee of low dislocation density. Every bar was recrystallized after cold reduction of 70% and then heat treated for 1h under pure Ar flow. Table 3.1 lists the irradiated alloys: its composition, annealing temperature, mean grain size and dislocation density. Fig. 3-6(a,b) show TEM images of Fe and Fe-10%C alloys respectively where dislocations can be observed for pure Fe in Fig. 3-6(a) and no dislocation appears for Fig. 3-6(b).

Composition & Microstructure	Fe	Fe-5%Cr	Fe-10Cr	Fe-14Cr
C	4	3	4	5
O	4	6	4	4
S	2	3	4	7
N	1	3	3	5
P	< 5	<5	< 5	< 10
Cr	< 2	5.40 wt %	10.10 wt %	14.25 wt %
Annealing Temperature	700 °C	750 °C	800 °C	850 °C
Mean Grain Size	183 µm	68 µm	82 µm	141 µm
Dislocation Density	1,2 x 10^8 cm^{-2}	1,2 x 10^8 cm^{-2}	No disloc.	No disloc.

Table 3.1: Detailed microstructure of studied materials: impurity content (ppm), grain size and dislocation density.

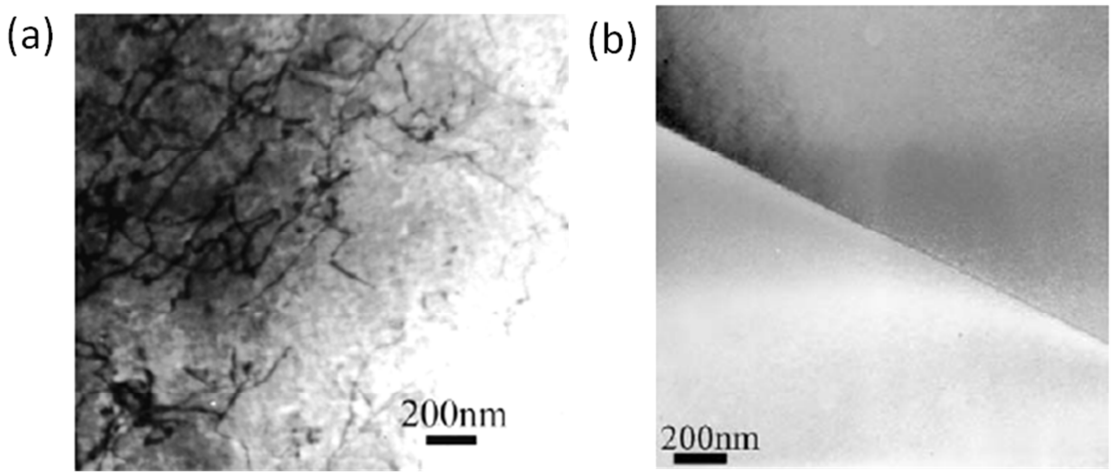

Fig. 3-6: TEM images showing dislocations in pure Fe and dislocation free grain boundary in Fe-10%Cr alloy [79].

In order to ensure minimum alterations on the "as received" microstructure intense research and many testing was done. The samples were prepared to obtain a clover-leaf shape as it has been detailed explained in previous section (see Fig. 3-2). Special care was taken concerning the thickness of the specimens given that they need to be sufficiently thin in order to ensure quite uniform bulk irradiation. The samples thickness must allow bulk resistivity measurements as well. In order to obtain a homogeneous distribution of damage throughout the bulk with energetic protons, samples have to be thin enough so that the Bragg´s peak is well beyond the thickness of the sample. For 5 MeV protons this condition determines a maximum thickness of 70 µm according to SRIM simulations [80]. Thus, ~50 µm plane-parallel foils had to be obtained from the delivered bars. As previously commented, the sample preparation process was designed to minimize any modifications to the microstructure of the departing material. Firstly, 0.5 to 1 mm thick slices were cut by spark erosion from the original bars and then 4 clefts where performed using the same technique to obtain the "clover leaf" shape. Next, the thin overlying oxide

layer was removed using a low temperature (-20 ºC) electrochemical process with ethanol and perchloric acid. Then, the samples were grinded using 320, 600, 1200 and 2500 paper-grit. Finally, they were polished on a plane-parallel automatic polishing machine, employing diamond suspensions from 3 to 0.25 μm. Eventually, the size of the specimens was ~50 micrometers thick with a mirror-like surface finish (see for example Fig. 3-8(a), 3-9(d), 3-9(f), 3-9(g), 3-10(a) and 3-10(b)). Although mechanical polishing can induce a damage deformation surface in some cases, deformation-free surfaces can be obtained by correct choice of the cutting device (manual, automatic), polishing methods (purely mechanical or chemical-mechanical process) and abrasives used [81,82]. Indeed the ≤3 μm grade of polycrystalline diamond used here as the carrier paste added to a short-nap cloth produced a surface with a shallow low-strain-damaged layer which eventually should be neglected with respect to the bulk of the sample. Electrochemical polishing was also considered as the final treatment to remove possible surface mechanical stresses but after several tests it was rejected given that control over the geometry of the sample was not accurate and plane-parallelism and shape where degraded (e.g. in Fig. 3-7(c)) Concerning thermal treatments, some tests were done in vacuum conditions, but the appearance of a thin oxidation layer on the surfaces was considered to be much worse than the few nanometer damage produced by the mechanical polishing (see Fig. 3-8). From these considerations we ruled out the use of cold–rolling techniques to produce a long rectangular sample (bridge type), as this method needs a high temperature thermal treatment around 1100 K to remove the high density of dislocations produced. Considering the 50 μm thickness, this treatment could alter the original microstructure, the SRO parameter and can segregate Cr ions to the surface.

Once the thin samples are made, further manipulation is required to make the electrical connections. Three different method of contact welding were tested in our samples- First we contacted a micro-welding company (“microsoldadura.com”) which made some test for us using High Frequency Resistance Welding (HFRW) technique. As it is shown in Fig. 3-9(a) and (b) the weldings exhibited good mechanical resistance but the technique resulted very harmful for thin samples. Second, we run some test by a collaboration with “Laser Center” from Universidad Politécnica de Madrid (UPM).) Some test shown again and well defined position and area of the welding spot (see Fig. 3-9(e)). However it resulted very difficult to control the power of the laser in order to not damage the 50μm sample. Also the reproducibility was not easy. Finally we tested some spot welding technique at CIEMAT and it succeed to weld both Cu wires and thermocouples to the sample (see Fig. 3-9(f) and (g)). As spot-welding ensured bulk resistivity measurements and as there is reasonable tolerance concerning the position of the probes this was the method finally used. The final procedure of the sample assembly to the sample holder is described in the next section. Some examples of the huge variety of test made in order to obtain the final simple preparation procedure and probe welding are provided in Fig. 3-7, Fig. 3-8 andFig. 3-9.

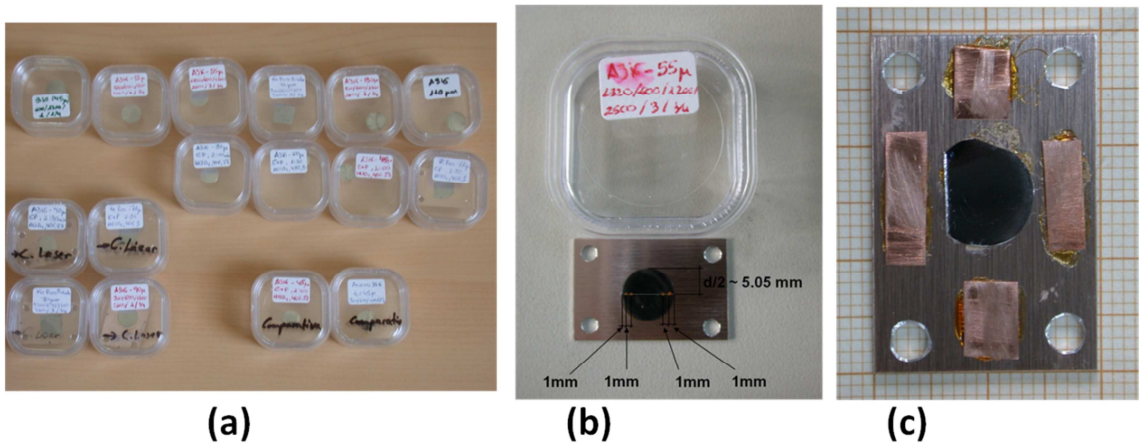

Fig. 3-7: Preliminary tests on sample preparation were made to combine the most suitable preparation method: (a) bunch of samples ready to test the soldering technique: mechanically polished, mechanically polished + annealed, mechanically polished + electropolished (b) 55 µm test simple of 316-steel sticked to a test-substrate, it is indicated a posible configuration for electrical contacts which eventually wasn't used (c) example of electropolished Fe sample, the sample geometry is lost.

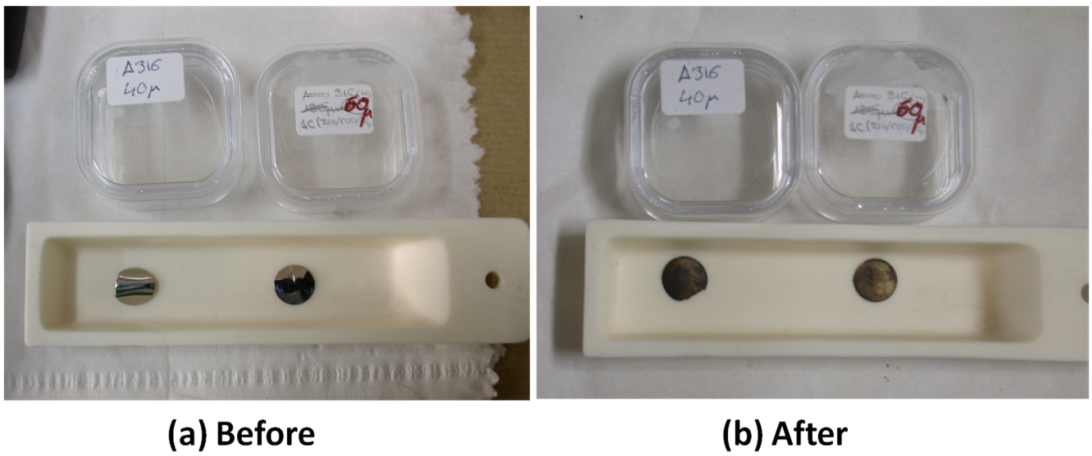

Fig. 3-8: Heat treatment in vacuum (5 ·10^{-3} atm): ramp-up rate 5K/min, hold step at 700 K for 30 min and then free cooling down. Evident deterioration of the surface can be observed.

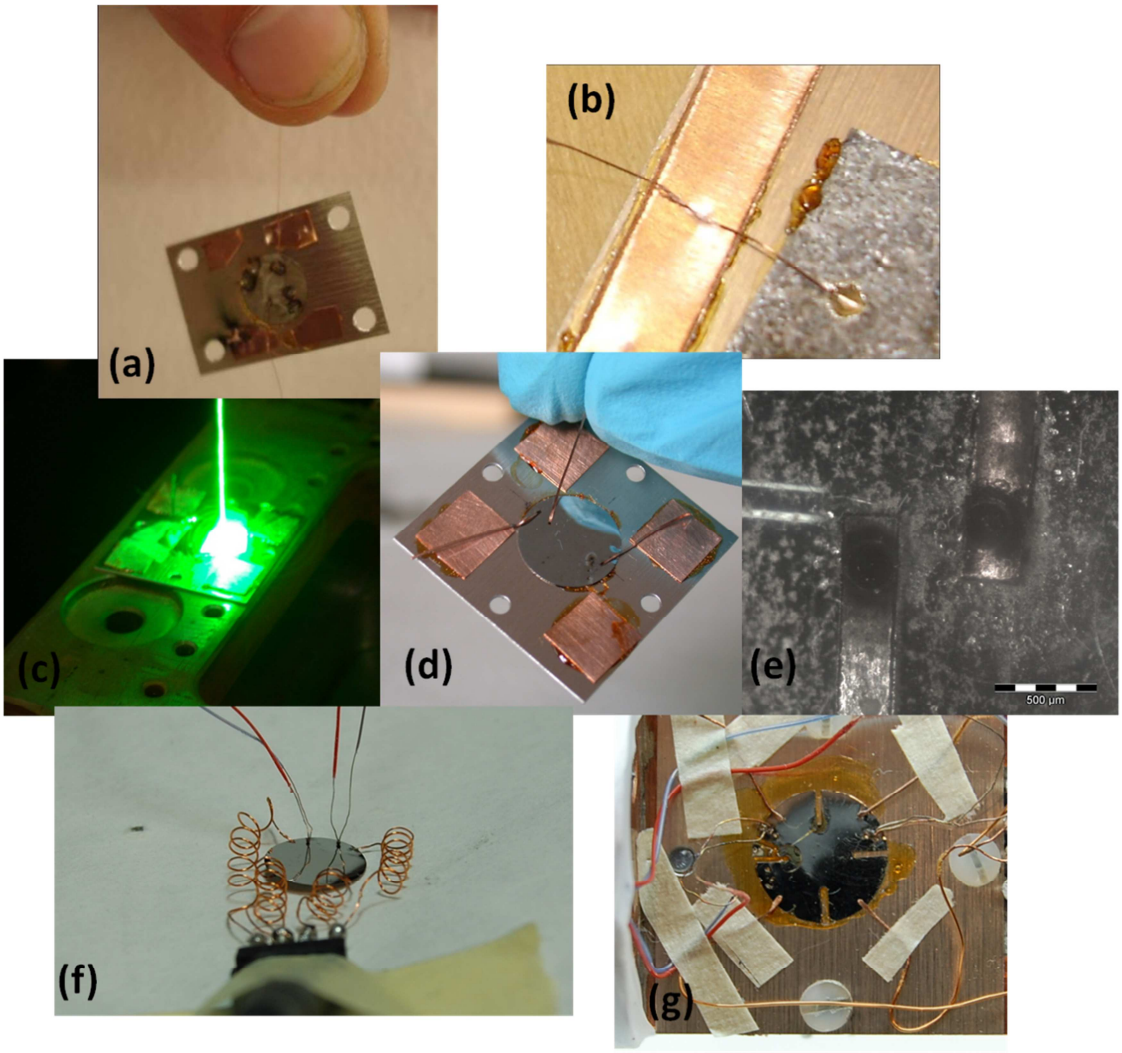

Fig. 3-9: Welding tests: (a) HFRW test showing good mechanical resistance but very harmful for thin samples, (b) detail of (a), (c) laser spot-welding test, (d) good mechanical resistance (c), (e) area of contac of the lase-spot welding, (f) Spot welding test at CIEMAT, cheap, easy, reproducible, this was the chosen welding method, (g) final sample geometry, mirror-like finish after polishing, resistivity probes and thermocouples spot-welded to the sample.

3.5. Set-up

In order to perform the experiments proposed, large part of the efforts were devoted to design, built and install a dedicated test chamber, in a line of the ion accelerator of CMAM. The test chamber was designed in such a way that sample can be irradiated while simultaneously performing resistivity measurements, monitoring and controlling the temperature of the sample simultaneously. The set-up for the experiment undertaken here consisted in placing the sample at the end of the cold finger of a continuum flow cryostat; model ST-400 by Janis Research Co. (Wilmington, MA), together with an oven, a temperature control system and corresponding electrical connections for the resistivity measurements. The cryostat is attached to the top of the experimental chamber. In addition, there is a rotary feedthrough on this top used to hold ionoluminescent quartz in front of the sample before starting the irradiation in order to determine the position, size

and homogeneity of the proton beam. With this system, `in situ' cooling down, irradiation, isochronal annealing and resistivity measurements can be done, avoiding post-irradiated manipulation of the sample.

The cryostat was accommodated to a vacuum chamber. Feedthroughs provide connections for electrical and temperature measurements. As standard inner temperature controls, the cryostat includes one high temperature (500K) standard curve silicon diode and a 50 Ω cartridge heater. The cold finger is protected with an adjustable height gold plated OFHC Copper radiation shield 3.3 cm O.D. The specimen holder (see Fig. 3-12) assembles all the systems for measurement, heating and control. The sample holder system had to handle a wide range of temperatures, i.e. from liquid helium up to 500 K. This implied that good contact at the thermal boundaries (between the heat sink and the sample) had to be maintained over a range of ~500 K. Also the metallic sample had to be electrically isolated from the rest of the system but at the same time a good thermal conductivity between sample and warm and cool sources was required in order to get an accurate and robust temperature control. Variations of resistivity due to irradiation are in the order of hundreds of nΩ·cm and variation of resistivity due to temperature changes (near LHe) is 1/10th smaller (i.e. Δρ ~10 nΩ·cm, per degree at 30 K), thus the control of temperature at the sample has to be very sensitive and stable, otherwise large experimental error could be amplified during the calculation of the derivative of the RR curve. Under the above demanding requirements the choice of the sample substrate (the plate over which the sample will be stuck prior to be mounted in the sample holder), its material and geometry, was a non-straightforward decision. Fig. 3-10 indicates the candidate substrates that were tested. At first anodized aluminum plates were used but didn't show that good thermal behavior at cryogenic temperatures. Then some test were preformed on sapphire plates which had very good behavior at low temperatures but in return its mechanizing was very difficult and they showed terrible heat conductivity at higher temperatures making impossible to perform an isochronal annealing up to 500K. Eventually the most suitable was option (c), a Cu plate covered by a sputtered thin film of SiO_2 which makes the surface electrically isolating but keeps good thermal conducting at low temperatures.

The sample holder has been made of OFHC cooper and fixed to the end of the cold finger with screws and indium foil. For easy and non-damaging handling, the sample is stuck with varnish GE-7031 to a thin (0.3 mm) cooper plate (Fig. 3-10(c)). This varnish was tested under ion-irradiation and was able to withstand high ion fluxes before being denatured (see details in Fig. 3-11). The four-probe electrical connections were made by spot welding on the edges of the sample. Four cooper AWG32 wires link the sample with an intermediate pin-like connector on the sample holder. Two type E thermocouples are spot welded at the upper and lower edges of the sample respectively in order to determine the sample temperature and any possible temperature gradient along it. Also, since thermocouples may not be totally reliable at the very low temperatures employed, a silicon diode is attached to the plate close to the sample. It should also be noted that, as described before, an additional silicon diode is placed inside the cold finger of the cryostat in order to achieve good temperature control of the heat sink. Finally, the heat source for raising the sample temperature is a coaxial cable electrical heater (11 Ω) which is placed

at the rear part of the sample holder. All the temperature probes, the four-probe sample connections and the heater are connected to their respective UHV feedthroughs by thermally anchored suitable extension cables.

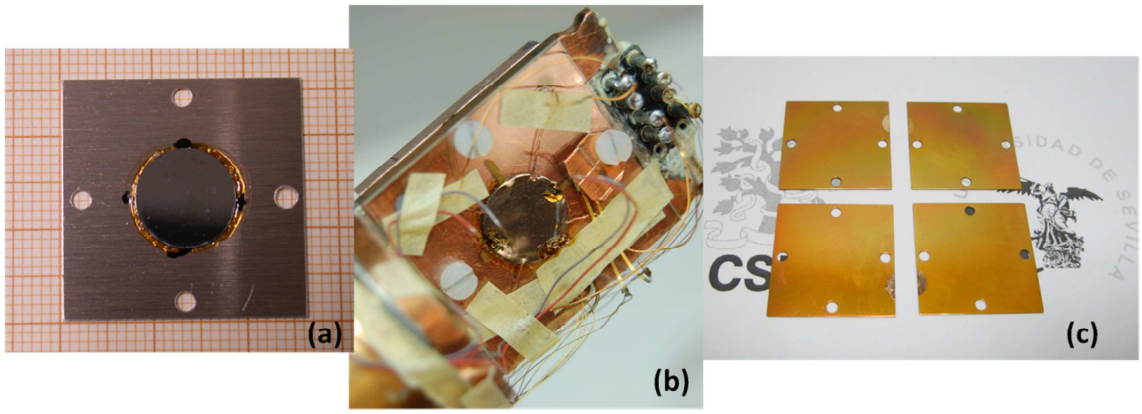

Fig. 3-10: Several substrates where tested: (a) commercial anodized aluminum, (b) sapphire, (c) Non commercial Cu substrate with a deposited layer of SiO_2 (~3 µm).

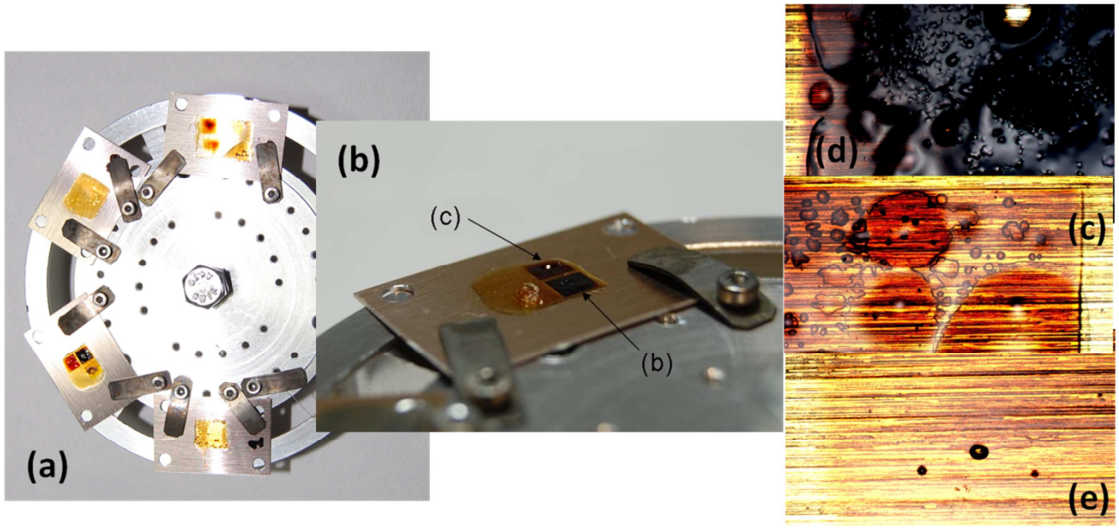

Fig. 3-11: Varnish VGE-7031 integrity tests: (a) varnish samples after proton irradiation tests at CMAM, (b) detail on one tested sample, (c) E = 2 MeV, I = 100 nA, fluence = $1.2 \cdot 10^{16}$ cm^{-2}, (d) E = 2 MeV, I = 120 →380→500 nA, fluence = $2.6 \cdot 10^{16}$ cm^{-2}, (e) E = 3 MeV, I = 700 nA, fluence = $3.4 \cdot 10^{16}$ cm^{-2}. The higher the p energy, the less the damage in varnish.

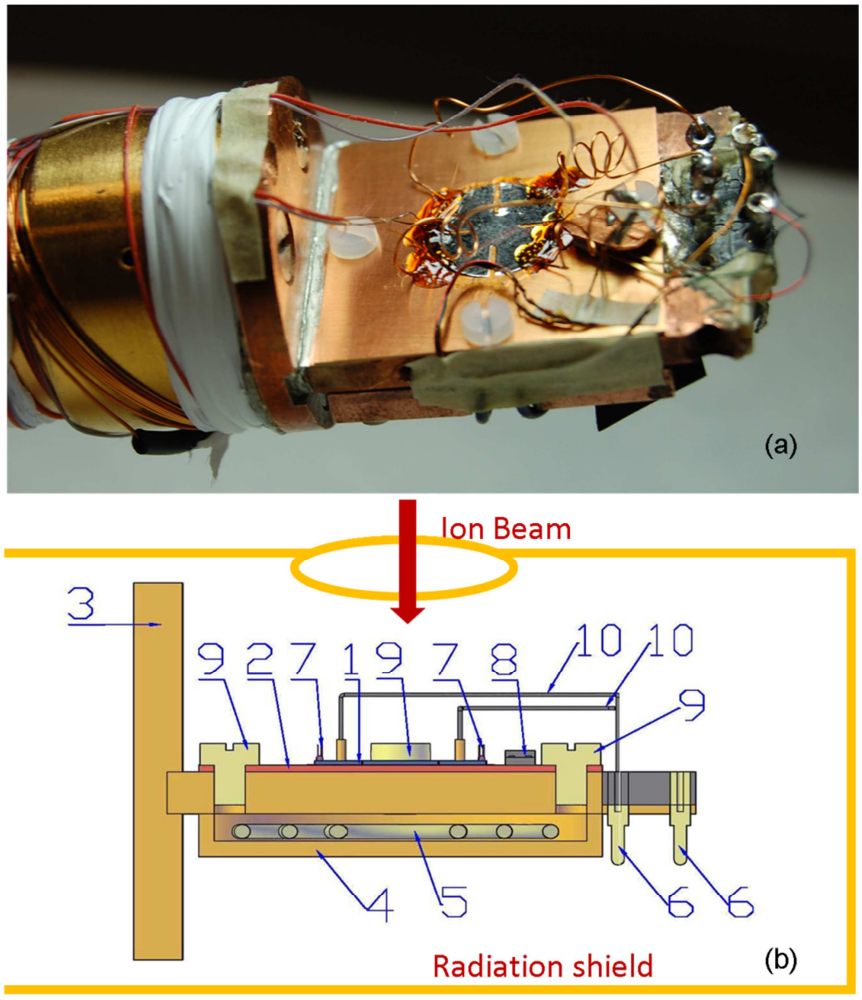

Fig. 3-12: (a) A close-up view of the sample holder, without the radiation shield, as mounted on the cold finger. (b) A cross-sectional profile of the sample holder: 1. Sample – 2. Cu plate with a deposit layer of SiO_2 – 3. OFHC Cu sample holder which adapts to the cryostat cold finger – 4. Copper holder which contains the heater – 5. Thermocoax® heater - 6. Pin-like intermediate connectors – 7. Type E thermocouples – 8. Silicon diode – 9. Nylon screws – 10. Electrical connections for resistivity.

Once the sample is placed on the cold-finger, the whole system is placed in a vacuum chamber at the end of one of the beam line of the ion accelerator. During irradiation the collimated ion beam passes through a 15 mm diameter hole in the radiation shield and impacts the sample. After testing several current values, finally beam current of 30 nA (for samples of 50 μm) was used in order to minimize the increase in sample temperature during irradiation (T_{irr}, ~50 K). In order to measure the beam current with accuracy, two independent devices where used: a Faraday cup and a transmission Faraday cup. They were placed in the irradiation line before the vacuum chamber, as it can be seen in Fig. 3-14, which pictures schematically the whole assembly in the beam line. Concerning the beam shape, an over focused homogenous irradiation area (around 7.5 x 7.5 mm^2) into the sample was carried out. The beam positioning, and its homogeneity, was set using the ionoluminescence from a fused silica plate that was placed temporarily in front of the sample on a rotary feedthrough.

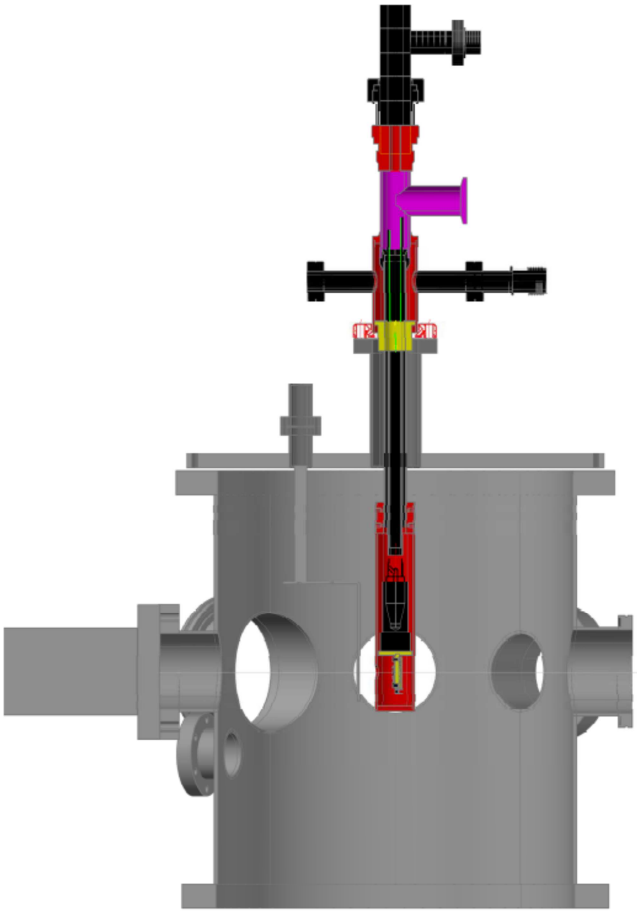

Fig. 3-13: Left: detail of beam positioning on the ionoluminiscent fused silica. Right:Close view of the cryostat inserted in the vacuum chamber at the end of ERDA-TOF. line at CMAM.

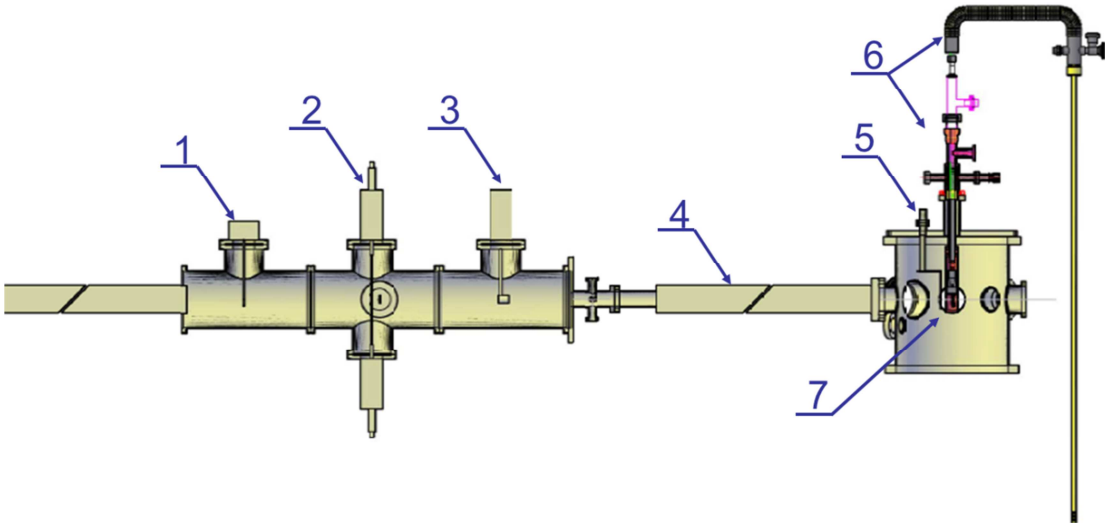

Fig. 3-14: Beam alignment and irradiation set-up: 1. Transmission Faraday cup – 2. Collimation slits – 3. Faraday Cup – 4. Beam line – 5. Rotary feedthrough with ionoluminiscent quartz – 6. Cryostat and LHe transfer line – 7. Sample holder.

3.6. Resistivity and temperature measurements

Electrical measurements were made in DC mode with the 4-point-probe method in the VdP configuration [66]. As explained before, the resistivity of the sample has to be measured in both configurations R_{12} and R_{23} as shown in Fig. 3-2. Current and voltage leads where connected to a high precision current source (model 6221 by Keithley Instruments Inc, Cleveland, OH) and to a nano-voltmeter (model 2182A by Keithley Instruments Inc, Cleveland, OH) which were connected to each other with an RS-232 bus and a trigger link. Combination of such current source and nano-voltmeter was used to perform Delta mode (see section 3.2), that is, a delta current-reversal technique that is used to cancel the effects of thermal EMFs [74]. The sample voltage is measured with an accuracy of 10^{-8} V while applying 100 mA (±0.1%). When considering the standard deviation of the experimental value (at a given temperature) it is in the order of 1 – 0,1 nΩ·cm, thus for measuring resistivity differences, the standard deviation is the error considered. Reproducibility of the resistivity values strongly depends on the stability of the sample temperature, and sensibility and control of the system up to the mK is required. For instance 1 nΩ·cm accuracy corresponds to a 0.1 K of uncertainty at 30 K. The tolerance increases if T_{base} is smaller, i.e. 1 nΩ·cm accuracy corresponds to a 0.2 K of uncertainty at 15 K. It must be noted that measurement of the true sample temperature while resistivity is being measured is always a challenge at these low temperatures. In the current set-up, the only sensors that maintain contact with the sample are the spot-welded thermocouples. However, as thermocouples are not very reliable at temperatures below 77 K, an alternative silicon diode was placed over the Cu plate and separated from the sample by only 1 mm (see Fig. 3-12). This sensor is used to control the base temperature for the measurements with the proportional-integral derivative (PID) controller. In order to make clear the orders of magnitude, Table 3.2 summarizes values and errors of resistivity and temperatures measured with each sensor in the set-up, the absolute values can vary slightly from sample to sample, the example of Fe5 (well described in section 5.2.) values is given. It also must be noted that the temperature sensors were tested in a liquid nitrogen bath in order to check its good performance under isothermal conditions at low temperature. The sensors agreed to within 0.5 K with a mean temperature of 77 K.

	ρ (nΩ·cm)	T_{SD670} (K)	T_{TC} (K)	$T_{ID\ ST\text{-}400}$ (K)
Room T	33033.1 ± 0.9	300.0706 ± 0.0002	299.47 ± 0.07	300.234 ± 0.008
Base T	10367.5 ± 1.2	11.331 ± 0.012	29.78 ± 0.18	4.53 ± 0.09
Min. T in cryostat	9893.0 ± 0.6	7.676 ± 0.002	23.27 ± 0.11	4.0235 ± 0.0014
HeL immersion	9864.5 ± 1.1*	4.23903 ± 0.00005	-	-

Table 3.2: Values for sample of Fe5: ρ is the resistivity of the sample, T_{SD670} is the temperature of the silicon diode placed on the sample holder, T_{TC} is the temperature read by the thermocouples and $T_{ID\ ST\text{-}400}$ is the temperature of the inner diode of the cryostat ST-400.

As it has been detailed in previous description, the classical RR method (section 2.4), consist on a low temperature irradiation followed by a step-like isochronal annealing. The residual resistivity was registered during low-temperature irradiation to obtain the curve of radiation induced resistivity (RIR). RIR measurements where performed at minimum temperature in the cryostat and RR measurements at minimum temperature (T_{min}) of

~20K in thermocouples and ~10 K in SD670. The RR curves where obtained along step-like annealing procedure: the temperature was raised in steps of 2.5 K between 50 to 90 K, $\Delta T/T = 0.03$ from 90 to 400 K and 20 K steps above 400 K. The temperature ramps had a rising velocity of 10 K/min and annealing time is $\Delta t = 120$ s. The ultimate annealing temperature reached was close to 500 K and the complete annealing and measurement process took over 60 hours after irradiation. It is worth noting that the key point for measuring RR curves is to understand how well the system is capable of returning to the base T_{base} (~25 K in thermocouples and ~15 K in SD670) after cycling, bearing in mind that as the annealing proceeds, the LHe flow can vary and also the spot-welded electrical connections and thermal boundaries could be slightly modified due to the temperature cycles. In order to estimate a more representative value of the resistivity error of the presented RR results in the next chapter (named "Fe5", "Fe5(Pre)", "Fe10", "Fe10(Pre)" and "Fe14(Pre)"), a value of twice the standard deviation of the first points (7-14 points) of the annealing process (30-55 K) -where recovery can be barely appreciated- has been taken; giving a maximum value of 3 nΩ·cm. This provides an upper limit value for error but it is considered a better estimate of the whole experimental errors commented above (i.e. resistivity measurement accuracy 0.1-1 nΩ cm). When these uncertainties are expanded to the RR derivative curves it is observed that the errors rise dramatically at lower temperatures of the annealing and get reduced as the annealing rises temperatures. It can feel striking to the reader but this comes from the error formula itself. As it is a derivative, it takes into account the temperatures difference between each pair of points. At very low temperature, the points are very close, so dividing by this difference gives higher numerical errors, but not experimental errors. Paradoxically, the more spaced are the points in the annealing, the lower error in derivative is provided. Despite of this, it has been considered that high temperature resolution is better to reveal the structure of the RR peaks. Some results with higher experimental error will be presented, such as "Fe", "(2)Fe", "(3)Fe", "(2)Fe10", "(3)Fe10" or "Fe14". These results cannot be used as validation tool for modelling and its derivative would drag high error, nevertheless the results are presented given that some useful information can be extracted from them. The source of error had two different origins, in some samples the accuracy of the resistivity measurements was bad (~10 nΩ cm) in others the accurate control of the oven and the temperature sensors induced an error in T_{base} which equivals to ~8nΩ cm dispersion in resistivity.

The reproducibility of the RR data has been checked, in Fig. 3-15 it is show an example of reproducibility of RR cuves in the case of Fe-10%Cr and an example of stage I in Fe-5%Cr. This first stage of the RR spectrum where more errors normally appear is well reproduced and also small sub-stages before main stage I_D are revealed (see chapter 4). Such sub-stages have not been shown in other experiments of concentrated Fe-Cr alloys sometimes due to the large annealing intervals used or missing data.

Once the low-error resistivity curve is obtained a smooth treatment of the RR curve is made using Matlab. The derivative is made working on the smoothed data and taking into account the temperature interval between the experimental points (as the annealing steps have not constant interval) and the resultant peak spectrum obtained. In this work strong effort has been made to obtain a reliable RR spectrum, treating the whole uncertainties of

a resistivity measurement in an explicit way because very restricted information is usually found in literature.

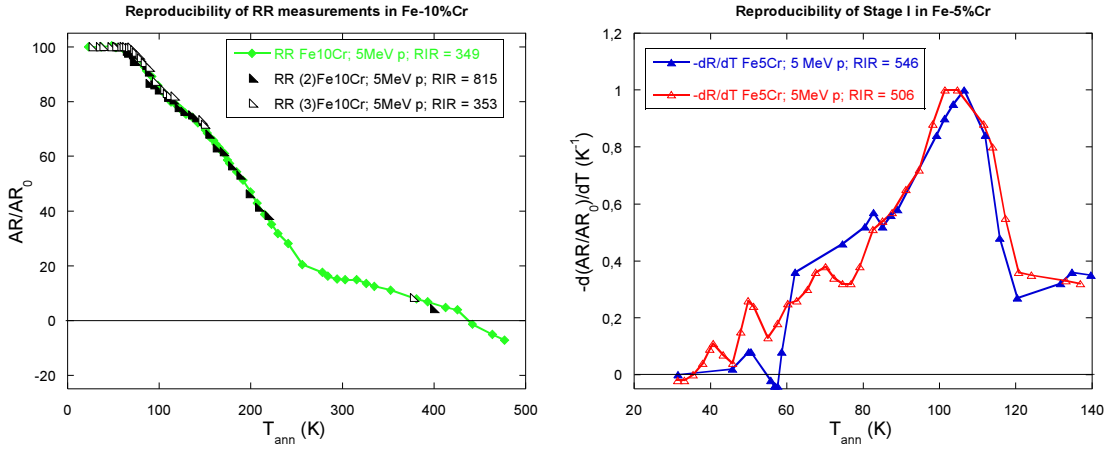

Fig. 3-15: Proof of reproducibility of RR curves and RR derivatives.

Chapter 4. State of the art

The starting point of this chapter is that the picture which is being established to explain the defect kinetics in Fe-Cr concentrated alloys is based on the model accepted for pure Fe, where agreement has been found between RR and PA validation experiments [24,41] and combination of ab-initio and kMC simulation codes [39]. Although this is a starting point, differences clearly appear when Cr is introduced in the iron lattice. Complementary studies, both experimental [28] and theoretical [63], have been made evaluating the initial distribution of the damage in pure Fe defect kinetics, revealing new stages. Concurrently the theoretical and experimental study on the effects on adding Cr impurities to pure Fe have helped to reveal new migration energy values, and interaction processes between defects [30,37,83]. It has also been revealed that the presence of other impurities produce strong modifications of the RR curves by interaction of impurities with defects [26,29,64]. All these studies have contributed to build the Fe-Cr picture. In addition, few isolated experimental works have been performed on concentrated Fe-Cr alloys [32,38,84,85]. Scale limitations of computational codes make not possible up to date to simulate high damaged concentrated alloys. Nevertheless good approaches are being achieved [40].

It is important to notice that, in general, published RR results usually appear represented at different scales and the experimental conditions are different as well. Thus direct visual comparisons between authors are barely impossible. A great work on digitalization and choice of most comparable RR results published along the past 30 years of previously published results has been made in this chapter. The scales have been normalized to the one presented in our results, and purest materials with similar RIRs have been selected for different irradiation probes. A critical review of the state of the art is made here, a work which it is worth mentioning, has not been done before. The structure of this chapter is as follows: The first part (section 4.1) is a revision of results for pure iron, followed by a critical discussion of the existing interpretations/models (section 4.2), next the equivalent information but for Fe-Cr alloys (section 4.3) and finally the contribution of computational simulations is explained (section 4.4).

4.1. Accepted picture in pure Fe

The work of Fu *et al.* in 2005 [39], which is aligned with the results of RR in ultra-pure Fe made by Takaki *et al.* in 1983 [24], provides a quite complete revision where kinetic of simple defects in electron irradiated pure Fe is quite well identified. The initial damage distribution is supposed to be isolate FPs with a mean I-V distance of $3a_0$ [40]. The overall model which describes the diffusion of defects in pure Fe has replicated the experimental recovery stages and interpreted them as follow (see also Fig. 2-12 and Fig. 2-13):

- **Close pair stages (0-100 K)**: a set of peaks or sub-stages named I_{A0}, I_{A1}, I_A, I_B and I_C. Every peak is associated to a different activation energy[12], their position does not change with irradiation dose. All the reactions are of first order. Because of these characteristics, it is generally accepted that such sub-stages arise from recombination of close vacancy-interstitial pairs that where produced in tight-close configuration by the irradiation. Similar sub-stages set with similar characteristics was formerly found and analysed in pure Cu [86,87]. The discrete energy migrations associated with sub-stages arise from discrete separations involving different configurations of the I-V pairs.

- **Stage I_D (101-108 K)**: this stage is also made of two sub-stages I_{D1}(101,5K) and I_{D2} (107,5K), they are also close-pair stages and exhibit the same characteristics than I_{A0-C}. The two sub-stages are so close in temperature that it is difficult to distinguish both peaks sometimes in the experiments, and thus it is usually referred as I_D or I_{D2}. Their main characteristic is the intensity of the peak, which 5 to 10 times higher than the previous close-pair stages, being the highest of all stages. Stage I_D is thus related to recombination of correlated defects, that is, of unbound I-V pairs belonging to the same FP by free migration of the interstitial.

- **Stage I_E (120-144 K)**: a single peak which is associated to the recombination of i and V belonging to different FPs, as a result of I migration with migration energy E_m^i = 0.27 ± 0.04 eV, i.e., the same migration energy than I moving in I_D stage. The rate reaction is of order $\gamma \sim 2$. The position of the peak varies with irradiation dose which confirms that its origin comes from long-range migration (LRM) of interstitials. As interstitials can migrate as free defects, they will not only recombine but also will create small interstitial clusters (I_n).

- **Stage II (150-200K)**: it shows a single peak proposed to result from I_2 (di-interstitial) migration, with E_m^{i2} = 0.43 ± 0.03 eV. In the experimental results of Takaki *et al.* , the authors has to extent the temperature scale of the RR derivative in order to properly observe such peak (see Figure 4 in [24]). This peak also depends on the dose, as it depends on the I_2 concentration and defects spatial separation.

- **Stage III (200-300 K)**: another single process of order $\gamma \sim 2$ suggested to result from free migration of the remaining vacancies, with E_m^V = 0.55 ± 0.03 eV. Vacancy recombination and clustering (V_n) occur in this stage, whose peak position is also dose dependent.

- **Stage IV (520-550 K):** an extra stage observed at high doses, is attributed to dissociation of V_3 clusters formed during stage III.

Such clear picture can become altered when the nature of the particle irradiation changes. Masui *et al.* [28] and Ortiz and Caturla [63] have made experimental and modelling studies respectively where the initial irradiation damage was not electron-like.

[12] The activation energies are calculated with the change of slope method. Further details on this technique can be found in the wonderful book of Damask and Dienes [62].

In the first case Matsui performed fusion (E = 14 MeV) and fission (E > 1MeV) neutron irradiations with similar fluences. It was argued that for those irradiation conditions, where the mean PKA energy exceeded 5 keV, the average V-V or I-I distance remained essentially the same, and thus the peaks attributed to LRM of defects did not show changes in T_a. He could not appreciate important differences in the RR spectra but, in contrast with Takaki's research he found an **extra broad stage (named II_B)** between 170 and 210 K. It was interpreted, in alignment with PA results [88], in terms of correlated vacancy migration within collision cascades. Thus it was concluded that there is a category of vacancies which have smaller activation energy (E_M^{IIB} = 0,47 eV) than "normal" vacancies. He also suggested that V_2 could migrate with slightly smaller energy (E_M^{V2} = 0,52 eV) than the "normal" vacancies, so broad stage III could be a result of such phenomenon. In the work of Ortiz and Caturla, they simulated cascades by irradiation of 30 keV Fe ions, the result of the radiation damage was a broad spectrum interstitial and vacancy clusters (n=1-16). Annealing of such defects, revealed essentially the same migration phenomena described by Takaki with evident changes in height and peak positions, but also three new stages appeared and where described as:

- **Peak III_A (230K)**: suggests recombination of close correlated V-$I_{n\geq3}$ pairs.

- **Peak IVA (400 K):** it is associated to a double dissociation mechanism. On one hand the I_3 clusters dissociate ($I_3 \rightarrow I_2 + I$) leading to migration and recombination of single interstitials which are mobile at such temperatures. On the other hand V_4 clusters might also dissociate following $V_4 \rightarrow V_3 + V$ and $V_3 \rightarrow V_2 + V$. Vacancies and di-vacancies thus migrate and recombine with remaining clusters.

- **Peak IVB (650K):** it is indeed a very broad peak which starts at 450 K and broads up to 800 K. As dissociation energies of small I_n and large V_n are very similar this stage is associated to simultaneous dissociation of these two types of defects.

In the Fig. 4.1[13] the RR rates of pure irons of Takaki and Matsui have been digitalized and plot compared. In the legend it is indicated the energy of the irradiating particle and the radiation induced resistivity. The respective purities of the samples where RRR = 5000 (Takaki) and 1000 (Matsui) (Matsui didn't appreciated differences between samples with different purity degrees (1500 and 1000)). The slight differences described in the text seem much more pronounced when comparing visually the results. Nevertheless the physics underlying is well explained and both results seem to be in agreement.

[13] From now on every RR result plotted will be assigned a specific symbol and color combination. The information contained in the legend is, in the following order: the RRR (purity indicator of the sample, but only in the case of pure Fe), the author, the studied material followed by his solute composition (%) if any, the energy of the irradiating particle, the type of particle, and the RIR in nΩ·cm as an indicator of dose.

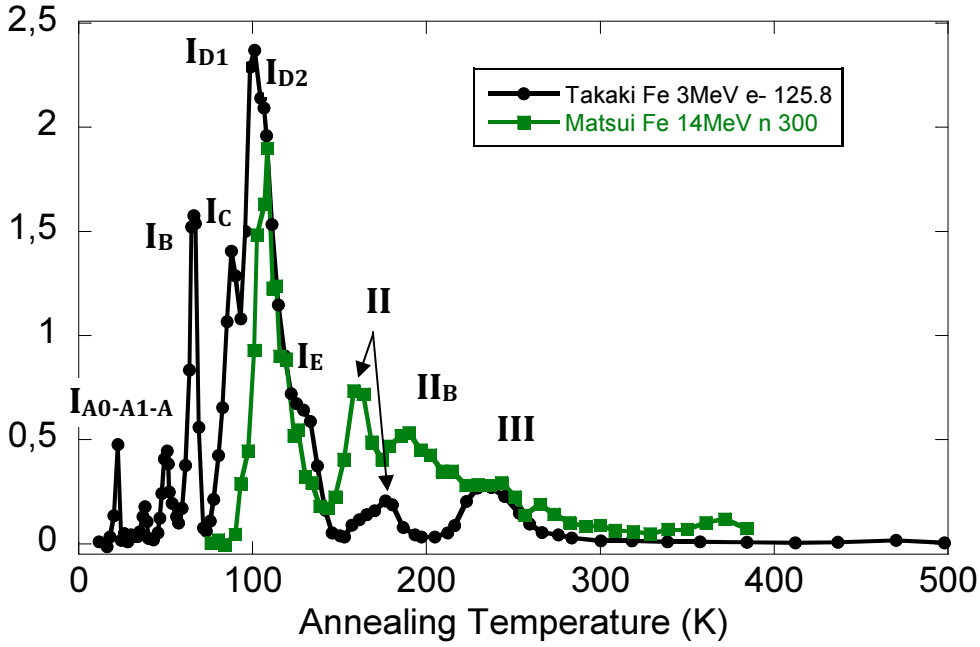

Fig. 4.1: Comparative of RR derivatives on pure Fe irradiated with electrons and neutrons respectively. The graphs belong to the works of Takaki *et al.* and Matsui *et al.*

4.2.Critical review of pure Fe accepted picture

Careful revision of the literature reveals few more RR studies on pure Fe specimens. Maury *et al*., Omar, Nikolaev and Abe and Kuramoto have also reported measurements of RR in pure Fe. There is a broad spectrum of parameters which differ among every RR experiments such as, impurity content, irradiation particle, irradiation energy, irradiation temperature, measurement temperature, dose and dislocation density. A part of the work of this thesis was therefore an attempt to sum up the most important features of every experiment and to draw some conclusions on the effects of the above mentioned parameters in the RR spectrum.

First, a comment must be made, related to the experimental conditions which have surrounded the resistivity measurements in pure Fe. Most of the studies made on pure Fe (but not all of them [84]) where made after application of a longitudinal magnetic field. The purpose of this is to control the magnetorresistivity contribution to the resistivity, (ρ_{mag}, due to ferromagnetism in Fe) and reach a minimum value of the residual resistivity which should only depend on the impurity content of the sample and the created defects [89]. There is a parameter called residual resistivity ratio (RRR) which is defined as the quotient between the resistivity at room temperature ρ(298K) and the residual resistivity ρ_0(4,2K). It is used to determine the purity of the Fe specimen, but in order to be used for this purpose in pure Fe, it requires previous de-magnetization of the samples given that with increasing purity of iron specimens, the contribution of ρ_{mag} becomes larger. Concerning the sample purity, the impurity content has been proven to interact with interstitial atoms (IAs) and affect their mobility, altering consequently the RR spectra peaks. The specific features of the main experiments in pure Fe are summed up in Table

4.1 including impurity content and nature and energy of irradiating particle. Also both, the RR curves and RR derivatives corresponding to the samples on Table 4.1 are plotted in Fig. 4.2 and Fig. 4.3 respectively.

Observation and evaluation of irradiation and specimen characteristics allows making some comments concerning the behavior of defects and the effects of the irradiation particle in stages I and II. First, in Fig. 4.2 the impact of the nature of the irradiating particle is clearly observed. The curves appear naturally grouped as a function of the particles, RR is faster on samples irradiated with electrons and it is prevented when irradiating with protons and even more with neutrons. This is an indicator of the distribution of damage: the separation of created FPs is increased as the mean energy of the PKAs is higher (i.e. when coming from electrons to neutrons). The PKA energy depends on the energy of the particle but also on its mass. The electrons which are very light particles will be able to produce spatially separated FPs and at high enough energies (~5MeV) could be able to produce small displacement cascades of two or three neighboring FP [29]. The protons will produce much more displacement damage specially at energies close to 14 MeV, but as they are charged particles they will lose energy also by electronic interaction with the sample, resulting in an effective lower mean PKA energy that the 14 MeV fusion neutrons [90]. Protons will mainly lose their energy in the samples by coulomb collisions leading to proper formation of displacement cascades which will lead to cluster formation together with FP creation with less correlation than the FP created by electron irradiations. The impact on the type defect creation and distribution affects the amplitude and position of the stages as it has been clearly described in the cases of Takaki and Matsui.

Next, regarding the RR spectra in Fig. 4.3, an overall agreement is observed on the appearance of correlated migration stage I_{D1-2} and some close-pair stages. But when it comes to the presence of Stage I_E, the picture becomes less clear, given that a broadening of peak I_E can be observed in some of the spectra. It has been observed that the presence of solutes like C [89], Mo, Cr, Si [30], Ni, Mn or Co [26] diminishes the amplitude of Stage I_E. The created mixed IAs have different mobility and hence recombine before or after stage I_E affecting thus the amplitude of the stage and possibly the shape of the main peak.

In the case of electron irradiations, it can be seen in Fig. 4.2 that as the energy increases, the RR is slightly smaller at the end of Stage I, the higher separation of I-V of correlated FPs could be the responsible of this. The free migration of interstitials will then be favored by this larger separation, leading to higher I_E Stage and shorter I_D. In the case of Stage I of Nikolaev I_{D1-2} and I_E seem to bunch up in one broader peak. It would also have to be taken into account the influence of the isochronal annealing conditions, temperature rising rate and annealing time at every step, given that this influences the amount of recovery possible at every step [32], nevertheless possible differences derived from this do not have much impact on the general analysis that it is being done in this section. Also further manipulation of such sensitive data that has already been digitalized would multiply the error on the curves and its reliability will become compromised. Concerning proton and neutron irradiated RR spectra, clear reduction of Stage I and increase in the intensity of stages II and III is observed. This is due to the damage created by cascades and

cluster formation (In and Vn) that migrate, dissociate and recombine at higher temperatures as it has been explained in the previous section

Work	RRR	Impurity (appm)	Irradiating Particle	Energy (MeV)	RIR (nΩ cm)	Comment
Maury [37]	330	?	Electrons	1.6	68	RRR=10075/31 (nΩcm) [91]
Abe [30]	3000	?	Electrons	2.5	71	T_{Irr} = 77 K. Normalized at 90 K as Nikolaev´s data. No RR curve presented.
Takaki [24]	5000	C < 1	Electrons	3	126	
Takaki [24]	1076	C ~15	Electrons	3	134	
Takaki [24]	290	C ~66	Electrons	3	138	
Nikolaev [84,91]	155	C+ N ~70 Ni ~100	Electrons	5	146	(C+N) interstitial impurities Ni substitutional impurity
Nikolaev [84]	95	C+ N ~130 Ni ~100	Electrons	5	133	In the work of 2011 [91] the RR curves appear re-normalized at 20 K, previously in 1999 [84] the presented curves where normalized at 90 K. Th re-normalization criterion (0.72) is taken from a Dimitrov's private communication.
Omar [23]	21	?	Protons	14	324	As-received, i.e. presence of dislocations.
Omar [23]	117	?	Protons	14	270	Same specimen but after 2h annealing at 600ºC (less dislocation)
Matsui [28]	1000	C ~13	Neutrons	14	300	

Table 4.1: Main characteristics of irradiated pure Fe samples studied under RR experiments.

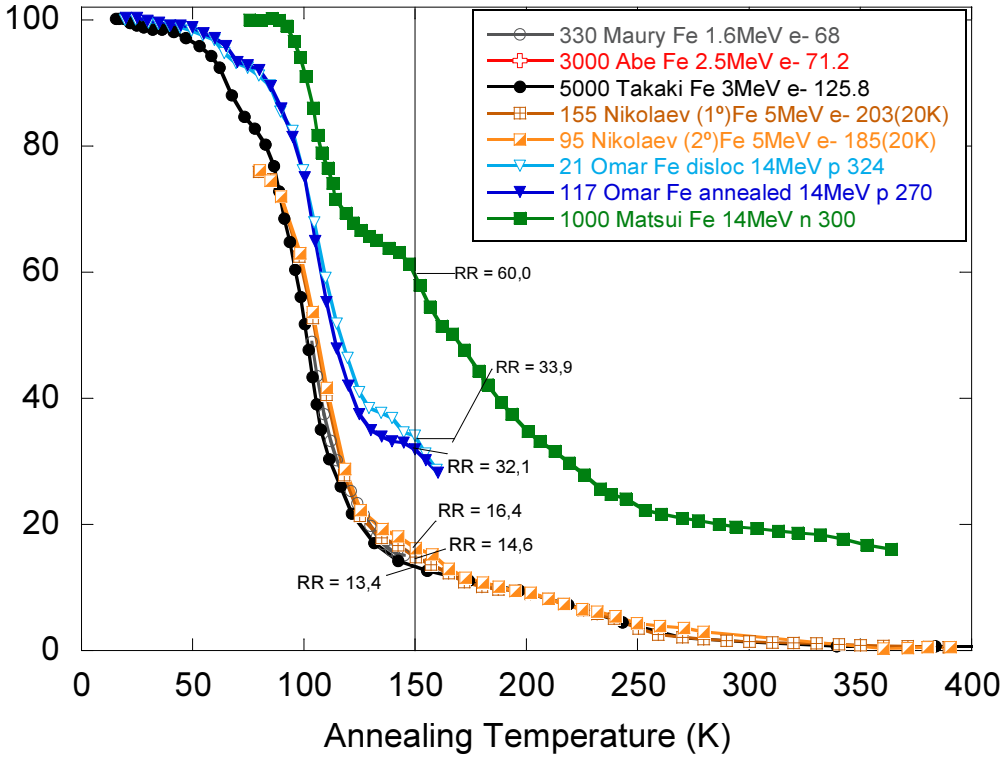

Fig. 4.2: Comparative of RR curves of pure Fe found in the literature.

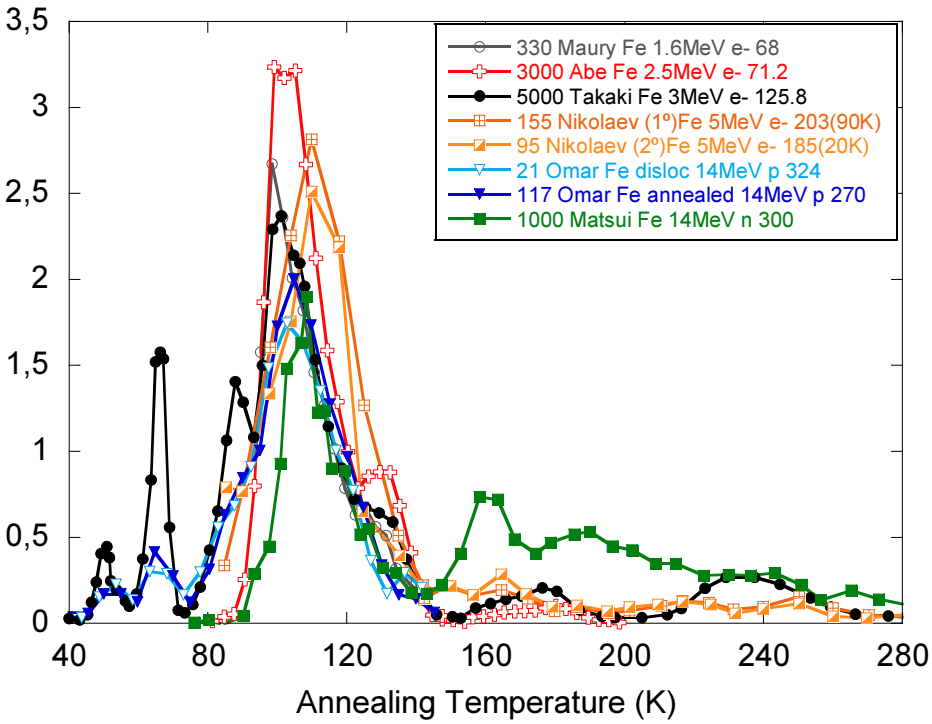

Fig. 4.3: Comparative of RR spectrum of pure Fe samples found in the literature.

4.3.The effect of Cr

The Fe-Cr alloys are much more complex systems with respect to pure Fe in terms of possible defect types and energetic interactions with the Cr solutes. An interstitial atom present in a metal lattice has to be understood as a pair configuration, i.e. it won't be a perfect lattice with one atom out of its lattice site, but a perfect lattice with a pair of atoms placed around a lattice site as it can be seen in Fig. 4.4. Thus, in the BCC lattice, depending on the crystallographic direction the interstitial pair can be called a dumbbell (<110>) or a crowdion (<111>). In pure Fe, every interstitial will be made of course of Fe-Fe pair, but in the case of Fe-Cr systems interstitial pairs can also include one or two Cr atoms. Thus we can rename the interstitials in Fe-Cr systems as follows: Fe-Fe pair is called self-interstitial atom (SIA), Fe-Cr pair is called mixed interstitial atom (MIA) and Cr-Cr pair has not a specific acronym given that is concentration is small with respect to SIAs and MIAs. The acronym FIA (foreign interstitial atom) is usually referred to interstitial impurities.

Such broad defect variety implies the appearance of new defect creation energies, new migration energies, new binding energies (between defects and solutes and between the defects themselves) and thus new dissociation energies. The manifestation of these new migration and dissociation energies strongly modifies the defect kinetics resulting in changes in RR curves and their derivatives with respect to pure Fe. As it has been mentioned in previous section the presence of small amount of impurities affects to the appearance or partial suppression of peaks in the RR spectra.

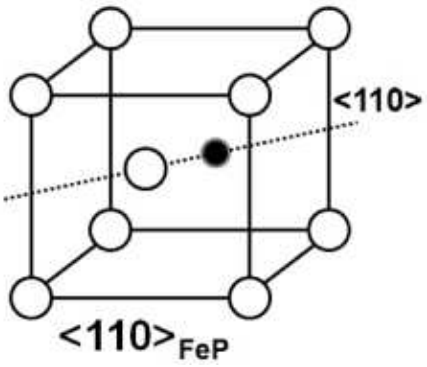

Fig. 4.4: Example of Fe-P <110> dumbell in bcc Fe.

Before going into the effects of Cr in RR experiments some work has been done on other primary features of Cr addition to Fe. On one hand, the specific resistivity of Cr in Fe, which was defined by Maury [37,92] as:

$$\rho^*_{Cr} = \frac{\rho_{4,2K}(FeCr) - \rho_{4,2K}(Fe)}{C_{Cr\ (ppm)}} \qquad 4\text{-}1$$

This parameter has been used to study the effects of Cr on the residual resistivity. It was found an anomalous increase of ρ_{Cr}* at very dilute Cr concentrations, and such behavior was justified by the two current model which establishes that α_{Cr} = 0,17 and is

independent on chromium concentration (C_{Cr}), at least below 0,6%, and in the case of other solutes it can provide information on the need of spin-mixing term [92]. No measurements on concentrated pure Fe-Cr alloys have been found in the literature, so in chapter 5 the obtained experimental values in concentrated alloys (Fe5, Fe10 and Fe14 as detailed in Table 5-1) will be shown and analyzed. Some conclusions will be drawn on the value of α_{Cr} parameter on our alloys and the spin-mixing term. Furthermore the effects of radiation damage as a function of defect concentration in alloys have also been analyzed. Maury has extensively studied this topic in several dilute iron-based alloys irradiated with electrons [25,26,37,92], and specifically in Fe-Cr alloys for different dilute concentrations [37]. He defined the resistivity change rate (RCR) as the variation of RIR as a function of the fluence:

$$RCR = \frac{\partial \Delta\rho}{\partial \phi} \qquad 4\text{-}2$$

Two special characteristics were found: on one hand the RCR was decreasing with electron fluence up to a saturated value and its decrease was lower the higher the C_{Cr}; on the other hand the absolute value of RCR was increasing with increasing C_{Cr} up to 3%. This last observation was explained by deviations of Matthiessen's rule and the former was also justified by the two-current model for dilute alloys. Nevertheless, no justification of progressive diminish of RCR in concentrated alloys (1 and 3%) could be provided with the available model.

The overall increase in RCR with the Cr concentration (0-3%) indicates an increase on the specific resistivity of FPs. In many works which study Fe and other irradiated dilute alloys, as for example in the work of Abe and Kuramoto [30], the specific resistivity of FPs ($\rho_{F,}$ defined in eqn. 2-44) in pure Fe (30μΩ cm/at%) [61] is taken as the reference value to estimate the defect concentration from RIR experimental values. This consideration, has been proven not to be accurate for dilute alloys and definitely wrong for concentrated ones (>1%). When C_{Cr} keeps increasing (5-15%) [27] the specific resistivity of FPs has shown a progressive decrease: ρ_F(Fe-5%Cr) = 21,2 or 15,1 nΩcm appm, ρ_F(Fe-10%Cr) = 20,6 or 14,7 nΩcm appm and ρ_F(Fe-15%Cr) = 19,3 or 13,7 nΩcm appm. The change of such values could depend on a change in the defect creation cross-section with the amount of Cr or intrinsically on the specific resistivity of the FPs in every alloy. Further discussion of the experimental data of the present work is provided in chapter 5.

Concerning RR experiment in Fe-Cr, some results on stages I and II have been provided in dilute alloys by Maury *et. al* [37] and Abe & Kuramoto [30]. Their experimental results are depicted in Fig. 4.5 and Fig. 4.6. Basically the main conclusion obtained from these works concerning the defect kinetics is that suppression of Stage I_E is experimentally observable from 1% of C_{Cr}. The drift of peak I_E towards lower temperatures and the reduction of the amplitude of the peak found at 180K indicated that mixed-dumbbells migrate and get trapped by solutes below I_E and get release from them and thereby annihilate with vacancies above I_E.

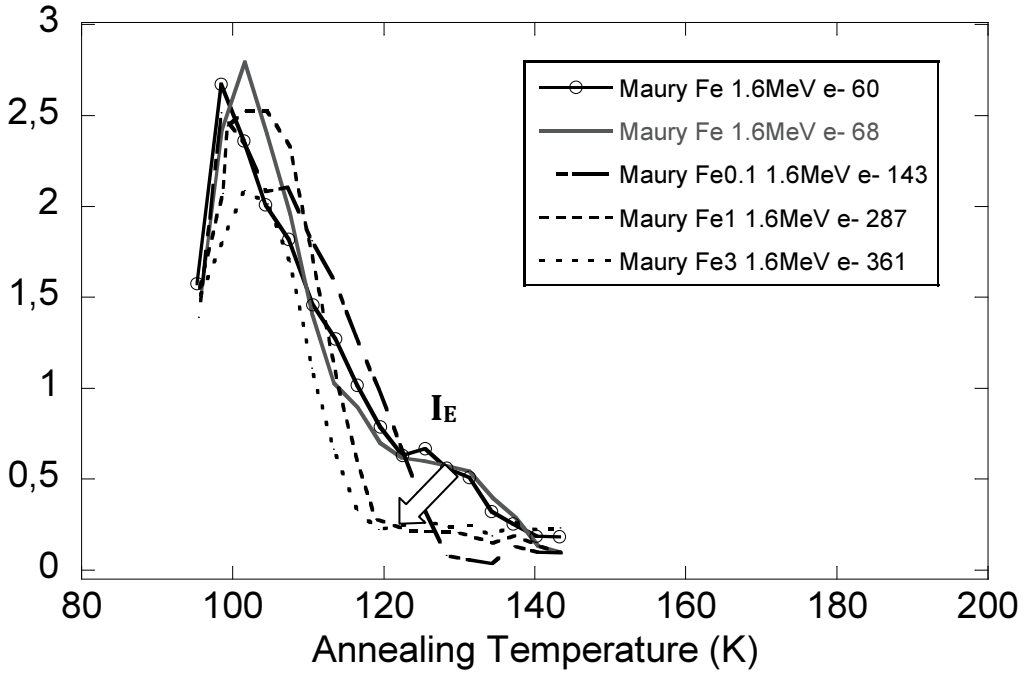

Fig. 4.5: Study of Stage I for different samples (pure Fe, Fe-0,1%Cr, Fe-1%Cr and Fe-3%Cr) digitalized from Maury et al.

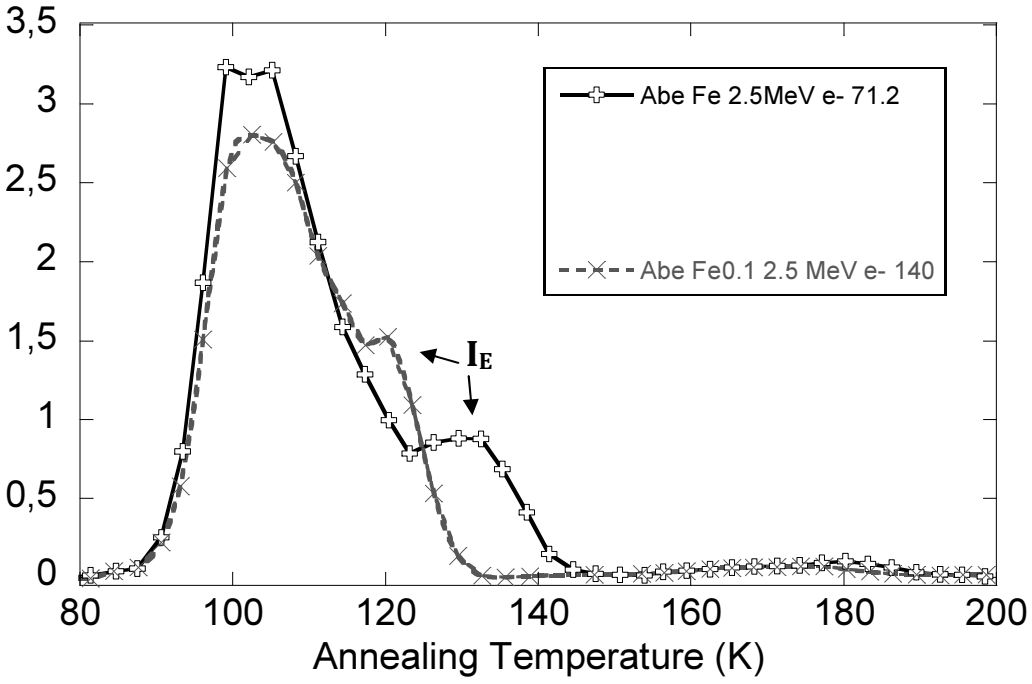

Fig. 4.6: Study of Stages I and II for different samples (pure Fe and Fe-0,1%Cr) digitalized from Abe and Kuramoto.

Regarding the impact of other impurities in RR results, the presence of carbon atoms acts as vacancies traps which inhibits the 190K stage recombination and creates a new recombination stage at ~350K [24,64]. Nitrogen acts also as a trap for vacancies but the detrapping occurs at temperatures around 250K-260K [64]. Also silicon doping is known

to form complexes with vacancies and impurity atoms which diminish the recombination stages [84]. The use of impurity dopants has been extensively used by Nikolaev to study resistivity stages of concentrated Fe-Cr alloys.

There are two principal authors which have made RR measurements of concentrated Fe-Cr alloys, the work of Benkaddour in 1982 [27] and the measurements of Nikolaev between (1997, 1999, 2007 and 2011) [29,32,84] . The results of both authors are depicted in Fig. 4.7 and Fig. 4.8. In the published papers the curves are depicted over the experimental points by applying spline fits in such a way that beautiful and smooth RR derivative curves were shown. But when depicting the results without such fit it is surprising the poor resolution in temperature obtained for the results of Benkaddour. In the case of Nikolaev's results only the RR rate curves of purest materials (minimum impurity content) with doses as close as the ones used in this work are represented. The collected curves correspond to separated stages and thus no complete RR in the range of interest of this work can be observed. Moreover, the irradiations were not all made at the same temperatures and none the normalizations of the RR curves (Nikolaev irradiated and measured at 77K and normalized the RR values at 90K whereas Benkaddour did it at 21 K). Although Nikolaev provided some of his data renormalized to 21 K in his paper of 2011 [91].

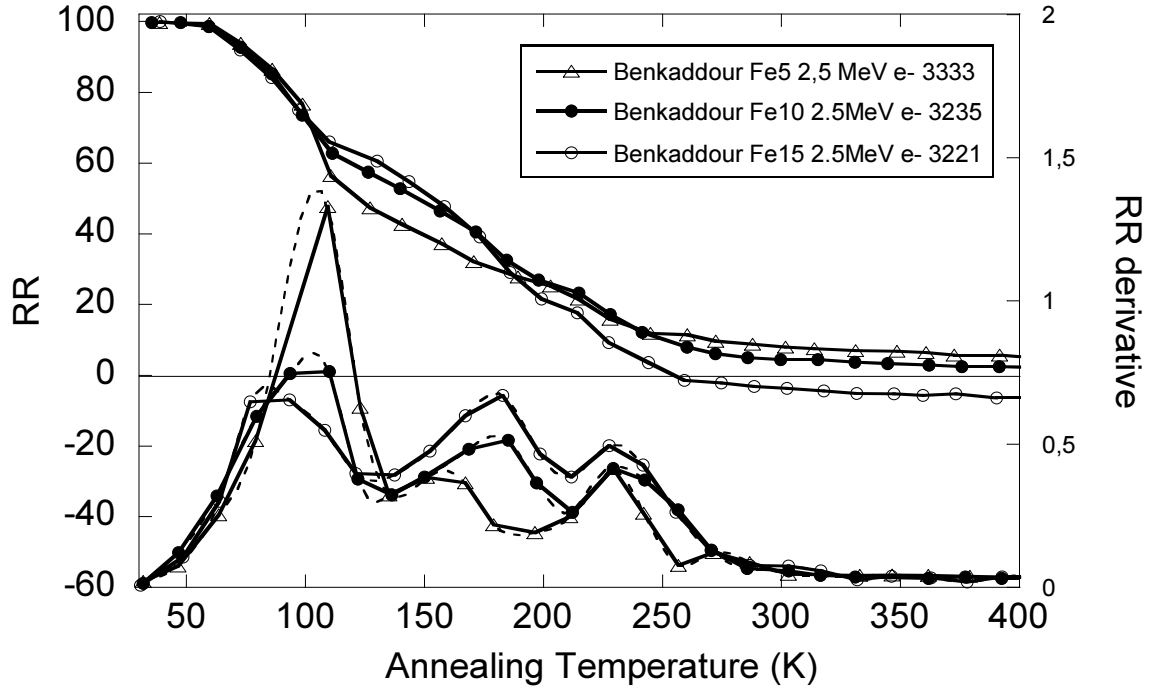

Fig. 4.7: RR curves and derivatives from electron irradiated concentrated Fe-Cr alloys (Fe-5%Cr, Fe-10%Cr, Fe-15%Cr) after isochronal annealing. Data obtained by Benkaddour et al.

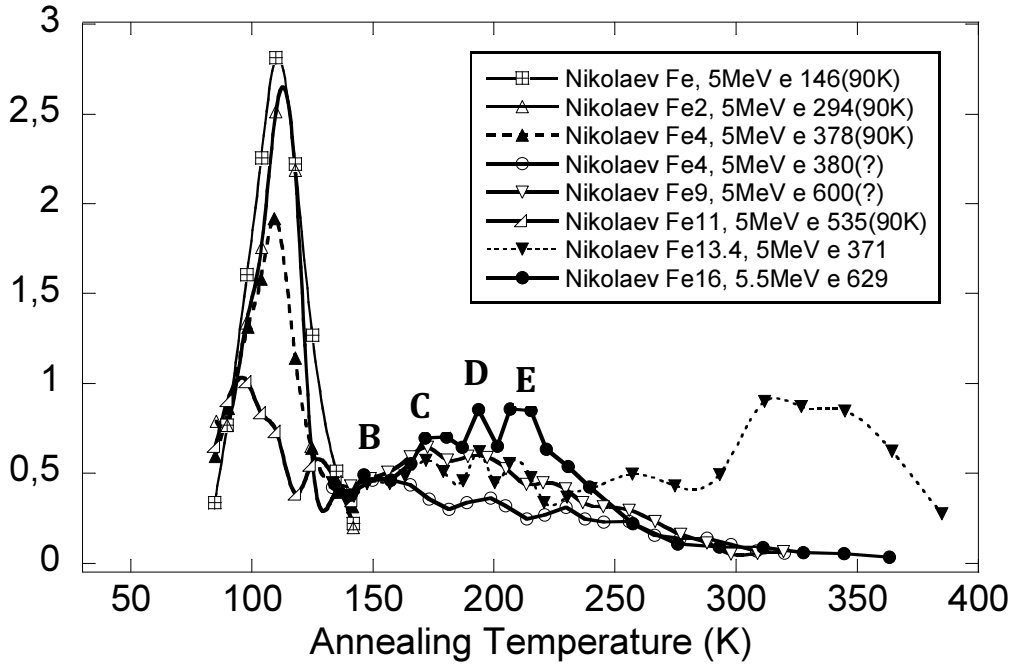

Fig. 4.8: RR derivatives from electron irradiated concentrated Fe-Cr alloys (0 - 16%Cr) after isochronal annealing. Data obtained by Nikolaev

Despite of all these experimental issues, these works and others subsequent revisiting these results and complementing them with other techniques (mainly PA) [38,64,93] have put in evidence some significant differences in the kinetics of the defects in concentrated Fe-Cr alloys mainly concerning stages I, II and III. Earlier, it has been shown [37] that the addition of small amounts of chromium (up to ~0,1 at. %) to iron brings about the configuration of IAs, viz. the formation of mixed Fe-Cr dumbbells, whose mobility is similar or even higher than that of SIAs in pure Fe. Further increase in $C_{Cr,}$ above 1 at. %, leads to the capture of these mixed dumbbells by configurations consisting of various Cr atoms (configurational trapping, which will be better explained in next section) [37,84]. In concentrated Fe-Cr alloys is observed experimentally a progressive suppression of stage I and shift towards lower temperatures. This suggests that Cr interacts strongly with interstitials inhibiting their free migration as the Cr concentration increases. A total suppression of stage I_{D2} is observed in both Fig. 4.7 and Fig. 4.8. Also, the scrolling of stage I to lower temperatures indicates that the non-trapped interstitials undergo correlated recombination with lower migration energies than in pure Fe. As for stage II, Benkaddour (peaks from 155 to 175 increasing Cr%) suggested that SIAs (Fe-Fe dumbbells) which were trapped at stage I were able to change to MIA configuration (Fe-Cr dumbbell) at stage II temperatures (authors on modelling also suggest re-arrangements of I-complexes interacting with Cr in order to explain the stage II at Maury's results [94]), and given that MIAs had been able to migrate at stage I_C then the recombination peak would appear in stage II. Nikolaev on the other hand found 3 peaks which he called B, C, and D in the range of stage II (between 150 and 200K) [29] (indicated in Fig. 4.8). He assigned IA nature to peak B and close-pair vacancy nature to peaks C and D: specifically short-range migration within FP (peak C) and short-range migration between neighboring FPs created within irradiation cascades (peak D). The lack of peak sub-structure in Benkaddour could be due

to low temperature resolution and/or dose effect (10 times higher dose) which hidden the effects of SRO, which diminish their relative impact. Concerning stage III, Benkaddour *et al.* couldn't observe any effect in its third RR peak. Apart from slight change in the peak amplitude, which he attributed to SRO of different signs for Fe5 and Fe15, he associated stage III as free vacancy migration stage and concluded that the Cr solutes produced no interaction with the vacancies leading to an unchanged stage III. Nevertheless Nikolaev gave a more complex discussion on the stage III in Fe-Cr alloys. He introduced a new methodology of analysis which I am going to describe in detail in a separate paragraph, given that its discussion is a bit messy.

Stage III evaluation by Nikolaev

First it must be noticed that he has introduced the concept of difference RR (DRR) analysis, based on the assumption that when a free migration stage (SFM) occurs, the peak position in RR derivative spectrum changes with dose, whereas the other recombination mechanisms do not change. Thus a difference of RR curves of equal specimens irradiated up to different doses (high (H) and low (L) dose) might lead to a peak of negative amplitude, which is a prove of the presence of a SFM and he calls it the DRR peak. A graphical representation of the outcome of DRR peak is given in Fig. 4.9. Nikolaev proceed to analyze the RR results obtained on his samples of Fe-4%Cr and Fe-9%Cr after irradiations with several doses [32]. To his understanding, the onset of free migration of vacancies and interstitials occur at very close temperatures (205-210 and 220K respectively). Also he suggested immobility of di- and tri- vacancies at these temperatures which is in agreement with available PA data [38]. Thus, along his analysis he was trying to find evidence of presence of SFM at 205 and 220K, i.e. he was expecting to find the appropriate DRR peaks. It turned out that his analysis resulted the other way around, i.e. he never found the appropriate DRR peaks in the studied samples: he found a non-DRR peak in Fe-4%Cr and an inverted DRR peak. Nevertheless through his discussion some interesting conclusions could be elucidated. It became clear that from 155 up to 220 there are many overlapped processes which give rise to several peaks that overlap. The sign and amplitude of such peaks varies a lot as a function of the Cr concentration, the radiation dose, the amplitude and sign of SRO, and the vacancy-trapping effect of impurities. The processes identified were:

- **Stage at 155K**: this stage is identified as independent of the C_{Cr} but its nature remains unexplained.

- **Stage at 170 K**: is identified as a close-pair vacancy recombination stage which only appears in high-concentrated Fe-Cr alloys (from 9% C_{Cr}) where the amount of Cr has been enough to inhibit in Stage I, not only the free migration but also the correlated and close-pair recombination. Thus the close-pair recombination manifests now through vacancy short movements in this higher temperature range.

- **Stage at 190 K**: Such stage appears in both studied samples, Fe4 and Fe9. It is associated to correlated recombination of vacancies and it ends at around 205 K.

In Fe4 the amount of Cr is enough to restrain Stage I correlated recombination but not the close-pair, this is why Fe4 doesn't show Stage 170K.

- **SFM of vacancies**: Nikolaev states that it starts at 205K but it is not visible in the RR spectrum as a proper peak, this feature together with the DRR analysis (he found a non-DRR peak in Fe-4%Cr and an inverted DRR peak). Such features are explained by the hypothesis that the forming di-vacancies have abnormal high value of specific resistivity. From my point of view this is one of the most daring suggestions of this author as he is not able to provide a physical explanation, not even considering the two current model. Computing simulations shall in the future indicate if such abnormal high specific resistivity of di-vacancies is possible. Although, consequent works of same author [64] show indications that the abnormal resistivity of di-vacancies would be, in fact, aligned with the results.

- **Stage at 220K**: Nikolaev suggests that this is the first visible stage of free migration which is due to the interstitials that get enough energy to escape from configurational trapping and are able to recombine with vacancy clusters. Liberating at the same time mono-vacancies which are able to migrate.

Another important feature that drastically impacts on RR curves and spectra that was taken into account by Nikolaev, and has to be taken into account in the analysis of the RR results, is the effect of SRO. It has been discussed theoretically in chapter 2 and it has been shown how residual resistivity is affected by the solute non-random arrangement. From a more experimental perspective it has to be said, that indeed every alloy presents different SRO equilibrium configurations for every solute concentration and temperature [50]. Every equilibrium configuration will also depend on the thermo-mechanical process that the material has suffered [53,95], for example the presence of dislocations created by mechanizing processes which will act as defect sinks or its absence achieved by thermal treatments. Besides, the studied samples usually are not in their equilibrium SRO configurations. Moreover, the solute SRO rearrangements are possible in the presence of migrating defects [48,49,51] which have been traditionally introduced in the materials by means of quenching experiments or particle irradiations [52]. In the case of RR, the migration stages of defects are going to favor such solute short-range redistribution setting the solute arrangements closer to their equilibrium configurations at every temperature.

The Fe-Cr alloys have shown a very characteristic behavior concerning their SRO parameters, it has been observed by diffuse neutron scattering and resistivity measurements [17,18,96] that SRO parameters change their sign at Cr concentrations close to 10%. At low concentrations the SRO becomes more negative, i.e. the Cr ions tend to distribute as far as possible from each other in the Fe matrix in order to minimize the internal energy of the system. When the Cr ordered distribution reaches saturation (around 10%), the number of configurations which maximizes the Cr-Cr separation decreases. Below 10%, the repulsion of diluted Cr atoms can be understood as magnetic frustration effect given by its antiferromagnetic quality. The SRO depends strongly on Cr concentration and also on temperature [96]. At higher C_{Cr} the Cr tends to clusterize,

lowering the total energy by forming anti-ferromagnetic domains in the ferritic matrix. It is known that at relatively low C_{Cr} and low temperatures, the Cr solubility easily reaches saturation, leading to the miscibility gap of the Fe-Cr phase diagram where the bcc structure starts to decompose in two phases, α and α', enriched with Fe and Cr respectively [96,97].

Thus it might be expected that migration stages in RR would increase the residual resistivity of Fe-Cr alloys with C_{Cr}<10% and the other way around for C_{Cr}>10% as it has been experimentally observed in [17]. The SRO component of the resistivity was defined in chapter 2 as ρ_S in eqn. 2-64 and their increments or decrements induced by irradiation or by annealing step will be defined by $\Delta\rho_S$. Nikolaev, concurrently to the DRR formalism analyzed the $\Delta\rho_S$ of his RR curves of Fe4 and Fe9 in [93]. He argues that $\Delta\rho_S$ should be always the same amount at a certain annealing step in presence of free migrating defects (i.e. certain annealing time) independently of the defect concentration. Thus at different initial defect concentrations, the normalized RR curves should exhibit differences at the temperature ranges of free migration of defects and SRO. As he cannot see any difference he concludes that the SRO effects are not visible in his curves and that the SRO contributions to RR are negligible. But his assumption is not necessarily true because it implies that SRO changes are maximum in the low dose sample and thus they cannot change further at higher doses. Indeed with higher defect concentrations at certain annealing step the number of jumps will be higher than in a sample with lower defect concentration and thus the possibility that $\Delta\rho_S$ will be larger exists. On the other hand is also true that the overall number of defect jumps in a recombination stage is more or less the same in high and low doses given that the mean separation distance between the migrating defects and their counter-partners (i.e. vacancies or interstitials) is shorter in the high dose than in the low dose. Indeed it makes sense that the SRO contribution is small in his specimens, but definitely non zero as the RR after isochronal annealing does not fully reach its original value, i.e. RR $\approx$ 0. It must be said, at 400K all I and V are expected to be recombined. The positive values of RR found at 400 K in Fe4 and Fe9 might be related either to SRO effects or to the presence of remaining defect clusters which have not annihilated yet. As we will see in our measurements in proton irradiated Fe5 specimens the $\Delta\rho_S$ is definitely non negligible.

By further development of the DRR approach, Nikolaev was able to describe signs in the DRR curves and their derivatives which could be indicators of SRO. In particular, an inflection point in the DRR curve will be an indicator of the onset of long range migration of defects of faster specie (it could be V or IA depending on the studied sample). The sign of the slope after this inflection point will indicate the sign of the SRO parameters; if negative slope it will be ordering (negative SRO) and if the slope is positive it will be clustering. In order to clarify his approach, detail explanation of his conclusions on Fe4 (70 appm N) and Fe4C (70 appm N + 1800 appm C) is given in next paragraph together with Fig. 4.9.

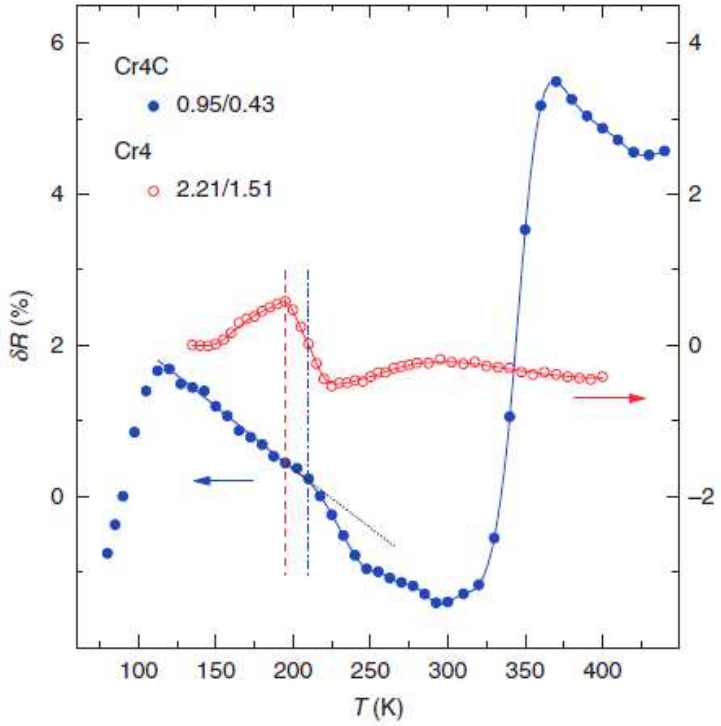

Fig. 4.9: DRR plot from Nikolaev 2011 of Fe4 and Fe4C. Figures in the legend indicate the $\Delta\rho_H/\Delta\rho_L$ values at 90 K.

In that work [64] the aim was to use the carbon doping as trapping for vacancies in order to confirm the picture presented for Stage III up to date in [32,93]. In the Fig. 4.9 the vertical dotted lines indicate the inflection point which characterizes the onset of long range migration of defects. In samples Fe4 the vacancies start this migration close to 195 K and in the sample Fe4C the inflection point at 210 indicates free migration of IAs given that the vacancies are trapped by the C atoms. Further inflection point close to 225 K in the Fe4 DRR curve is related to change in SRO detrapping of N impurities which tend to clusterize with Cr. And finally the inversion of the slope at 350 K of Fe4C DRR curve towards abrupt positive slope is related to the onset of vacancy-carbon defect migration. This last process instead of promoting negative SRO behavior as free vacancies will do, enhances clustering of C with Cr. This is another example of the huge complexity that arises when interpreting RR results in samples with any minor change in composition.

4.4. The contribution of modelling

Up to date density functional theory (DFT) studies of SIA in bcc Fe have shown that [39,98–101]:

(i) The single SIA (<110> dumbbell) migrates via translation-rotation jump and the corresponding E_m is 0.34 eV. (although Takaki measured E_m^i = 0.27 ± 0.04 eV)

(ii) Di-SIA (I_2) and tri-SIA (I_3), which are clusters of parallel Fe-Fe dumbbells, migrate via the same mechanism with E_m = 0.42-0.43 eV. (Takaki E_m^{i2} = 0.43 ± 0.03 eV)

(iii) I_4, I_5 and probably larger clusters have been proved to form small clusters with complex structures. Such non-parallel <110> clusters occupy practically immobile configurations due to the excess of vibration entropy at finite temperatures [102]. This new family of defects provides an explanation for the assumption made in [39] that large clusters were immobile.

In dilute Fe-Cr alloys the mobility and stability of point defect clusters is being intensively studied lately by simulations. As it has been indicated at the beginning of the previous section, and as is clearly depicted, for instance, in Fig. 4.10, the type and position of defects in Fe-Cr systems are enormously increased with respect to pure Fe. Therefore when the study of the interaction between certain IA with substitutional Cr (Cr_s) atoms surrounding is also considered, the number of possible combinations shoots up. Thus, simulations are being able to delimitate the study of every particular defect, simplifying the picture. The study of dilute C_{Cr} focusing in most probable configurations makes it possible. The migration mechanisms of small SIA clusters where studied in dilute alloys by atomistic calculations, and main conclusions shown were [94]:

(i) SIAs (I = Fe-Fe dumbbell): The effective energy characterizing the stage I_E (in pure Fe) is the migration energy of an Fe-Fe dumbbell (E_m = 0.34 eV), but the position of the stage is determined by Cr given that surrounding Cr_s act as shallow traps (see #2, #6 and #11 in Fig. 4.10). They form ICr_s which are immobile at low T. Also SIAs can become MIAs when interacting with Cr_s.

(ii) MIAs (ICr = Fe-Cr dumbbell): Recent *ab-initio* calculations have shown that Fe-Cr <110> dumbbell (ICr) is stable and its migration energy (via movement of Cr) is lower than that of the Fe-Fe dumbbell by ~0.1 eV (E_m = 0.23 eV) [103]. In addition, a weak binding energy between ICr and Cr_s was also found giving rise to the formation of a mixed dumbbell trapped at another neighboring Cr atom (see #4 and #12 in Fig. 4.10) [104]. The dissociation energy of the ICr-Cr_s complex is low (E_d=0.31 eV). Such dissociation energy agrees well with the presence of I_E found in dilute Fe-Cr alloys. The intensity of I_E should be governed by the dissociation of ICr-Cr complexes which are able to drag Cr atoms during this stage. This might affect to the SRO state equilibrium.

(iii) One important consequence is that: in the range 150-180 K the stages found [37] should be better explained by re-arrangements of complexes of self-interstitials interacting with Cr atoms [94] rather than by the dissociation of IAs from Cr_s traps.

(iv) Mixed di-SIAs: Cr-Cr close pairs exhibit binding energy with MIA dumbbell thus forming di-SIAs: I_2Cr (SIA and MIA parallel dumbbells) and I_2Cr_2 (two parallel MIA dumbells). In the case of I_2Cr the Cr-Cr pair does not act as a trap of the SIA given that its migration energy has relatively low values. In [94] the

obtained value was 0.38 eV but in further work which combined parametrized DFT calculations and rate theory the migration energy provided was 0.30 eV [83]. But it does in the case of I_2Cr_2 which remains immobile until it dissociates with energies [83]: $E_b(I_2\text{-}Cr_2)$ = 0.316 eV and $E_b(I_2Cr)$ = 0.062 eV. So as this last configuration is unstable and dissociates spontaneously it was concluded that di-SIA migration is not affected by the presence of Cr-Cr close pairs, i.e. by the C_{Cr}. As the mixed di-SIAs can drag Cr atoms, this might also affect the SRO formation or change in equilibrium.

(v) Di-SIAs (I_2): different calculations, found different values of the migration energies of Fe-Fe dumbbells, 0.39 [94] and 0.43 eV [99].

(vi) I_3 cluster: The formation of I_3Cr and I_3Cr_2 becomes possible at stages I_E and II by reactions involving I, ICr, I_2 and I_2Cr mobile complexes. Clusters involving more than 3 SIAs were considered to be immobile up to the temperature corresponding to the onset of vacancy migration and its energy migration was estimated to be $E_m \geq 0{,}53$ eV.

(vii) Regarding at the migration energies of n = 2 clusters, it is possible that they migrate at similar temperatures (both I_2 and I_2Cr) resulting in a stage II similar to the stage II of pure Fe, especially for the dilute Fe-Cr alloys. However as most of the I_3 and larger SIA clusters would contain Cr atoms and their migration will happen beyond stage II, his intensity should be strongly reduced as C_{Cr} increases. Also the progressive suppression of single IAs migration would reduce the formation of IA-clusters, resulting in an additional reduction of Stage II.

The above described types of defects and the calculated migration energies in dilute Fe-Cr alloys provided up to date are resumed in Table 4.2. Also, I have included two columns noticing the migration Stages at which every defect could migrate or dissociate, in dilute and concentrated Fe-Cr alloys.

Specie(s)	Name	Migration (E_m), binding (E_b) and dissociation[14] (E_d) energy, all data given in eV	Stage of possible migration in dilute Fe-Cr	Stage of possible migration in concentrated Fe-Cr
SIA: Fe-Fe dumbbell	I	E_m = 0.34-0.37 [99,100], 0.36 [94], 0.34 [83], 0.27 [24] (experimental)	Stage I (close-pair, correlated and uncorrelated)	Stage I (close pair, correlated) But almost suppressed by C_{Cr}
Di- and tri SIA: clusters of parallel Fe-Fe dumbbells	I_2, I_3	$E_m(I_2)$ = 0.43 [24,83,99], 0.39 [94] ; $E_m(I_3)$ = 0.43 [83], ≥0.53 [94]. Larger clusters have distinctively higher migration energy and can occupy non-mobile configurations [102].	I_2 can move at Stage II but its interaction with Cr will affect. I_3 will move closer to vacancy migration temperatures (E_m^V~0.55).	I_2: Stage II, but strongly delimited by Cr. At higher C_{Cr} is possible that most cluster will eventually become mixed with Cr_s either by migration or during irradiation. I_3: should migrate beyond stage III.
MIA: mixed Fe-Cr dumbbell	ICr	E_m =0.23 [103], 0.21 [94]; E_b = 0.08 [104]; E_d = 0.34+0.08 = 0.42	Stage I, at close pair positions. And effective migration beyond stage III if they get trapped.	Stage I, at close pair positions, most will get trapped by Cr_s (next line). If existing beyond III, they can migrate and dissociate.
Trapped MIA: mixed Fe-Cr dumbbell trapped at another neighboring Cr_s atom.	ICr_2	Immobile, E_b(ICr-Cr) = 0.08 [104]; E_d = 0.31	Dissociate at I_E	Dissociate at I_E but get re-trapped
Mixed di-SIA: formed by Fe-Fe and Fe-Cr dumbbells	I_2Cr	E_m = 38 [94], 0.30 [83]; $E_b(I_2\text{-Cr})$ = 0.11 [94], 0.02 [83]; E_d = 0.43 + 0.02 = 0.45	According to [94] they determined Stage II. According to [83], they can migrate at I_E.	Stage II, if trapped by Cr can migrate at vacancy recombination stage III.
Mixed di-SIA: formed by two Fe-Cr dumbbells	I_2Cr_2	Immobile, $E_b(I_2\text{-}Cr_2)$=0.1-0.2 [94], 0.316 [83], $E_b(I_2Cr\text{-Cr})$ = negative [94], 0.062 [83]; Dissociation results in the formation of I_2Cr-Cr E_d = 0.38 + 0.062 = 0.44	Only by dissociation at stage III	Only by dissociation at stage III
Tri-SIA formed by two Fe-Fe and one Fe-Cr dumbbells	I_3Cr	Immobile; $E_b(I_3\text{-Cr})$ = 0.11 [94]; E_d = 0.63 [94]	Only by dissociation beyond stage III	Only by dissociation beyond stage III
Tri-SIA formed by one Fe-Fe and two Fe-Cr dumbbells	I_3Cr_2	Immobile; $E_b(I_3\text{-}Cr_2)$ = 0.2-0.3 [94]; Dissociation occurs via release of I_3 E_d = 0.73-0.83 [94]	Only by dissociation beyond stage III	Only by dissociation beyond stage III

Table 4.2: Properties of small interstitial clusters with respect to their mobility and trapping by Cr and Cr-Cr close pairs. Data provided by DFT and EP calculations and used in Rate equation model

[14] Dissociation energy is the sum of the binding energy plus the migration energy of the released mobile specie.

The just presented ab-initio data has been included in rate theory formalism (so as the one explained in section 2.3.2) in order to predict defect evolution in electron–irradiated dilute Fe-Cr alloys [83], trying to simulate RR experiment of Abe and Kuramoto [30] which shown stages I and II (see section 4.3 and Fig. 4.6). A good correlation was found between the prediction of the model and the experimental RR results, as the model predicts a shift of Stage I_E towards lower temperature, mainly attributed to the migration of highly mobile Fe-Cr mixed dumbbells. The good agreement validates the *ab-initio* parameters used as well as the kinetic model which is considering the following rate processes in Stages I and II (the reactions indicated in red color produce defects which cannot migrate at that Stage):

State I_E (100-150 K):

$$I + V \rightarrow 0 \quad \text{4-3}$$
$$I + Cr_s \rightarrow \text{ICr} \quad \text{4-4}$$
$$ICr + V \rightarrow Cr_s \quad \text{4-5}$$
$$ICr + Cr_s \leftrightarrows ICr_2 \quad \text{4-6}$$
$$ICr + ICr \rightarrow I_2Cr_2 \quad \text{4-7}$$
$$I + Cr_2 \rightarrow I_2Cr_2 \quad \text{4-8}$$
$$I + ICr \rightarrow I_2Cr \quad \text{4-9}$$
$$I_2Cr + V \rightarrow ICr \quad \text{4-10}$$

(controversy, according to [94] I_2Cr cannot move up to Stage II)

$$I_2Cr + Cr_s \rightarrow I_2Cr_2 \quad \text{4-11}$$

Stage II(150 – 200 K), onset given by I_2 and I_2Cr_2 (also by I_2Cr according to [94]):

$$I_2 + V \rightarrow I \quad \text{4-12}$$
$$I_2 + Cr_s \rightarrow I_2Cr \quad \text{4-13}$$
$$I_2 + Cr_2 \rightarrow I_2Cr_2 \quad \text{4-14}$$
$$I_2 + I_2Cr_2 \rightarrow I_4Cr_2 \quad \text{4-15}$$
$$I_2Cr_2 + V \rightarrow ICr_2 \rightarrow ICr + Cr_s \quad \text{4-16}$$
$$I_2Cr_2 + I \rightarrow I_3Cr_2 \quad \text{4-17}$$
$$I_2Cr_2 + ICr \rightarrow I_3Cr_3 \quad \text{4-18}$$
$$I_2Cr_2 + I_2Cr \rightarrow I_4Cr_3 \quad \text{4-19}$$

As I, ICr, and I_2Cr will re-created during stage II, reactions from 4-3 to 4-11 will also occur in stage II.

Concerning Stage III we can deduce from presented statements that recombination will come from vacancy recombination and interstitial cluster dissociation or migration:

$$V + I_nCr_m \rightarrow I_{n-1}Cr_m \quad \text{4-20}$$
$$I_2Cr + Cr_s \leftarrow I_2Cr_2 \quad \text{4-21}$$
$$I + Cr_s \leftarrow ICr \quad \text{4-22}$$

It has to be noticed that all of the presented calculations and energy values and RR simulations have been done in dilute alloys systems and thus it hasn't been taken into account the possible effect of the Cr background in concentrated systems, on the Cr-IA binding energy, long-range Cr-Cr interaction and de-trapping mechanisms. Specific

calculations on these issues should be made prior to draw any conclusion in concentrated alloys.

Concerning concentrated alloys, modelling of Fe-Cr systems has been able to find an explanation for some of the experimental observations described in previous section. *Ab-initio* calculations have been used to study the stability of dumbbells and crowdions in bcc Fe-Cr structures [104]. The binding energy of one defect was calculated taking into account every the possible Fe-Cr interstitial configurations and the possible presence of one or two neighbouring Cr atoms in the bcc cell. Calculations with different codes were made and presented for comparison (DFT and EP). The main results are shown in Fig. 4.10. In summary, every configuration have different levels of stability, some configurations where strongly bounded whereas others where strongly repulsive. For instance, configurations #11 (SIA + 2 Cr atoms), #4 and #12 (MIA + Cr atom) or #9 (Cr-Cr crowdion) were found to be strongly attractive whereas #3 (Cr-Cr dumbbell) and #10 (<110> MIA + Cr atom) strongly repulsive. Thus <110> dumbbell may become unstable and rotate into <111> crowdion configuration depending on the local atomic environment. However, the frequency of such different configurations is not the same for every type. The most likely IA configurations are the SIAs in the presence of one or two Cr atoms (#2, #8 and #11) and MIAs surrounded or not by a Cr atom (#1, #4 and #5).

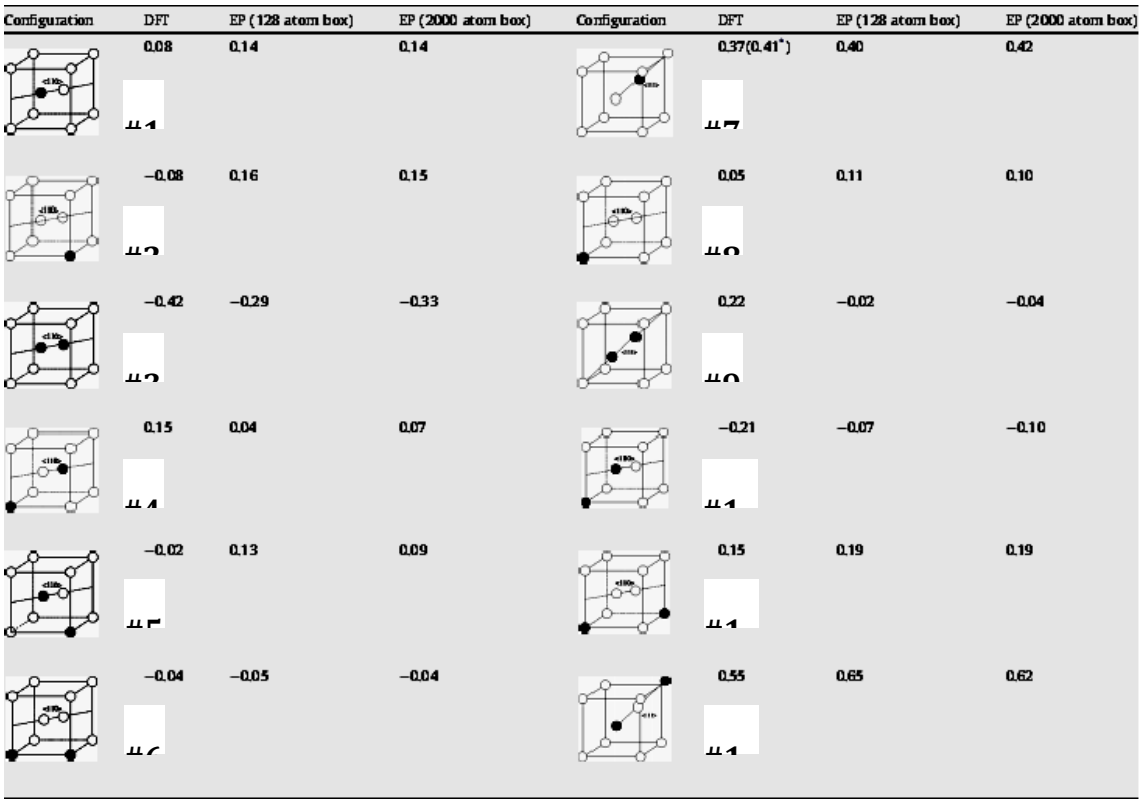

Fig. 4.10: Binding energies of different IA configurations: DFT and EP calculations, obtained by Terentyev et al. All values are given in eV. Positive values mean attractive interaction.

Moreover it has to be understood that every configuration have a different formation energy. Thus, the Fe-Cr defects cannot be treated any longer as pure Fe systems where there was only one energy formation value of the Fe-Fe dumbbell. In the case of pure Fe, the migration energy (E_m) is the energy that an Fe-Fe dumbbell needs to overcome the saddle point and jump into a new interstitial position with the same formation energy. In the case of interstitial defects in Fe-Cr systems, the formation energy is not a Dirac delta function any longer, but the formation energy probability becomes a broader distribution. And such distribution becomes broader as the C_{Cr} is increased in the Fe-Cr system as it is indicated in Fig. 4.11. Such broadening has high impact on the behaviour of defect migration. The dumbbell will only be able to jump to 8 different positions, thus only the configurations with a probability of existence equal or higher to 1/8 (0,125) will be able to migrate freely when they reach the E_m, as they will be surrounded by configurations with their same formation energy or lower. In the case of configurations with lower energy formation and lower probability of existence, their energy migration will no longer be E'_m but E'_m plus an energy increment (ΔE_m) required to overcome the formation energy difference with their neighbouring configurations. In the case of Fe-5%Cr the increments was estimated about ~0,3 eV while in the case of Fe-10%Cr and Fe-15%Cr this binding energy is about 0,4-0,5 eV. Hence, the migration energy is no longer a static concept but more a dynamic one. This effect thus is well aligned with the **configurational trapping** indicated by Nikolaev and which would be responsible on the free migration of defects beyond I_E.

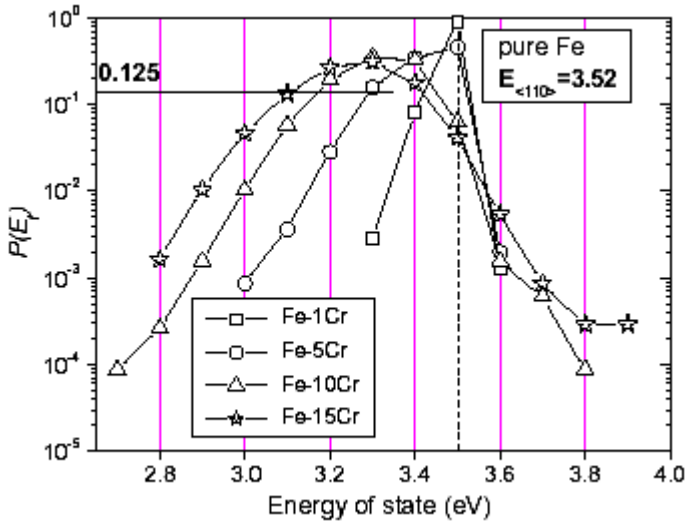

Fig. 4.11: Formation energy probability distribution, $P(E_f)$. Vertical dotted line corresponds to delta function of pure Fe.

Another fact that gives explanation to experimental data has been investigated by using MD. It is generally accepted and confirmed by calculations made with some specific potential [19], that the threshold displacement energy of Cr atoms in Fe-Cr alloys is essentially the same as for an Fe atom in the same alloy. In the studied case of Fe-10%Cr, the displacement energies are close to the 40 eV used in SRIM simulations for pure Fe [61].

According to this result it is reasonable to accept that defect production cross-section is not affected by C_{Cr}, although, the recombination processes during the relaxation of the cascade might slightly differ. This was confirmed by simulations of collision cascades up to 50 keV made by MD which indicated that presence of Cr does not affect the ballistic phase of the cascades and eventually the number of dpa's, volume and density and the final population of defects and clusters is only slightly altered [19]. The model just predict slight increase in the number of FPs, more dumbbell (mainly Fe-Fe and Fe-Cr) and less defect clusters (n>5). Such conclusions indicate that comparatives between RR experiments of pure Fe and Fe-Cr alloys are reasonable in terms of initial damage. However, the fraction of Cr atoms in interstitial positions greatly exceeds the statistical value expected from alloy concentration, close to 75% for low PKA energies (1keV). This effect takes place in the post-collisional and post-relaxation phases of the displacement cascades, where Fe interstitials migrate until they remain trapped at Cr atoms. Therefore this indicates the strong affinity of Cr for interstitial positions as a consequence of its affinity to Fe interstitials.

Finally there is a very recent and interesting work [40], whose results are absolutely aligned with the modelling and experimental validation scheme presented in the motivation chapter and that frames the purpose of the present thesis. In [40] MD, AKMC and mean field RT methods were combined to model evolution of point defects as in RR experiments in Fe-Cr using electrons [the experiments from Abe and Kuramoto, Maury et al. and Benkaddour et al. [27,30,37]]. The approach developed was able to simulate the whole RR process: from the spatial distribution of FPs introduced by the electron irradiation, providing an accurate calculation of point-defect migration energies (Vs and SIAs) in concentrated Fe-Cr alloys by the used of nudged elastic band method [105] and artificial neural network [106], then modelling correlated recombination stages with AKMC and finally modelling of further recovery stages of LRM of single SIAs and Vs using mean field rate theory. Every part of this work provides interesting results and clarifying information that helps interpretating concentrated Fe-Cr alloys. First, the PKA energy spectrum of 2.5 MeV is calculated and consequently the mean distance between I-V pairs which is going to have an impact on close-pair, correlated and uncorrelated recombination stages (and trapping). As part of the results provided in this thesis, we also calculated the PKA spectrum of our 5 MeV protons and some simple MD calculations that will also give the distribution of distance between IAs and V.

Second, concerning the migration energies of IAs (the authors do not distinguish between SIAs or MIAs) the average free migration energy is found to increase as increasing C_{Cr} (E_m^{IA}(eV) = 0.33, 0.44, 0.46, 0.47 for C_{Cr} = 0, 5, 10, 15 % respectively). Analysing the migration trajectories of IAs and the number of jumps it was found that the IA remains trapped in a number of spatially interconnected configurations. The reason for this configurational trapping was provided in [104] by the differences in energy formation of IAs in concentrated Fe-Cr alloys, and explained in detail in former paragraph. The IA cannot release from this 'non-localized trap' until it gets an energy close to 0.45 eV. The concentration of these traps appears to increase with the C_{Cr} and it increases from ~50 appm up to 2400 appm for the alloys containing from 1 up to 15% C_{Cr}. This implies that the mean distance between traps goes from $27a_0$ up to $7a_0$ from 1 up to 15% C_{Cr}. The

configurational trapping is affecting the LRM free migration of IAs but it will also affect the correlated recombination stages if the spatial separation of I-V is comparable to the mean distance between configurational traps, as it is observed in Fe-15%Cr [27]. Besides, this trapping will be responsible of almost total suppression of free migration of IAs at I_E temperatures, thus suppressing the cluster formation at this stage.

Third and final, despite of the good agreement on reproduction of experimental results of correlated recombination obtained by AKMC, the LRM evolution was modeled by RT, and the code was just fitted to the experimental peaks in order to obtain the migration energies for stages II and III in Fe-5%Cr, Fe-10%Cr and Fe-15%Cr. The migration energies obtained where E_m^{II} = 0.40(5%Cr), 0.45 (10 and 15%Cr) and E_m^{III} = 0.45 (5, 10 and 15%Cr). E_m^{II} was associated to migration of de-trapped IAs (clustering should be allowed here then) and E_m^{III} to free vacancy migration. It is very important to point out, that despite of the good agreement found between the predicted migration energies from AKMC and the fit values of RT which at the same time fit with Benkaddour et al. experimental results, the model presented is very simple. Processes observed by Nikolaev, such as close-pair and correlated recombination of vacancies which might have strong impact at temperatures between 160 - 190 K have not been included in the model and nor the free migration of dissociated IAs at temperatures close to vacancy migration. Modelling of Nikolaev's results and assumptions hasn't been presented up to date. Moreover, it has to be noticed that the model only simulates a single recombination process in Stage II. In addition, the model was not able to reproduce the amplitude of Stage III accurately. This last limitation is, as the authors' state, probably due to SRO effects which are not included in the model. This is actually one of the main limitations of computational simulations that are devoted to reproduce RR results, because they assume that resistivity is only driven by the defect populations (along the post-irradiation thermal annealing). Accurate models such as AKMC and MD still cannot calculate the proper value of the residual resistivity of an alloy depending on its non-random solute distribution (ρ_S). On the other hand, object kMC (OKMC) and RT which do not take into account the local environment are even further away from being able to reproduce such SRO effects.

Chapter 5. Results and discussion

Originally the idea of the present thesis was to try to reproduce similar results to those acquired by Benkaddour *et al.* [27], on samples with Cr contents of 5, 10 and 15%, with a well-controlled composition and microstructure and to study specifically the effect of proton irradiations. With this purpose, the first task was to fully develop the sample preparation method, the RR set-up itself, the data acquisition system and data treatment. Each of these sub-tasks was indeed a delicate work, as it was presented in the experimental section, because, concerning results any deviation could affect their reliability. Afterwards, the considerations which have been made about SRO and its effects enhanced by defect migration in chapter 2 came out along the experimental and analysis process. Thus, the new method to avoid SRO effects, which is described in section 2.5, was also performed in order to check the importance of such effects on the RR experiments. For this reason it has been decided to present in a common chapter both the results and the discussion, given that some of the measurements were performed as a consequence of the discussion of previous ones.

Hence, the chapter is divided in five main sections. The first section of this chapter is devoted to the analysis and calculations which were made on the characteristics of the proton irradiation and the produced damage. Next, residual resistivity of studied Fe-Cr alloys is characterized and the effects of Cr addition to pure Fe are evaluated prior to irradiations. The third part provides description of specimen characteristics and irradiation runs, the experimental measurements of resistivity values of studied specimens along low-T-Irr. This section includes the analysis of effects of irradiation as a function of C_{Cr}. The fourth part includes RR curve and RR spectrum from a proton-irradiated pure Fe specimen. Their analysis is very useful given that it allow comparisons with many experimental results found in the literature and that have been described and critically reviewed in section 4.2 and help to identify the temperature intervals at which the processes should be occurring in proton irradiated samples. Finally the fifth part is the most important, where RR results of concentrated Fe-Cr alloys will be provided and discussed. An initial analysis on the results obtained under the classical RR method put in evidence the important SRO effects. Then RR results obtained with the proposed improved RR method, its discussion, as well as some complementary Mössbauer measurements are given.

5.1. Defect production by 5 MeV H^+

Up to now many discussions have been made in this thesis around the RR measurements from many perspectives. But few words have been said on the fact that current

experiments have been done irradiating with protons whilst most of the experiments in the literature have been made using electrons as irradiating particle, and few using fission and fusion neutrons. It is easy to understand, almost immediately, that despite of the difficulty to perform irradiations in neutron irradiation facilities, this type of experiments have to be done in order to approximate to fusion neutrons effects. On the other hand electron irradiations have been historically used to study irradiation effects because of its easier accessibility and the capability to make computational simulations provided the "small" displacement damage that they produce. Aligned with such approach ion irradiations are becoming an excellent tool to keep developing modelling inputs and codes. As it will be discussed in the next paragraph, protons produce a type of damage closer to the one generated by neutrons, but still close to ~MeV electrons for 5 MeV protons, which is the energy used in this work. So in this case protons are used as first approach to neutrons but in an energy range that still allow us to make comparisons with interpreted RR results of electron damaged specimens.

Electrons lose most of its energy by ionization interaction with the materials, which in the case of metals is not going to produce any displacement damage[15]. The damage created arises from production of displaced atoms by elastic collisions of very energetic electrons. If the energy transferred to the lattice atoms by elastic collisions is higher that the displacement energy (E_d), then the lattice atom will be displaced from its position. This is the PKA atom, it can just produce a single interstitial with his associated vacancy if his energy is low ($E_{PKA} \leq E_d$), or produce a displacement cascade creating more FPs or clusters if $E_{PKA} >> E_d$. In the case of the widely used 2.5 MeV electrons the calculated mean energy of the PKA spectrum is 0.06 keV [107]. Therefore it can be assumed that the created damage is mainly spatially separated single FPs.

By the contrary, the 14 MeV fusion neutrons are expected to produce high energy recoils which will be responsible for the formation of a large amount of defects. High energy protons (10-18 MeV) would reproduce the high energy recoils but also would produce a higher number of lower energy recoils which may end up in a larger proportion of single FP's than in the case of neutron irradiation. Indeed, as it was shown by Omar *et al* [90], the differential cross-sections and damage energy distributions of 10-16 MeV protons approximate to 14 MeV neutrons for energy recoils greater than few keV. However, protons deposit a larger fraction of their damage energy through collisions with energy transfers lower than 1 keV compared to neutrons. Thus, except in the low energy part, the PKA spectrum expected for high-energy protons is very similar to the one obtained with 14 MeV neutrons.

For the present work, the PKA spectrum of 5 MeV protons in a 50 μm Fe sample was calculated by using two independent BCA codes: SRIM [80] and MARLOWE [108]. These codes can simulate the complete path of an ion inside a target material. Every single collision between the incoming particle and a target atom (nucleus) is treated by solving the classical scattering integral between two colliding particles for the impact

[15] In metals, where electrical conductivity is high, the ionization produced by irradiation is very rapidly neutralized by the conduction electrons which have a relaxation time for charge redistribution extremely short ~10^{-19} s.

parameter of the incoming particle. In this way the codes are able to calculate the energy of every recoil produced by the incident particle. This provides the PKA energy spectrum which characterizes the displacement damage and allow its evaluation for different types of incident particle. The obtained results are plotted in Fig. 5.1 and good agreement between both calculations is observed. The obtained mean energy of PKA spectrum is about 0.35 keV (six times higher than 2.5 MeV electrons). It is worth mentioning again that the sample thickness and proton energy were chosen in such a way that the produced damage is quite constant in the entire sample. At this energy, the protons pass-through the sample and therefore the Bragg peak occurs well behind (in the sample holder).

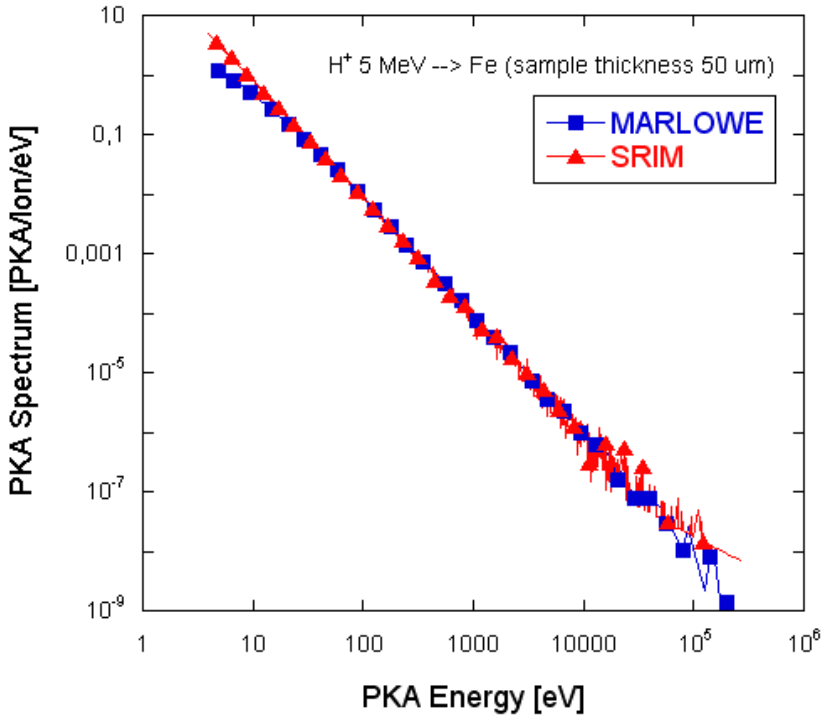

Fig. 5.1: PKA spectra of 5 MeV protons in 50 µm sample. Squares correspond to calculations made with MARLOWE code and triangles correspond to calculations made with SRIM code.

Therefore, although it is expected that in electron and proton irradiation mainly FPs will form during irradiation, some differences could be expected. In particular, it seems reasonable to think that the created FPs will have a different spatial distribution, mainly a higher separation distance between the SIA and its vacancy than in the case of electron irradiation. Indeed they do: a MD calculation of 6 and 15 cascades of 0.35 and 0.06 keV PKA respectively has been made on 50x50x50 cells using the Ackland potential (2004). The experiment has been repeated twice by changing the size criteria to find a vacancy or an interstitial. The distribution distances obtained from the simulations are plotted in Fig. 5.2 and Fig. 5.3. The average mean distances obtained for I-V pair distance are approximately $8a_0$ in the case of proton irradiation and $4a_0$ in the case of electron irradiation. This last value coincides with the value obtained by Terentyev et al. in 2012 [40]. Thus for 5 MeV protons, the I-V mean separation is the double that in the electron irradiation experiments and simulations. Following this reasoning, this larger separation would lead to a reduction of stage I amplitude for proton irradiated samples

caused by a reduction on correlated recombination. This is just what is experimentally observed (see section 5.4).

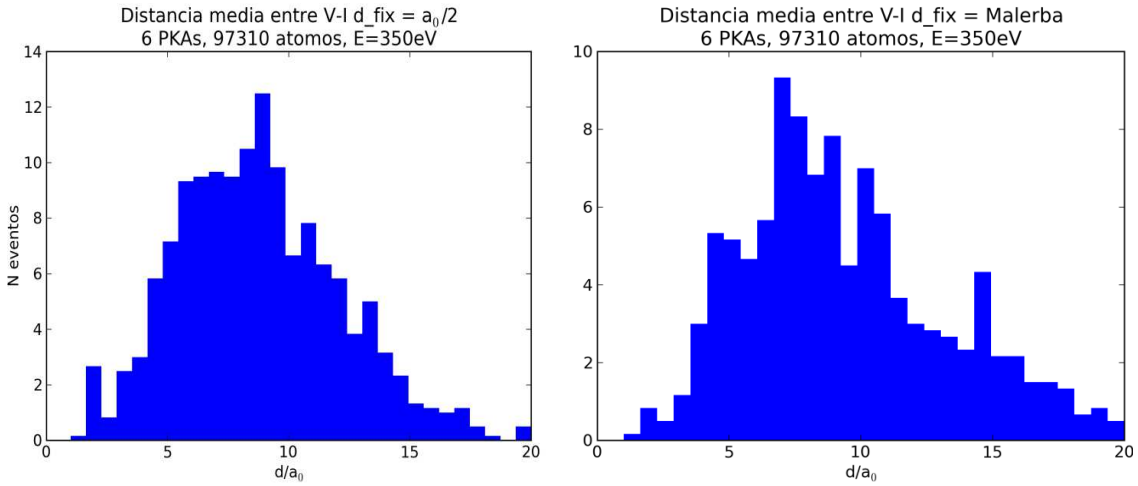

Fig. 5.2: Mean I-V pair distance in 5MeV proton irradiation (7-9a_0). Two different MD simulations where made using different criteria for the V or i size: $a_0/2$ (d_{fix} = 1.4276Å) and Malerba criterion (d_{fix} = 1.1745Å).

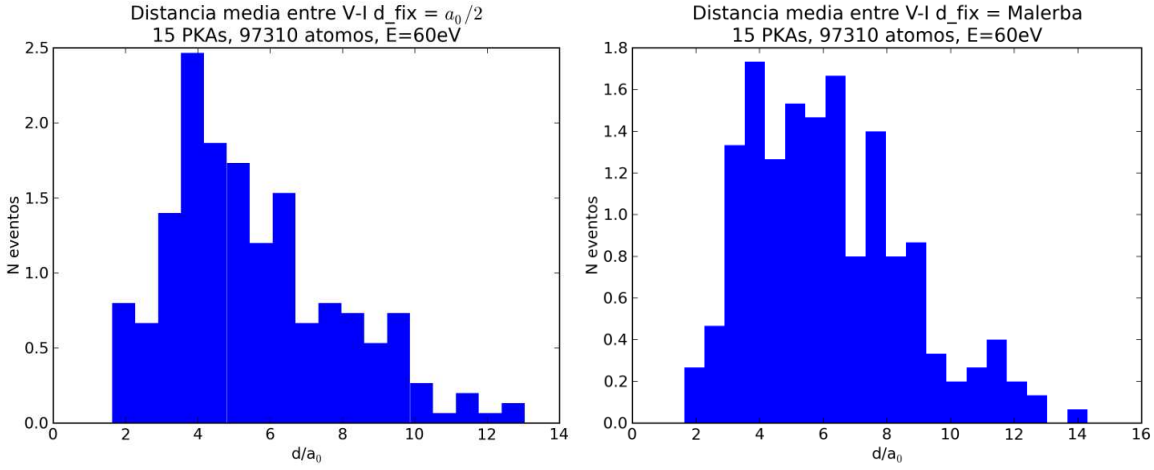

Fig. 5.3: Mean I-V pair distance in 2.5MeV electron irradiation (~4a_0). Two different MD simulations where made using different criteria for the V or I size: $a_0/2$ and Malerba criterion.

Usually in experimental works the calculations of the number of FPs are made using SRIM in the case of ion irradiations, thus, although is not the best code, using SRIM results as a reference of damage creation is interesting because it allows comparison with most experimental works previously made with ion irradiations. Thus, we made the calculations for proton irradiation in pure Fe, obtaining an initial concentration of 100 appm for a fluence of $3.7 \cdot 10^{15}$ cm^{-2}. The values obtained corresponding to every irradiated sample are indicated in Table 5-2. Instead of SRIM, calculations with Marlowe should be more accurate given that it can take into account the crystal structure of the atomic net and a subsequent analysis of the arrangement of defects allows considering the possible recombination of created FPs that might recombine if they are close enough (if the I-V are

separated by a distance smaller that the capture radii). Therefore, for more realistic calculations, including recombination, MARLOWE code was also used to estimate FP density, obtaining only **18 appm** using the accepted capture radius of 3.3 a_o for I-V recombination [109]. This illustrates the large difference when considering fast recombination of FP's.

It has to be noticed that the increase in resistivity is the parameter used for comparisons in terms of dose of most RR experimental works, independently of the number and type of defects created. It seems reasonable, to assume that RIR value is linearly related to the number of defects created in the cases of same monoenergetic particle irradiations on samples of different C_{Cr}, given that the MD calculations showed that final FPs populations were similar in pure Fe and Fe-10%Cr specimens hit by PKA with $E_{PKA} \leq 50$ keV [19]. For that reason, besides damage calculations, this RIR parameter has been widely used to compare different irradiations.

5.2. Fe-Cr residual resistivity characterization

As it has been said in the previous chapter, binary alloy systems, in this particular case Fe-Cr systems, are much more complex systems than pure non-alloyed metals. As we are using the resistivity as a technique to study the radiation damage in them, in the first place is good to establish some basis on how C_{Cr} affects the residual resistivity of the material. Thus, first results which are a matter of interest are related to the values of residual resistivity of the specimens previous to the irradiation. The apparent solute specific resistivity, which has been defined in eqn. 4-, has been calculated for the present Fe-Cr alloys. In our case, the formula is applied at the minimum temperature reached in the sample holder, of 20K, Table 5-1 summarizes the results obtained in our Fe-Cr with different C_{Cr}:

C_{Cr} (ppm)	ρ_{Cr}* (nΩ cm/ppm)
$5 \cdot 10^4$	200 ± 16[16]
$10 \cdot 10^4$	136 ± 10
$14 \cdot 10^4$	95 ± 2

Table 5-1: Apparent specific resistivity values of Cr calculated for the studied Fe-Cr specimens

In Fig. 5.4 the results of the apparent specific resistivity of Cr have been depicted, combining current data and results provided by Maury in dilute Cr alloys [37]. The high values of solute specific resistivity in dilute alloys, depends on the C_{Cr} as a consequence of non-additivity of the resistivity of the solute with that of the residual impurities. This interpretation have been done on the basis of the two current model [58] by approximating dilute alloys to ternary FeCrSi dilute alloys (eqn. 2-39 in chapter 2). It can be observed in the Fig. 5.4 that when Fe-Cr alloys start to become concentrated around 1%, the apparent specific resistivity reaches a plateau (constant value). This was

[16] To determine the experimental error it has been chosen twice standard deviation of the calculated specific resistivities, two values for each C_{Cr}.

explained in [37] by the two current model, given that the effects of residual impurities become negligible. Thus it was accepted by Maury *et al.* that in concentrated alloys the residual resistivity should be proportional to the solute concentration and therefore the specific resistivity of a solute should not depend on the solute concentration. Nevertheless in later work, [57], such independency was not found in Fe-V alloys of 1% and 3% V concentration. This was explained by the existence of a non-negligible spin-mixing term in the two-current model (see eqn. 2-42). As in the case of Fe-3%V, the residual resistivities measured on 10 and 14% C_{Cr}, exhibit a decrease of ρ_{Cr}^* with respect to measurements on Fe-1%Cr [37] and Fe-5%Cr [present]. Thus similar analysis as in [57] is made on our experimental data below.

The α parameter (at $C_{Cr} \leq 0.6\%$ $\alpha_{Cr} = 0.17$ [58]) is re-defined as z parameter according to eqn. 2-41. The z parameter is a monotonic function which varies between -1 and +1 (see Fig. 5.5(left)). The residual resistivity of a concentrated binary alloy predicted by the two-current model without neglecting spin-mix term, $\rho_{0\uparrow\downarrow} = \rho_m$, can be expressed analogously as eqn. 2-42:

$$\rho(Fe5) = \frac{\rho_0 + \rho_m}{1 + (1 - z^2)\,{}^{\rho_m}/_{\rho_0}} \qquad 5\text{-}1$$

If we would assume that spin-mixing term is negligible and that specific resistivity of Cr is not dependent on C_{Cr}, then it would follow:

$$\rho(Fe5) = \rho_0 = \frac{1}{2}\rho(Fe10) \qquad 5\text{-}2$$

and:

$$\rho(Fe5) = \rho_0 = \frac{1}{3}\rho(Fe15) \qquad 5\text{-}3$$

But, the experimental data reveals that this is not fulfilled, indeed:

$$\frac{\rho(Fe10)}{2\rho(Fe5)} = 0{,}64 \qquad 5\text{-}4$$

and:

$$\frac{\rho(Fe15)}{3\rho(Fe5)} = 0{,}42 \qquad 5\text{-}5$$

Thus if the spin-mix term is considered to be non-negligible and is defined as a function of the spin-mixing term of Fe5:

$$\rho_{\uparrow\downarrow}(Fe10) = y\rho_m \qquad 5\text{-}6$$

The residual resistivity of Fe10 and Fe15 can be described in terms of Fe5 values:

$$\rho(Fe10) = \frac{2\rho_0 + y\rho_m}{1 + (1 - z^2)\,{}^{y\rho_m}/_{2\rho_0}} \qquad 5\text{-}7$$

and:

$$\rho(Fe15) = \frac{3\rho_0 + y'\rho_m}{1 + (1 - z^2)\,{}^{y'\rho_m}/_{3\rho_0}} \qquad 5\text{-}8$$

Pairs of equations (5-1, 5-7) and (5-2, 5-8) can provide solutions for residual (ρ_0) and spin-mixing (ρ_m) terms respectively if we are able to fix the values of z(α) and *y* respectively. It must be notice that the equations would depend on α by means of z^2. For convenience and clarity in the following analysis, the relationships of z and z^2 with α parameter are depicted in Fig. 5.5. The graphical solutions for the equations are depicted below. The Fig. 5.6 represents the graphical solution of eqn. 5-1 for different values of the α_{Cr}. Reasonable values of ρ_0 and ρ_m are obtained if $\alpha_{Cr} \leq 0.17$, which limits possible values of z and z^2 (see Fig. 5.5). In Fig. 5.7, graphical solutions for eqn. 5-7 are evaluated for two different values of $\alpha_{Cr} \leq 0.17$ (z = -0.71 and z = -0.82) and different values of *y*. In any case it is observed that the spin-mixing term is required to abruptly diminish in Fe-10%Cr. Similar situation is observed in the analysis of Fe-15%Cr, in this cases the spin-mixing term is suppressed, but it is required that α_{Cr} has a value definitely lower than 0.17.

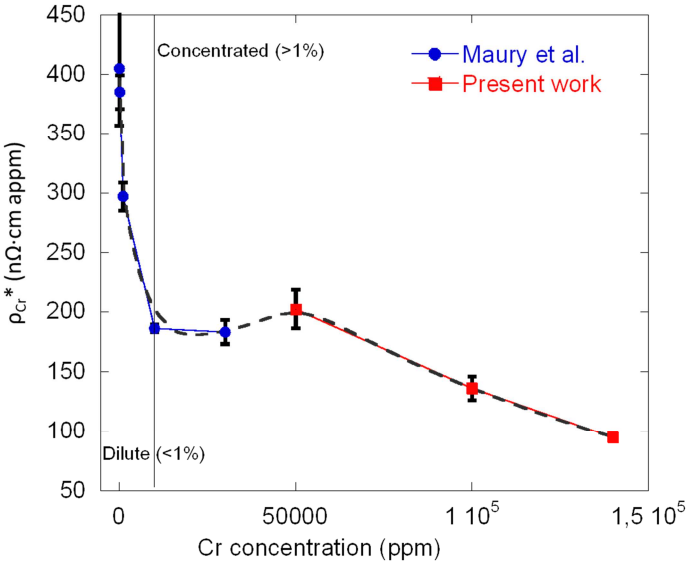

Fig. 5.4: Apparent Cr specific resistivity on Fe-Cr alloys. Circles (blue) are data from Maury et al. [37] and squares (red) are data from the present work.

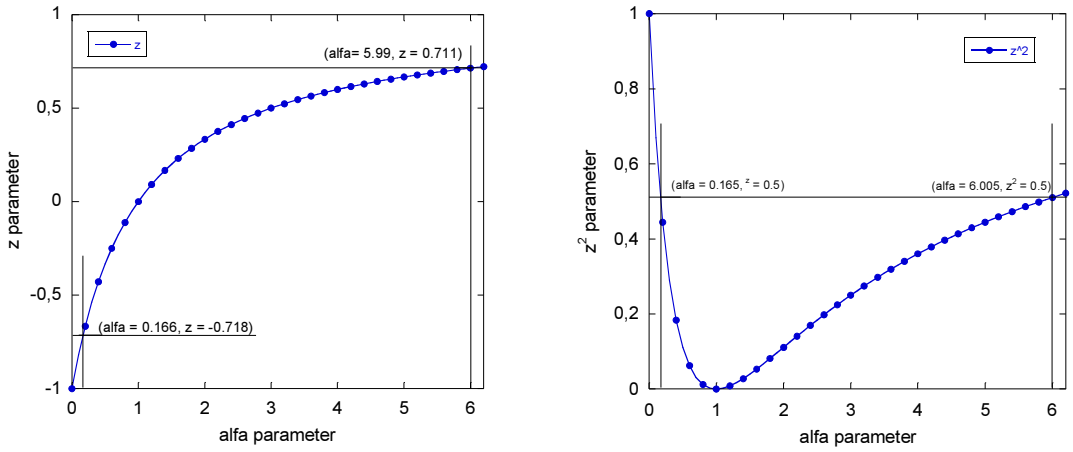

Fig. 5.5: Values of z (left) and z^2 (right) parameters as a function of α parameter.

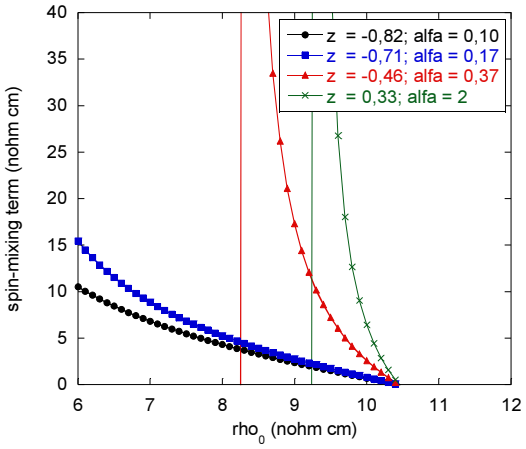

Fig. 5.6: Graphical solution of residual resistivity in Fe-5%Cr for different possible values of α_{Cr}.

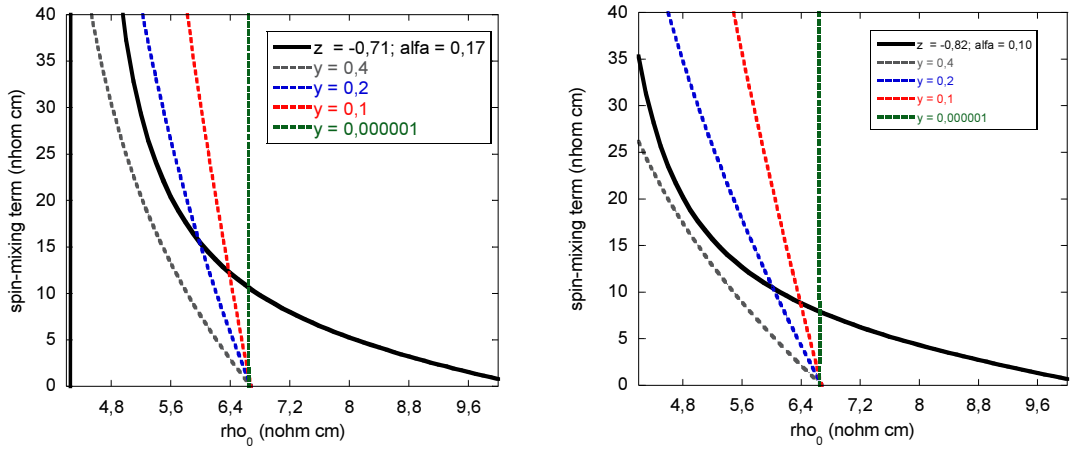

Fig. 5.7: Graphical solutions for the resistivity of Fe-10%Cr alloy compatible with solutions of fig. 5-6, two different values of z evaluated (left and right), *y* is varied for a fixed z.

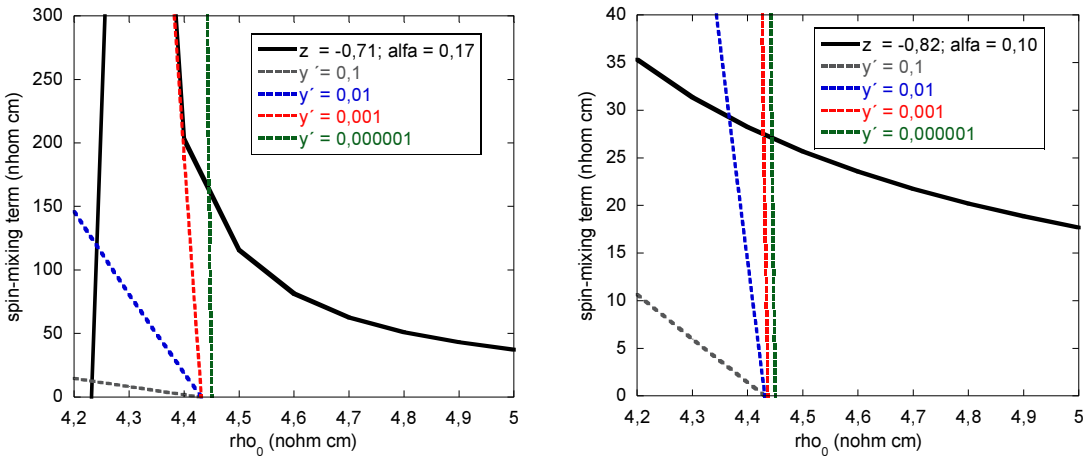

Fig. 5.8: Graphical solutions for the resistivity of Fe-15%Cr alloy. Two different values of z evaluated (left and right), *y* is varied for a fixed z

From the graphical resolution of equation systems it can be concluded that:

- The spin-mixing term is required to justify the resistivity value at 5% C_{Cr}, but it tends to diminish up to zero in very concentrated alloys: Fe-10%Cr and Fe-15%Cr.

- At the same time α parameter should no longer be independent on the solute concentration but its value has to decrease as the C_{Cr} is increased in order to accomplish the two-current model. A more reasonable value at 15% C_{Cr} would be $\alpha_{Cr} \sim 0.10$.

Although these conclusions do not directly affect to the RR experiments, the information obtained will be used in the discussion of next section.

5.3. Irradiation runs: effects of C_{Cr}

It is important, for the interpretation of RR measurements, to understand if radiation affects the resistivity of concentrated Fe-Cr alloys equally. In the present work, the interest is to understand whether defect production is the same in pure Fe irradiations than in the Fe-Cr alloys at the studied concentrations; additionally, if the contribution of every defect to the resistivity value is dependent or not on the C_{Cr}. In the first part irradiation runs are described. Then the RIR results are presented and discussed.

In addition to the commissioning process which implied several irradiations to test and improve the whole system, six RR experiments have been performed on the Fe-Cr samples. Three experiments on Fe-%5Cr, Fe-10%Cr, Fe-14%Cr samples respectively were performed with classical “Low-T-Irr” at 50 K plus subsequent isochronal annealing. Analogously, new specimens of the same concentrations where studied by the new proposed method which included a 400 K “pre-Irr” step in order to saturate SRO before the “Low-T” irradiation plus the isochronal annealing. In order to check experimentally that the high temperature irradiation do change the Cr distribution, extra irradiations

were made on 30 μm samples of different Cr concentrations to be measured by transmission Mössbauer spectroscopy technique which was used to support our hypothesis on the behavior of Cr atoms in terms of SRO. Additionally, the data corresponding to a pure Fe irradiated specimen is also presented. The classification of the measured samples and the irradiation runs and doses can be found in Table 5-2. In order to keep a very low temperature in the sample during the ion irradiation, a low current around 20 to 40 nA was used for the ion beam. The currents used in the pre-Irr step where higher (in the order of 150 – 400 nA).

Cr (%wt)	Name	Thickness (μm)	*Pre-Irr(400K)* Fluence (cm^{-2})	*Pre-Irr(400K)* Dose (dpa)	*Low-T (50K)* Fluence (cm^{-2})	*Low-T (50K)* Dose (dpa)
0	Fe	41.5 ± 0.5	-	-	$3.9 \cdot 10^{15}$	$100 \cdot 10^{-6}$
5	Fe5	52.0 ± 1.2	-	-	$3.7 \cdot 10^{15}$	$103 \cdot 10^{-6}$
5	Fe5(Pre)	54.7 ± 1.5	$10.7 \cdot 10^{15}$	$271 \cdot 10^{-6}$	$3.6 \cdot 10^{15}$	$102 \cdot 10^{-6}$
10	Fe10	50.5 ± 0.6	-	-	$3.1 \cdot 10^{15}$	$83 \cdot 10^{-6}$
10	Fe10(Pre)	56.7 ± 1.2	$15.4 \cdot 10^{15}$	$404 \cdot 10^{-6}$	$3.1 \cdot 10^{15}$	$83 \cdot 10^{-6}$
14	Fe14	66 ± 3	-	-	$3.9 \cdot 10^{15}$	$120 \cdot 10^{-6}$
14	Fe14(Pre)	60.8 ± 1.0	$24.4 \cdot 10^{15}$	$723 \cdot 10^{-6}$	$3.5 \cdot 10^{15}$	$102 \cdot 10^{-6}$
5	M5.1	36 ± 1	-	-	-	-
5	M5.2	31 ± 1	$9.7 \cdot 10^{15}$	$232 \cdot 10^{-6}$	$4.5 \cdot 10^{15}$	$107 \cdot 10^{-6}$

Table 5-2: Specimen characteristics and irradiation runs.

For the sake of clarity regarding the visual representation and easy interpretation of the experimental results it has been decided to associate one specific colour and mark shape to represent every specific RR experiment. Table 5-3 resumes the chosen nomenclature. Other marks might appear along the presentation of the results or the discussion, but other notation will refer to results from literature which are plotted here in order to make comparisons.

Unfortunately, some comments have to be made concerning the experimental issues. RR experiments results exceptionally cumbersome given that a very precise measurement system has to be run in coordination with LHe supply, authorized irradiation date, good performance of the particle beam and beam diagnostics. Such tight coordination make the experiments very expensive and difficult to repeat without spending high amounts of time and personal effort (as the annealing takes longer than 60 h, remember, in continuum He flow regime). Thus when technical problems appear, the best approach is definitely trying to overcome them and profit the information that even a non-perfect experiment can provide. A quick look to the literature evidences that people working on this topic has suffered similar problems [29,64,91]. This does not mean that within this work the experiments haven't been repeated, if required, in order to check reproducibility of the experimental data, which indeed was done in pure Fe and Fe-5%Cr and Fe-10%Cr samples, but is explained as a justification, given that in Table 5-3 some remarks on the experimental issues have been provided.

Cr (wt %)	Name	Irradiation type	Tag	RIR(PreRIR) (nΩ cm)	Experimental issues
0	Fe	Low-T	Open circles Black	109	Poor T resolution. 200-300K missing
5	Fe5	Low-T	Full triangles Blue	546	
5	Fe5(Pre)	Pre-Irr + LowT	Open triangles Red	506 (255)	
10	Fe10	Low-T	Full diamonds Green	349	
10	Fe10(Pre)	Pre-Irr + LowT	Open diamonds Light blue	348 (-224)	Sudden switch-off of the ion source, low RIR Lost stage I due to power cut in beam line.
14	Fe14	Low-T	Full circles Yellow	400	High error: unfinished commissioning.
14	Fe14(Pre)	Pre-Irr + LowT	Open circles Brown	352 (-368)	

Table 5-3: Legend and description of studied samples.

The samples where irradiated at Low-T with 5 MeV protons with low currents (20 – 40 nA). The RIRs of the six specimens under study are plotted in Fig. 5.9 and Fig. 5.10 as a function of ion fluence. At first sight, the resistivity increase behaviour is linear with fluence and it should be if we combine equations 2-44 and 4-2. In order to evaluate the specific resistivity of FP, ρ_F, the derivative of the increase of resistivity with respect to the irradiation fluence is calculated, i.e. the RCR [37]:

$$\frac{\partial \Delta\rho}{\partial \phi} \approx \rho_F \sigma \qquad 5\text{-}9$$

Table 5-4 indicates the slopes of the RIR curves which have been obtained by regular linear regression and the correlation coefficients which indicate the goodness of the fits. The last column shows the quotient between the slopes of Fe-Cr and the slope of RIR in pure Fe. Such quotients indicate the relation between the specific resistivity of FPs in pure Fe with respect to the specific resistivity of FPs in Fe-Cr alloys with different C_{Cr}, only if the defect production cross-section is assumed to be the same for every material as it has been accepted in section 4.4.

Typically in studies of pure Fe and dilute Fe based alloys some simple calculations can be done based on the linear behavior of RIR at low temperatures in high purity samples. Based on eqns. 2-44 and 2-45 and on values of RIR, fluence and estimated dose, quantitative values related to the damage cross-section and the specific FP resistivity can be provided. On one hand, if we accept the value given in the literature for **ρ_F(Fe) = 3 nΩ·cm appm** [24], the obtained value of the damage cross-section is $\sigma_D = 0{,}92 \cdot 10^{-14}\text{cm}^2$ and the number of created defects calculated in this way is **~36 appm** for a fluence of 3.7 10^{15} cm^{-2} (whereas in section 5.1 calculations with Marlowe provided 18 ppm). On the other hand, if instead of believing the value of ρ_F(Fe), it is calculated from the value of estimated damage, the experimental value in our case gives ρ_F^{exp}(Fe) = ~1.1 nΩ·cm appm and ρ_F^{exp}(Fe) = ~5.6 nΩ·cm appm using SRIM or MARLOWE respectively. Thus there is a deviation between the two models and literature of a factor 3 and 1.9 respectively.

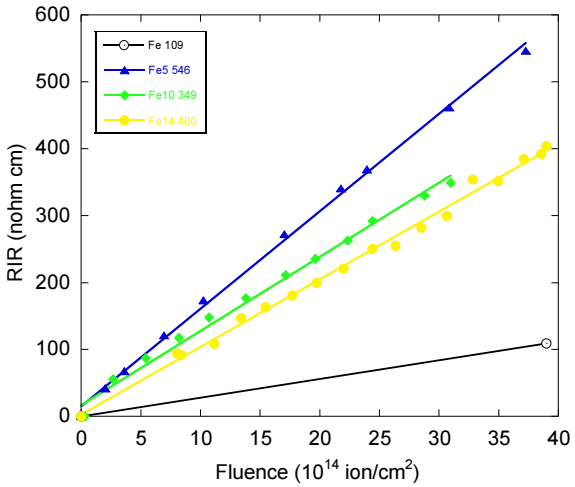

Fig. 5.9: Radiation induced resistivity of samples Fe5, Fe10 and Fe14.

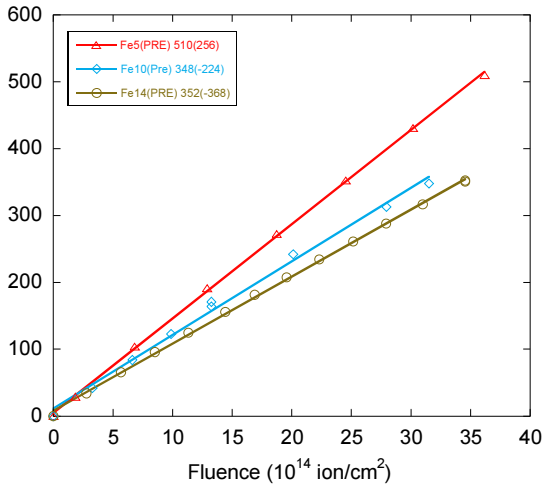

Fig. 5.10: RIR of samples Fe5(Pre), Fe10(Pre) and Fe14(Pre).

In the case of concentrated Fe-Cr alloys the model is not that simple anymore and such type of calculations are not usually found in the literature. Nevertheless it could be assumed that the defect creation cross-section is the same for Fe and Cr atoms in the Fe-Cr matrix, on the basis that the average displacement energy has a similar value for both type atoms [19], and from such assumption define which would characterize every alloy, ρ_F^*, this value is usually compared to ρ_F(Fe) and the analysis of such data provided in the next chapter will allow the study of some characteristics of the alloy electronic structure under the two-current model formalism. The experimental quotient ρ_F^*/ρ_F(Fe) is provided in Table 5-4 as well as the apparent FP specific resistivity values calculated from the experimental data and from references [24,27].

Sample	$\rho_F^*\sigma$ (10^{-14} nΩ cm^3)	R	ρ_F^*(nΩcm appm)	ρ_F^*(nΩcm appm)	ρ_F^*/ρ_F(Fe)
Fe	2.76 ± 0.04	-	3 [24]		
Fe5	14.6 ± 0.2	0.9990	15.8	15.1 [27]	5.3
Fe5(Pre)	14.11 ± 0.11	0.9998			
Fe10	11.1 ± 0.3	0.9959	12.0	14.7 [27]	4.9
Fe10(Pre)	11.0 ± 0.3	0.9972			
Fe14	10.10 ± 0.18	0.9974	11.0	13.7 [27]	3.7
Fe14(Pre)	10.03 ± 0.08	0.9996			

Table 5-4: RCR values for every studied Fe-Cr alloy, regression coefficients and relative increase of RCR with respect to pure Fe for C_{Cr} 5, 10 and 14%.

The above values are a way to analyze the effects of spatially separated FPs in alloys. In other discussions sometimes the apparent specific resistivity is defined to have separated contributions coming from Vs and Is separately, $\rho_F^* = \rho_v + \rho_i$, and therefore it is assumed that every type of defect is modifying the spin-up/spin-down population of states, so several values of α parameter, α_v and α_i, can be found in some discussions [37].

What can be concluded from the presented results is that the RCR (and consequently ρ_F^*) depends on C_{Cr}: at 5% is higher than ρ_F(Fe), and it starts decreasing at higher C_{Cr}, 10 and 15%. Results of RCR in alloys with C_{Cr} between few appm and 3 % have been reported in the work of Maury *et al.* [37]. The comparison of electron-irradiated and proton-

irradiated results has been possible by finding an equivalence in fluence. Comparing RIR values of samples of pure Fe (e^- and p irradiated). The RIR of 68 nΩ cm in Maury's pure Fe is equivalent to a proton fluence $\varphi = 2.54\ 10^{14}$ ion/cm2 in our Fe samples. The results are depicted in Fig. 5.11, showing the dependence of ρ_F^* on C_{Cr}, and a very good agreement between both groups of data. This would confirm a maximum effect of Cr on RCR for concentrations around 3-4%.

The justification of increasing RCR in the work of Maury *et al.* was well provided based again on the development of the two-current model formalism which has been introduced in chapter 2, section 2.1.6 and in [57]. The specific resistivity of the FP did depend on parameters, z and z_F but not any longer on defect concentration as it is indicated in eqn. 2-43. The parameter z was defined in eqn. 2-41 for a concentrated alloy and z_F is a mean value of z_i contributions of defects created (we could think of it as i = vacancies, interstitials or clusters of them contributing separately to the effective value z_F). From previous discussion in section 5.2 it has been determined that $\alpha_{Cr} \leq 0{,}17$ in concentrated alloys and this is equivalent to $z \leq -0.71$. It can be checked again by a graphical solution of the eqn. 2-41 evaluating different values of defect contributions to resistivity in the two-current model, z_F. In Fig. 5.12 the solutions of eqn. 2-41 with $z_F = 0.9$, 0.992, 0.995 and $z \leq -0.71$ are plotted as well as the horizontal lines indicating the experimental values of $\rho_F^*/\rho_F(Fe)$. From such graphical results the two-current model justifies the reduction of the specific FP resistivity on concentrated Cr alloys if α parameters are suitably chosen. Fit values of z_F are about -0,995 or -0,992 (i.e. $\alpha_F = 0.003$-0.004). The consequence of such values of z_F, assuming that the model presented by Maury *et al.* is valid our high concentrated alloys, would be that the presence of ~100 appm of FPs would slightly diminish the population of minority spin carriers.

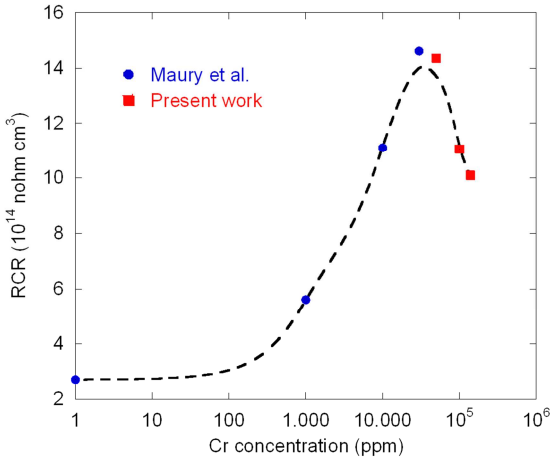

Fig. 5.11: Resistivity change rate as a function of C_{Cr}, experimental results from Maury et al. and present work.

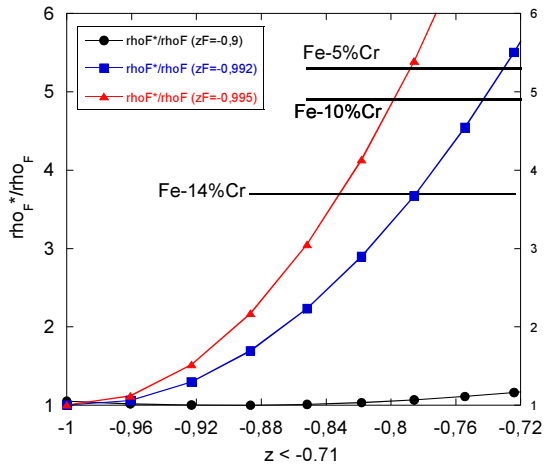

Fig. 5.12: Variation of relative specific resistivity of FPs as a function of solute concentration (z), for different test values of z_F.

If, instead of assuming that RCR is constant as the dose increases, the derivative of experimental RIR points as a function of fluence (as defined in eqn. 4-2) is calculated, then it can be observed (in Fig. 5.13) an actual reduction of the resistivity change rate with proton fluence, of 14-35% depending on the sample. Despite the experimental uncertainties a clear tendency to decrease is observed for every sample.

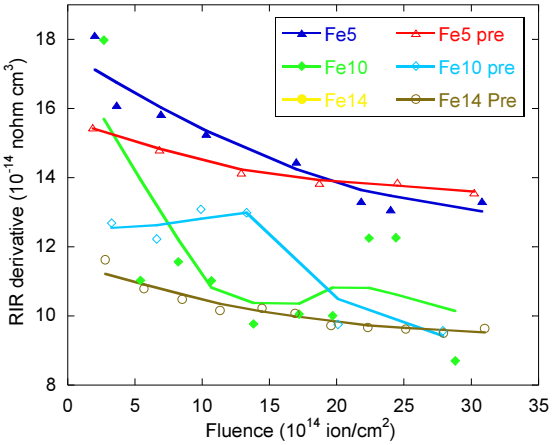

Fig. 5.13: RCR, i.e. experimental derivative of RIR data with respect to proton fluence.

According to the model [57]:

$$\rho_F^* = \rho_F \left[1 + \frac{(z - z_F)^2}{(1 - z_F^2 + (1 - z^2) c_F \rho_F / \rho_0)} \right] \qquad 5\text{-}10$$

the resistivity change rate should not vary more than 0.2%. This point is the only one not explained by the model. It is a fact that this effect has been observed widely in

concentrated alloys [26,27,37,92] and no explanation has been provided up to date. Nevertheless the variation of the apparent FP concentration is negligible in concentrated alloys, indeed the linear adjustment of RIR curves shows very high values of the correlation coefficient (see Table 5-4). Thus no correction of the RR will be necessary as the annealing T is increased and consequently c_F (concentration of defects) is decreased.

The best explanation for the slight decrease in RCR observed in Fig. 5.13 is that they are pure radiation effects. It is well known that at increasing doses the displacement cascades slightly start to overlap and thus the efficiency of particle irradiations slightly decreases, see for example [31,110]. Anyway, it is a minor effect and, as it does not influence the RR recovery and the experimental curves it will not influence the discussion.

In summary, an analysis of effects of Cr addition to residual resistivity and specific resistivity of FPs has been made under the two-current model and the main conclusions are:

- The addition of Cr affects the spin-up/spin-down populations of conducting electrons. Parameter α_{Cr} decreases with increasing C_{Cr}, thus addition of Cr diminishes the spin-down population. Which is aligned with the loss of ferromagnetism as the C_{Cr} is increased.

- The spin-mixing term exist in Fe-5%Cr specimens but is highly reduced in Fe-10%Cr and Fe-14%Cr.

- The effect of irradiation defects on two-current populations has a negligible effect.

- The reduction of ρ_F* is due to the reduction of α_{Cr} as C_{Cr} increases.

- The small reduction of RCR as the dose is increased is probably due to changes in the effective defect production cross-section by overlapping of cascades or spontaneous recombination volume [31], and it will not have impact on the RR curves nor their derivatives.

5.4. RR result in pure Fe

The measurements made on the pure Fe specimen are very useful given that they allow comparisons with many experimental results found in the literature and that have been described and critically reviewed in section 4.2 and help to identify the temperature intervals at which the processes should be occurring in proton irradiated samples. A RR measurement of pure Fe specimen obtained in this work is presented in Fig. 5.14. It must be reminded that the conditions of the isochronal annealing in every RR measurement are: steps of 2.5 K between 50 to 90 K, $\Delta T/T = 0.03$ from 90 to 400 K and 20 K steps above 400 K. The temperature ramps had a rising velocity of 10 K/min and annealing time is $\Delta t = 120$ s. The normalized RR curve is associated to the left-hand side ordinate axis and the RR derivative goes with the right-hand side ordinate axis. This criterion will be repeated for the rest of graphical representations of RR + RR spectrum curves presented. A deeply detailed description of impurity content indicated by the supplier and characteristics of

the sample and the irradiation is given in Table 5-5 [79], which has analogous form as Table 4.1 from section 4.2.

Work	RRR	Impurity (appm)	Irradiating Particle	Energy (MeV)	RIR (nΩ cm)	Comment
Present Work	126	C ~3 N ~4 O ~4 Si ~3	Protons	5	109	Irradiated at 50K Normalized at 20K

Table 5-5: Main characteristics of irradiated pure Fe sample studied under RR experiments.

It has to be noticed that the presented measurement was taken along the commissioning of the experimental set-up and the inaccuracy of the resistivity measurements is about one order of magnitude higher than the optimized measurements (details on experimental errors have been given in section 3.6) but as the statistics of measured points is high (100 measurements), the obtained RR curve is not completely useless. Besides, as we had two extra "problematic" experimental measurements in pure Fe ("(2)Fe" and "(3)Fe" already described in section 3.6), we could appreciate similar main features after proper data treatment which mainly consisted in smoothing of RR curves with Matlab (procedure normally used by other authors). Therefore, although our measurement made in pure Fe, has lower temperature resolution and the experimental error is systematically larger than in the Fe-Cr spectra (where better use of the oven and the temperature sensors was made after commissioning) the analysis of the stages I and II and comparison with literature can provide interesting information about the damage that 5 MeV proton irradiation has produced in the material.

In the RR spectrum of Fig. 5.14, before 200 K, several peaks can be identified at temperatures of: ~85, ~105, ~116, ~136 and ~190 K. The presented curve is lacking of data between 200 and 300 K because of a cut-off of the continuum He flow along the night, thus, in the graph we have plotted the Stage III results from other pure Fe specimens studied under similar characteristics. No clear peaks can be appreciated in stage III because of the inaccurate data, but indeed recovery stages were observed in this temperature range, as it has also been observed in experiments using electrons or neutrons. No clear peaks have been recorded but more a continuum stage up to 280K. Finally a small broad peak appears at ~335 K. The obtained results are compared in the following text to the already reviewed experimental results found in literature. From such comparison and discussion, a better understanding of the effect of proton irradiations in our samples is achieved.

Based on the critical revision on pure Fe accepted picture, we are providing the following interpretation of the obtained pure Fe spectrum. It is resumed in Fig. 5.14, and also direct comparison with the results of literature is also shown in Fig. 5.15 and Fig. 5.16. The first important result is that the obtained curve of RR is clearly closely related to the previous proton irradiations (14 MeV protons) and between electron and neutron curves (see Fig. 5.15.) This result confirms, using a different set-up and sample origin, that the proton irradiation produces a different ""RR signature" than electron/neutron experiments. Thus, the different damage structure has a clear effect in the annealing

stages, consequence of different defect kinetics at atomic level, supporting the RR technique as a useful tool for damage studies. This would allow for example to classify other irradiations (medium or heavy ions, etc…) and how similar the produced damage is compared to neutrons.

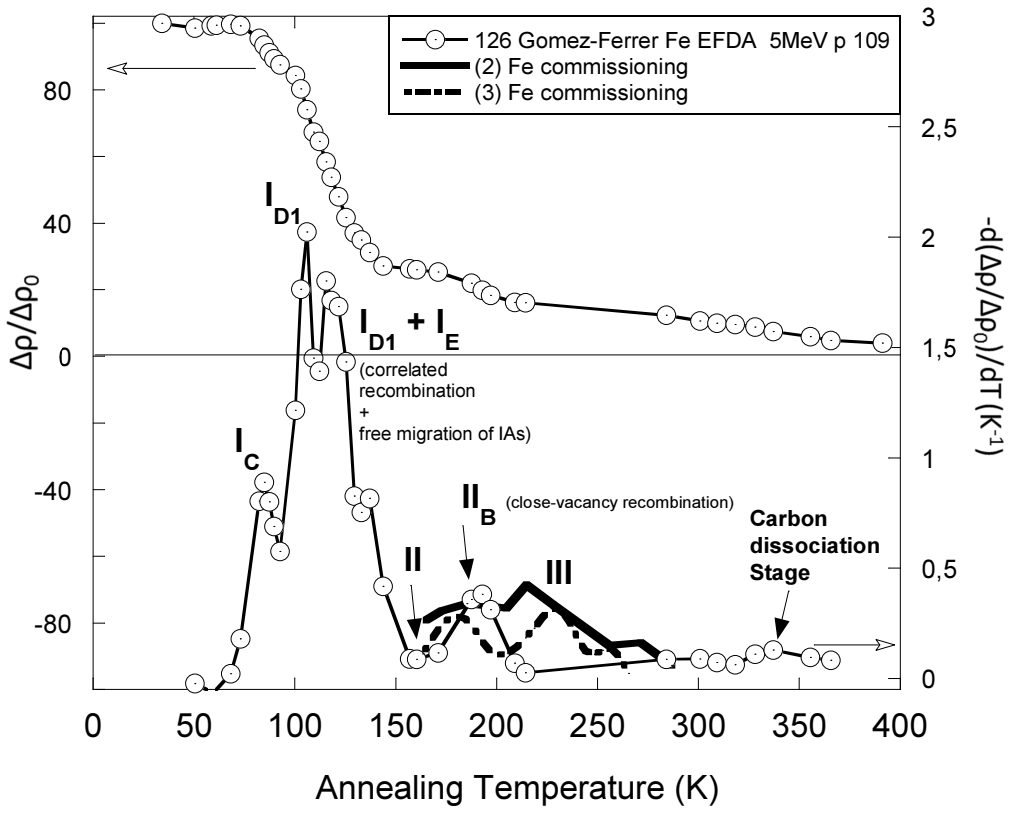

Fig. 5.14: RR and differential isochronal recovery curve of Fe irradiated with 5 MeV protons

Going into details, regarding the RR spectrum, in the low temperature range, close pair stages I_C and I_{D1} are clearly found. In the case of correlated recombination stage I_{D2} it is clearly shifted toward higher temperatures (117 K) and overlaps with uncorrelated recombination stage. As in the case of Nikolaev's pure (1°)Fe it is interpreted by a variation of the diffusion coefficient by the higher distance separation of I-V pairs, which has been confirmed by MD calculations presented in section 5.1. The stage I_E related to free migration of interstitials is observed at 136 K, and it is worth noting that its amplitude is higher than in electron-irradiated samples. This is because the larger I-V separation provides bigger chances to interstitials to "escape" from their correlated vacancy. The effect is to reduce I_D and increase I_E. Regarding at the RR curves in Fig. 5.15 it is also observed that in Stage I as a whole in samples irradiated with protons and neutrons of higher energies than our 5 MeV, the RR is highly prevented. The numerical values of the % of recovery at the end of each Stage are indicated in Table 5-6. Progressive prevention of resistivity recovery is observed as changing energy and nature of irradiating particle: 73% RR in our Fe sample (5MeV, p), 68% in Omar's (14 MeV, p) and 40% in Matsui's (14 MeV, n). Despite of the recovery prevention, in the RR spectra (Fig. 5.16) the stage I peaks are broad enough to assure that there is single IA recombination, in any of their forms up to at

least 140K. In other words, the highly probable clustering formation diminishes the intensities of the processes in stage I and favours appearance of recombination peaks at higher temperatures. Beyond 150K the amplitude of Stage II in our Fe sample (small $I_{2,3}$ cluster recombination) is similar to the amplitudes found in electron irradiated specimens (Takaki, Abe, Nikolaev), and thus it is suggested that the energies used in present experiments are not going to produce a high increase in cluster formation as it would happen at higher energies. At higher temperatures, the change in damage distribution is again observed in our spectrum given that a close-vacancy recovery peak is observed at 190 K. Missing data between 200K and 300K has not made possible to observe free vacancy migration Stage III. But as indicated in previous paragraph, some sort of broad recovery is found with probably lower intensity than the close-pair vacancy recombination stage. Further recording of the RR data beyond 300 K has shown a small stage around 340K which coincides with a carbon dissociation stage found by Takaki in their 67 appm C doped samples (RRR = 290). The possible presence of C impurities is strongly supported by the fact that our RRR measured in absence of magnetic field is quite low, RRR = 126 (see Table 5-5 or Table 5-6). This value indicates that the purity of our sample is close to the purity of Nikolaev's Fe specimens which were determined to have 70 appm of N impurities[17] and to Omar's samples (but no information on impurities was presented by this author). Thus one of our conclusions, despite the evident change in damage distribution produced by 5 MeV protons, is that the studied Fe specimens may not be as pure as it is indicated in the specifications. The pure Fe samples seem to contain about ~70 appm of C impurities. And thus such impurities could also be present in the rest of Fe-Cr alloys studied. In order to check the purity of our samples, X-Ray fluorescence was made, the results confirmed the high purity (in Fe, Fe-5%Cr, Fe-10%Cr and Fe-14%Cr) but due to the limitation in the sensibility of the technique impurity contents below 1000 ppm could not be detected. Therefore the results of analysis were inconclusive. Besides, in concentrated Fe-Cr alloys, the RRR value is not relevant anymore, given that the strong perturbation on the electronic states makes the decrease in resistivity much lower when lowering the temperature. Moreover, the decrease of ferromagnetism takes off the magnetoresistivity contribution. The effect of the impurities cannot be noticed by RRR measurements anymore (RRR(Fe-Cr) =3,3).

Work	RRR	Irradiating Particle	E (MeV)	RIR (nΩcm)	%Recovery Stage I (150K)	%Recovery Stage II (200K)	%Recovery Stage III (300K)
Maury	330	Electrons	1.6	68	~85.5	-	-
Takaki	5000	Electrons	3	126	86.6	90.8	98.5
Nikolaev	155	Electrons	5	203	85.1	90.8	98.5
Gómez-Ferrer	126	Protons	5	109	73.2	82.5	89.3
Omar	117	Protons	14	270	68.2	-	-
Matsui	1000	Neutrons	14	300	40.1	65.2	80.7

Table 5-6: RR at the end of Stages I (in cluding I_{A-C}, I_{D1-2} and I_E), II and III.

[17] As N and C are both light elements, its influence as impurities in FeCr alloys is assumed to be very similar.

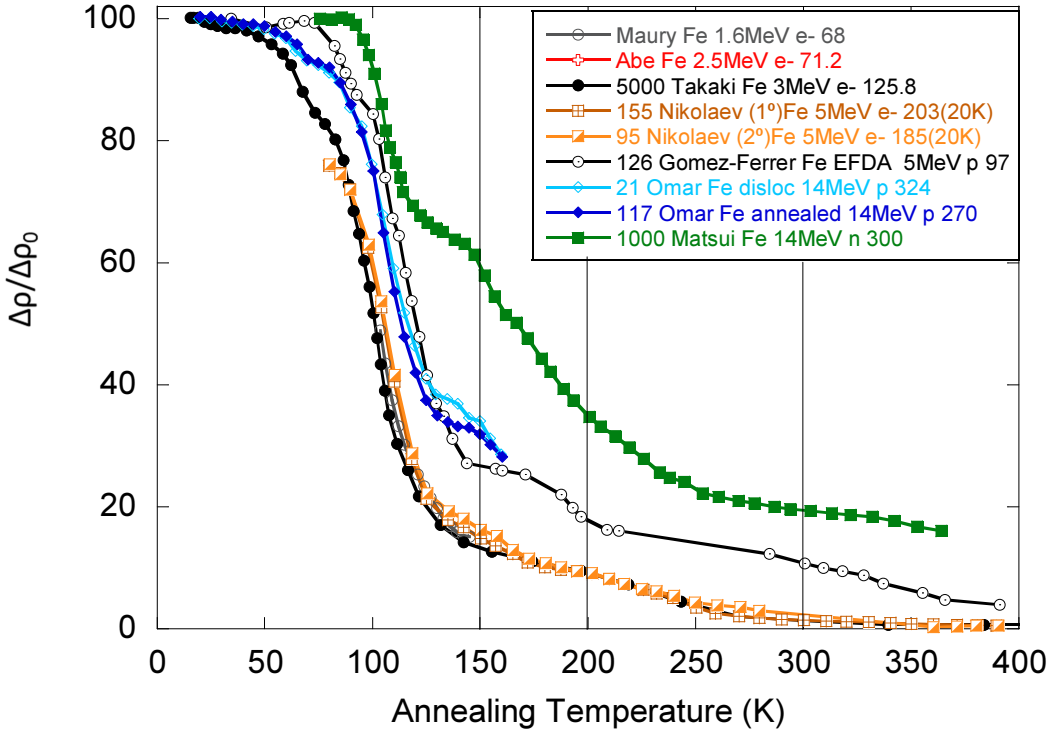

Fig. 5.15: Comparative of RR curves of pure Fe found in the literature with our experimental values (Gomez-Ferrer)

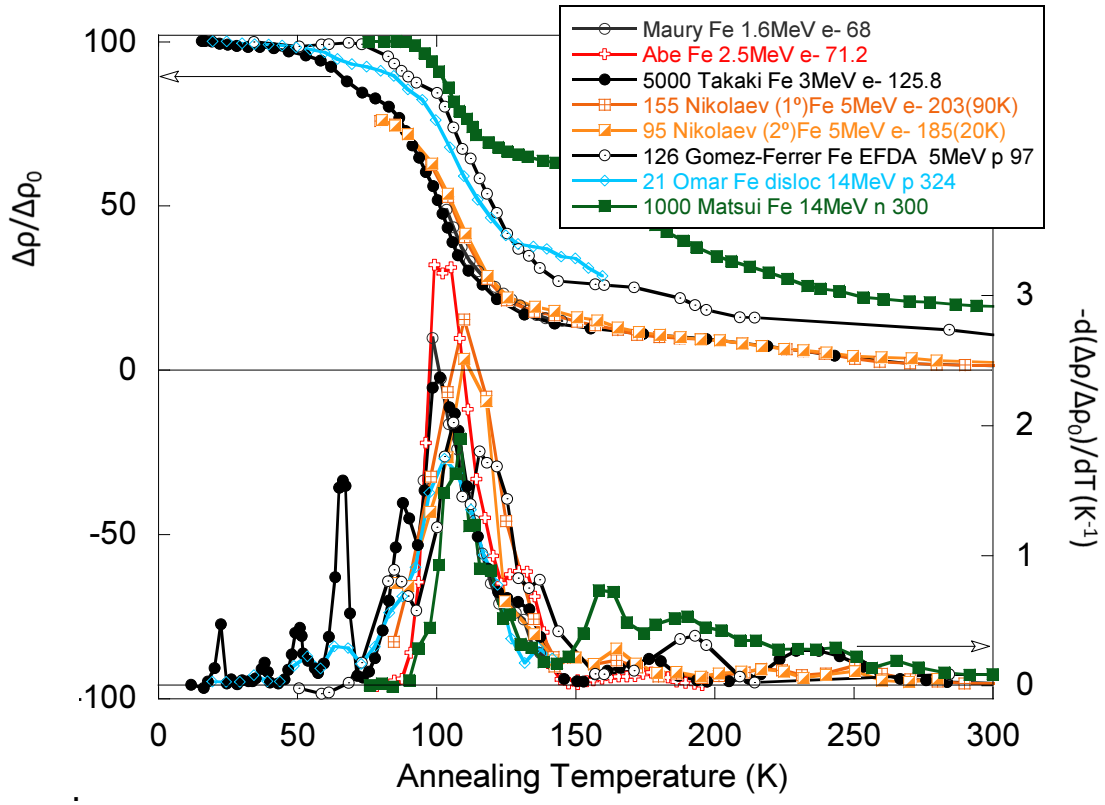

Fig. 5.16: Comparative of RR spectra of pure Fe samples found in the literature with our experimental curve (Gomez-Ferrer).

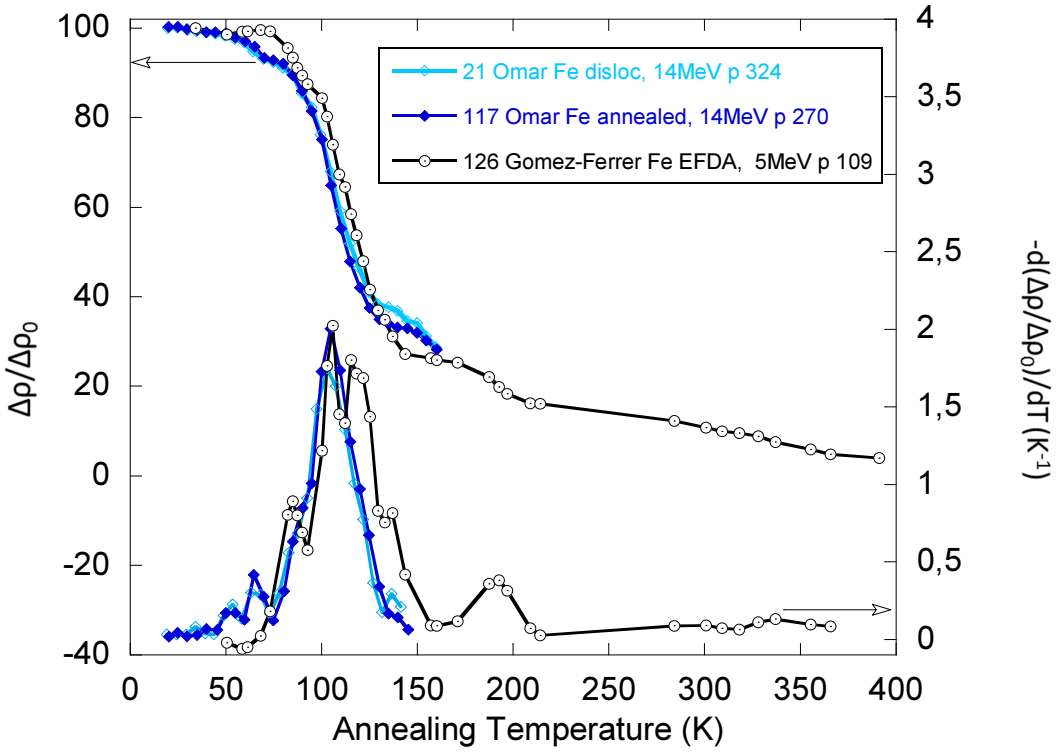

5.5. RR results in Fe-Cr

Finally, after the presented revision of the theory and the state of the art, detailed description of the technique and the developed experimental set-up and deep discussion of the results in pure Fe and the effect of the proton irradiation, the RR results in concentrated Fe-Cr alloys are presented and discussed.

5.5.1. The effect of C_{Cr} in classical RR results

Three specimens with different C_{Cr} (5, 10 and 15%) were investigated with the classical RR method (low-T-Irr + isochronal annealing). The details of the specimen characteristics and the irradiation runs can be found in tables 3-1, 5-2 and 5-3. Fig. 5.17 shows RR curves of samples Fe5, Fe10 and Fe14 over the interval 20 to 480 K, and in the lower part of the figure shows the differential recovery curves. Left axis indicates RR values whereas right axis indicates the RR spectra values. Concerning Fe14 data only the RR curve with very poor resolution is depicted (yellow full circles). This is the only reliable data that we have of this sample. During system commissioning it was necessary to identify the reliability of the temperature sensors which allowed making recurrent measurements at base temperature after each annealing step. As mentioned in chapter 3, the accuracy of the base temperature is one of the keys to minimize the experimental error on the RR curve. When sample Fe14 was measured the temperature sensors reliability had not been yet well-identified and the only reliable experimental points are the ones which were also measured at minimum temperature in the sample holder rather than at base temperature. The experiment has not been repeated yet due to time and schedule issues (it must be understood that only a few days per year can be allocated at CMAM for irradiations).

Nevertheless, a graphical comparison with the results obtained in Fe14(Pre) does no exhibit significant differences with Fe14 RR curve op to 365 K (to be discussed in detail later), thus the results of Fe14(Pre) are depicted in dotted brown line. In Fig. 5.18 same curves of Fig. 5.17 are compared with RR results of Fe sample.

Regarding at differential curves in the presented results it can be observed that close-pair and correlated recombination stages of IA recombination are progressively suppressed with increasing C_{Cr}. Specimens with 10 and 14% of Cr exhibit same suppression of stage I_D up to 120 K, as can be observed, the RR peaks coincide from 95 to 120K, although, some extra recovery has been recorded at close-pair recovery stages (I_C) in 14% Cr samples. The stage I_E is absolutely suppressed in agreement with previous measurements [37]. Thus, although MIAs and SIAs would have enough thermal energy to migrate according to *ab-initio* calculations in dilute alloys, this is not observed because of configurational trapping effects. Besides, in the case of some IA migration, these would interact with Cr_s atoms binding configurations which wouldn't allow the migration to be free. Nevertheless in the temperature range of I_E (120- 150 K) small stages are identified for all samples: a plateau between 130-155 K in Fe5, a small peak at 125 K in Fe10 and a small plateau in Fe14(Pre) between 120-140 K. The processes attributed to the RR in this range are rearrangement of interstitial complexes interacting with Cr.

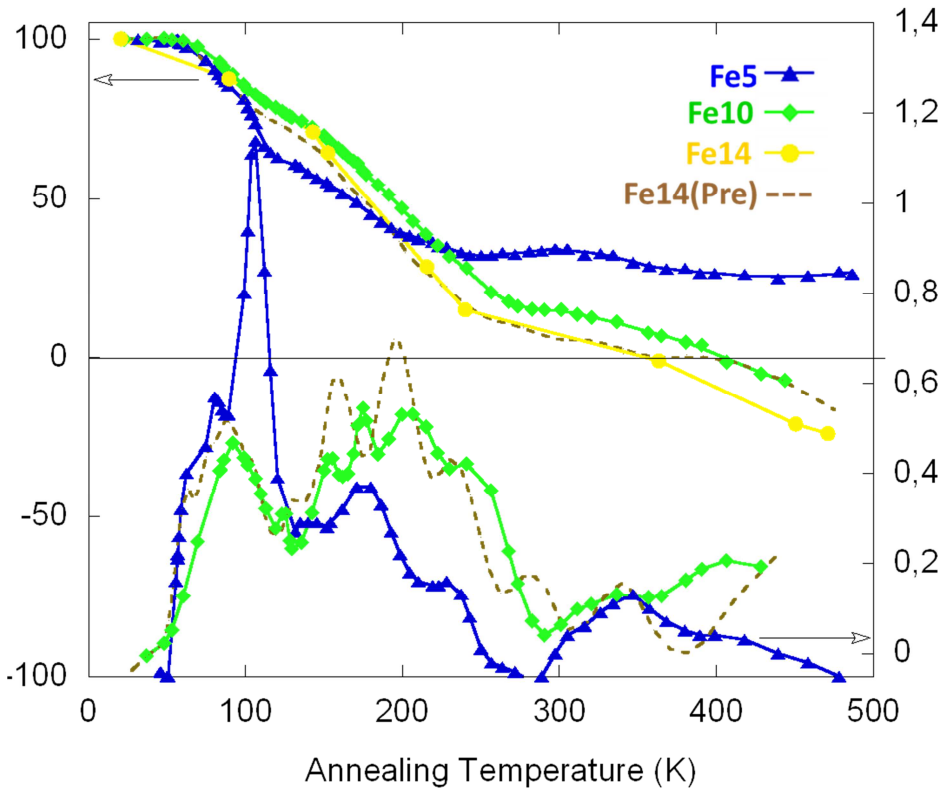

Fig. 5.17: RR isochronal recovery and recovery spectra of Fe5, Fe10 and Fe14 alloys after 5 MeV proton irradiation at 50K. From sample Fe14 only the RR curve is indicated. Dotted line depicts Fe14(Pre) sample results for comparison, as no significant difference has been observed in the RR curve.

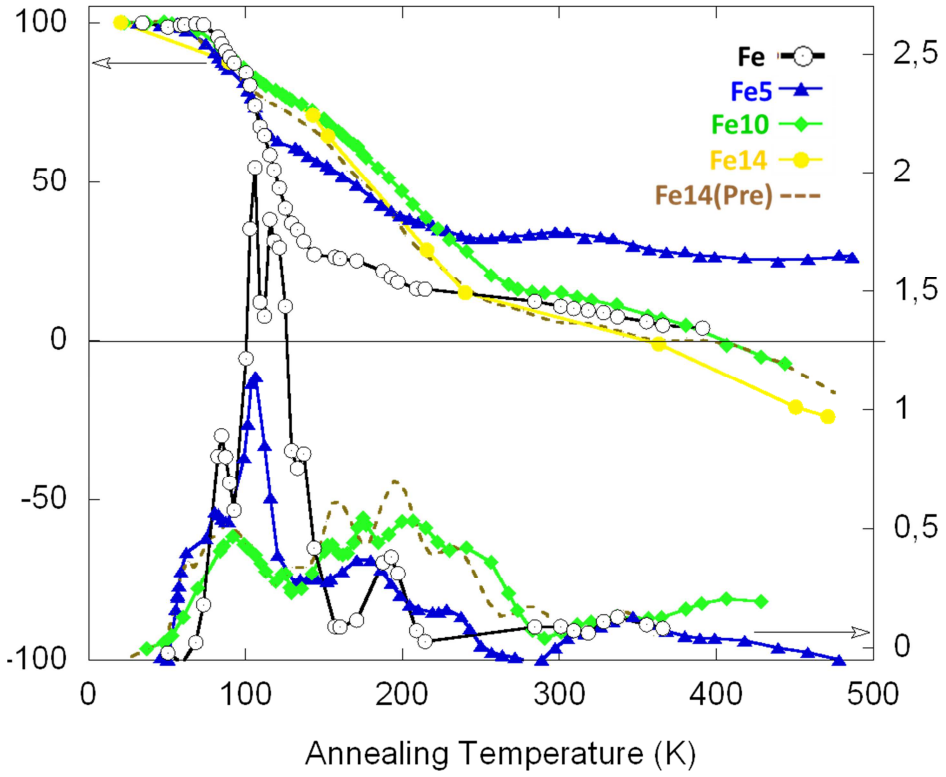

Fig. 5.18: RR results of figure 5-8 compared with RR data of Fe sample

Concerning **Stages II and III**, they present more complicated spectra:

(i) Fe5 shows a broad recovery peak centered at 175 K. This recovery stage is raised in contrast to the small stage II found in pure Fe (Fig. 5.14). Its nature has remained unexplained in past experimental works, but according to simulations, the only reactions predicted at this temperature interval (130 - 180 K) are re-arrangement of interstitial complexes interacting with Cr, de-trapping of MIAs and dissociation of mixed di-SIAs. In other words, the dominating migrating species would be ICr (either by formation or dissociation) and I_2 and I_2Cr could also migrate but their free migration would be limited by their strong interaction with Cr_s as indicated by the calculated migration energies. As vacancies are assumed not to interact with Cr, the close vacancy recombination should occur around 190 K as in pure Fe. Beyond 200K, there is a small plateau (as a result of a sum of overlapped peaks) followed by another stage recovery whose maximum is determined to be at 230K. The "tail" of this peak becomes negative, indicating an increase in the RR curve instead of an expected decrease in this range. The recorded plateau up to 230K should include free migration of di-vacancies and vacancies. These processes can be overlapped with migration of "de-trapped" (from configurational trapping) SIAs and MIAs, and migration of di-SIAs or mixed di-SIAs created as a consequence of vacancy recombination (see eqn. 4-20). The strong slowdown of RR beyond 230 K which leads to "negative" values of the RR derivative is attributed to SRO effects triggered by free migration of defects, by the

mechanism explained in section 2.5. We will see that this effect has important implications. Finally a broad recovery stage is found between 285 and 400 K and at higher temperatures the RR derivative seems to go towards reverse values again. The recovery which was associated to C contamination in pure Fe is also observed.

(ii) In Fe10 sample, at Stage II temperature range, overlapped peaks can be identified centered at 153 and 175 K. The intensity of the recovery is higher than in Fe and Fe5, thus confirming that this stage increases as C_{Cr} increases, which is aligned with the expected processes that have been described in the former paragraph. Close-vacancy recombination recovery remains in the same position and with higher intensity than in Fe and Fe5. As Stage I has been highly suppressed, there are more unrecovered vacancies than in Fe5. In Stage III there is a broad and high peak in 205 K and a shoulder appears at 240 K, revealing overlapped processes of V_2, V, IA and I_nCr_m recombination. From 290 K on there is a continuum recovery stage recorded up to 430 K. Again the C dissociation stage is observed at 340 K.

(iii) As it has not been possible to obtain a recovery spectrum corresponding to Fe14 data, we can only analyze the RR spectrum results of Fe14(Pre) sample. The peaks observed are overlapped but still very well defined with peaks at temperatures: 157, 195, 230 and 280 K. It is confirmed that the intensity of recovery between 130 and 180K is dependent on C_{Cr}. Nevertheless the total recovery of stage III is higher than in Fe5 but equal to Fe10. This could indicate that similar amount of non-recovered vacancies survive in both Fe10 and Fe14 or that the free migration of defects in stage III is similar, indeed the graphical representation of the intensity of stages in Fig. 5.19 confirms it. The differential recovery overlaps with samples Fe5 and Fe10 from 300 up to 365K (including the C dissociation stage), further data of Fe14(Pre) is not shown in the spectra as it is observed a divergence in the RR curves between Fe14 and Fe14(Pre) from 365 K on.

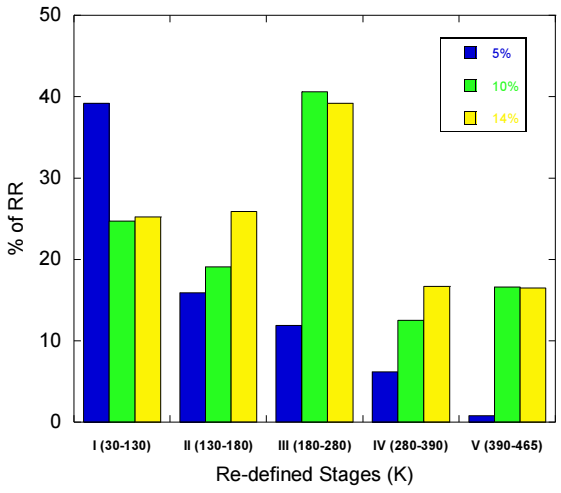

Fig. 5.19: Comparative amplitude of RR re-defined Stages

In view of the results just described for Fe-Cr alloys, temperature intervals of Stages are re-defined (see Fig. 5.19) with respect to description given in chapter 4. As Stage I_E is fully suppressed at C_{Cr} > 3% [37], combining this information with the experimentally observed RR spectra it can be assumed that the processes related to generic Stage I are expected to occur up to ~130 K. These processes are mainly MIA and SIA migration and their trapping with Cr_s. Higher temperatures would normally be associated to I_E (120-150K) processes (free migration of IAs) and to free migration of I_2 and I_3 (150-200K). Nevertheless, in concentrated alloys from 130 K, the recovery is mainly attributed to ICr, I_2 and I_2Cr or re-arrangements of Cr complexes. Thus the stage II in our discussion is defined to finish just beneath the close-vacancy recombination temperature, i.e. at 180 K, given that the vacancies are supposed to not interact with Cr and thus their recombination temperature should not be influenced by C_{Cr}. From 180 K to 280 K high recovery stages are observed in every RR spectrum and their shape and intensity are observed to depend on the C_{Cr}. The processes expected in this re-defined Stage III are close-vacancy recombination, free migration of vacancies and free migration of interstitial-like defects which result from dissociation of clusters and vacancy recombination. Next Stage, named IV in this work, includes possible dissociation of I_3 clusters or C-trapped IAs up to 390 K which is the temperature just previous to the Pre-Irr (400 K). We have named Stage V to the rest of temperatures beyond 400 K until we have enough experimental data to make comparisons.

Finally, table Table 5-7 sums-up the amount of recovery that the sample resistivity has achieved after annealing. The data is obtained from the normalized RR curves. The resistivity recovery in the pure Fe sample is total by 400 K. The value given arises from the average of all RR results that we obtained from pure Fe during commissioning (Fe, (2)Fe and (3)Fe) the error is twice the standard deviation. It is important to notice that signs of SRO are observed beneath or at 400 K in Fe5 (26% of retained resistivity) and Fe14 (~10% of extra-recovery) but no SRO signs are observed in Fe10 (resistivity recovers its original value). Beyond 400 K the resistivity does not evolve with further annealing in Fe5, but it starts to decrease in Fe10 and probably keeps decreasing in the case of Fe14. The final recovery values of the normalized resistivity, 25%, -7% and -20% respectively, are understood as direct consequence of SRO effects, where the residual resistivity values do not fully recover to their original values but increase or decrease enhanced by Cr redistribution induced by the migrating defects. Nevertheless it seems that the Cr re-arrangements are not occurring in the same temperature ranges for every alloy.

Sample	RR at 400 K	RR at ~450 K	Observations
Fe	97% (±5)		Average values of all Fe samples. Full recovery at 400 K
Fe5	74%	75%	Ordering of Cr has prevented full recovery at 400 K
Fe10	99%	107%	Full recovery at 400 K. SRO signs above 400 K
Fe14	109% (±8)	120%	Clustering of Cr brings RR to negative beneath 400 K
Fe5(Pre)	90%	93.5%	Ordering effects are reduced. Full recovery at 490 K
Fe10(Pre)	109%	118%	Stronger SRO signs than in Fe10
Fe14(Pre)	100%	109%	Full recovery at 400 K. SRO signs apparently erased

Table 5-7: Per-centage of resistivity recovery by the end of the annealing.

As a consequence of apparent signs of SRO detected in Fe-5%Cr and Fe-14%Cr samples. We came up with the improved RR method which has been described in detail in section 2.5. This improved method which is an important outcome of this work, has been tested in our Fe-Cr alloys and the results are presented and discussed below.

5.5.2. The effect of improved RR method

Bearing in mind that the initial proposal of this research, which was to provide reliable experimental validation data, as well as shed light on the unclear interpretation of concentrated Fe-Cr stages under proton irradiation, and bearing in mind the further hypothesis that the RR peaks will be distorted by SRO re-arrangements which has come along the development of the present work, it results very difficult to make a clear discussion of the experimental data as many known unknowns entangle. A separate analysis on the results found for every Cr concentration is going to be provided. Concerning SRO behavior, it will be explained how the presented hypothesis of SRO effects theory fits very well with the experimental results in Fe5%Cr, showing that for this measurement the new method indeed works and is able to erase the SRO. Further analysis of Fe-14%Cr and Fe-10%Cr will bring about the unknown unknowns. Finally the specific approach introduced by Nikolaev and presented in chapter 4, will be applied to our experimental measurements in order to identify SRO signs which cannot be directly observed by the RR curves and rates. Finally, some comparisons of the spectra with electron irradiated similar samples found and previously analyzed in the literature will be included. Thus some effects of the dose, proton irradiation, and Cr effects could come out.

Pre-Irr Step

In view of the apparent strong effects of SRO Cr redistribution on the classical RR results, especially in Fe5 and Fe14, a new method had to be developed and then applied to obtain new RR measurements to “erase” the SRO marks. The method has been explained in detail in section 2.5, but the motivation is clearer now. Samples Fe5(Pre), Fe10(Pre) and Fe14(Pre) underwent a pre-Irradiation (pre-Irr) at 400 K up to a fluence which was considered to be enough to reach equilibrium state in SRO (based on some external results presented at EFDA meetings but still unpublished). The temperature of 400 K was chosen because it represents almost the end of the RR experiment but also, as has been shown, and because is the temperature where resistivity (i.e. defects) is fully recovered in Fe. The proton fluence was doubled and tripled as the C_{Cr} went from 5 to 10 and to 14% Cr. This has also been observed to be necessary as the kinetics is slower at higher Cr contents.

The experimental observations recorded after pre-Irr at 400 K are reported in Fig. 5.20, the dotted lines denote the qualitative saturation behavior that we are expecting when performing the pre-Irr. The residual resistivity increased in the case of Fe5(Pre) because of the Cr ordering and decreased in the case of Fe14(Pre) because the short-range clustering, both generated by irradiation (similar to ion mixing process). Change of SRO with ion irradiation was also observed by Dubiel [111]. The decrease of residual resistivity of sample Fe10(Pre) is also a sign of clustering. As 10% C_{Cr} has been reported to be close to the change of sing in SRO, the change expected in resistivity was small or close to zero,

but the recorded decrease is definitely not close to zero. The values of the pre-Irr resistivity increments are given in Table 5-2.

The free migration of defects (V, V_2, IAs, MIAs and di-SIAs, at least) that occur at 400 K pre-Irr step do change the residual resistivity of studied specimens. In the case of 5% Cr, the resistivity increases 255 nΩ·cm (as a sign of ordering, i.e. Cr tends to "spread" in the lattice by effect of proton irradiation). On the contrary, in the case of 10 and 14 % Cr alloys, the residual resistivity diminishes by -224 and -368 nΩ·cm respectively (as a sing of clustering). This result coincides with the expected resistivity behavior for resistivity changes as a function of C_{Cr} [17,18] and has been confirmed by Mössbauer measurements in the case of Fe-5%Cr, which are presented below. The exhibited changes in resistivity represent a first prove of the validity of the presented improved RR method.

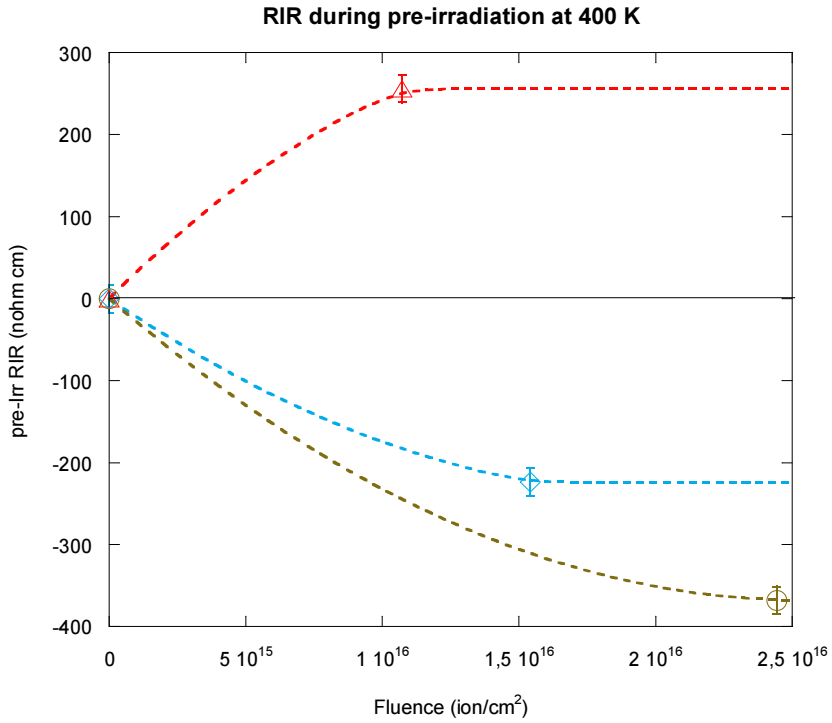

Fig. 5.20: Changes in resistivity after 400K pre-Irradiation. Experimental values of Fe5(Pre), Fe10(Pre) and Fe14(Pre) are shown with their error bars. Dotted lines represent qualitatively the expected tendency (from other experiments).

RR after pre-Ir

Subsequent to pre-Irr step, samples Fe5(Pre), Fe10(Pre) and Fe14(Pre) where irradiated at 50 K in similar conditions than Fe5, Fe10 and Fe14 up to a similar doses (see Table 5-2). The results are presented comparing first the results of specimens with the same C_{Cr}. Finally a comparison as a function of Cr content analogous to the one did before is described and depicted.

Fig. 5.21 show comparative data of the RR curves respectively of samples **Fe5** and **Fe5(Pre)**. The effects of ordering can be appreciated in Fe5 because, in some temperature ranges, ρ is increasing instead of decreasing, as one would expect due to the recombination of defects, and the recovery of the resistivity is prevented up to 26%. The figure clearly evidences that at the end of the thermal treatment, the residual resistivity has almost recovered in Fe5(Pre), which is a prove of ordering effects suppression. The recovery in Fe5(Pre) is not total but definitely much larger (90%) than that of Fe5 (74%) by 400 K, and it is total at further temperatures (close to 480K). In the figure it is additionally plotted the difference between both experimental RR curves and therefore evidences the SRO effects on the conventional RR curve of a concentrated alloy. The RR curves clearly separate from 120 K on. At 400 K it was expected to find a total recovery of original value of residual resistivity after pre-Irr.

Concerning the RR differential recovery of Fe and Fe5(Pre), whose comparative is depicted in Fig. 5.22, the close-pair and correlated recombination coincide in both measurements, which is just what is expected., as in this very short recombination movements, no Cr relocation is expected. At stage I_E range temperatures, the recovery increases, some recovery between 130-155 K still appears but the peak found at 175 K in Fe5 is shifted to lower temperatures in Fe5(Pre): 168 K. This is indicating that in Fe5 the re-arrangements of Cr complexes where inducing Cr ordering which increased the $\Delta\rho_S$ term. The continuum recovery stage found at Stage III also increases its amplitude, it starts to increase from ~192 K and it ends at ~240 K. Stage III recovery does not go towards negative values in Fe5(Pre). As free migration of Vs and IAs is expected in Stage III, such stage increase is a clear proof that the free migration of defects in Fe5 induced Cr ordering and that in Fe5(Pre), as the Cr ordering has been maximized with the pre-Irr, no extra-ordering is being produced along RR. And therefore the amplitude of Stage III observed in Fe5(Pre) spectrum is purely due to defect recovery. Some discrete continuum recovery is also found between 285 and 400 K, at higher temperatures the RR derivative seem to go towards positive values indicating further recovery, just the contrary that in Fe5.

In order to support the arguments relative to the change Cr distribution by both pre-Irr and migration of defects along isochronal annealing we performed Mössbauer analysis on 30μm thick samples (see Table 5-2) of the same material and prepared following the same irradiation conditions as described before: three Mössbauer spectrum have been recorded of sample Fe-5%Cr material after the following treatments: (O) “as prepared”, (I) after 400 K “pre-Irr” and (II) after 400 K “pre-Irr + 50 K irradiation + 400K annealing”. The spectra were recorded at room temperature using a conventional constant acceleration spectrometer and a ^{57}Co(Rh) source. The velocity scale was calibrated using a 6 μm α-Fe foil and the isomer shifts were referred to the centroid of the spectrum of α-Fe at room temperature. The spectra of the three samples (Fig. 5.23) were fitted considering three magnetic sextets having the following Mössbauer parameters: δ_1=0.005 mms^{-1}, $2\varepsilon_1$=0.00 mms^{-1}, H_1=33.1 T; δ_2=-0.010 mms^{-1}, $2\varepsilon_2$=0.00 mms^{-1}, H_2=31.0 T; δ_3=-0.40 mms^{-1}, $2\varepsilon_3$=-0.02 mms^{-1}, H_3=28.2 T. The data fit well with previous interpretations [112] in which the sextet with the largest hyperfine magnetic field, H, corresponds to Fe atoms having no Cr atoms as nearest neighbors (NN), the sextet with intermediate H corresponds to Fe atoms having 1 Cr atom in the 1NN shell and no Cr atoms in the 2NN shell and the sextet with the

smaller H represents the situation of Fe atoms with 1 Cr atom in the 1NN shell and 1Cr atom in the 2NN shell.

Inspection of Fig. 5.23 shows an increase of the relative area of the intermediate sextet: 45.6%, 50.8% and 52.1% for the “as received”, “pre-Irr” and “pre-Irr + low-T-Irr + 400K annealing” samples, respectively. Such increase indicates that the irradiation conditions promote the migration of Cr from the 2NN to the 1NN (the relative areas of the corresponding H_3 sextet decrease accordingly). This means that Cr ions tend to be more separated, i.e., SRO evolves to more ordered states (as previously defined). It is clear from the data that the major change in the spectra is brought about by the pre-irradiation treatment and that the subsequent low temperature irradiation treatment has only a significantly smaller influence in the final configuration of the neighboring Cr atoms. This is in good agreement with the rest of observations of this experiment supporting that pre-Irradiation almost saturates the local rearrangement of Cr atoms allowing the sample to reach the SRO equilibrium value at 400 K.

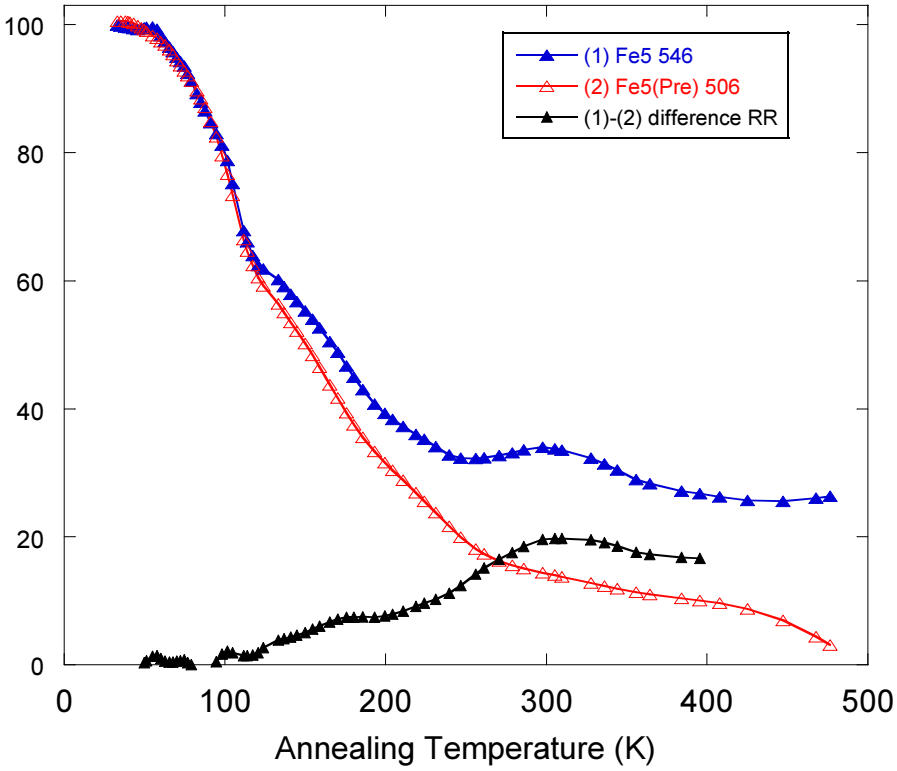

Fig. 5.21: Fe-5%Cr samples irradiated with 5 MeV protons. Comparison of experimental RR curves with and without SRO effects after pre-irradiation at 400 K.

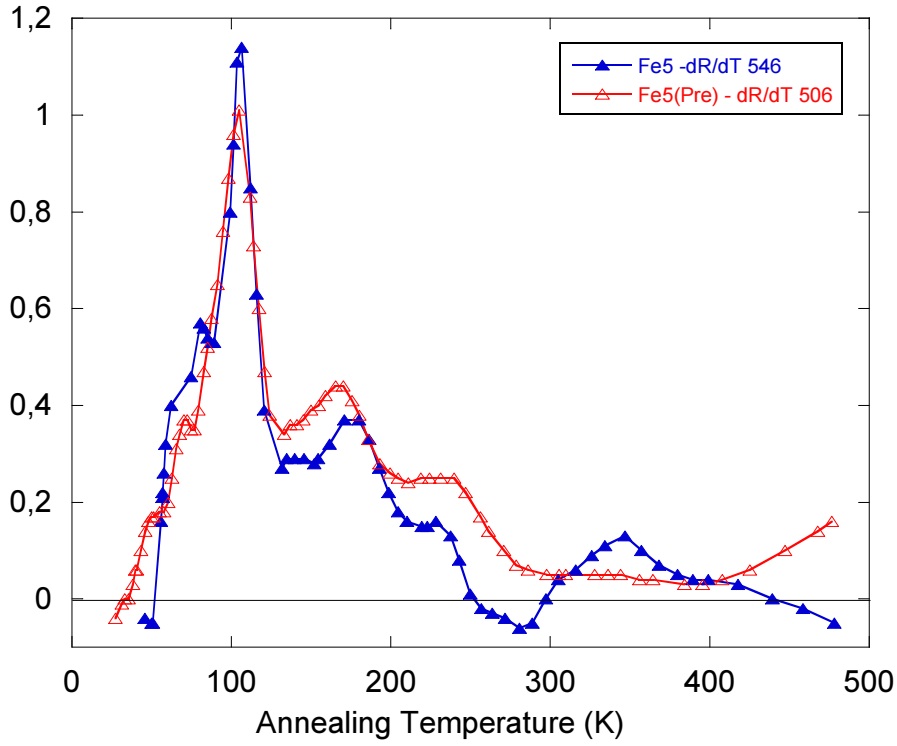

Fig. 5.22: Differential RR curves of classic RR and pre-Irr+classic Fe-5%Cr samples. Marked differences can be found above 120 K.

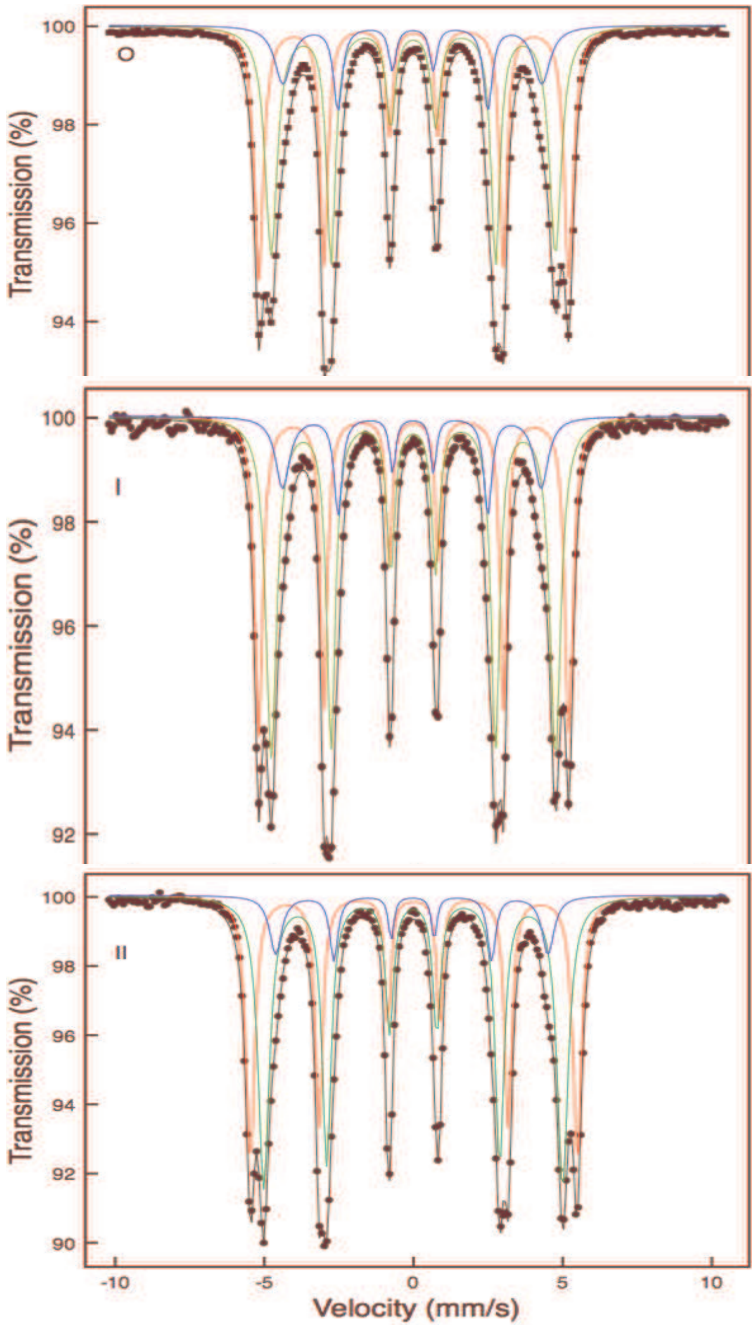

Fig. 5.23: Mossbauer spectra of Fe-5%Cr 35 µm sample. Red sextet refers to pure Fe phase, green corresponds to Fe with 1 Cr in the 1NN, and blue corresponds to Fe having 1 Cr in 1NN and 1Cr in 2NN. (O) is the spectrum of "as-received" sample, (I) is the sample after 400K pre-Irr up to a dose of 240·10^{-6} dpa and (II) corresponds to the sample after pre-Irr (240·10^{-6} dpa), low-T-Irr (100·10-6 dpa) and annealing at 400K. All Mössbauer measurements were taken at room temperature.

Fig. 5.24 depicts the comparison between experimental data of **Fe14** and **Fe14(Pre)**. As it has been explained, the available data of Fe14 is limited, and no reasonable derivative can be obtained from the reliable RR data. Hence, although comparison of differential data is not available, some information can be extracted from comparison of RR curves. As it is indicated by the RR value of Fe14 closer to 400 K, which is around -9% (some value

between 0 and -20%), and by the reduction of residual resistivity of Fe14(Pre) after the pre-Irr, the sign of SRO is positive (according to definition in section 2.5.), i.e. Cr rearrangements tend to cluster. Looking at compared RR curves apparently no important change is observed along the isochronal annealing up to 365 K. However, data registered at higher temperatures indicate that the RR in Fe14(Pre) at 400 K is barely total (100% indicated in Table 5-7) whereas it reaches a negative value (109%) in Fe14. Again it seems that SRO effects in the RR curve have been removed as in the case of Fe5%Cr. The choice of using higher pre-Irr dose has revealed better saturation of SRO state at 400 K leading to a full recovery by 400K. Beyond 400 K, both samples show further recovery toward lower RR values. Negative values at the end of the recovery curve have been reported in high C_{Cr} (13-16%) Fe-Cr alloys [27,29,85]. Such phenomenon have never been clearly explained in the literature but have been typically attributed to SRO effects [29] even in the case of dilute alloys [24]. In our case, at 400 K as the defects are apparently all recovered, the creation and diffusion of thermal vacancies at high temperature annealing steps (> 400 K) could be responsible of new SRO re-arrangements in the high Cr concentration samples. The temperature of negative recovery in Fe-13%Cr changed from ~250 K in electron irradiated, up to ~500 K in proton irradiated [85], and it has been observed to appear in samples of pure Fe and C-doped Fe (+15-67 C appm) only at very low doses (RIR ~6-30 nΩ·cm) and at temperatures from 400 K. Such phenomena are still not well understood as it seems that they are not only due to SRO changes but also to a dose effect.

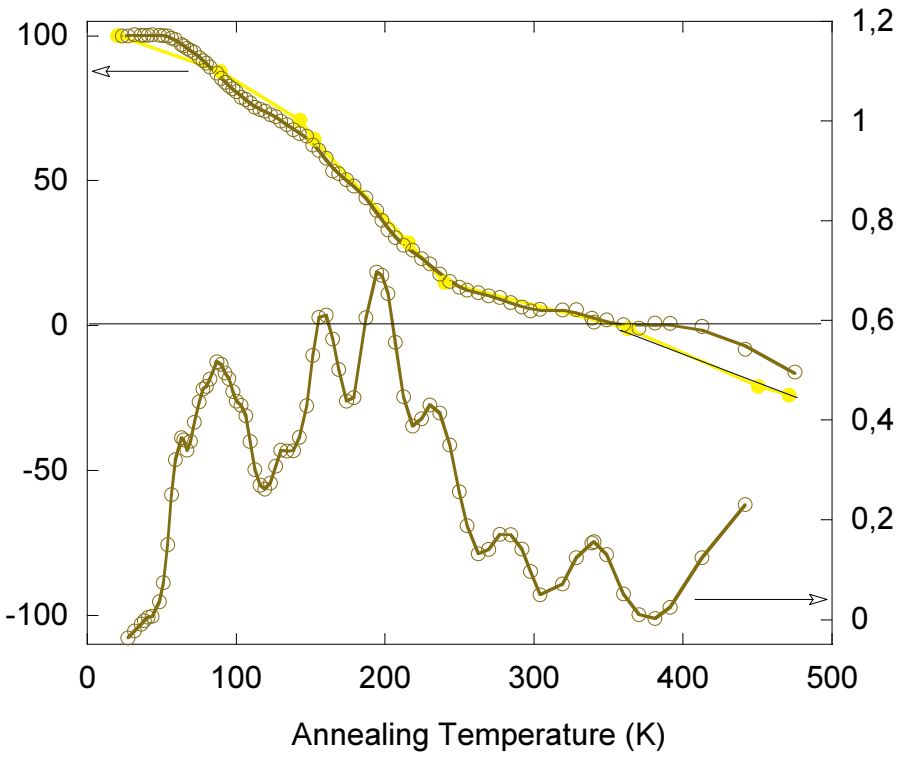

Fig. 5.24: RR isochronal recovery and recovery spectra of Fe14 and Fe14(Pre) alloys after 5 MeV proton irradiation at 50K.

Finally the data concerning **10% C_{Cr}** is presented. The comparative of the RR curves and the difference RR are shown in Fig. 5.25 and Fig. 5.26. It has to be pointed out that because of a failure of the power supply of the accelerator beam line, the experimental points of Fe10(Pre) were missed between 60 and 113 K. One experimental point could be recorded at 85 K after the black-out and the consequent loss of vacuum in the chamber. But the RR didn't start to behave normally up to 113K. The recovery up to 120 K approximately coincide as in the case of Fe5 and Fe5(Pre), then again from 120 K the differences become more intense. These results are the most striking given that the expected behavior is not found. First, it has to be noticed that full recovery was achieved at 400 K in Fe10. This is an indication that the arrangement of Cr atoms in Fe10 sample was at his equilibrium state prior to the RR experiment, and that after the isochronal annealing and defect recovery the migration of defect did not induce changes in the SRO state. However, the value of residual resistivity experienced a decrease enhance by the migration and recombination of defects during the pre-Irr at 400 K (see Table 5-2 and Fig. 5.20). This is sign of clustering. Then, after low-temperature irradiation and isochronal annealing the resistivity not only did not experience a full recovery, but also its value decreased up to -9%. This is a sign of further clustering, indicating that the specimen not only didn't reach the equilibrium SRO state in pre-Irr but also that the processes occurring during isochronal annealing enhanced further clustering. In other words, the experimental evidence indicates that the clustering induced by pre-Irr, enhances further clustering along the isochronal annealing instead of suppressing this effect. Nevertheless, this result (unclear effect of the pre-Irr on SRO) is not so surprising for the 10% Cr alloy. From the literature it is known that whereas 5%Cr has a strong tendency to ordering and 15%Cr, in the case of 10%Cr there is no clear agreement, as its behavior is mostly undefined (see Appendix B).

Concerning the differential recovery peaks, depicted in Fig. 5.26, it is observed overall increase of intensity in the regions including the peaks 153, 175 and 205 K. In the case of peak at 205 the increase in the recovery rate is well noticeable. The shoulder at 240 K does not appear now, indicating that this stage either has been reduced or removed. There is RR rate interchange observed between 290 and 430 K. The % of recovery in this temperature range is of the same amount (~20%) in both Fe10 and Fe10(Pre) samples.

Finally, the comparison of the three pre-Irr samples is provided in Fig. 5.27and with our Fe samples in Fig. 5-28. Based on our hypothesis these should be the curves where SRO have been removed or highly minimized. Nevertheless, it cannot be assured for Fe-10%Cr sample given the unexpected results.

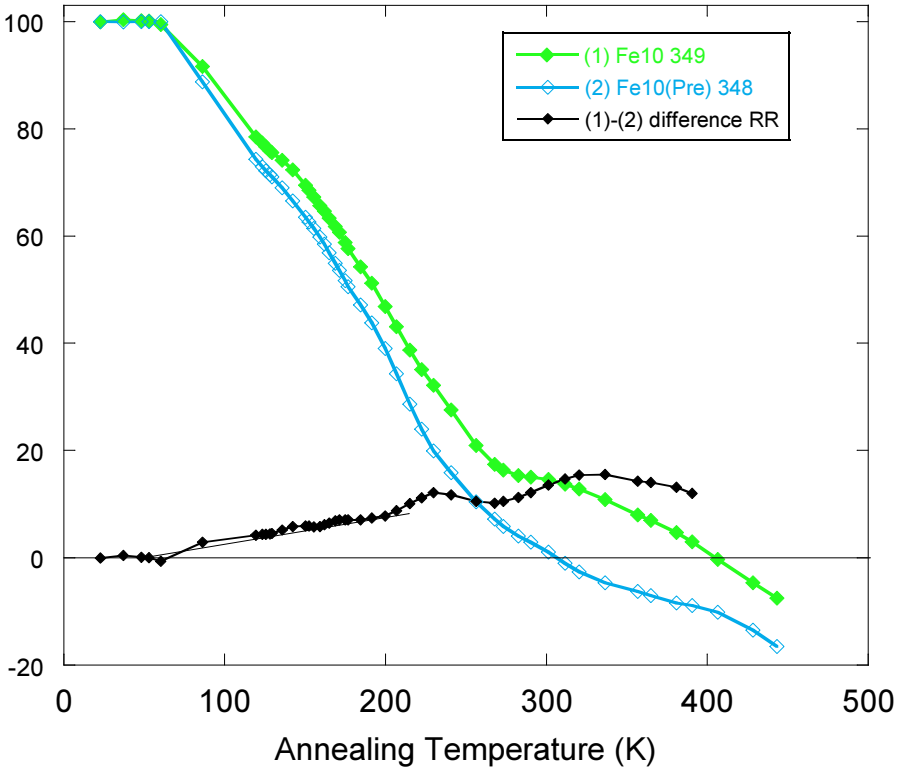

Fig. 5.25: Fe-10%Cr samples irradiated with 5 MeV protons. Comparison of experimental RR curves with and without SRO effects after pre-irradiation at 400 K.

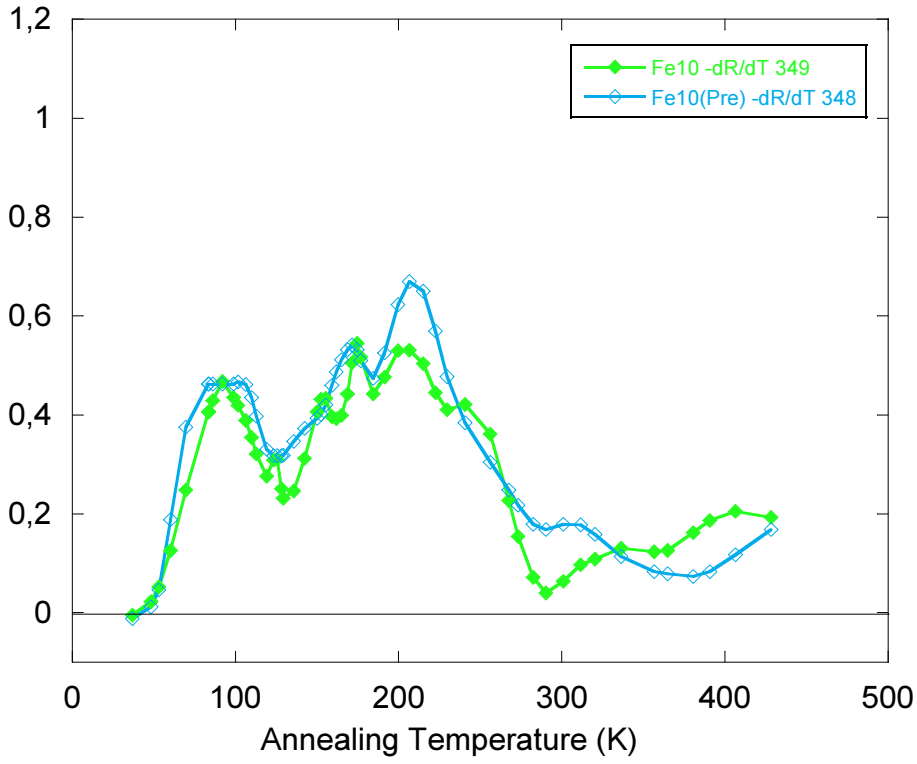

Fig. 5.26: Differential RR curves of classic RR and pre-Irr+classic Fe-10%Cr samples.

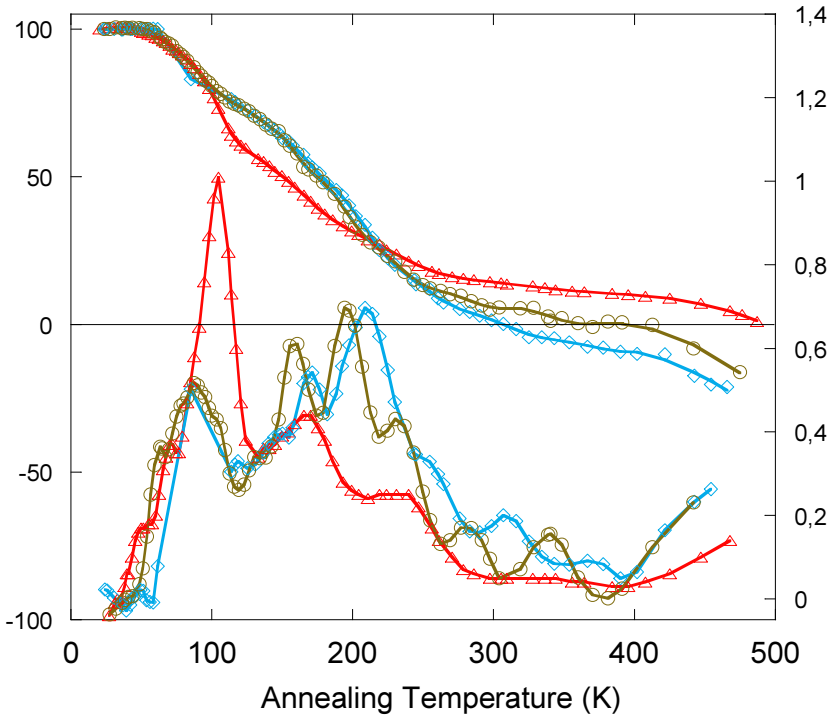

Fig. 5.27: RR isochronal recovery and recovery spectra of Fe5(Pre), Fe10 Fe5(Pre) and Fe14 Fe5(Pre) alloys after 5 MeV proton irradiation at 50K. In sample Fe10 data is missing between 60 and 85 K, although lacking of detail, apparently the Stage I recovery is well observed.

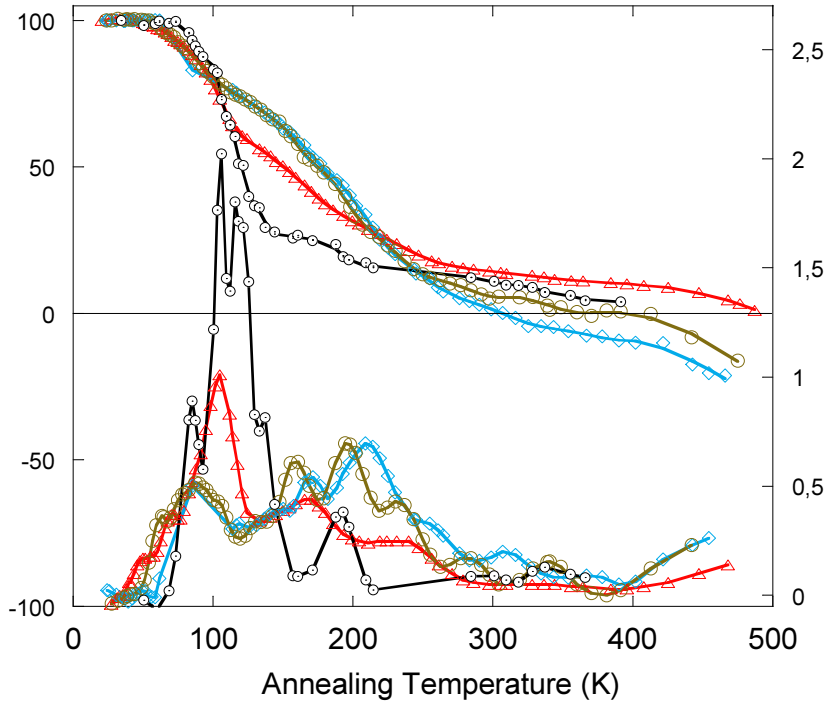

Fig. 5-28: RR results of figure 5-8 compared with RR data of Fe sample.

5.5.3. Final discussion

The implementation of the improved RR method has shown to produce wide changes in the RR curves and RR spectra. Such changes have not been observed previously in electron irradiations. Indeed the obtained results after applying our improved RR method result quite striking given that not in all the cases they show the expected behavior. In the first place, let's state the clear main conclusions that have been revealed by the presented results:

(i) An interesting result is that the RIRs induced by low-temperature irradiations have same slope (RCR) for the same C_{Cr} in samples with and without pre-Irr, therefore, the low-T-Irr effects are independent of the previous irradiation and hence of the SRO state.

(ii) SRO changes are clearly evidenced in the pre-Irr step, 5%Cr (negative SRO), and 10% and 14%Cr (positive). These results agree with the accepted theoretical models for equilibrium SRO in Fe-Cr alloys that state that, near room temperature [113], 5% C_{Cr} tends to be ordered and at 10% and 15%, it tends to clustering. Indeed 10% C_{Cr} is close to the inversion of sign so SRO parameters, and therefore it is the concentration which is less understood. A quick overview of recent results from experimental and theoretical works is given in Appendix B.

In summary, the behavior of RR curve of Fe5(Pre) exhibits a clear decrease of re-ordering effects and, as a consequence, almost total recovery of the resistivity is reached by the end of the annealing, confirming the initial idea of the new method. This is also confirmed by Mössbauer results. The behavior of Fe14(Pre) also exhibits a decrease of clustering up to 400 K given that the recovery do not reaches negative values up to this temperature. Although apparently the differences between Fe14 and Fe14(Pre) RR curves are very small up to 365 K, it will be shown in further analysis that such differences are not that small and indeed comparable to the differences found in Fe-5%Cr. Finally the sample Fe10(Pre) shows an unexpected tendency: the RR curve exhibits signs of clustering after pre-Irr as the RR curve reaches negative values prior to 400 K, indicating no only the effect of defect annihilation but also re-arrangements of Cr induced by defect migration which were expected to be eliminated or highly reduced. Because of (i) the possibility that the low-T-Irr would "undo" the effects of pre-Irr is eliminated. Thus the observed effects are consequence of the processes occurring exclusively during the isochronal annealing.

Difference RR approach.

It could be also possible to apply Nikolaev's DRR analysis to our curves. According to his analysis, in our difference RR curves we should not find any differences due to differences in dose, i.e. differences induced by SFM cannot appear as the number of defects produced is approximately the same. Thus only changes should be due to differences in SRO and

could be revealed. The signs of SRO, are indicated by a change of the slope from a monotonic background. In the case of "Nikolaev Fe4" (explained in section 4.3), the DRR curves are obtained by subtracting the low-dose sample (L, which has bigger relative contribution of SRO effects) from the high-dose sample (H, which exhibits relative smaller SRO effects). In the present samples, the subtraction is inversed, given that pre-Irr RR curves are subtracted from classical RR curves, and thus samples with the supposed smaller SRO effects are subtracted from curves exhibiting stronger SRO effects. Hence, in the present DRR results, the appearance of a positive slope is sign of ordering and a negative one is a symptom of Cr clustering.

In the Fig. 5.29 the difference RR curves from the subtraction of pre-Irr RR curves to classic RR results have been depicted. In the **Fe-5%Cr** difference RR curve an inflection point is observed at 195 K which is a sign of ordering. Considering that this is the temperature of SFM of vacancies in Fe-5%Cr, it is initially generated by these vacancies. This mechanism has been proposed in section 2.5 (Fig. 2-14) as an effective change in SRO has been identified in the literature by thermal vacancy migration, for instance in Ni-Cr alloys [65]. It is also observed that ordering is still increasing up to a maximum near 300 K, indicating that other long-range migrating defects can also facilitate Cr reordering (or vacancies de-trapped from more complex defects). Above this temperature and after a small plateau, there is change at 320 K and now some clustering could be occurring (negative slope) due to liberation of C-traps in Fe5 (which would cluster with Cr [114]). This is possible given that in the presented RR rates (Fig. 5.18), we have identified a peak corresponding to C contamination. Therefore, the initial hypothesis concerning our improved RR method is quite correct, and it can be seen that the predicted large change on SRO due to LRM of vacancies can be very well observed in the Fe-5%Cr.

Looking at the **Fe-10%Cr** difference RR curve, the inflection point also found at 195 K can be interpreted either as a sign of extra-clustering in Fe10(Pre), or ordering in Fe10, but this possibility would imply a positive SRO parameter in the as-received specimens. Then a second inflection point at ~230 K indicates clustering prevention in Fe10(Pre) (or clustering in Fe10 if Fe10(Pre) only shows defect recombination). Again, from ~267 K the slope of difference RR changes again indicating either extra-clustering in Fe10(Pre) or ordering in Fe10. Finally there are signs of clustering (higher in Fe10) from 330 K whose origin could also rely on C-de-trapping effects, as in the case of Fe-5%Cr. In this case the method does not seem to be very useful because Fe-10%Cr shows too many changes in SRO direction that cannot be easily explained with only these 2 curves. Further measurements would be needed. It is worth mentioning that concentrations 9-10% are especially complicated because equilibrium SRO parameter is very close to zero and its behavior is not very clear in literature [17,18,96,113,115] (see Appendix B).

Both materials Fe-5%Cr and Fe10%Cr, prior to the plain region (~170 - 200 K, close-vacancy recombination), exhibit a positive slope in difference RR curves which is symptom of ordering (to be discussed in the next paragraph). Concerning **Fe-14%Cr**, only a very rough difference RR curve can be obtained. It seems that the increase tendency up to ~150 K is also reproduced in this material although high experimental error makes the curve not highly reliable. Then the DRR curve shows an evident decrement along the Stage III

which is a sign of clustering that would be in agreement with the expected trend of 14%, although the absolute value is lower than expected (comparing with the change observed during pre-Irr at 400 K).

The only obscure point is what happens during Stages I and up to ~150K, where it was not expected that close-pair recombination or Cr complexes re-arrangements would change significantly SRO value. This would indicate that mixed interstitials recombine in such a way that the Cr ion has some "freedom" either staying in the interstitial position or going to the vacancy, depending on the local environment. With multiple recombination events, a small local re-arrangement is then possible. This model has never been considered in literature. Another explanation would be that such increase of recovery observed in the initial stages of all the pre-Irr curves is that it is indeed an effect of the pre-Irr. This step can create few defect clusters in the samples; therefore, an small extra recovery due to Cr complexes is possible.

The application of the new proposed method has revealed that SRO changes occur and do change intensely the RR curve in Fe-5%Cr, Fe-10%Cr and Fe-14%Cr. However, the unexpected behavior of Fe-10%Cr indicates that the SRO effects are still not well understood. The changes in RR and RR rates are not only related to SFM as we initially believed.

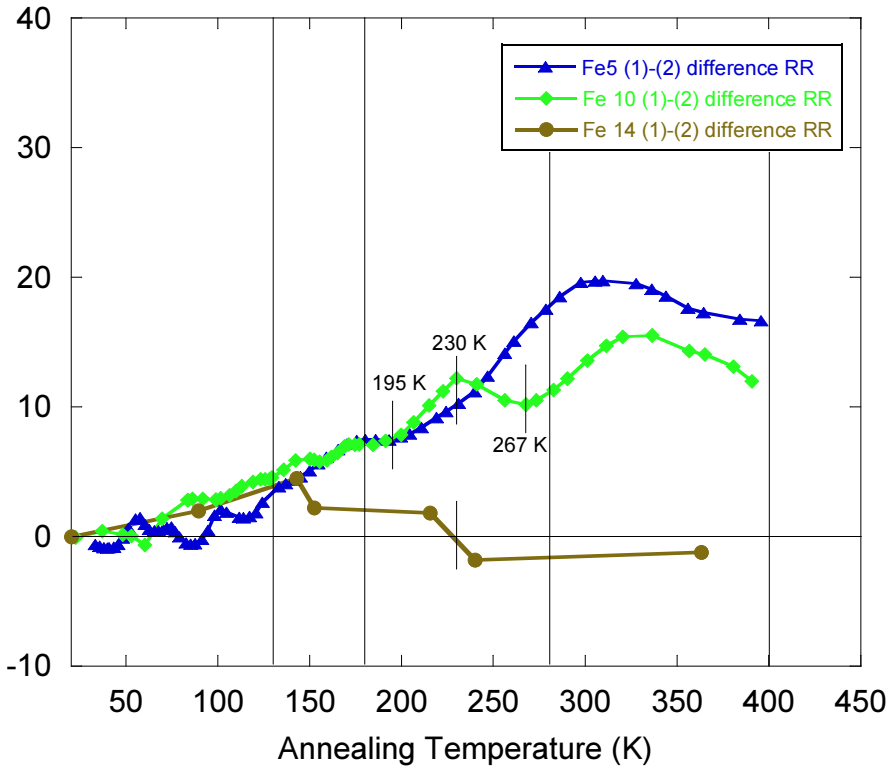

Fig. 5.29: DRR curves measured for Fe-5%Cr, Fe-10%Cr and Fe-14%Cr.

5.5.4. Comparisons with the literature

On the basis of the above presented Stages re-definition, we have made a quantitative comparison of the amount of recovery reached in every Stage, for the different C_{Cr} and comparing with experimental data available. Fig. 5.30 shows the numerical results of Nikolaev's samples irradiated with electrons up to RIR values of the same order of magnitude than ours.

Overall, it can be said that proton irradiations reduce the intensity of Stages I and II whereas it increases Stages III + IV and V. In the stage III + IV of sample "Nikolaev 13%(C+N)" the abnormal high amplitude is due to high C contamination in the sample (10000 appm) [85]. It must be said that direct comparison of our experimental data with the data of Nikolaev is not ideal given that the C_{Cr} are different in every case, especially when the C_{Cr} are around 10%. Direct comparisons are not very accurate in the case of Benkaddour´s data either, given that its RIR values are one order of magnitude higher than ours. But even with these considerations, the above mentioned conclusions can be observed.

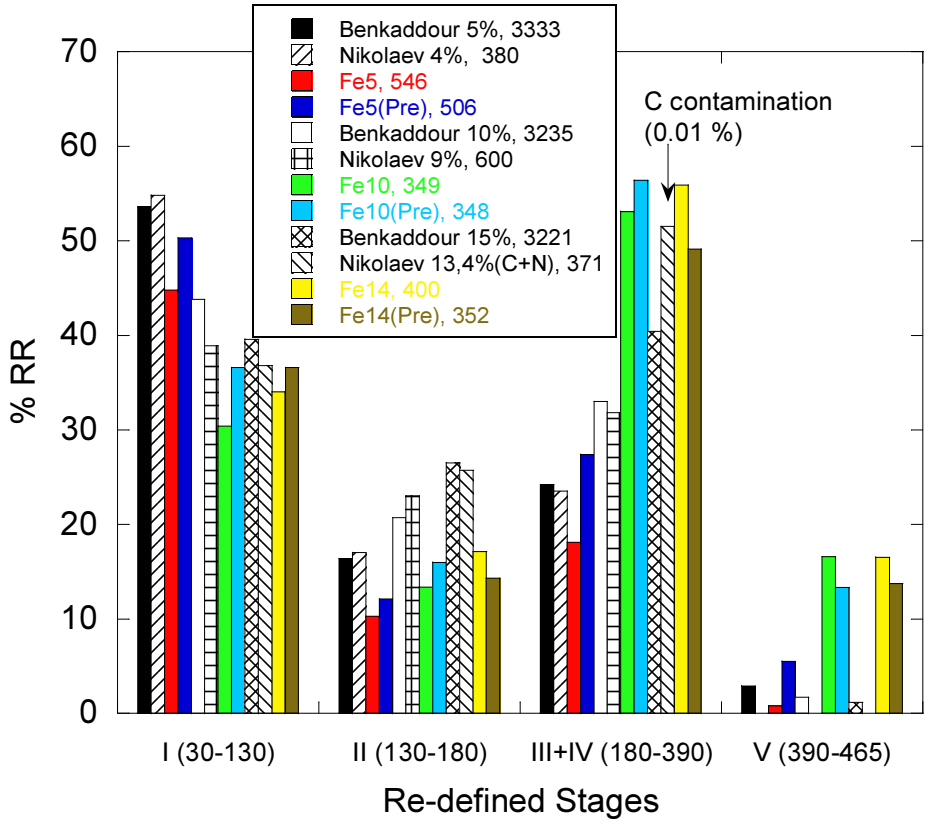

Fig. 5.30: Comparative amplitude of RR re-defined Stages in present Fe-Cr alloys and data from the literature [29,32].

Big impact has been observed on RR spectra peaks by the application of the new RR method proposed in this thesis, now we are presenting graphical comparison of the RR rates from the literature made under electron irradiations for the three families of Cr concentrations: ~5% (Fig. 5.31), ~10% (Fig. 5.32) and ~14% (Fig. 5.33). Regarding at the

curves it is easy to understand that no clear tendencies are observed either as a function of C_{Cr} or particle irradiations. The broad amount of different experimental variables (sample preparation method, C_{Cr}, impurity content, irradiating particle, irradiating temperature, dose, annealing conditions, temperature resolution) sensibly affect the appearance of the spectrum. Only a clear decrease of Stage I in proton irradiated specimens is manifested.

Finally an analogous comparison as the one provided with our results of the impact of C_{Cr} with respect to pure Fe (Fig. 5.34 and Fig. 5.35) is provided for the interest of the reader. In Fig. 5.34 it has been plotted Takaki's pure Fe against Benkaddour's data. Similarly in Fig. 5.35 the Pure Fe of Takaki is plotted against a compilation of curves from Nikolaev's works.

Such difficulty of obtaining experimental data comparable to other author's as well as the high temporal, technical and economical costs and the difficulty of interpreting the nature of the RR stages calls into question the viability of this technique as a useful tool for experimental validation, at least until measurements are well understood.

On the other hand is the only technique which is able to monitor the interstitial atoms. Nevertheless the big fundamental physics phenomena which are still not very well understood makes very difficult to use this technique with success in the rapid developing field of fusion technology. Perhaps its application is more suitable for changes in Fe-Cr alloys at high temperatures.

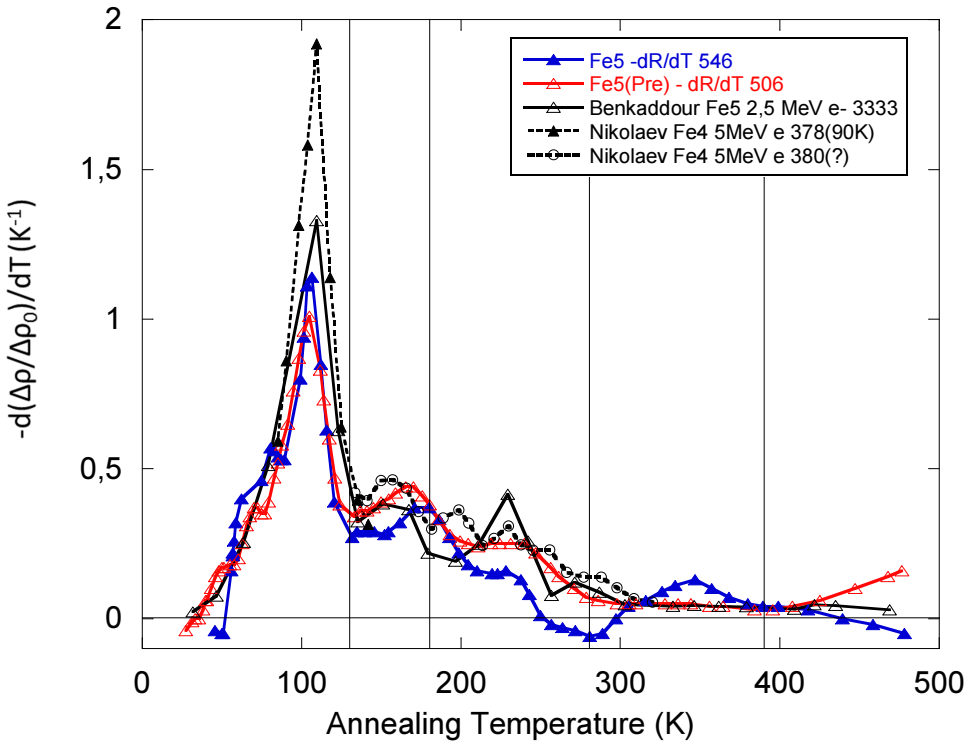

Fig. 5.31: Comparative of RR spectra on Fe-4%Cr and Fe-5%Cr alloys irradiated with protons or electrons. Results from present work, [27], [84] and [32].

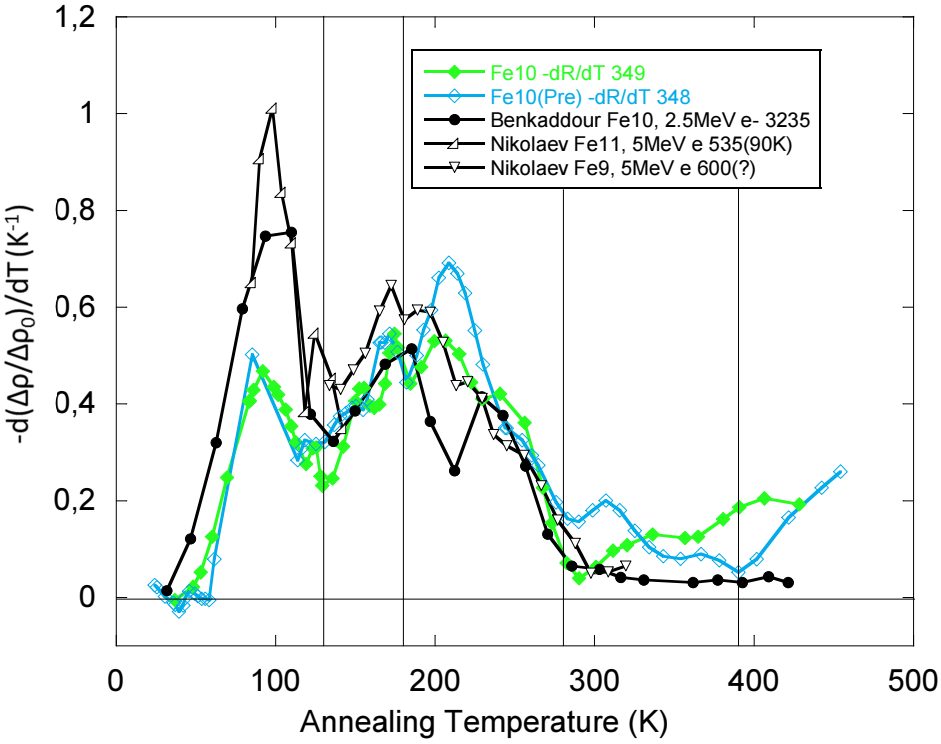

Fig. 5.32: Comparative of RR spectra on Fe-9%Cr, Fe-10%Cr and Fe-11%Cr alloys irradiated with protons or electrons. Results from present work, [27], [84] and [32].

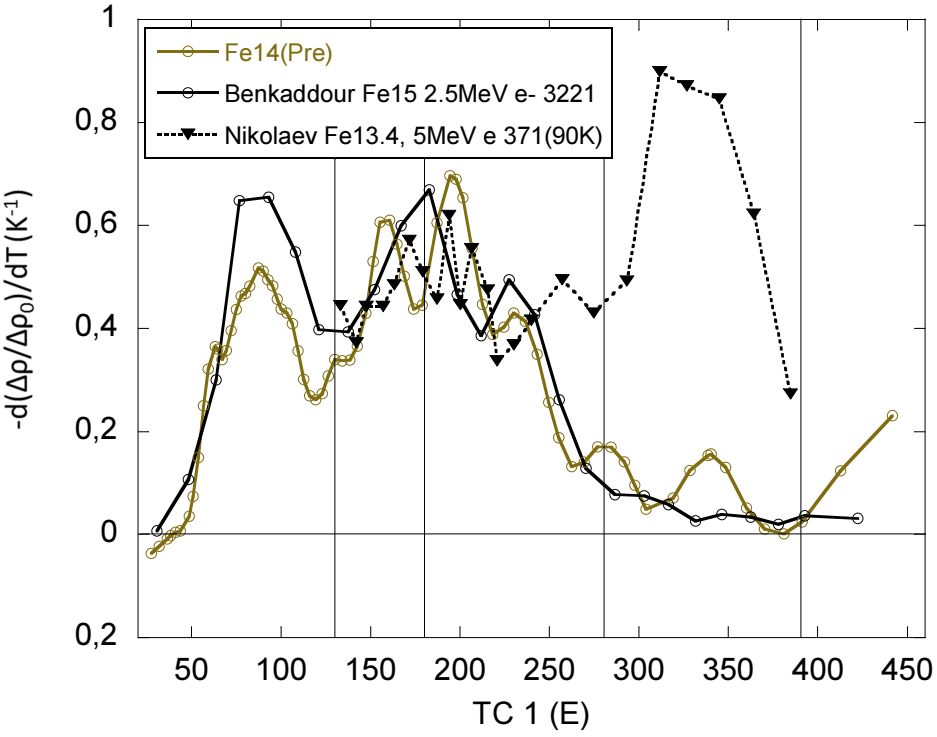

Fig. 5.33: Comparative of RR spectra on Fe-14%Cr, Fe-15%Cr and Fe-16%Cr alloys irradiated with protons or electrons. Results from present work, [27], [84] and [32]

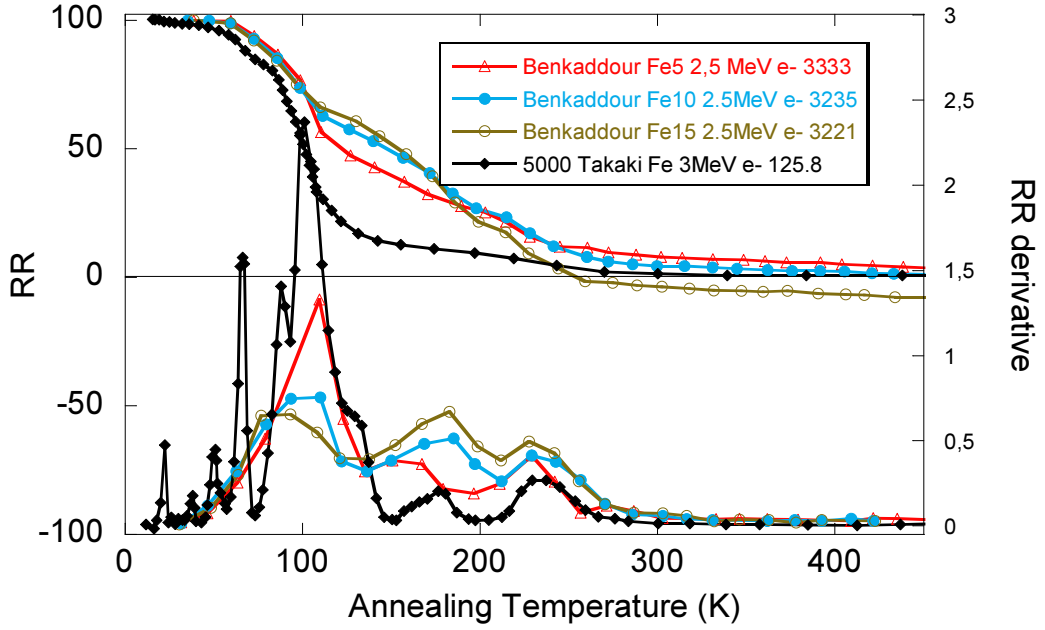

Fig. 5.34: Comparative of RR data of Fe [24], Fe-5%Cr, Fe-10%Cr and Fe-15%Cr [27] samples irradiated with electrons.

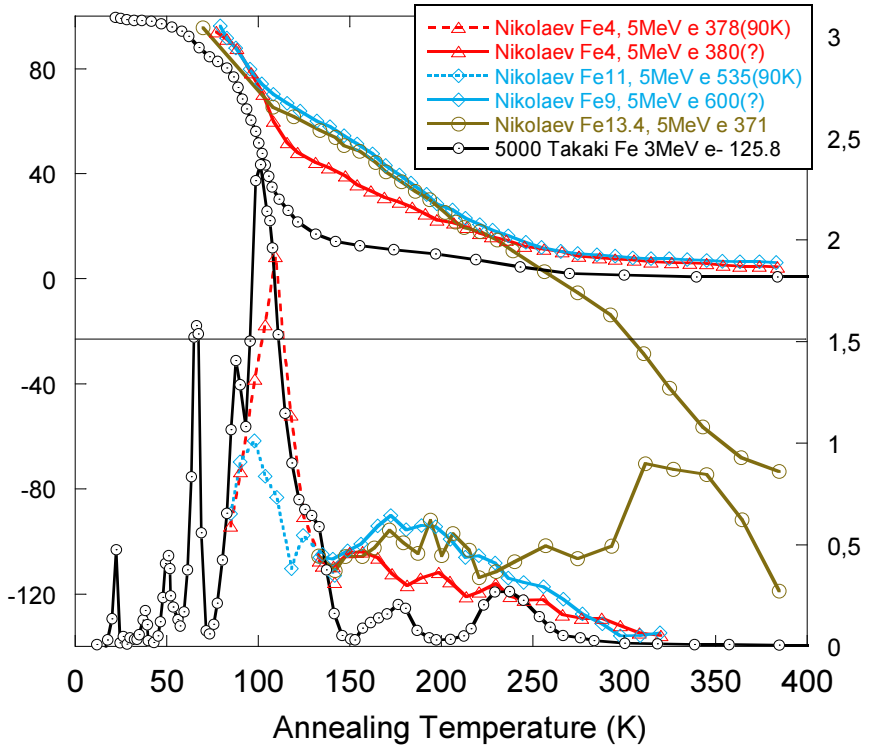

Fig. 5.35: Comparative of RR data of Fe [24], Fe-4%Cr, Fe-9%Cr, Fe-11%Cr and Fe-13.4%Cr [29,32,84] samples irradiated with electrons.

Chapter 6. Conclusions

6.1. Summary

To start with, a deep review on the basic aspects of the binary non-simple alloys has been provided, showing the explicit relationship of the resistivity with the SRO parameters and the effects of ferromagnetism in the resistivity of ferromagnetic alloys whose behavior is described by the two-current model. Additionally the effects of light particle irradiation in the simplest case (low dose) have been described. Such review is fundamental to understand the most important experimental works on RR which have also been described in detail.

Further description of the mechanisms of diffusion of irradiation defects in metals have allowed to explain the fundaments on which the experimental technique of RR is based. As a result of the full comprehension of the experimental principles and resistivity dependencies it has been possible not only to run RR experiments but also to modify the methodology in order to improve it.

The main objective of the work which was the development, testing and commissioning of the experimental technique has been achieved successfully. Therefore reliable RR curves have been obtained on samples of pure Fe, Fe-5%Cr, Fe-10%Cr and Fe-14%Cr, which have been measured under classical RR technique as well as under the new proposed improved RR method. Full details on the sample preparation method, the experimental set-up and experimental conditions have been provided. Additionally to support the validity of the new experimental method proposed, some Mössbauer measurements made on irradiated and non-irradiated Fe-5%Cr samples are presented.

Another great contribution of this work has been the deep review of the literature which has established a clear picture of RR results and specific terminology, in pure Fe and Fe-Cr alloys. This revision is very interesting given that this topic has been barely abandoned in the experimental field in the past two decades (there are only publications from one author in the last years) and the most recent scientific works using RR results come from modelling topical group.

Finally it must be pointed out that transversally along the thesis the proton irradiation has been a concern. The 5 MeV proton irradiation was chosen to irradiate the model Fe-Cr alloys as a first approximation to neutrons. Its effects have been analysed from the point of view of the effects on the resistivity, the damage type and spatial distribution. Besides comparative to electrons and proton irradiations have been made,

not only conceptually but also in the RR results. And additionally, specific calculations, using SRIM and MARLOWE, of PKA spectra generated by the 5 MeV protons and dose (dpas) have been provided. The main conclusions are given below.

6.2. Conclusions

The main conclusions of this work can be grouped in two main blocks:

Conclusions directly derived from the analysis of experimental RR results

(i) The 5 MeV proton irradiations used in this work produce a PKA spectrum with a mean energy of about 350 eV, which is of about one order of magnitude higher than typical electron irradiations in RR experiments. The mean I-V distribution distance is about the double than in typical 2.5 MeV electron irradiations in samples of 50 μm thickness. This has been given as the main reason for differences in RR spectrum.

(ii) Compilation of all the available data has demonstrated that the impact of the particle irradiation on the type of damage produced can be clearly identified in RR experiments. Especially in pure Fe where the RR curves clearly group in three bunches, each of them associated to electrons, protons or neutrons respectively. This is an important application to classify any other irradiation. Concerning the Fe-Cr alloys, a clear reduction of stage I and II and increase of final Stages (III, IV and V) are observed in proton irradiated samples with respect to electron irradiated.

(iii) It has been detected a discrepancy between the results given by Marlowe and SRIM respectively. There is a need to calculate the real FP's number and not only the dpa given that the damage creation efficiency depends on the energy of the PKA even at low doses. Still there is found some discrepancy with the bibliography concerning the value of the specific resistivity of FP in pure Fe or the number of defects created.

(iv) The RR curves investigated in concentrated Fe-5%Cr, Fe-10%Cr and Fe-14%Cr alloys, have shown to be strongly dependent on the initial arrangement of Cr in the microstructure. Such initial distribution can typically depend on in the thermo-mechanical processes that the sample has suffered (e.g. the sample preparation process).

(v) As a consequence of the analysis and understanding of all the effects that can change resistivity value in an alloy, a modified and original method has been proposed and tested. It is based on the idea of radiation – enhanced diffusion of defects (in this case also Cr) to trigger the evolution of the SRO state towards its equilibrium value (at the irradiation temperature). In our case it was a proton pre-irradiation step at 400 K.

(vi) The SFM of vacancies and other interstitial-type defects induce strong ordering effects in Fe-5%Cr specimens. These effects can be removed by leading the state of ordering of the sample to the equilibrium value by means of the above mentioned pre-irradiation step at 400 K, confirming the validity of the concept.

(vii) In Fe-14%Cr evidences of clustering with irradiation have been observed both along a classic resistivity recovery experiment and after 400 K pre-irradiation. Such effects have been apparently erased with the new proposed RR method. But the results should be confirmed by Mössbauer measurements.

(viii) Sample of Fe-10%Cr exhibits behaviors related to positive and negative values of the SRO parameters (changing with temperature). The mechanisms responsible of this behavior have not been identified and some proposals to clarify the observations are suggested in the next section of future works.

Other collateral conclusions derived from the work

(i) The application of the two-current model to the experimental resistivity values of concentrated Fe-Cr alloys (as-received and along low-T-Irr) has shown that the addition of high Cr concentrations to Fe, diminishes the values of α_{Cr} and the spin-mixing term. Besides, under the assumption of the model, it has been shown that the creation of few appm of defects has negligible impact on the weights of spin populations. An important consequence of such investigations has been that no specific correction has to be applied to RR data in concentrated Fe-Cr alloys.

(ii) As RR spectra are used to evaluate population defect evolution - which are used to validate models- the proposed method gives very valuable information, minimizing the SRO contribution of RR curve at least in Fe-5%Cr and therefore allowing an improved evaluation of defects recombination.

(iii) The critical analysis of the RR data (not only from the presented data but also from the literature database) has let concluding that the experimental complexity of RR experiments makes the available data not as abundant and reliable as it would be desirable. Thus, it is of primary importance to determine the best way of performing such type of experiments in order to take the most profit of them. Understanding of the experimental results should be aligned with the possibilities of modelling.

6.3. **Future work**

- An effort to provide reliable data for experimental validations has been made with interesting results, but some extra experiments should be done in order to complete this research:

(i) The Mössbauer investigation made in sample Fe-5%Cr should be done as well in Fe-10%Cr and Fe-14%Cr samples. Ideally some measurements just after irradiation at low temperature should also be done. But important modifications of the set-up should be implemented.

(ii) Classical RR should be repeated in sample Fe-14Cr with better temperature resolution in order to confirm the shape of the difference RR curve in this material. Reproduction of some other obtained results, but with the present accuracy of the set-up, would also be interesting.

(iii) Different proton doses should be used to obtain more information on the different stages (temperature position, maximum values, etc.). Proton energy could also be increased.

(iv) In the long term, RR measurements done in these samples but irradiating with electrons would give a reliable comparison between electron and protons effects, eliminating the uncertainty due to different sample origin and residual impurities. This would also need an important change in the set-up and its installation in another accelerator.

- Additionally, the changes in resistivity at different doses at 400K irradiation in samples Fe-5%Cr, Fe-10%Cr and Fe-14%Cr should be investigated in detail in order to confirm the expected saturation behavior which has been one of the major hypothesis made in this experimental work. In other words, in order to apply the improved RR method a full investigation of SRO behavior with 400 K pre-Irr should be performed, resulting in a proper knowledge of the behavior of the system in presence of migration defects as a function of dose and dose rate.

- Concerning to the performance of new RR experiments, these should be very well designed in terms of sample preparation procedure, microstructural and impurity content characterization. Moreover they should be made in order to validate a specific need that modelling would be requiring. Therefore it will be of primary importance to decide the type of irradiating particle, the specimen dimensions, the area of irradiation and desired fluence or dose.

- In a more general context I would suggest other kind of experiments before keep going with such complicated technique:

(i) As stages II and III contain many overlapped processes and regarding the effects of SRO re-arrangements, I would suggest the use of quenching experiments to investigate SRO kinetics and take experimental measurements of formation and migration energies of thermal vacancies.

(ii) Open question: Despite that in the literature, dislocations are considered just as unfillable sinks, the possibility that they act as traps of simple defects that could inhibit the recovery at certain temperatures and enhance it when de-

trapping should be investigated. Also the impact of the amount of dislocations on the % recovery should be investigated for a certain C_{Cr}.

Chapter 7. Conclusiones

7.1. Resumen

Inicialmente, se ha realizado una revisión profunda de los aspectos básicos de las aleaciones binarias no simples, donde se ha mostrado la relación explícita que hay entre la resistividad y los parámetros SRO y los efectos del ferromagnetismo en la resistividad de las aleaciones ferromagnéticas cuyo comportamiento es descrito por el modelo de las dos corrientes. Además, se han descrito los efectos de la irradiación con partículas ligeras para el caso más simple (dosis bajas). Está revisión resulta fundamental para comprender los trabajos experimentales más importantes de la literatura en experimentos de recuperación de la resistividad, que también han sido descritos con detalle.

Seguidamente, la descripción de los mecanismos de difusión de los defectos producidos por irradiación ha permitido explicar los fundamentos en los que se basa la técnica experimental de RR. Como resultado de la comprensión profunda de los principios experimentales y las dependencias de la resistividad, ha sido posible, no sólo realizar experimentos de RR sino también modificar la metodología con objeto de mejorar la técnica.

El principal objetivo del trabajo, que consistía en el desarrollo, testeo y puesta a punto de la técnica experimental se ha logrado con éxito. Posteriormente se han obtenido curvas de RR fiables de muestras de Fe, Fe-5%Cr, Fe-10%Cr y Fe-14%Cr, que se han medido con el método clásico así como con el nuevo método mejorado propuesto en este trabajo. Se han incluido en la memoria los detalles completos del método de preparación de las muestras, el montaje experimental y las condiciones experimentales.

Otra gran contribución de este trabajo ha sido la revisión profunda de la literatura que ha permitido establecer una imagen clara de los resultados típicos de RR y su terminología específica, en Fe puro y aleaciones Fe-Cr. Esta revisión resulta muy interesante dado que este tema ha estado prácticamente abandonado durante los últimos 15 años (sólo hay publicaciones de un autor en los últimos años) y los trabajos científicos más recientes que hacen referencia a resultados de RR provienen del grupo temático de las modelizaciones computacionales.

Finalmente, se debe indicar que transversalmente a lo largo de esta tesis, se ha tratado el tema de la irradiación con protones. La irradiación con protones de 5 MeV ha sido elegida para irradiar las aleaciones modelo Fe-Cr como una primera aproximación a los neutrones. Sus efectos se han analizado desde el punto de vista de sus efectos en la resistividad, el tipo de daño que crean y su distribución espacial. Además, no solo se han hecho comparativas conceptuales sino también experimentales, comparando los resultados de RR. Para terminar, también se han hecho cálculos específicos, utilizando Marlowe y SRIM, de los espectros de PKA generados por los protones de 5 MeV y de dosis (dpas).

Las principales conclusiones se resumen a continuación.

7.2. Conclusiones

Las principales conclusiones se dividen en dos bloques principales:

Conclusiones directamente derivadas del análisis de los resultados experimentales

(ix) Las irradiaciones de protones de 5 MeV utilizadas en este trabajo producen un espectro de PKA con una energía media de aproximadamente 350 eV, lo cual es del orden de 6 veces mayor que la eergía media típica en los experimentos con electrones. La distribución de separación media entre I-V es aproximadamente el doble que en una irradiación típica con electrones de 2.5 MeV en muestras de 50 μm de espesor. Se indica que esta es la razón principal de las diferencias en los espectros de RR.

(x) La compilación de todos los datos disponibles en la literatura ha demostrado que el tipo de daño producido puede ser claramente identificado utilizando experimentos de RR. Especialmente en Fe puro, donde las curvas RR claramente se agrupan en 3 zonas, correspondientes a electrones, protones y neutrones respectivamente. Esta es una aplicación importante que sirve para clasificar otras irradiaciones. Respecto a las aleaciones Fe-Cr, una clara reducción de las Etapa I y II (Stage I and II) y un aumento final de las Etapas finales (Stage III, IV y V) se observa en las irradiaciones con protones respecto a las irradiaciones con electrones.

(xi) Se han detectado discrepancias entre los resultados aportados por Marlowe y SRIM respectivamente. Hay una necesidad de calcular el número real de pares de Frenkel y no solamente los dpa, dado que la eficiencia de creación de defectos no es igual a uno y tiende a disminuir con la energía de PKA incluso a dosis bajas. Todavía se encuentran algunas discrepancias con la bibliografía en lo relativo a la resistividad específica de par de Frenkel in fe puro o al número de defectos creado.

(xii) Las curvas de RR investigadas en las aleaciones concentradas: Fe-5%Cr, Fe-10%Cr and Fe-14%Cr, han mostrado una fuerte dependencia con la disposición inicial del Cr en la microestructura. Esta distribución incial puede depender típicamente de los procesos termo-mecánicos a los que el material ha sido sometido, como por ejemplo, el proceso de preparación de la muestra.

(xiii) Como consecuencia del análisis y la comprensión de los efectos que pueden cambiar la resistividad de una aleación, se ha propuesto y probado un método modificado y original para medir RR. Está basdo en la idea de la difusión de defectos favorecida por la irradiación (en este caso también el Cr) para provocar la evolución de los estados de SRO hacia sus valores de equilibrio (a la temperatura de irradiación). En nuestro caso hemos propuesto una pre-irradiación a 400 K.

(xiv) La Etapa de migración libre (SFM)de vacantes y otros defectos intersticiales induce un fuerte ordenamiento del Cr en muestras de Fe-5%Cr. Estos pueden ser eliminados llevando el estado de ordenamiento del Cr en la muestra a su valor de equilibrio por medio de la pre-irradiación a 400 K mencionada anteriormente. De esta manera se ha confirmado la validez de la idea.

(xv) En Fe-14%Cr las evidencias de agrupación del Cr con la irradiación se han observado tanto a lo largo del experimento clásico de RR como tras la pre-irradiación. Estos efectos han sido aparentemente borrados con el nuevo método propuesto. Sin embargo estos resultados deben confirmarse con medidas de Mössbauer.

(xvi) Las muestras de Fe-10%Cr exhiben comportamientos relacionados con valores positivos y negativos de los parámetros SRO (cambiando con la temperatura). Los mecanismos responsables de este comportamiento no han sido identificados y en la siguiente sección se propondrán distintos trabajos para clarificar las observaciones experimentales.

Otras conclusiones colaterales de este trabajo:

(iv) La aplicación del modelo de las dos corrientes a los valores experimentales de resistividad residual de las aleaciones concentradas Fe-Cr (sin irradiar y a lo largo de la irradiación a baja temperatura) ha demostrado que la adición de grandes concentraciones de Cr al Fe, disminuye los valores del parámetro αCr y el término de combinación de espines.

(v) Como los espectros de RR se utilizan para evaluar la evolución de poblaciones de defectos –lo que a su vez se usa para validar los modelos- el nuevo método propuesto aporta información muy valiosa minimizando la contribución del SRO a las curvas de resistividad, al menos en las aleaciones Fe-5%Cr y por tanto permite una mejor evaluación de la recombinación de los defectos.

(vi) El análisis crítico de los datos RR (no solamente los de este trabajo sino también los de la literatura) ha permitido concluir que la complejidad

experimental de los experimentos RR hace que los datos disponibles no sean ni tan abundantes ni tan fiables como sería deseable. Por lo tanto es de vital importancia determinar la manera más adecuada para ejecutar este tipo de experimentos con el objetivo de sacar el mayor provecho de sus resultados. La comprensión de los resultados experimentales debe ser acorde con las posibilidades de las modelizaciones.

7.3. **Trabajos futuros**

- Se ha realizado un esfuerzo importante para obtener datos confiables para las validaciones experimentales obteniendo resultados muy interesantes, pero sería interesante hacer algunos experimentos extra para complementar esta investigación:

(v) Se deberían investigar con Mössbauer las muestras Fe-10%Cr y Fe-14%Cr, así como se han hecho en las muestras de Fe-5%Cr. Idealmente, también deberían hacerse algunas medidas de Mössbauer justo después de la irradiación a baja temperatura. Sin embargo, estas medidas requerirían modificaciones importantes del sistema experimental.

(vi) Se debería repetir el método clásico de RR en la muestra de Fe-14%Cr con mejor resolución en temperatura para confirmar la forma de la curva "difference RR" en este material. También sería interesante la repetición de algunos de los resultados obtenidos, pero con la precisión actual del sistema experimental.

(vii) También se deberían investigar diferentes dosis con protones para obtener más información relativa a las Etapas de recombinación (posición de la temperatura del pico, valores máximos, etc…). También se podría aumentar la energía de los protones.

(viii) A largo plazo, la realización de estas mismas medidas RR en las mismas muestras, pero irradiadas con electrones, supondría una forma muy fiable de comparar los efectos de protones y electrones, eliminando las incertidumbres relacionadas con el origen de las muestras y el contenido de impurezas. Esta tarea, también requeriría modificaciones importantes del sistema experimental y su instalación en otro acelerador.

- Además se debería investigar los cambios en resistividad a diferentes dosis en las irradiaciones a 400 K en las muestras Fe-5%Cr, Fe-10%Cr and Fe-14%Cr. Estos datos podrían confirmar el comportamiento de saturación que se espera y que ha constituido la mayor hipótesis de esta investigación. Es decir, para confimar la validez del método mejorado propuesto, la monitorización del comportamiento del SRO con la pre-irradiación a 400 K, proporcionaría información completa del comportamiento del sistema en presencia de migración de defectos en función de la dosis y de la tasa de dosis.

- Respecto a la realización de nuevos experimentos de RR, estos deberían estar muy bien diseñados en términos de procedimiento de reparación de muestras y caracterización de la microestructura y el contenido de impurezas. Además deberían diseñarse con el objetivo de satisfacer una necesidad concreta de las simulaciones. Por lo tanto es muy importante decidir previamente el tipo de partícula incidente, las dimensiones del espécimen, el área de irradiación y la fluencia o la dosis deseada.

- En un contexto más general, yo sugeriría otro tipo de experimentos para seguir obteniendo resultados relevantes, tanto para las simulaciones como para los experimentos RR:

(iii) Dado que las Etapas II y III contienen muchos procesos superpuestos y en vista de los efectos de SRO, yo sugeriría la realización de experimentos de revenido (quenching) para investigar la cinética del SRO y obtener medidas experimentales de las energías de formación y migración de vacantes térmicas.

(iv) Pregunta abierta: A pesar de que en la literatura las dislocaciones son consideradas simplemente como sumideros que pueden “atrapar” defectos infinitamente, debería ser investigada la posibilidad de que actúen como trampas de defectos simples que pueden inhibir la recuperación de la resistividad y favorecerla cuando liberan estos defectos atrapados. También se debería estudiar la influencia del número de dislocaciones en el porcentaje de recuperación en función de la concentración de Cr.

Appendix A

Analytical expression of the resistivity in non-simple alloys

When an electric field $\mathcal{E}$ is applied to a conductor, each electron will experience a force –eℰ and it will undergo an acceleration in the direction of that force. The electrons will then produce a net electron current. The current density j(r, t) at position r and time t is obtained by summing the contribution of the velocity ev(k) of all electrons. This is achieved by integrating over k and weighting each contribution by the distribution function of the electrons f(k, r, t):

$$j(r,t) = \frac{e}{4\pi^3}\int v(k) f(k,r,t) dk \qquad \text{A-1}$$

The distribution function defines the location of an electron state in six dimensional (r, k) phase space at time t. As the electrical resistivity is due to electron scattering, this is that an electron can discontinuously change its momentum from an initial state φ_k into a final state $\psi_{k'}$, then the Boltzmann equation for electron transport can be written as:

$$\frac{\partial f}{\partial t} + \frac{\partial f}{\partial r}\frac{\partial r}{\partial t} + \frac{\partial f}{\partial k}\frac{\partial k}{\partial t} = \left.\frac{\partial f}{\partial t}\right|_{scatt} \qquad \text{A-2}$$

The analysis of equation A-2 is necessary to solve A- and obtain an analytical expression for the resistivity. The number of electrons that can be scattered in a small time interval dt out of the volume dk about k into some new set of levels in dk' about k' is given by the product of:

$$\left(\frac{\partial f}{\partial t}\right)_{k\to k'} = \begin{array}{c}\text{Number of electrons available for scattering process}\end{array} \times \begin{array}{c}\text{Scattering probability in the time interval}\end{array} \times \begin{array}{c}\text{Number of available states}\end{array} \qquad \text{A-3}$$

$$\left(\frac{\partial f}{\partial t}\right) dt dk = f_k dk \times \frac{\Omega}{(2\pi)^3} dt \int Q_{kk'} \times (1 - f_{k'}) dk' \qquad \text{A-4}$$

where $Q_{kk'}$ is defined as the probability per unit time that an electron with wavevector k is scattered without change of spin direction into one of the levels on the volume dk' about k'. If such mathematics is applied to both processes, k→k' and k'→k and considering the principle of microscopic reversibility which requires $Q_{kk'}=Q_{k'k}$ then we can reach the Boltzmann equation in this form:

$$\left.\frac{\partial f}{\partial t}\right|_{scat} = \frac{\Omega}{(2\pi)^3}\int (f_{k'} - f_k)Q_{kk'}dk' \qquad \text{A-5}$$

In the case of non-simple metals, the distribution function is re-written as a variation from the equilibrium function f_0 (which gives no electron scattering), such description is called the variational principle[18] of Köhler:

$$f(k,r,t) = f_0(k,r) + \phi_k(k,r,t)\frac{\partial f_0}{\partial E_k} \qquad \text{A-6}$$

Where φ_k is a function defined in order that the former description of the distribution function (equation A-6) fits. And as f_0 is by definition the Fermi-Dirac distribution function for en electron gas at equilibrium temperature T in a uniform solid:

$$f_0(k,r) = \frac{1}{exp\left(\left[\frac{E(k) - E_F(k)}{k_B T(r)}\right] + 1\right)} \qquad \text{A-7}$$

Thus:

$$\frac{\partial f_0}{\partial E_k} = -\frac{f_0(1-f_0)}{k_B T} \qquad \text{A-8}$$

Then by combining A-5, A-6 and A-8 the Boltzmann equation is rewritten as:

$$\left.\frac{\partial f}{\partial t}\right|_{scat} = \frac{\Omega}{(2\pi)^3 k_B T}\int (\phi_k - \phi_{k'})f_0(1-f_0)Q_{kk'}dk' \qquad \text{A-9}$$

The intrinsic transition probabilities, $Q_{kk'}$, can be rewritten in terms of actual transition probabilities (equation 2-13):

$$\left.\frac{\partial f}{\partial t}\right|_{scat} = \frac{\Omega}{(2\pi)^3 k_B T}\int (\phi_k - \phi_{k'})P_{kk'}dk' \qquad \text{A-10}$$

The solution of the equation A-10 is much simplified if it is assumed that the distribution relaxes exponentially in time to the equilibrium form when the field is switched off, in which case:

$$\left.\frac{\partial f}{\partial t}\right|_{scat} = -\frac{f - f_0}{\tau_k} = -\frac{\phi_k}{\tau_k}\frac{\partial f_0}{\partial E_K} = \frac{\phi_k}{\tau_k}\frac{f_0(1-f_0)}{k_B T} \qquad \text{A-11}$$

A-11 is referred to the equilibrium time approximation. Thus the relaxation time can be expressed as a function of the transition probability:

$$\frac{1}{\tau_k} = \frac{\Omega}{(2\pi)^3}\int \left(1 - \frac{\phi_{k'}}{\phi_k}\right)Q_{kk'}dk' \qquad \text{A-12}$$

[18] El principio variacional establece que para cualquier función, el valor esperado de un operador es mayor o igual al menor autovalor del operador, i.e. $\left|\frac{\langle\psi|f|\psi\rangle}{\sqrt{\langle\psi\psi\rangle}}\right| \geq f_0$

Let's express k', the new momentum, in terms of its original value k and the exchange momentum term q: k'=k+q. The scattering probability is given to first order perturbation theory (Fermi's Golden rule) and is expressed as:

$$Q_{kk'} = \frac{2\pi}{\hbar}|\langle k+q|V(r)|k\rangle|^2 \qquad \text{A-13}$$

Where V(r) is the scattering potential. If the obtained form of relaxation time is used in the quantum Drude formula (Chapter 2, eqn. 2-12):

$$\rho = \frac{m^*}{n\hbar e^2}\frac{\Omega}{4\pi^2}\int\left(1-\frac{\phi_{k+q}}{\phi_k}\right)|\langle k+q|V(r)|k\rangle|^2 dq \qquad \text{A-14}$$

If we consider that the lattice potential is weak, we can apply the pseudopotential approximation V(r)≈W(r) and describe the pseudopotential W(r) as a sum of spherically symmetric individual ion pseudopotentials w(r). Also if we assume than the interaction matrix is symmetric and uniform we can express as a product of two terms (cf. Rossiter pg. 129 [16]):

$$Q_{kk'} = \frac{2\pi}{\hbar}|\langle k+q|W(r)|k\rangle|^2 = \frac{2\pi}{\hbar}N|S(q)|^2|\langle k+q|w(r)|k\rangle|^2 \qquad \text{A-15}$$

Where S(q) is the structure factor:

$$S(q) = \frac{1}{N}\sum_r \exp(-iqr) \qquad \text{A-16}$$

being N the total number of atoms, and the form factor:

$$\langle k+q|w(r)|k\rangle \qquad \text{A-17}$$

In the case of binary alloys containing atoms of A and B species the decomposition of the scattering term will be a little bit more complicated given that it will apply a different individual pseudopotential for each of the species, $w_A(r)$ and $w_B(r)$. Eventually after very simple calculations the decomposition can be made in terms of an average lattice potential matrix elements and a difference potential:

$$\langle k+q|W(r)|k\rangle = S(q)\langle k+q|\bar{w}(r)|k\rangle + S^d(q)\langle k+q|w^d(r)|k\rangle \qquad \text{A-18}$$

where the average lattice potential is defined by:

$$\bar{w}(r) = c_A w_A(r) + c_B w_B(r) \qquad \text{A-19}$$

and the difference or deviation potential is defined by:

$$w^d = w_A(r) - w_B(r) \qquad \text{A-20}$$

As the scattering term is squared in the expression of the resistivity we have to evaluate the squared terms averaged and differential in order to make some simplifications. As we are still not considering atomic displacement effects the cross terms vanish, but they will not when we will considered the presence of radiation defects in the lattice. Thus it can be

shown that two independent terms evolve from the square of equation A-18, one due to the average lattice when q=g_n (g_n is the distance between scattering centers in k-space) given that at this value the deviation term vanishes and the other way around when q≠g_n. The square of the average structure factor $|S(q)|^2$ is zero except when q=g_n, in which case it has the value of unity. This term gives the Bragg scattering of conduction electrons but does not contribute to the resistivity because of the integration over q. Therefore the resistivity becomes only dependent on the deviation term:

$$\rho = C \int \left(1 - \frac{\phi_{k+q}}{\phi_k}\right) \left|S^d(q)\right|^2 \left|\langle k+q \left| w^d(r) \right| k \rangle\right|^2 dq \qquad \text{A-21}$$

where:

$$C = \frac{m^*}{n\hbar e^2} \frac{\Omega}{4\pi^2} \qquad \text{A-22}$$

In absence of any atomic displacements the structure factor of the deviation term can be expressed in terms of average probabilities of site occupation <$\sigma_i\sigma_j$> (see Chapter 2, eqn. 2-21 or 2-22) and interatomic distances of a perfectly ordered lattice R_{ij}:

$$\left|S^d(q)\right|^2 = \frac{1}{N} \sum_{ij} \langle \sigma_i \sigma_j \rangle \exp(-iqR_{ij}) \qquad \text{A-23}$$

Giving:

$$\rho = \frac{C}{N} \int \left(1 - \frac{\phi_{k+q}}{\phi_k}\right) \sum_{ij} \langle \sigma_i \sigma_j \rangle \exp(-iqR_{ij}) \left|\langle k+q \left| w^d(r) \right| k \rangle\right|^2 dq \qquad \text{A-24}$$

This expression can be further simplified, as the integral does not depend on the direction of q, part of the structure factor can be rewritten in terms of an oscillating function which depends on q and decays as i grows, also by using the equation 2-22, we can rewrite A-24 in terms of Warren-Cowley SRO parameters. The resistivity expression is thus:

$$\rho = \frac{C}{N} c_A c_B \int \left(1 - \frac{\phi_{k+q}}{\phi_k}\right) \sum_i c_i \alpha_i \frac{\sin(qr_i)}{qr_i} \left|\langle k+q \left| w^d(r) \right| k \rangle\right|^2 dq \qquad \text{A-25}$$

As the oscillating function decays, only the first few coordination spheres will have an impact. For example, it is reasonable to think that it is proportional to the α12 parameter, which is the weighted average of α1 and α2 Warren-Cowley parameters. Therefore now is evidenced how SRO parameters have a direct influence on the resistivity of a non-simple alloy. Thus if SRO parameters change their value in a material, its residual resistivity value will change as well.

It must be noticed, that it is assumed that the relaxation time is isotropic, i.e. it is not dependent on the direction of k, and that the alloy is simple, i.e. its Fermi surface can be approximated to a sphere. Consequently the expression of the resistivity becomes much simpler. Integration over the Fermi surface gives the following expression of the resistivity:

$$\rho = \frac{C'}{N} c_A c_B \int_0^{2k_F} \sum_i c_i \alpha_i \frac{\sin(qr_i)}{qr_i} \left|\langle k+q \left| w^d(r) \right| k \rangle\right|^2 q^3 dq = \quad \text{A-26}$$

or:

$$\rho = \frac{C'}{N} c_A c_B \sum_i c_i \alpha_i Y_i \quad \text{A-27}$$

being C' and Y_i:

$$C' = \frac{3\pi m^2 \Omega}{4\hbar^3 e^2 k_F^6} \quad \text{A-28}$$

$$Y_i = \int_0^{2k_F} \frac{\sin(qr_i)}{qr_i} \left|\langle k+q \left| w^d(r) \right| k \rangle\right|^2 q^3 dq \quad \text{A-29}$$

De esta forma es más sencillo de ver la relación entre la resistividad de los parámetros Warren-Cowley. La figura B-1 ejemplifica el carácter oscilante y el decaimiento rápido de las funciones Y_i.

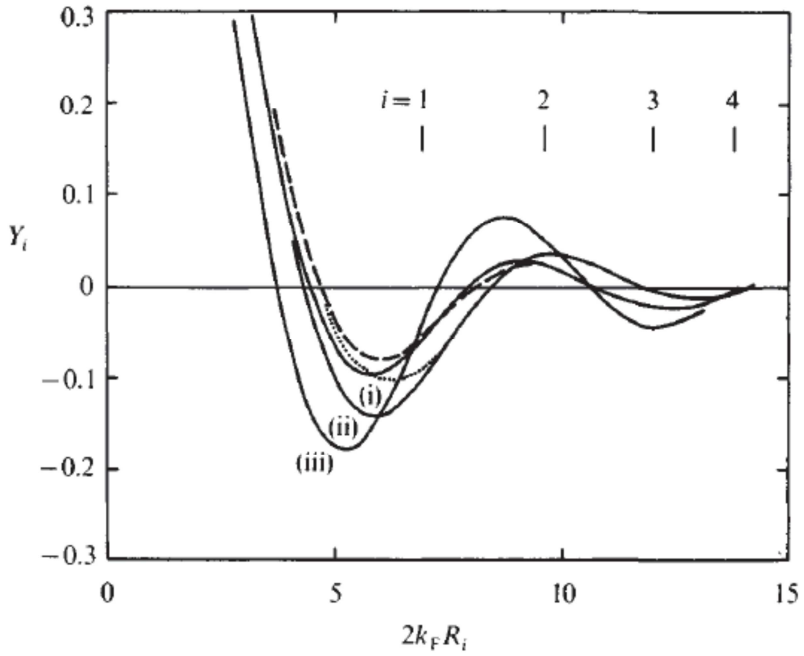

A-1: The integrals Y_i for Cu-25%Au normalized to unity at q-->0. Each curve, (i), (ii) and (iii), represent different model pseudopotentials used to perform the calculations. Also shown by vertical bars are the values of $2k_F R_i$ for the first 4 shells of neighbors.

Appendix B

Overview of experimental and theoretical data of the average value of first and second SRO parameters in Fe-Cr alloys.

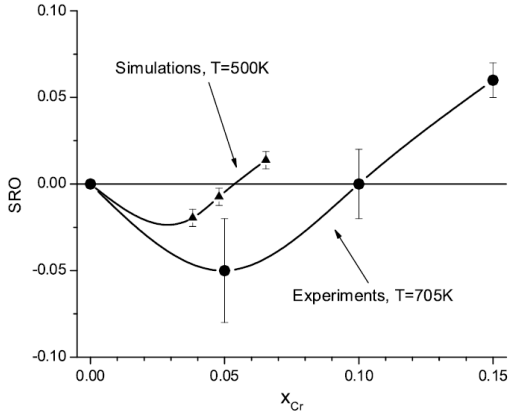

Fig. B-1: Simulation [113] and experimental [17] values for SRO parameters in Fe-Cr at different temperatures.

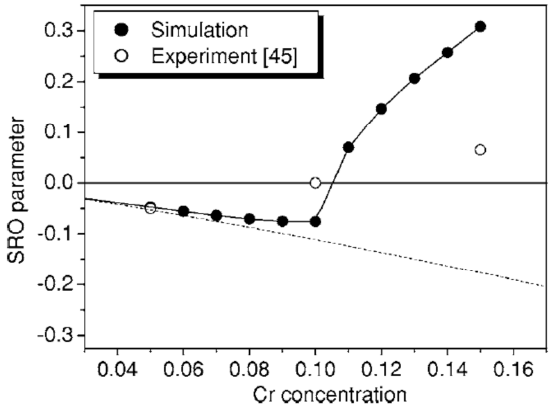

Fig. B-2: Calculated averaged values of first and second Warren-Cowley parameters in Fe-Cr solid solution at T = 750 K. Simulation data from [115] and experimental from [17] (T_{exp} = 705 K).

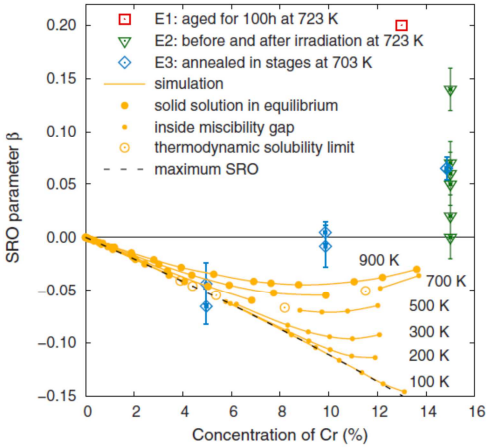

Fig. B-3: Dependence of SRO parameter on the total C_{Cr}. Dashed line represents the maximum possible order. Data from experiments: E1 from [116], E2 from [117] and E3 from [17].

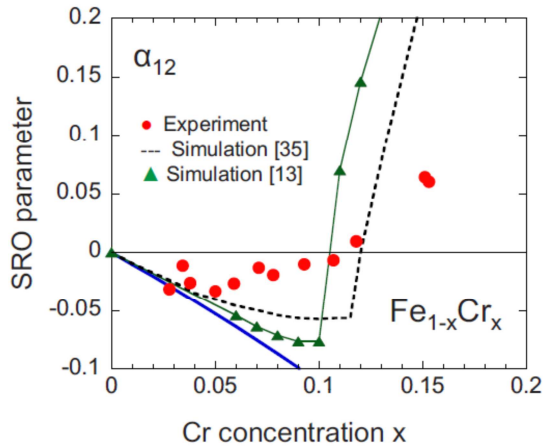

Fig. B-4: Averaged values of first and second Warren-Cowley parameters. Experimental values at T = 705 K [18]. Simulation: dotted lines from [96] and triangles from [115].

Publications

"ANNUAL PROGRESS IN THE TECHNICAL DEVELOPMENT OF THE TECHNOFUSION MATERIALS CHARACTERIZATION AREA",
E. Carella, B. Gómez-Ferrer, M. González, R. González-Arrabal, C. Salgado and R. Vila.
First Workshop on Fusion Technologies and the Contribution of Technofusión, in: Sección de Publicaciones Escuela Técnica Superior de Ingenieros Industriales, Universidad Politécnica de Madrid, 2011.

"STUDY OF RADIATION DAMAGE IN Fe-Cr UNDER RESISTIVITY TECHNIQUES".
B. Gómez-Ferrer, R. Vila and D. Jiménez-Rey.
Second Workshop on Fusion Technologies and the Contribution of Technofusión, Escuela Politécnica Superior, Universidad Carlos III de Madrid, Leganés, 2012.

"LOW-TEMPERATURE RESISTIVITY MEASUREMENTS FOR MATERIALS DEVELOPMENT IN FUSION RESEARCH",
B. Gómez-Ferrer, R. Vila and D. Jiménez-Rey.
Energy Procedia 41 (2013) 34.

"RESISTIVITY RECOVERY MEASUREMENTS ON PROTON IRRADIATED Fe and $FeCr_x$ ALLOYS",
B. Gómez-Ferrer, R. Vila, D. Jiménez-Rey, C.J. Ortiz, F. Mota, J.M. García, A. Rodríguez.
Journal of Nuclear Materials 447 (2014) 225.

"FIRST TESTS OF THE ION IRRADIATION AND IMPLANTATION BEAMLINE AT THE CMAM"
D. Jiménez-Rey, M. Benedicto, A. Muñoz-Martín, D. Bachiller-Perea, J. Olivares, A. Climent-Font, B. Gómez-Ferrer, A. Rodríguez, J. Narros, A. Maira, J. Álvarez, A. Nakbi, A. Zucchiatti, F. de Aragón, J.M. García, R. Vila.
Nuclear Instruments and Methods in Physics Research Section B: Beam Interactions with Materials and Atoms 331 (2014) 196.

"DECOUPLING OF DEFECT AND SHORT-RANGE ORDER CONTRIBUTIONS TO RESISTIVITY RECOVERY MEASUREMENTS IN BINARY ALLOYS".
B. Gómez-Ferrer, i. García-Cortés, J.F. Marco, D. Jiménez-Rey, R. Vila.
Physical Review B (accepted for publication).

References

[1] F. F. Chen, *An Indispensable Truth: How Fusion Power Can Save the Planet* (Springer, New York, 2011).

[2] *World Energy Outlook 2009* (International Energy Agency, Paris, 2009).

[3] T. J. Dolan, *Fusion Research: Principles, Experiments and Technology* (Pergamon Press, New York, 1982).

[4] Janeschitz, G., *The Physics and Technology Basis of ITER and Its Mission on the Path to DEMO* (IEEE International Conference on Plasma Science, San Diego, California, 2009).

[5] ASTM E693 - 12, *Practice for Characterizing Neutron Exposures in Iron and Low Alloy Steels in Terms of Displacements Per Atom (DPA), E 706(ID)* (ASTM International, 2012).

[6] M. J. Norgett, M. T. Robinson, and I. M. Torrens, Nuclear Engineering and Design **33**, 50 (1975).

[7] F. Mota, C. J. Ortiz, R. Vila, N. Casal, A. García, and A. Ibarra, Journal of Nuclear Materials **442**, S699 (2013).

[8] Y. Serruys, P. Trocellier, S. Miro, E. Bordas, M. O. Ruault, O. Kaïtasov, S. Henry, O. Leseigneur, T. Bonnaillie, and S. Pellegrino, Journal of Nuclear Materials **386-388**, 967 (2009).

[9] R. S. Averback, R. Benedek, and K. . Merkle, Journal of Nuclear Materials **75**, 162 (1978).

[10] T. Tanaka, K. Oka, S. Ohnuki, S. Yamashita, T. Suda, S. Watanabe, and E. Wakai, Journal of Nuclear Materials **329-333**, 294 (2004).

[11] D. J. Bacon, F. Gao, and Y. N. Osetsky, Journal of Nuclear Materials **276**, 1 (2000).

[12] S. J. Zinkle, Fusion Engineering and Design **74**, 31 (2005).

[13] Y. V. Konobeev, A. M. Dvoriashin, S. I. Porollo, and F. A. Garner, Journal of Nuclear Materials **355**, 124 (2006).

[14] H. Kayano, A. Kimura, M. Narui, Y. Sasaki, Y. Suzuki, and S. Ohta, Journal of Nuclear Materials **155-157**, 978 (1988).

[15] M. Dusek and C. Hunt, *Test Methods for Evaluating the Reliability of PCB Finishes Using Lead-Free Alloys - a Guide* (2002).

[16] P. L. Rossiter, *The Electrical Resistivity of Metals and Alloys* (Cambridge University Press, Cambridge [Cambridgeshire]; New York, 1987).

[17] I. Mirebeau, M. Hennion, and G. Parette, Phys. Rev. Lett. **53**, 687 (1984).

[18] I. Mirebeau and G. Parette, Physical Review B **82**, (2010).

[19] D. A. Terentyev, L. Malerba, R. Chakarova, K. Nordlund, P. Olsson, M. Rieth, and J. Wallenius, Journal of Nuclear Materials **349**, 119 (2006).

[20] T. H. Blewitt, R. R. Coltman, and C. E. Klabunde, Aust. J. Phys. **13**, 347 (1960).

[21] J. A. Tesk, E. C. Jones, and J. W. Kauffman, Phys. Rev. **133**, A288 (1964).

[22] F. Maury, M. Biget, P. Vajda, A. Lucasson, and P. Lucasson, Radiation Effects **38**, 53 (1978).

[23] A. M. Omar, Low Temperature Irradiation of Iron, Zirconium and Copper by 10 to 16 MeV Protons, Materials Science, McMaster University, 1978.

[24] S. Takaki, J. Fuss, H. Kuglers, U. Dedek, and H. Schultz, Radiation Effects **79**, 87 (1983).

[25] F. Maury, A. Lucasson, P. Lucasson, P. Moser, and Y. Loreaux, Journal of Physics F: Metal Physics **15**, 1465 (1985).

[26] F. Maury, A. Lucasson, P. Lucasson, Y. Loreaux, and P. Moser, Journal of Physics F: Metal Physics **16**, 523 (1986).

[27] A. Benkaddour and O. Dimitrov, C.and Dimitrov, Materials Science Forum **(15 - 18)**, 1263 (1987).

[28] H. Matsui, S. Takehana, and M. W. Guinan, Journal of Nuclear Materials **155-157**, 1284 (1988).

[29] A. L. Nikolaev, V. L. Arbuzov, and A. E. Davletshin, Journal of Physics: Condensed Matter **9**, 4385 (1997).

[30] H. Abe and E. Kuramoto, Journal of Nuclear Materials **271-272**, 209 (1999).

[31] Y. Chimi, A. Iwase, and N. Ishikawa, Journal of Nuclear Materials **271-272**, 236 (1999).

[32] A. L. Nikolaev, Philosophical Magazine **87**, 4847 (2007).

[33] J. L. Boutard, M. J. Caturla, S. L. Dudarev, and F. Willaime, *Strategic Objectives for Fusion Materials Modelling and Experimental Validation (http://www.efda.org/downloads/)* (EFDA, 2009).

[34] D. Stork and et al., *Assessment of the EU R&D Programme on DEMO Structural and High-Heat Flux Materials* (2012).

[35] C. Linsmeier, C.-C. Fu, A. Kaprolat, S. F. Nielsen, K. Mergia, R. Schäublin, R. Lindau, H. Bolt, J.-Y. Buffière, M. J. Caturla, B. Décamps, C. Ferrero, H. Greuner, C. Hébert, T.

Höschen, M. Hofmann, C. Hugenschmidt, T. Jourdan, M. Köppen, T. Płociński, J. Riesch, M. Scheel, B. Schillinger, A. Vollmer, T. Weitkamp, W. Yao, J.-H. You, and A. Zivelonghi, Journal of Nuclear Materials (2013).

[36] *Fusion Electricity – A Roadmap to the Realisation of Fusion Energy (http://www.efda.org/downloads/)* (EFDA, 2013).

[37] F. Maury, P. Lucasson, A. Lucasson, F. Faudot, and J. Bigot, Journal of Physics F: Metal Physics **17**, 1143 (1987).

[38] C. Dimitrov, A. Benkaddour, C. Corbel, and P. Moser, Annales De Chimie-Science Des Materiaux **16**, 319 (1991).

[39] C.-C. Fu, J. Dalla Torre, F. Willaime, J. L. Bocquet, and A. Barbu, Nature Materials **4**, 68 (2005).

[40] D. Terentyev, N. Castin, and C. J. Ortiz, Journal of Physics: Condensed Matter **24**, 475404 (2012).

[41] A. Vehanen, P. Hautojärvi, J. Johansson, J. Yli-Kauppila, and P. Moser, Phys. Rev. B **25**, 762 (1982).

[42] L. Malerba, A. Caro, and J. Wallenius, Journal of Nuclear Materials **382**, 112 (2008).

[43] L. D. Dulca, Cluster and Short-Range Order Influence on the Electrical Resistivity of Binary Alloys, Universität Bremen, 2000.

[44] B. Segall, Physical Review **124**, 1797 (1961).

[45] H. M. Rosenberg, *The Solid State: An Introduction to the Physics of Crystals for Students of Physics, Materials Science, and Engineering*, 2d ed (Clarendon Press, Oxford, 1978).

[46] M. Isshiki and K. Igaki, Transactions of the Japan Institute of Metals **19**, 431 (1978).

[47] I. A. Campbell, A. Fert, and R. Pomeroy, Philosophical Magazine **15**, 977 (1967).

[48] H. A. Schulze and K. Lücke, Journal of Applied Physics **39**, 4860 (1968).

[49] E. Balanzat and J. Hillairet, Journal of Physics F: Metal Physics **11**, 1977 (1981).

[50] K. Kohl, W. Scheffel, R. Heidsiek, H. Lücke, Acta Metallurgica **31**, 1895 (1983).

[51] V. Pierron-Bohnes, I. Mirebeau, E. Balanzat, and M. C. Cadeville, Journal of Physics F: Metal Physics **14**, 197 (1984).

[52] R. Poerschke and W. Pfeiler, Scripta Metallurgica **19**, 1085 (1985).

[53] W. Pfeiler, Acta Metallurgica **36**, 2417 (1988).

[54] A. Schulze and K. Lücke, Acta Metallurgica **20**, 529 (1972).

[55] I. A. Campbell and A. A. Gomès, Proceedings of the Physical Society **91**, 319 (1967).

[56] J. M. Ziman, Canadian Journal of Physics **34**, 1256 (1956).

[57] F. Maury, A. Lucasson, P. Lucasson, P. Moser, and F. Faudot, Journal of Physics: Condensed Matter **2**, 9269 (1990).

[58] A. Fert and I. A. Campbell, Journal of Physics F: Metal Physics **6**, 849 (1976).

[59] J. W. F. Dorleijn, Philips Res. Rep. **31**, 287 (1976).

[60] J. W. F. Dorleijn and A. R. Miedema, Journal of Physics F: Metal Physics **7**, L23 (1977).

[61] F. Maury, M. Biget, P. Vajda, A. Lucasson, and P. Lucasson, Physical Review B **14**, 5303 (1976).

[62] A. C. Damask and G. J. Dienes, *Point Defects in Metals* (Gordon and Breach, 1963).

[63] C. J. Ortiz and M. J. Caturla, Physical Review B **75**, (2007).

[64] A. L. Nikolaev, Philosophical Magazine **91**, 879 (2011).

[65] H. Heidsiek, R. Scheffel, and K. L"{u}cke, Le Journal de Physique Colloques **38**, C7 (1977).

[66] L. J. van der Pauw, Philips Research Reports **13**, 1 (1958).

[67] D. K. Schroder, *Semiconductor Material and Device Characterization* (Wiley-Interscience, 1998).

[68] L. B. Valdes, Proceedings of the IRE **42**, 420 (1954).

[69] M. P. Albert and J. F. Combs, IEEE Transactions on Electron Devices **11**, 148 (1964).

[70] ASTM F76 - 86, *Test Methods for Measuring Resistivity and Hall Coefficient and Determining Hall Mobility in Single-Crystal Semiconductors* (ASTM International, 1996).

[71] X. Huang, C. Gao, Y. Han, M. Li, C. He, A. Hao, D. Zhang, C. Yu, G. Zou, and Y. Ma, Applied Physics Letters **90**, 242102 (2007).

[72] X. Huang, C. Gao, D. Zhang, M. Li, C. He, A. Hao, C. Yu, C. Sang, C. Liu, Y. Wang, R. Guan, D. Li, G. Zou, and Y. Ma, Applied Physics Letters **90**, 204102 (2007).

[73] Y. Sun, J. Shi, and Q. Meng, Semiconductor Science and Technology **11**, 805 (1996).

[74] D. Adam, *Low-Voltage Measurement Techniques* (2005).

[75] A. Climent-Font, F. Pászti, G. García, M. T. Fernández-Jiménez, and F. Agulló, Nuclear Instruments and Methods in Physics Research Section B: Beam Interactions with Materials and Atoms **219-220**, 400 (2004).

[76] D. A. Thompson, A. M. Omar, and J. E. Robinson, Journal of Nuclear Materials **85-86, Part 1**, 509 (1979).

[77] O. Dimitrov and C. Dimitrov, Journal of Nuclear Materials **105**, 39 (1982).

[78] *Http://www.efda.org/* (n.d.).

[79] J. Le Coze, *Procurement of Pure Fe Metal and Fe-Based Alloys with Controlled Chemical Alloying Element Contents and Microstructure* (ARMINES Ecole Nationale Superieure des Mines, 2007).

[80] J. F. Ziegler, Nuclear Instruments and Methods in Physics Research Section B: Beam Interactions with Materials and Atoms **219-220**, 1027 (2004).

[81] L. E. Samuels, *Metallographic Polishing by Mechanical Methods*, 4th ed (ASM International, Materials Park, OH, 2003).

[82] Vander Voort, G. F., *ASM Handbook Volume 09: Metallography and Microstructures* (ASM International, Materials Park, OH, 2004).

[83] C. J. Ortiz, D. Terentyev, P. Olsson, R. Vila, and L. Malerba, Journal of Nuclear Materials **417**, 1078 (2011).

[84] A. L. Nikolaev, J. Phys.: Condens. Matter **11**, 8633 (1999).

[85] V. Arbuzov, B. Goshchitskii, V. Sagaradze, S. Danilov, and A. Kar'kin, The Physics of Metals and Metallography **110**, 366 (2010).

[86] J. Corbett, R. Smith, and R. Walker, Physical Review **114**, 1452 (1959).

[87] A. Sosin and H. Neely, Physical Review **127**, 1465 (1962).

[88] P. Hautojärvi, L. Pöllänen, A. Vehanen, and J. Yli-Kauppila, Journal of Nuclear Materials **114**, 250 (1983).

[89] S. Takaki and K. Igaki, JIM **17**, (1976).

[90] A. M. Omar, J. E. Robinson, and D. A. Thompson, Journal of Nuclear Materials **64**, 121 (1977).

[91] A. L. Nikolaev and T. E. Kurennykh, Journal of Nuclear Materials **414**, 374 (2011).

[92] F. Maury, A. Lucasson, P. Lucasson, P. Moser, and F. Faudot, Journal of Physics: Condensed Matter **2**, 9269 (1990).

[93] A. L. Nikolaev, Philosophical Magazine **89**, 1017 (2009).

[94] D. Terentyev and N. Castin, Computational Materials Science **46**, 1178 (2009).

[95] R. Reihsner and W. Pfeiler, Journal of Physics and Chemistry of Solids **46**, 1431 (1985).

[96] P. Erhart, A. Caro, M. Serrano de Caro, and B. Sadigh, Physical Review B **77**, (2008).

[97] A. Caro, M. Caro, E. M. Lopasso, and D. A. Crowson, Applied Physics Letters **89**, 121902 (2006).

[98] F. Willaime, C. C. Fu, M. C. Marinica, and J. Dalla Torre, Nuclear Instruments and Methods in Physics Research Section B: Beam Interactions with Materials and Atoms **228**, 92 (2005).

[99] C.-C. Fu, F. Willaime, and P. Ordejón, Physical Review Letters **92**, (2004).

[100] E. Vincent, C. S. Becquart, and C. Domain, Journal of Nuclear Materials **359**, 227 (2006).

[101] P. Olsson, C. Domain, and J. Wallenius, Physical Review B **75**, (2007).

[102] D. Terentyev, T. Klaver, P. Olsson, M.-C. Marinica, F. Willaime, C. Domain, and L. Malerba, Physical Review Letters **100**, (2008).

[103] P. Olsson, Journal of Nuclear Materials **386-388**, 86 (2009).

[104] D. Terentyev, P. Olsson, T. P. C. Klaver, and L. Malerba, Computational Materials Science **43**, 1183 (2008).

[105] G. Henkelman, B. P. Uberuaga, and H. Jónsson, The Journal of Chemical Physics **113**, 9901 (2000).

[106] N. Castin, R. Pinheiro Domingos, and L. Malerba, International Journal of Computational Intelligence Systems **1**, 340 (2008).

[107] A. Iwase, T. Hasegawa, Y. Chimi, T. Tobita, N. Ishikawa, M. Suzuki, T. Kambara, and S. Ishino, Nuclear Instruments and Methods in Physics Research Section B: Beam Interactions with Materials and Atoms **195**, 309 (2002).

[108] M. Robinson and I. Torrens, Physical Review B **9**, 5008 (1974).

[109] A. Souidi, M. Hou, C. S. Becquart, and C. Domain, Journal of Nuclear Materials **295**, 179 (2001).

[110] A. V. Barashev, D. J. Bacon, and S. I. Golubov, Journal of Nuclear Materials **276**, 243 (2000).

[111] S. M. Dubiel and J. Cieslak, Phys. Rev. B **83**, 180202 (2011).

[112] S. M. Dubiel, J. Cieślak, and H. Reuther, Nuclear Instruments and Methods in Physics Research Section B: Beam Interactions with Materials and Atoms **302**, 48 (2013).

[113] A. Caro, D. Crowson, and M. Caro, Physical Review Letters **95**, (2005).

[114] A. L. Nikolaev, Philosophical Magazine **91**, 879 (2011).

[115] M. Lavrentiev, R. Drautz, D. Nguyen-Manh, T. Klaver, and S. Dudarev, Physical Review B **75**, (2007).

[116] V. V. Ovchinnikov, N. N. Zvigintsev, V. S. Litvinov, and V. A. Osminkin, Fiz. Met. Metalloved **42**, 310 (1976).

[117] V. V. Ovchinnikov, B. Y. Goloborodsky, N. V. Gushchina, V. A. Semionkin, and E. Wieser, Applied Physics A **83**, 83 (2006).